In-Operando Investigations on Lithium-Ion Battery Cells to Improve Performance for the Use in Electric Vehicles

Dissertation

zur Erlangung des Doktorgrades der Naturwissenschaften (Dr. rer. nat.) der Fakultät für Chemie und Pharmazie der Universität Regensburg

vorgelegt von

Janik Scharf

aus Marburg an der Lahn

im Jahr 2025

Die vorgelegte Dissertation entstand in der Zeit von Mai 2021 bis April 2024 in Kooperation des Instituts für Analytische Chemie, Chemo- und Biosensorik der naturwissenschaftlichen Fakultät Chemie und Pharmazie der Universität Regensburg

zusammen mit dem

Lehrstuhl der strukturellen Chemie am Ångstrom Labor der Universität Uppsala,

sowie

der Technologie Werkstoff und Verfahrensanalytik der BMW AG.

Die Arbeit wurde angeleitet von: Prof. Dr. Frank-Michael Matysik (Uni Regensburg).

Das Promotionsgesuch wurde eingereicht am:	5. Februar 2025
Termin des Kolloquiums:	24. April 2025

Prüfungsausschuss:

Vorsitzender:	Prof. Dr. Alkwin Slenczka
Erstgutachter:	Prof. Dr. Frank-Michael Matysik
Zweitgutachter:	Prof. Dr. Erik Berg
Drittprüfer:	Prof. Dr. Arno Pfitzner

"Man merkt nie, was schon getan wurde,
man sieht immer nur, was noch zu tun bleibt".

Marie Curie (1867 - 1934)

Danksagung

Zuallererst möchte ich mich bei Prof. Dr. Frank-Michael Matysik für die gute Betreuung während meiner Promotion bedanken. Ihre Erfahrung im Bereich der Industriepromotionen und den damit verbundenen Herausforderungen waren stets eine große Bereicherung für mich. Darüber hinaus gilt mein Dank Prof. Dr. Erik Berg für die vertiefende fachliche Betreuung während der gesamten Promotionszeit. Ohne sein Engagement wäre die Inbetriebnahme des OEMS-Teststands auf diesem Level wohl kaum möglich gewesen. Er stand mir jederzeit für Detailfragen bezüglich technischer Probleme, weiterer Optimierungen und Interpretation der Messungen zur Verfügung. Die vielen persönlichen Austauschrunden an der Universität Uppsala oder in der Technologie- und Werkstoffanalytik der BMW Group waren außerordentlich wertvoll! Auch möchte ich an dieser Stelle Casimir Misiewicsz für die tolle Zeit und den fachlichen Austausch am Lehrstuhl der Universität Uppsala danken. Neben einer detaillierten Einarbeitung in den "Arbeitsalltag" am dortigen OEMS, führten wir hier auch die ersten Formierungs-Experimente an großformatigen Zellen durch. Vielen Dank für die ausführlichen Hilfestellungen bei der Datenauswertung und -interpretation. Dem weiteren Prüfungsausschuss bestehend aus Prof. Dr. A. Slenczka und Prof. Dr. Pfitzner danke ich für die Begutachtung der Dissertation und Durchführung des Promotionskolloqiums.

Auf Seiten der BMW Group möchte ich mich zuerst bei Dr. Michael Leitl bedanken, der als mein anfänglicher Betreuer, das OEMS-Projekt initiierte und mich hervorragend in die Prozesse und das Team der Zellanalyse integrierte. Die sehr gute Einbindung in diverse andere Fachbereiche mit zahlreichen Ansprechpartnern, sowie die anfänglichen Leitfäden zu OEMS-Fragestellungen erleichterten mir den Start, gerade während der Coronapandemie, enorm. Ein weiterer großer Dank geht an Prof. Dr. Johannes Wandt, der die fachliche OEMS-Betreuung seitens BMW übernahm. Ohne Dich wäre das OEMS-Projekt bei BMW nicht so tiefgehend vorangetrieben worden. Die Diskussionen bezüglich Dichtigkeit und experimenteller Durchführbarkeit waren stets sehr inspirierend und halfen mir, den Status des Teststands und meine Expertise kontinuierlich zu hinterfragen und zu verbessern. Ebenfalls danken möchte ich Filippo Maglia für die Unterstützung bei der Materialbereitstellung und den Absprachen mit Lieferanten im Hinblick auf die bevorstehenden OEMS-Aktivitäten. Dr. Christian von Lüders möchte

ich für seine Hilfe bei der Formierung von prismatischen Zellen danken. Die ersten Tests und Einblicke in die industrielle Zell-Formierung, sowie die strikten Prozesse zur Zellfertigung halfen mir einerseits, den Teststand auf großformatige Zellen umzurüsten, als auch andererseits die Notwendigkeit der Formierungsstudie an großen Zellen, zu erkennen. Nicht zuletzt möchte ich auch Hugo-Hans Rhein von der BMW Metallwerkstatt für die vielen spontanen Lösungen kleinerer und größerer Probleme danken. Sei es bei Fräsarbeiten an der Modellzelle oder der Konstruktion von größeren Teilen für den Teststand - ich konnte mich jederzeit auf seine Unterstützung und zügige Arbeitsweise verlassen.

Im weiteren Sinne danke ich meinen Teamkollegen aus der Zellanalyse, insbesondere Cornelius Hupbauer und Sebastian Foith, sowie den BMW-Kollegen aus meinen Produktions- und Orientierungseinsätzen für die vielen kleinen Hilfestellungen und Einblicke in ihren Arbeitsalltag. Auch danken möchte ich Michael Berg, der mich im Rahmen seiner Bachelorarbeit mit dem Schwerpunkt auf die Gasanalyse der siliciumhaltigen Elektroden excellent im Bereich Rundzellen unterstütze. Darüber hinaus möchte ich mich beim BMW-Doktoranden-Netzwerk bedanken, dem ich zwei Jahre lang als Gebäudesprecher des Batterie-Kompetenz-Zentrums angehören durfte. Der Austausch und das Networking innerhalb des Unternehmens waren sehr wertvoll und wurden durch eine zweiwöchige Reise zu BMW nach China (Shenyang und Peking) belohnt, was die Tragweite dieses Netzwerks unterstreicht und absolut einzigartig macht. Auch danken möchte ich an dieser Stellen den Doktoranden innerhalb des BMW-Batterieforschungsumfeldes. Insbesondere Hyojeong Kim, Sabrina Schönemeier, Marco Düsdieker, Fatma Uelke und Johannes Brehm, sowie Sebastian Hölle und Marlene Zink. Die kurzen Gespräche, Kafferunden, spontanen Partyabende und (Ski)-Ausflüge haben die Promotionszeit um einiges annehmbarer und entspannter gestaltet, vielen Dank!

Zu guter Letzt möchte ich meiner Familie und Freunden für ihre Unterstützung aber auch Verständnis danken. Ganz besonders danke ich an dieser Stelle meiner Freundin Pauline, für die viele Unterstützung in der entbehrungsreichen Zeit des Schreibens, insbesondere im letzten Jahr. Du hast immer an mich geglaubt und auch in schwierigen Situationen stets die richtigen Worte für mich parat gehabt. Darüber hinaus hast du mir auch gezeigt, dass die Welt nicht nur aus Schreiben besteht, sondern aus so viel mehr, vielen Dank! Nach nun insgesamt 13 Jahren "Ausbildung" hat das Warten ein Ende. Danke für eure Geduld!

Contents

Eidesstattliche Erklärung / Statement of authorship

Hiermit erkläre ich an Eides statt, dass es sich bei der von mir eingereichten schriftlichen Dissertation, zur Erlangung des akademischen Grades eines Doktors der Naturwissenschaften, mit dem Titel

"In-Operando Investigations on Lithium-Ion Battery Cells to Improve Performance for the Use in Electric Vehicles"

um eine von mir selbstständig und ohne fremde Hilfeleistung verfasste schriftliche Arbeit handelt. Ich erkläre zudem, dass ich sämtliche verwendeten Angaben aus der Literatur (Internet, Bücher, wissenschaftliche Zeitungen und wörtlich übernommene Tabellen und Graphiken etc.) als solche kenntlich gemacht habe. Abbildungen und Tabellen, die aus eigenen Veröffentlichungen stammen, sind ebenfalls als solche kenntlich gemacht.

Niemand hat von mir weder unmittelbar noch mittelbar geldwerte Leistungen für Arbeiten erhalten, die im Zusammenhang mit dem Inhalt der vorgelegten Dissertation stehen. Insbesondere habe ich hierfür nicht die entgeltliche Hilfe eines Promotionsberaters oder anderer Personen in Anspruch genommen. Von den in §27 Abs. 5 vorgesehenen Rechtsfolgen habe ich Kenntnis genommen.

Die Arbeit wurde bisher weder im In- noch im Ausland in gleicher oder ähnlicher Form einer anderen Prüfungsbehörde vorgelegt. Die vorgelegten Druckexemplare und die dem Prüfer/der Prüferin zur Verfügung gestellte elektronische Version (PDF-Datei) der Arbeit sind identisch.

Regensburg, den 10. Juni 2025

. . . . . .
(Janik Scharf)

Erklärung zur Zusammenarbeit / Declaration of collaboration

Most of the practical and theoretical work of this thesis was performed solely by the author. Parts of the obtained results were achieved in cooperation with other researchers. In accordance with § 8 Abs. 1 Satz 2 Punkt 7 of the Ordnung zum Erwerb des akademischen Grades eines Doktors der Naturwissenschaften (Dr. rer. nat.) an der Universität Regensburg vom 18. Juni 2009 (Änderungssatzung vom 18. Dezember 2023), the nature of these collaborations is described in this section.

I.) Study of the Response Characteristics of an OEMS System Using Chronoamperometry:

The experimental work and data evaluation was carried out by the author. The author wrote the initial draft of the manuscript. The article was revised and discussed with the corresponding author Frank-Michael Matysik.

II.) Impact of Electrode Densification on the Electrochemical Performance and Gassing Behavior of NMC955:

The experimental work and data evaluation was carried out by the author. Casimir Misiewicz provided the laser-perforated current collector substrate. Johannes Wandt provided knowledge for electrode densification process as well as data evaluation. M. Sc. Marlene Zink provided support during SEM measurements. The corresponding section within this thesis was written solely by the author. The section was revised and discussed with the corresponding parties Frank-Michael Matysik, Johannes Wandt and Erik Berg.

III.) Gas Evolution in Large-Format Automotive Lithium-Ion Battery During Formation; Effect of Cell Size and Temperature:

The experimental work and data evaluation was carried out by the author. The author wrote the initial draft of the manuscript. Christian von Lüders supported regarding the methodology on large format cell experiments. First OEMS experiments on large-format cells were carried out with Casimir Misiewicz in Uppsala. Johannes Wandt provided knowledge regarding the methodology on model cell experiments as well as review and editing of the manuscript. Frank-Michael Matysik and Erik Berg were responsible for supervision, conceptualization, as well as reviewing and editing. The authors acknowledge the EuBatIn (16BZF205), the Federal Ministry of Economics Affairs and Climate Action and the Bavarian Ministry of Economic Affairs, Regional Development and Energy for financial support. C.M. and E.J.B. acknowledge the Swedish Electromobility Centre (SEC), Knut and Alice Wallenberg (KAW) Foundation (Grant 2017.0204), Swedish Research Council (2016–04069), and the Swedish Foundation for Strategic Research (SSF, FFL18-0269) for financial support and StandUP for Energy for base funding.

IV.) Gas Evolution in SiOx-containing Battery Cells:

Cell chamber development and scope of the work was planned and carried out by the author. Main fundamental studies, including electrode production, model cell experiments and large format cell analysis were carried out by Michael Berg within his B.Sc. thesis.

Kurzfassung

Eine Lithium-Ionen-Batterie stellt derzeit die teuerste Einzelkomponente dar, die in einem Elektrofahrzeug integriert ist. Da der Marktwert, sowie etwaiige Garantieansprüche eines Elektrofahrzeuges ganz erheblich mit der Qualität des Hochvoltspeichers einhergehen, kommt der Lebensdauer einer Batteriezelle eine ganz spezielle Bedeutung zu. Hochautomatisierte Fertigungsprozesse, sowie abgestimmte Lade-/ Entladeprotokolle helfen die Lebensdauer zu erhöhen und gleichzeitig das Potential der jeweiligen Zellchemie voll ausnutzen.

In diesem Kontext spielt das Verständnis über Alterungsmechanismen und deren Ursache & Auswirkung eine immer bedeutendere Rolle in der Batterieentwicklung. Ein wichtiger Aspekt liegt in der Echtzeitanalyse parasitärer Nebenreaktionen, mit gasförmigen Komponenten. Um diese gasförmigen Nebenprodukte zeit- und potentialaufgelöst analysieren zu können, sind fortschrittliche analytische Techniken mit hoher Selektivität und Empfindlichkeit erforderlich. Die Online-Elektrochemische-Massenspektrometrie (OEMS) hat sich bisher als am leistungsfähigsten erwiesen, um nicht nur den Beginn und das Ausmaß der Gasbildung, sondern auch die interne Gaszusammensetzung unter realen Betriebsbedingungen innerhalb der Batteriezelle bestimmen zu können.

Diese Doktorarbeit mit dem Titel "In-Operando-Untersuchungen an Lithium-Ionen-Batteriezellen zur Verbesserung der Leistung für den Einsatz in Elektrofahrzeugen" konzentriert sich auf die Implementierung eines OEMS-Systems und die Durchführung detaillierter Echtzeit-Analysen von Lithium-Ionen-Batteriezellen. Besonderes Augenmerk wurde hierbei auf die Analyse großer Fahrzeugbatteriezellen (prismatisch und zylindrisch) gelegt. Die hervorragende Anpassungsfähigkeit & Skalierbarkeit, sowohl für Forschungszellen (Swagelok-Zellen) als auch großformatige Zellen, wie auch die volle Mobilität und der hohe technische Standard des OEMS-Teststands hinsichtlich Sauberkeit und Robustheit, machen das hierin beschriebene OEMS-System bisher einzigartig. Die aus dieser Arbeit abgeleiteten Erkenntnisse tragen dazu bei, sowohl die Leistung von Batteriezellen als auch die Produktionskosten insbesondere für Elektrofahrzeuganwendungen zu optimieren. Der Ergebnisteil der Dissertation besteht aus vier Schlüsselkapiteln:

I.) Studie über die Ansprechcharakteristik eines OEMS-Systems unter Verwendung von Chronoamperometrie: In diesem Kapitel wurden die Echtzeitansprechcharakteristiken von Lithium-Ionen-Batteriezellen unter konstanten Strombedingungen (chronoamperometrisch) untersucht. Die Studie konzentrierte sich auf die Bewertung der Ansprechzeit, Empfindlichkeit und Genauigkeit des OEMS-Systems bei der Erkennung verschiedener Gasarten wie Wasserstoff, Sauerstoff und Kohlendioxid, die üblicherweise während des Batteriebetriebs erzeugt werden. Der Einfluss des Stromkollektor-Substrats auf das Gasbildungsverhalten wurde ebenfalls untersucht, um ein umfassendes Verständnis der Fähigkeiten und Grenzen des OEMS-Systems zu schaffen.

II.) Auswirkungen der Elektrodenverdichtung auf das elektrochemische Leistungsverhalten von NMC955: Dieses Kapitel konzentriert sich auf die Untersuchung, wie sich die Verdichtung des Elektrodenmaterials auf dessen elektrochemische Leistung auswirkt. Durch Variation der Elektrodendichte durch sogenanntes Kalandrieren wurden die Auswirkungen der Kompaktierung auf Schlüsselleistungsparameter wie Kapazität, Leistungsfähigkeit und Gasfreisetzung untersucht. Ziel war es zu verstehen, wie parasitäre Nebenreaktionen vom Grad der Elektrodenverdichtung abhängen, um die elektrochemischen Eigenschaften des zukünftigen Hochenergiematerials zu optimieren und so die Energiedichte, Leistungsabgabe und Lebensdauer - alles entscheidende Faktoren für Elektrofahrzeuganwendungen - zu verbessern. Des Weiteren wurde aufgezeigt, dass sich die OEMS-Technik hervorragend zur schnellen Untersuchung einzelner Produktionsparameter (wie z. B. dem Kalandrieren) eignet.

III.) Gasfreisetzung in großformatigen Automotive-Lithium-Ionen-Batterien während der Formierung: Auswirkung der Zellgröße und Temperatur: Dieses Kapitel untersucht das Gasfreisetzungsverhalten in großformatigen Zellen während des kritischen SEI-Formierungszyklus. Der Prozess, bei dem die Batterie erstmals geladen und entladen wird, ist bekannt dafür, dass verschiedene Gasarten wie H_2, CO, CO_2, und C_2H_4 entstehen, die vor dem Verschluss der Zelle entfernt werden sollten. Die zeitaufgelöste Sicht auf die Gasungsprozesse kann daher die Zellproduktion erheblich beschleunigen und die Kosten in der Zellfertigung senken. Die Experimente wurden an zwei unterschiedlichen Zellgrößen durchgeführt, um die Auswirkungen der Zellgröße auf die Gasbildung zu beurteilen. Zusätzlich wurden die Zellen bei unterschiedlichen Temperaturen von + 10 °C bis + 45 °C geladen, um die thermischen Auswirkungen auf das Gasfreisetzungsverhalten und die SEI-Zusammensetzung zu verstehen. Durch die Analyse der Gasdaten in Verbindung mit anderen *ex-situ* Methoden zielte die Studie darauf ab, Einblicke in die zugrunde liegenden Mechanismen zu gewinnen, die die Gasbildung in großformatigen Lithium-Ionen-Batterien steuern. Die Erkenntnisse aus diesem Kapitel können Batteriehersteller und Systemdesigner dabei unterstützen, die Formierungsprotokolle und die SEI-Eigenschaften von großformatigen Lithium-Ionen-Batterien zu verbessern.

IV.) Gasfreisetzung in SiO_x-haltigen Batteriezellen: Dieses Kapitel konzentriert sich auf die Untersuchung der Gasfreisetzung in Lithium-Ionen-Batteriezellen, die Siliziumoxid (SiO_x) als Teil des Anodenmaterials enthalten, welches eine entscheidende Rolle für die Kommerzialisierung von Hochenergie-Lithium-Ionen-Batterien darstellt. Ziel ist es, die Gasentwicklungsmechanismen und -dynamiken in dieser Art von Batteriechemie zu verstehen, was bei der Entwicklung verbesserter Silizium-basierter Elektroden helfen kann. Zunächst wurde das Gasfreisetzungsverhalten von Modellbatteriezellen mit SiO_x-basierten Anoden unter Verwendung verschiedener Elektrolytzusammensetzungen detailliert untersucht. Zweitens wurden zylindrische Zellen in automotive Auslegung (Typ 4695) mit Hilfe einer neuartigen *in-opeando* Analysenkammer untersucht. Dies beinhaltet eine Analyse der Gasfreisetzung während des Formierungszyklus, mit besonderem Fokus auf den Einfluss der Temperatur auf das Gasfreisetzungsverhalten.
Darüber hinaus präsentiert dieser Abschnitt eine Machbarkeitstudie zur Gasentwicklung in einer 4695-Zelle, unter normalen Betriebssbedingungen (Lade-/ Entladezyklus). Als Proof-of-Concept zeigt dieser Abschnitt die Anwendbarkeit der entwickelten Analysenkammer, dass die zeit- und potenzialaufgelösten Gasanalyse für jede Art von Batteriezelle in jeder Phase der Lebensdauer angewendet werden kann. Darauf aufbauend können weitere Studien erfolgen, die die Gasentwicklung unter normalen Betriebsbedingungen (Laderate, Abschaltspannung, Temperatur, Zellchemie, etc.) detailliert untersuchen. Auch die Wirksamkeit spezieller Additive, die die Gasbildung unterdrücken bzw. verringern, können so gezielt untersucht werden. Zuletzt besteht die Möglichkeit, mithilfe des dargestellten Setups eine *in-operando*-Analyse spezifischer Batteriezellen auf die zuvor genannten Parameter durchzuführen.

Zusammenfassend bietet die Entwicklung und Anwendung der *in-Operando*-Gasanalyse, insbesondere an großformatigen Zellen, eine einzigartige Gelegenheit, leistungs-/ und lebensdauer-begrenzende Nebenreaktionen während des Betriebs elektrochemischer Zellen aufzuklären und so zukünftige Zellchemien besser ausnutzen zu können, bei gleichzeitiger Optimierung der Lebensdauer. Die Anwendung der *in-Operando* Versuchszelle bietet hierbei die Gelegenheit ein grundsätzlich fundamentales Verständnis über die elektrochemischen Degradationsprozesse auf Materialebene zu erforschen und zu charakterisieren.

Abstract

An automotive lithium ion battery cell is currently the most expensive single component integrated in an electric vehicle. As the market value and any warranty claims of an electric vehicle are very much dependent on the quality of the high-voltage battery pack, the lifetime of a battery cell is of particular importance. Highly automated production processes and optimized charging / discharging protocols help to increase the lifetime and at the same time utilize the potential of the respective cell chemistry to its maximum.

In this context, the understanding of aging mechanisms and their cause & effect is playing an increasingly important role in battery development. One important aspect is the real-time analysis of parasitic side reactions with gaseous components. In order to analyze these gaseous by-products in a time- and potential-resolved approach, advanced analytical techniques with high selectivity and sensitivity are required. Online electrochemical mass spectrometry (OEMS) has hitherto been proven most powerful to determine not only the onset and extent of gas evolution, but also the internal composition under *operando* conditions.

This PhD thesis, titled "In-Operando Investigations on Lithium-Ion Battery Cells to Improve Performance for the Use in Electric Vehicles," focuses on the implementation of an OEMS system and conducting detailed real-time analyses of lithium-ion battery cells to gain insights that help to enhance their performance and reducing production costs, especially for electric vehicle applications. The various possible settings, excellent adaptability and scalability towards large format cells makes the herein described OEMS system comparable to nothing else. The results section of the thesis consists of four key chapters:

I.) Study of the Response Characteristics of an OEMS System Using Chronoamperometry: In this chapter the real-time response characteristics of lithium-ion battery cells under constant current (chronoamperometric) conditions were studied. The study focused on evaluating the OEMS system's response time, sensitivity, and accuracy in detecting various gas species, such as hydrogen, oxygen, and carbon dioxide. The influence of the current collector substrate on the gas evolution behavior was also studied to establish a comprehensive understanding of the OEMS system's capabilities and limitations.

II.) Impact of Electrode Densification on the Electrochemical Performance of NMC955: This chapter focuses on the investigation of how the compaction of the electrode material affects its electrochemical performance. By varying the electrode density through so-called calendering, the effects of compaction on key performance parameters such as capacitance, efficiency and gas release were investigated. The aim was to understand how parasitic side reactions depend on the degree of electrode compaction in order to optimize production parameters as well charge/discharge parameters of this future high-energy material. Thus improving energy density, power output and lifetime - all crucial factors for electric vehicle applications. In this work it was also shown that OEMS technology is ideally suited to do rapid investigation of individual production parameters, such as calendering, and their influence on the electrochemical performance of the produced electrode/battery.

III.) Gas Evolution in Large-Format Automotive Lithium-Ion Battery During Formation: Effect of Cell Size and Temperature: This chapter examines the gas evolution behavior in large-format prismatic cells during the critical SEI formation. The process, which involves the initial charging and discharging of the battery, is known to be accompanied by the generation of various gaseous species, such as H_2, CO, and CO_2, which might be removed before the cell can be sealed and shipped. Hence, a time-resolved view on those gas evolution processes, can speed up production and reducing costs in manufacturing. The experiments were conducted on two different cell sizes to assess the impact of cell scale on gas generation. Additionally, the cells were charged at different temperatures, ranging from + 10 °C to + 45 °C, to understand the thermal effects on the gas evolution behavior. By analyzing the OEMS data in conjunction with other *ex-situ* methods, the study aimed to provide insights into the underlying mechanisms governing gas generation in large-format cells. The findings from this chapter help battery manufacturers and system designers optimize the formation protocols and cell chemistry.

IV.) Gas Evolution in SiO_x-containing Battery Cells: This chapter focuses on the study of gas release in lithium-ion battery cells containing silicon oxide (SiO_x) as part of the anode material, which plays a crucial role in the commercialization of high-energy lithium-ion batteries. The aim is to understand the gas evolution mechanisms and dynamics in this type of battery chemistry, which can help in the development of improved silicon-based electrodes. First, the gas release behavior of model battery cells with SiO_x-based anodes was investigated in detail using different electrolyte compositions. Secondly, cylindrical cells in automotive design (type 4695) were investigated using a novel *in-operando* analysis chamber. This includes an analysis of the gas release during the formation cycle, with a special focus on the influence of temperature on the gas release behavior.

In addition, this section presents a feasibility study of gas evolution in a 4695 cell under normal operating conditions (charge/discharge cycle). As a proof-of-concept, this section demonstrates the applicability of the developed analytical chamber that time- and potential-resolved gas analysis can be applied to any type of battery cell at any stage of its life cycle. Based on this, further studies can be carried out to investigate the gas development under normal operating conditions (charging rate, cut-off voltage, temperature, cell chemistry, etc.) in detail. The effectiveness of special additives that suppress or reduce gas formation can also be specifically investigated in this way. Finally, an *in-operando* analysis of selected battery cells for the above-mentioned parameters can also be carried out with the setup shown.

In summary, the development and application of *in-operando* gas analysis, especially on large-scale cells, offers a unique opportunity to elucidate performance- and lifetime-limiting side reactions during the operation of electrochemical cells and thus to better exploit future cell chemistries while optimizing lifetime. The application of the introduced *in-operando* model cell (coin cell) offers the opportunity to explore and built a fundamental understanding of the electrochemical degradation processes at the material level.

List of Abbreviations

AC	alternating current
Al	alumina
AAM	anode active material
ASSB	all solid state battery
BET	brunauer-emmett-teller
BEV	battery electric vehicle
BMW AG	bayerische motoren werke aktiengesellschaft
CA	chronoamperometry
CAM	cathode active material
CATL	contemporary amperex technology co. limited
CCCV	constant current constant voltage
CE	coloumbic efficiency
CEI	cathode electrolyte interface
CI	chemical ionization
CLO	crimped capillary leak open
Cu	copper
CT	computed tomography
CV	cyclic voltammetry
DC	direct current
DCA	differential capacity analysis
DEC	diethyl carbonate
DEMS	differential electrochemical mass spectrometry
DMC	dimethyl carbonate
DOE	US department of energy
DVA	differential voltage analysis (dV/dQ)
EC	ethylene carbonate
EI	electron ionization
EIS	electrochemical impedance spectroscopy
EMC	ethyl-methyl carbonate
EoL	end of life
ESI	electro-spray ionization
EV	electric vehicle
FEC	fluoroethylene carbonate
FFKM	perfluoroelastomeric
FT-IR	fourier transform-infrared spectroscopy
FWHM	full width at half maximum
GC	gas chromatography
GCPL	galvanostatic cycling with potential limitation
HDPE	high density polyethylene
HOMO	highest occupied molecular orbital
HOPG	highly oriented pyrolytic graphite
ICA	incremental capacity analysis (dQ/dV)
ICE	internal combustion engine

ICEMS	intermittently closed electrochemical mass spectrometry
ICP-MS	inductively coupled plasma-mass spectrometry
IR	infrared spectroscopy
LC	liquid chromatography
LCO	$LiCoO_2$
LEDC	lithium ethylene dicarbonate
LFP	$LiFePO_4$
LIB	lithium-ion battery cell
LiBOB	lithium-bis-(oxalato)borate
LiDFBOB	lithium-difluoro-(oxalato)-borate
LiDODFP	lithium-difluorobis-(oxalato)-phosphate
LiOTFP	lithium-tetrafluoro-(oxalato)-phosphate
LiTFSI	lithium-bis-(trifluoromethane-sulfonyl)-imide
LMO	$LiMn_2O_4$
LNO	$LiNiO_2$
LNMO	$LiNi_{0.5}Mn_{1.5}O_4$
LTO	$Li_{14}Ti_{15}O_{12}$
LUMO	lowest unoccupied molecular orbital
MALDI	matrix assisted laser desorption/ionization
MRI	magnetic resonance imaging
MS	mass spectrometry
NCA	lithium nickel cobalt alumina-oxide
NMC	lithium-nickel-manganese-cobalt-oxide
NMP	n-methyl-2-pyrrolidone
NMR	nuclear magnetic resonance spectroscopy
OECD	organization for economic co-operation and development
OCV	open circuit voltage
OEM	original equipment manufacturer
OEMS	online electrochemical mass spectrometry
pc	poly crystalline
PC	propylene carbonate
PEEK	polyether ether ketone
PES	1,3-propane sultone
POM	polyoxymethylene
PTFE	polytetrafluoroethylene
PVDF	polyvinylidene difluoride
QMS	quadrupole mass spectrometer
sc	single crystalline
SEI	solid electrolyte interface
SEM	scanning electron microscopy
SECM	scanning electrochemical microscopy
SOC	state of charge
SOH	state of health
SS	stainless-steel
STA-MS	simultaneous thermal analysis-mass spectrometry
TM	transition metal
TMO	transition metal oxide
TOF	time of flight
UHV	ultra high vacuum
UPS	uninterruptible power supply
VC	vinylene carbonate
WCA	weakly coordinated anion
WE	working electrode
XRD	x-ray diffraction
XPS	x-ray photoelectron spectroscopy

Physical Abbreviations and Universal Constants

B	BET-Constant		
c	speed of light	$2.9 \cdot 10^5$	/ $\mathrm{m \cdot s^{-1}}$
C_x	charge/discharge capacity		/ $\mathrm{mAh \cdot g^{-1}}$
δ_{diff}	diffusion layer		/ m
d	field free flight path		/ m
D	diffusion coefficient		/ $\mathrm{m^2 \cdot s^{-1}}$
E_0	standard electrochemical potential		/ V
E_{g}	electrolyte stability window		/ V
E_{OCV}	open circuit voltage potential		/ V
E_{A}	absorption energy		/ $\mathrm{kg \cdot m^2 \cdot s^{-2}}$
$E_{\mathrm{g/e}}$	energy of ground / excited state		/ $\mathrm{kg \cdot m^2 \cdot s^{-2}}$
E_γ	energy of γ-quantum		/ $\mathrm{kg \cdot m^2 \cdot s^{-2}}$
F	Faraday constant	96485	/ $\mathrm{C \cdot mol^{-1}}$
h	Planck constant	$6.026 \cdot 10^{-34}$	/ $\mathrm{J \cdot s}$
η	over-potential		/ V
j_0	exchange current density		/ $\mathrm{mA \cdot cm^{-2}}$
I	charge/discharge current		/ A
$j_{\mathrm{A/C}}$	anodic/cathodic current density		/ $\mathrm{mA \cdot cm^{-2}}$
$\mu_{\mathrm{A/C}}$	anodic/cathodic chemical potential		/ mA
m	mass of particle		/ kg
$m_{El.}$	weight of electrode		/ kg
M	molar mass		/ $\mathrm{g \cdot mol^{-1}}$
n	amount of substance		/ mol
$\dot{n}$	material flow rate		/ $\mathrm{mol \cdot min^{-1}}$
N_{A}	Avogadro constant	$6.02 \cdot 10^{23}$	/ $\mathrm{mol^{-1}}$
$N \cdot m$	Newton meter		/ $\mathrm{N \cdot m}$
p	pressure		/ Pa
p/p_0	relative pressure of adsorbate		
R	ideal gas constant	8.3145	/ $\mathrm{J \cdot (mol \cdot K)^{-1}}$
S	specific surface area		/ $\mathrm{m^2}$
σ	molecular cross section		/ $\mathrm{m^2}$
T	temperature		/ K, °C
T_{vap}	evaporation temperature		/ K, °C
T_{M}	melting temperature		/ K, °C
t	time		/ s
τ_r	retention time		/ s
τ_R	response time		/ s
V	volume		/ L
$V_{\mathrm{abs.}}$	volume of absorbed gas		/ $\mathrm{m^3}$

V_m	gas volume to form monolayer	/ m^3
$\dot{V}$	volume flow rate	/ $\mathrm{mL} \cdot \mathrm{min}^{-1}$
Θ	mass loading	/ $\mathrm{mg} \cdot \mathrm{cm}^{-2}$
θ	surface area via BET-theory	/ $\mathrm{m}^2 \cdot \mathrm{g}^{-1}$
ρ	specific density	/ $\mathrm{kg} \cdot \mathrm{m}^{-3}$
z_e	sum of transferred electrons	
χ_AM	ratio of active material in coating	

Introduction

In 2023, the global daily consumption of oil was estimated to be 102 million barrels, which equates to 16 billions liters. With a global population facing nearly 8 billion inhabitants, the daily consumption of each person is just around 2 liters. It´s the same amount you are advised to drink water! So some readers could argue that human race don´t have to take action, using this little amount of oil each day. However, there is a huge discrepancy among the globe, when it comes to oil consumption. The organization for economic co-operation and development (OECD) countries and the middle east region consume the most oil per capita, leading-up to 10 liters per person each day in the United States and Canada, while emerging markets consume the least. For instance, the oil consumption in the democratic republic of Congo is estimated to be only 0.03 L per person per day.[1–3]

The intense use of fossil fuels results in a massive emission of carbon dioxide (CO_2), which is the main greenhouse gas. Hence a global impact on the climate results from usage of fossil fuels. Now, and in the coming decades. In order to tackle the global warming and to fulfill the Paris agreement (COP21), our energy infrastructure must be reformed by shifting towards renewable energy sources and reducing fossil fuel consumption. However, even in 2023 the global oil demand was still growing, mainly due to emerging countries and the rising demand in road transportation. The global car fleet expanded by more than 600 million cars over the last 20 years, and road freight activity has increased by almost 65 %. Today, internal combustion engine (ICE) based cars make up to 25 % of the global emitted greenhouse gases. Road transportation now accounts for almost 45 % of the global oil demand, which is far more than any other sector.[1–3] Hence, the electrification of the transportation sector towards electric vehicles (EVs) is crucial in order to fulfill COP21.

Almost all major car manufacturer have committed themselves to develop and to release battery electric vehicles (BEVs). The basic concept of lithium-ion battery cells (LIBs) as we know them today, was achieved by the profound and long lasting research effort of

John B. Goodenough, Stanley Wittingham and Akira Yoshina[1]. Based on their research, the nickel-metal hybrid battery was subsequently replaced within all major portable electronic devices like laptops, cell- or head-phones in the late 1990s. Following that, a rapidly evolving market grow of wearable consumer electronics due to production cost reduction has finally let to the begin of electrification of the individual transportation sector in the last ten years. Nowadays, e-scooters, e-bikes and electric cars are part of our daily life. Hence, the usage of LIBs as energy storage devices has become the main topic in the field of energy conversion and the key technology in our modern society.[1]

Additionally, two key buying factors by the customers have to be considered: Firstly, the available driving range of a BEV and secondly, the cost of a BEV compared to an ICE based vehicle. The driving range depends on the total energy of the battery pack and is a function of the energy density of the individual cell and the energy consumption of the car per mile/km. *Blomgren*[4] as well as *Andre et al.*[5] estimated a driving range of $>$ 300 miles as key requirement to bring EV´s successfully to the mass market. The US department of energy (DOE) estimated that a price of $<$ 125 \$/kWh on pack and $<$ 75\$/kWh on battery level needs to be achieved to make BEVs comparable to ICE cars.[6,7] The price for pack level in 2023 already hit a minimum of 139 \$/kWh, which shows that the development is on its path.[8] The newest bayerische motoren werke aktiengesellschaft (BMW AG) Mini Cooper-e has a nominal capacity of 40.7 kWh (36.8 kWh are usable) with an electric range of 190 miles and an energy consumption of 11 kWh/100 km (62 miles).[9] Taken the costs of the study above per kWh as given, a pack price of 5600 \$ is calculated. This is already a fair price, compared to former electric vehicles, where cost where nearly doubled. The Tesla Model 3 which is one of the most successfully sold BEVs comes along with a 60 kWh battery pack (57.5 kWh usable), allowing a driving range of up to 250 miles with an energy consumption of 14.2 kWh/62 miles.[10] The price of the battery pack could be somewhere around 8500 US\$. However, Tesla is using cheaper $LiFePO_4$ (LFP)-based battery cells in this model, making it more affordable. Those two cars show exemplary that BEVs are already competitive to ICE cars even in the mid-price segment.

In order to foster efficient and future proof car assembly processes, huge efforts have been made in terms of mass scale production technologies and process optimization, as well as employee re-training for these new technologies. It is important to note, that the battery pack of an electric vehicle and the vehicle itself underlies strict international regulations towards safety and lifetime, more than any other electronic device.

[1] elected for the noble price in chemistry in 2019

Also a lot of research attention has paid on energy density, lifetime, and safety of LIBs. In the following a short overview about the individual research topics and their current progress & hurdles in regards to BEV application, is given.

1. Screening of Electrode Materials: One crucial aspect of battery performance is the choice of electrode materials. By evaluating various electrode materials regarding their electrochemical performance, structural changes during cycling, and their impact on the overall battery performance, insights into the most suitable electrode materials for enhanced performance and extended lifespan under BEV applications, can be gained. Several hundred kilogram of active material are needed for a high voltage battery pack, therefore also the cost-to-performance ratio is crucial.

2. Electrolyte Optimization: The liquid electrolyte, including solvents, salts and additives plays a vital role in battery performance and safety. By studying different electrolyte formulations, a fundamental understanding of the impact of those components onto cell capacity, cycle life, and safety can be gained. Advanced analytical techniques such as nuclear magnetic resonance spectroscopy (NMR) and electrochemical impedance spectroscopy (EIS) can be employed to analyze electrolyte behavior and its interaction with the electrode materials.

3. Safety and Thermal Management: Battery safety and thermal management are critical, especially for EV applications. By analyzing the impact of different cooling strategies (active/passive cooling) on temperature distribution, performance, and safety, the battery thermal management solutions can be improved and a thermal runaway of the cell can be prevented. The overall cell-pack housing consist of either strong metal parts or plastic components mixed with glass fiber to protect the batteries in case of a fatal accident from intrusion of shrapnel's or deformation. Also the electrical integrity has to be guaranteed, as the final battery-voltage pack comes along with several hundreds of volts.

4. Modeling and Simulation: Mathematical models and simulation tools were developed and can be used to predict battery behavior and performance. By incorporating electrode kinetics, diffusion processes, and thermal effects, these models can simulate battery performance accurately. Validation using in-operando experimental data will ensure the reliability of the models. Ultimately, these models can be used to optimize battery design, predict battery aging, and explore strategies for improving performance, lifespan and also safety requirements. Simulations are also needed for state of health (SOH) and state of charge (SOC) predictions, to precisely inform the driver about the remaining driving range.

5. Production of Battery Cells: Battery cell production requires a high level of precision, uniformity and automatization. However, they also represents a complete new field for existing original equipment manufacturers (OEMs). Based on the individual vehicle and its later application, e.g. city car, van, limousine the cell chemistry and cell design is chosen. Following that the integration of the single cells into the car via battery modules up to high voltage battery pack has to be precisely optimized, in order to achieve a good filling grade of the cars sub-body.

6. Characterization of Battery Degradation: Understanding battery degradation mechanisms is crucial for improving performance and lifespan. By investigating the effects of cycling, temperature, charging/discharging rates, and production steps, key factors contributing to capacity loss and reduced performance, can be identified. Techniques such as EIS and differential capacity analysis (DCA) can be employed to monitor changes in battery impedance and capacity over time.

7. Advanced Diagnostics Techniques: Developing novel in-operando diagnostic techniques can provide valuable insights into battery behavior during operation. Spectroscopic methods e.g. Raman spectroscopy or IR-spectroscopy can be used to analyze chemical and structural changes within the battery environment. Electrochemical techniques e. g. scanning electrochemical microscopy (SECM) can probe local electrochemical activity, while imaging techniques e. g., X-ray tomography or magnetic resonance imaging (MRI) will visualize the spatial distribution of battery components. The development and broad implementation of those techniques will enhance the understanding of battery performance and degradation phenomena and hence improve the development of future battery designs.

In the past and even today each of those topics were separately studied and improved. However, LIBs are complex systems were many requirements in terms of chemistry, material science, intrinsic and industrial limitations are often intimately related. For example increasing the LIB´s voltage would lead to a higher energy density and lower cost ($/kWh), but on the expense of battery lifetime and safety. Furthermore, especially in the automotive sector there was a strong seek of new materials including electrolyte formulations with high energy density to bring EVs to market penetration and to achieve the required power density, while intrinsic limitations and electrochemical degradation phenomena were often disregarded.

One common degradation phenomenon within battery cells is the spontaneous formation of a variety of gaseous species, like hydrogen (H_2), carbon monoxide (CO), carbon dioxide (CO_2), ethylene (C_2H_4), and oxygen (O_2). The origin, extent, and onset of those gas evolution reactions are often elusive and rarely investigated due to the complexity

of the involved parameters. This is particularly true, when it comes to large-format battery cells for automotive purposes. On one side, gas evolution reactions are well known to take place, within cell production, when the cell is charged for the first time and passivation layer formation as well as contamination reduction takes place, see figure 1 for illustration. On the other side, gas evolution reactions can take place during normal cell operation leading to undesirable cell volume expansion and pressure increase. This can cause cell-can deformation, cell failures up to violent short circuits and cell explosions and must be avoided. A detailed investigation of those gaseous components including a fundamental understanding of their origin in terms of chemical decomposition reactions as well as external forces and how to prevent them, can help to further optimize battery cell production, speed up future cell development and might help to further improve battery performance by optimizing charge/discharge protocols.

Figure 1: Single layer pouch cell after assembling (left) and after the first charging procedure (right) to highlight the intrinsic gas formation. The first charging process results in the partial decomposition of some of the liquid electrolyte ingredients and finally results in gas formation. The time-and potential resolved view on these gas formation processes within the first charging procedure is one of the questions, this work deals with.

The gas evolution reactions within battery cells has to investigated in-situ or in-operando during operation of the cell, as contamination and relaxation issues has to be avoided, which would occur during stopping and disassembling procedures. Moreover, the detection of gaseous species requires specialized analytical techniques, such as mass spectrometry. Therefore, the development and adaptation of an online electrochemical mass spectrometry (OEMS) system, especially for the use of large-format automotive cells is the aim of this work. Due to the combination of mass spectrometry in combination with electrochemical cycling procedures, a real-time observation within the battery environment, can be gained and allows to draw conclusion of the origin of those gaseous species under realistic electrochemical conditions.

In focus of this thesis is therefore the determination of the response-time of the developed OEMS-system (chapter 4), the degradation & gassing phenomena of various densified cathode materials (chapter 5), the process optimization of the first charging procedure within large-format prismatic cells, (chapter 6) as well as an out-view for the adaption of the newest cylindrical automotive cell format (chapter 7).

Fundamentals

2.1 Working Principle of a Lithium-Ion Battery

Originally designed as an energy storage device, a lithium-ion battery cell (LIB) converts chemical energy into electrical and vice versa. State of the art LIBs are based on the "rocking-chair" concept, where the lithium ions are shuttled back and forth between the electrodes.[11] This concept is the basis for the design of the electrodes. Intrinsically stable intercalation materials can reversibly store lithium-ions in their host structure, making them rechargeable.[11–13] According to common conventions in the field of LIBs, the electrode with the lower lithiation-potential is the negative electrode and is referred to as the "anode". The electrode with the higher lithiation potential is referred to the positive electrode and called "cathode". This nomenclature is applied consistently throughout this work. The main components of a LIB are illustrated in Figure 2. This essentially represents the 1st cell, introduced by Sony in 1991.[14]

The electrodes specific active materials are commonly mixed with a polymer binder and a conductive carbon agent, to ensure proper adhesion and conductivity between the particles itself, as well as between the current collector foil and the coating. The initially prepared slurry of those components is either water based (anode) or based on n-methyl-2-pyrrolidone (NMP) (cathode). The usage of latter one is heavily discussed due to its health hazards and its onerous recovery during electrode drying. The anode slurry is usually coated onto a copper (Cu) foil, whereas the cathode slurry is coated onto an alumina (Al) foil. Both current collector foils have a thickness of 8-12 µm.[15] The coating thickness of the active materials typically ranges from 50-200 µm. To prevent any mechanical contact that could cause short circuits, a poly-olefin separator with a thickness of 14-25 µm and slightly larger dimensions is placed in between the electrodes.[4] The separator´s pores and the active materials macropores are soaked with a non-aqueous electrolyte mixture, containing a dissociated lithium-salt, usually lithium hexafluorophosphate ($LiPF_6$).

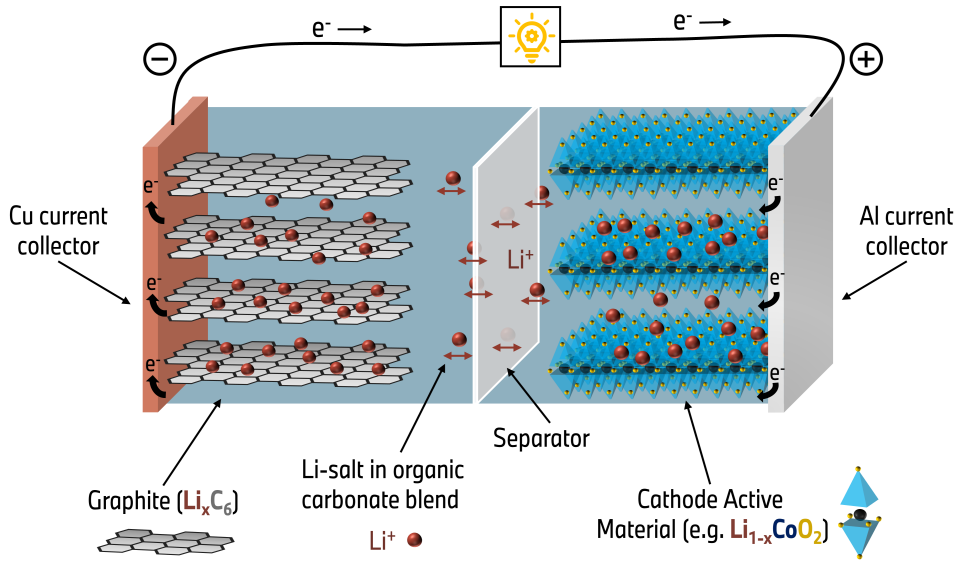

Figure 2: Schematic illustration of the main components and basic working principle of a Li-ion battery, using graphite as anode and $LiCoO_2$ (LCO) as cathode material. Lithium-ions migrate through the electrolyte between the electrodes and can be reversibly intercalated into the host structures, while electrons are transported through the external circuit. Drawn by the author in 2021.

The negative electrode usually comprises graphite as the active material. The redox reaction which is taking place due to oxidation/reduction, is shown in Eq. (2.1). During charge, Li^+-ions intercalate into the graphite host structure, accompanied by an uptake of electrons, forming various Li_xC_6 phases (from x = 0 to 1).

$$C_6 + x\,Li^+ + x\,e^- \underset{\text{discharge}}{\overset{\text{charge}}{\rightleftharpoons}} Li_xC_6 \tag{2.1}$$

Layered transition metal oxides with the general formula $LiMO_2$ (M = Ni, Co, Mn) are typically used within the cathode, from which lithium ions are extracted during charge and inserted during discharge. As an example, the redox reaction of $LiCoO_2$ is shown in Eq. (2.2). This material was 1st-time used by Sony in the 1990s and is still used due to its high volumetric capacity and excellent reversibility.[4]

$$LiCoO_2 \underset{\text{discharge}}{\overset{\text{charge}}{\rightleftharpoons}} Li_{1-x}CoO_2 + x\,Li^+ + \;x\,e^- \tag{2.2}$$

In the upper shown reaction, Co^{3+} is oxidized to Co^{4+} during charge and reduced during discharge as Li^+-ions are shuttled between the electrodes and incorporated into the host structure. The $Co^{3+/4+}$ redox couple serves for charge compensation of the cell, while the initial layered structure is preserved.

The overall cell reaction is simply the sum of the half-cell reactions and expressed in equation (2.3).

$$C_6 + LiCoO_2 \underset{\text{discharge}}{\overset{\text{charge}}{\rightleftharpoons}} Li_xC_6 + Li_{1-x}CoO_2 \tag{2.3}$$

Li^+ always appears as charge carrier through the cell, while the electrons are forced through an external circuit. In general, the following criteria have to be considered, when it comes to electrode active materials (for both electrodes) used in LIBs:

- high specific capacity & high operating cell voltage
- fast lithium diffusion rate
- high electronic conductivity
- abundant host sites for Li-ion accommodation
- excellent (electro)-chemical stability
- low cost, safety and low toxicity

In the following sections, a closer look onto the active materials, as well as the liquid electrolyte will be given.

2.2 Anode Active Materials

Figure 3 highlights the most important anode active materials (AAMs) used in the field of LIBs. The AAM should ideally exhibit a low reaction potential and a rather high specific capacity as both directly define the cell energy.

Back in the early 1980´s, metallic lithium was under serious consideration as active material due to its outstanding specific capacity of ≈ 3860 mAh·g^{-1}.[16] However, as lithium is an excellent reducing agent, it causes continuous side-reactions, leading to high electrolyte losses, within LIB´s.[17,18] One serious consequence is the undesired spontaneous formation of lithium dendrites, also known as Li-plating. The dendrites may penetrate through the separator and causes several cell failures including short circuits, which poses a significant safety risk.[18,19] As this must be avoided under all circumstances, the battery industry was in seek of alternative AAMs. However, lithium is still used until today in academia, due to its rather constant potential and inexhaustible Li^+-source. Lithium metal anodes are still under discussion and the main driver for research on all solid state battery (ASSB).

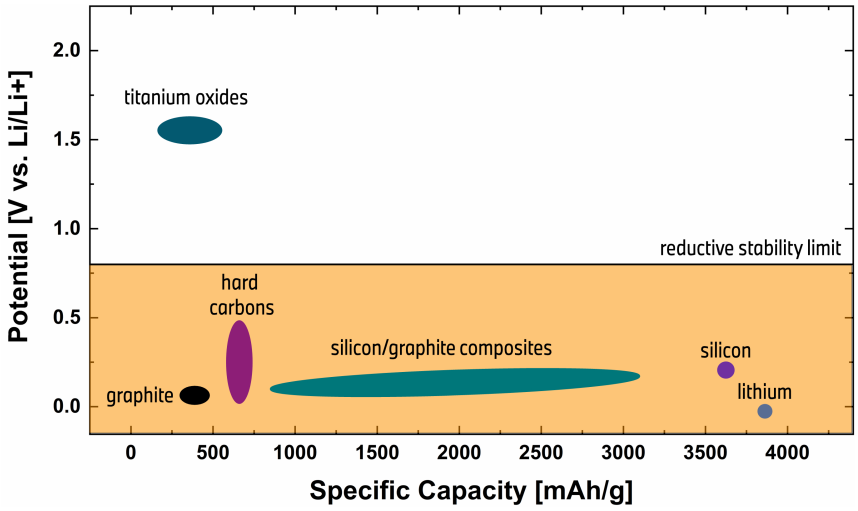

Figure 3: Lithiation potential vs. specific capacity for the most important AAMs. The orange area indicates the reduction window of carbonate-based electrolytes in the absence of a SEI layer. Figure redrawn by author from literature.[16]

Today´s predominantly used AAMs can be classified in intercalate compounds or lithium alloys.[20] The first class mainly rely on carbonaceous materials like graphite and amorphous (soft&hard) carbons, whereas many metals form alloys with lithium. Sony´s 1st cell used soft-carbon as AAM with a specific discharge capacity of ≈ 220 mAh·g^{-1}.[21] The 2nd cell generation by Sony in 1992 was than based on hard carbon material and reached a specific discharge capacity of ≈ 320 mAh·g^{-1}.[22] Hard-carbon materials were further optimized, reaching up to ≈ 550 mAh·g^{-1}.

Their lower sensitivity towards lithium plating and their sloped potential profile allowed faster charging and improved specific energies. Nevertheless, the fact that hard-carbons have a rather poor coloumbic efficiency and a lower volumetric density of ≈ 1.55 g·cm^{-3}, made them soon less favorable for LIB manufacturers. However, in the near future, the necessity of fast charging, might cause to a revival of this material class.[22]

Nowadays, graphite is considered as the state of the art AAM due to its high specific capacity of ≈ 372 mAh·g^{-1} and low, flat operational potential of ≈ 0.1 V vs. Li/Li$^+$ (see lower part of Fig. 4). Additionally, its high volumetric density of ≈ 2.2 g·cm^{-3} [23,24] compared with high abundance and low cost makes graphite the preferred material for mass-produced battery cells.[14,20,22] However, the quality of the graphite material, particularly the nature of its surface, might influence the properties and cycle life of the produced LIB batch.[22,25,26]

The intercalation of Li$^+$-ions in graphite is a highly ordered process that occurs in several stages, resulting in the formation of major compounds such as LiC_{12} and LiC_6.[20,27] In theory the intercalation should be fully reversible. However, in practice a charge recovery of only 80-90 % is observed after the first cycle.[20] The reason for those losses is due to the fact, that the Li$^+$-intercalation potential in graphite is below the thermodynamically stable range of the aprotic electrolyte solution. Therefore, the first intercalation process results in the formation of a nm-thick passivation layer at ≈ 0.8 V vs. Li/Li$^+$.[28]
This layer is known as solid electrolyte interface (SEI), a concept introduced by *Peled et al.*[29–31] in 1979 and further explored in chapter 2.5. Following SEI formation, the reversibility in the 2nd cycle is almost 100 %. The low working potential of graphite may appear beneficial for the specific energy, but it also carries the risk of undesired lithium-plating at high lithium intercalation rates, such as during fast charging.[32] At high charging currents, mass-transport between the liquid electrolyte phase and the solid graphite phase becomes limited.[33] This can cause the cell anode potential to drop locally below 0.0 V vs. Li/Li$^+$, making plating thermodynamically feasible.

To address these safety issues, the spinel-type lithium titanate $Li_{14}Ti_{15}O_{12}$ (LTO) has emerged as an alternative material. It´s high operating voltage of 1.55 V vs. Li/Li$^+$ prevents lithium-plating even under fast charging rates.[34,35] The robust crystal structure of LTO, exhibit almost zero volume change during de-/lithiation, making it a preferred material for long cycle life.[36,37] However, its widespread use is hindered by several disadvantages. LTO-based LIBs come along with a low volumetric density of 1.5-2.0 g·cm^{-3}, resulting in a rather low capacity of ≈ 175 mAh·g^{-1}.[34] The LTO particles additionally faces poor electronic conductivity, which necessitates an additional carbon surface coating and consequently reducing the amount of the active material within the electrode.[38]

Moreover, LTO does not generate a passivating SEI film. This might cause continuous side reactions, e.g. gas evolution reactions, for example when water is being introduced during assembly or when H^+ is formed due to electrolyte oxidation at the high voltage cathode. Both processes can generate a significant amount of hydrogen inside the cell. [39] Therefore, LTO is not considered as suitable material for automotive applications. Nevertheless, due to its excellent cycling stability, it can be used for back-up grid storage systems. [22]

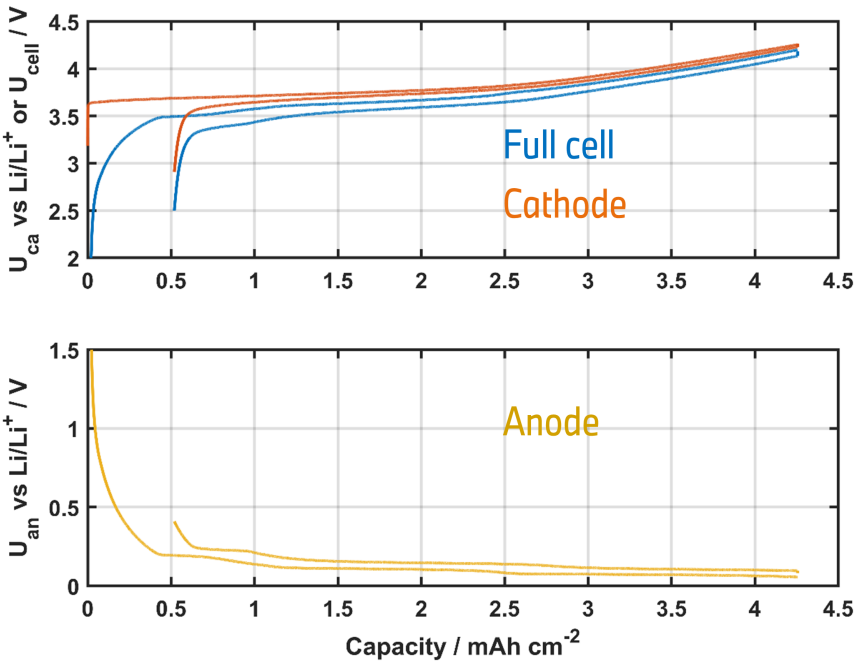

Figure 4: Voltage profile of the first cycle of an NMC811-graphite cell (blue) in commercial electrolyte (1 M $LiPF_6$ in EC:EMC:DEC 1:2:1.5 + Additives) including the respective half-cell potentials of the NMC811 cathode (orange) and the graphite anode (yellow, lower subfigure). The half-cell potentials are measured using a Li-reference electrode. Charge and discharge are performed at a C/10-rate. During charge at 4.2 V, a CV step with a current cut-off of C/50 is applied. Data thankfully provided by M. Duesdieker.

In search for other feasible anode materials, the group of lithium alloys has been investigated for several decades. Many metals can form lithium alloys, with silicon being the most promising candidate. [40] Silicon can be lithiated up to $Li_{15}Si_{14}$, offering a specific capacity of up to $\approx$ 3590 $mAh \cdot g^{-1}$ at a rather low working potential of $\approx$ 0.4 V vs Li/Li^+. This potential is high enough to minimize the risk of lithium dendrite formation. [17,41,42] However, the main limitation is caused by its significant volume changes, which can reach up to 300 % from Si to $Li_{15}Si_{14}$ upon lithiation. [43,44] In comparison to that, graphite only exhibit a volume expansion of $\approx$ 10 % during intercalation (C_6 to Li_xC_6). [45–47] These volume changes induce mechanical stress and particle disintegration.

Additionally, the protective SEI layer cannot withstand these large volume expansions, resulting in a steady SEI re-formation of the freshly exposed surface area, which led to a continuous consumption of electrolyte and ongoing gas evolution due to these side-reactions.[41,48]

Nowadays silicon-graphite composites (C+Si) are increasingly being used in practical applications, as even low amounts of Si can effectively increase the anode´s capacity.[49,50] These electrodes offer the advantages of both materials: graphite for long-term stability and less volume changes, and silicon for fast lithium intercalation and an increased working potential to prevent lithium dendrite formation. These materials are already present in state-of-the-art LIBs, such as Tesla's Model 3.[6,44]

2.3 Cathode Active Materials

Current cathode active materials (CAMs) rely on redox-active transition metal oxides (TMO) which release Li^+-ions upon reduction, making them the active lithium source and determining the capacity of the full cell. To increase the energy density of the cell, such as for extending the driving range of electric vehicles, the CAM should have a high reversible capacity and operating potential.[15] Latter point is particularly important since the anode is already limited by the use of graphite ($\approx$ 0.1 V vs. Li/Li^+).

To achieve electrochemical stability, the material must remain unchanged during the de-/lithiation processes. A highly ordered structure is beneficial to guarantee the long-term stability, as well as a rapid diffusion of Li^+-ions within the bulk material. The electronic conductivity is another key factor for the CAM of choice. If the conductivity of the material is too low, the material must be blended with conducting agents, which lowers the energy density of the whole cell, respectively battery pack. Additionally, the costs of the rather expensive raw metals, such as Co or Ni have become a crucial factor for the commercialization, particularly in the automotive market. Figure 5 provides an overview about the energy density versus the raw metal cost for various CAMs.

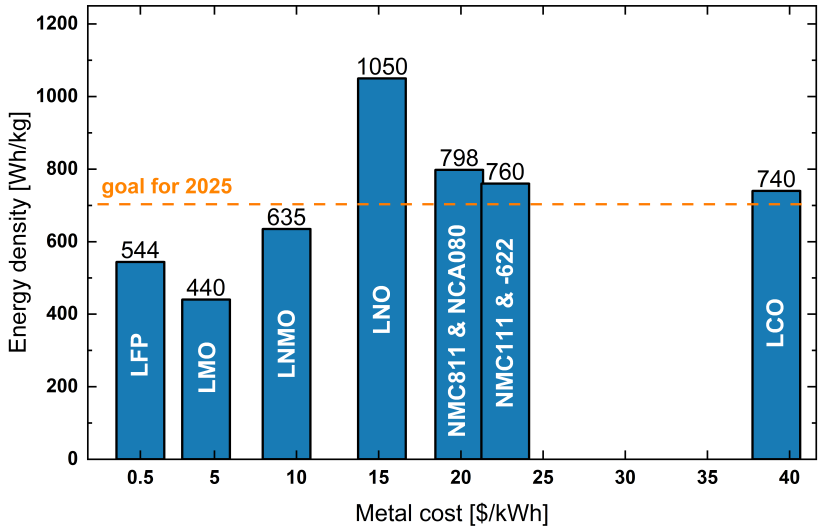

Figure 5: Energy density vs. raw metal cost, for commonly used CAMs. Lithium price is not included. For calculation, the actual metal prices were adapted in January 2024 from daily metal spot price.[51,52]

Lithium cobalt dioxide $LiCoO_2$ (LCO), discovered by Goodenough and coworkers[53] in 1980´s was the 1st material used in commercial lithium-ion cells by Sony in 1991. It has a layered structure and is typically synthesized in the lithiated state, which enables direct coupling with the Li-free anode, such as graphite. The trivalent Co^{3+} resides in octahedral sites within a cubic closed packed array of oxide ions.[54] The Li^+-ions

operate via the $Co^{3+/4+}$ redox couple, where the diffusion takes place via the tetrahedral voids, that share faces with the native octahedral sides. This results in a good Li-ion & electronic conductivity, as the LCO becomes metallic upon delithiation.[54] LCO further provides a working potential of 3.80 V vs. Li/Li^+ and an excellent rate capability. Its high practical press density of 3.9 $g{\cdot}cm^{-3}$ results in a high volumetric energy density. Although the theoretical charge capacity is 274 $mAh{\cdot}g^{-1}$, the practical usable specific charge capacity in the first material generation was only 145 $mAh{\cdot}g^{-1}$ ($\approx$ 544 $Wh{\cdot}kg^{-1}$),[54] which would be far below the current target of $\approx$ 700 $Wh{\cdot}kg^{-1}$ for EVs.[7,15] The capacity losses are a result of several phase transitions and accompanied oxygen-loss within the structure. The cycling stability and cut-off voltage was further improved by using different coating and doping strategies, with Al_2O_3, ZrO_2, or TiO_2 for example. Those optimization lead to an improved specific charge capacity of up to 190 $mAh{\cdot}g^{-1}$ and $\approx$ 740 $Wh{\cdot}kg^{-1}$.[7,55] However, the high Co-content in combination with i) global limited resources, ii) highly problematic mining conditions, and iii) a rather high price of 30 US\$$\cdot kg^{-1}$ [51] makes LCO unsuitable for powering EVs. Attempts to replace the expensive cobalt by the cheaper transition metals manganese and iron failed, as $LiMnO_2$ and $LiFeO_2$ do not crystallize in the O_3-structure-type.[54] Nowadays, LCO is still the most prevalent material for consumer electronics, where safety and volumetric energy density are key factors, e.g. ear/cell phones.[7,56] The developed coating strategies are furthermore used till today for other CAM classes.

Lithium nickel dioxide $LiNiO_2$ (LNO) can be synthesized in a similar way to its cobalt-equivalent (LCO).[57] It has an improved energy density of 240 $mAh{\cdot}g^{-1}$ at a working potential of 3.70 V vs. Li/Li^+ and a volumetric energy density of $\approx$ 1050 $Wh{\cdot}kg^{-1}$.[58] Additionally, it has the lowest metal cost of all stoichiometric layered oxides ($\approx$ 16 US\$$\cdot kg^{-1}$).[51] However, LNO experiences rapid capacity fading[59] as the layered oxide structure becomes unstable with increasing nickel content, especially at low degrees of lithiation ($\equiv$ charged state).[60] The rearrangement of the structure is accompanied by gas evolution, which poses serious safety issue.[61] Both, LCO and LNO are referred to as first generation cathode materials.

While searching for new materials, *Thackeray and Goodenough* discovered lithium manganese oxide $LiMn_2O_4$ (LMO) in 1983.[62] LMO is a spinel-type active material that is much cheaper and more environmentally friendly than other materials, e.g. LCO or LNO due to the absence of toxic metals. The octahedral sites in the LMO lattice are occupied by $Mn^{3+/4+}$, while Li^+-ions are located in the tetrahedral sites.[63] The structure enables a high Li-ion conductivity and better rate capability than LCO due to a 3D diffusion network via the octahedral voids. The operating voltage is with 4.0 V vs. Li/Li^+ rather high, but the practical usable specific charge capacity of 110 $mAh{\cdot}g^{-1}$ and energy density of $\approx$ 440 $Wh{\cdot}kg^{-1}$ are rather low.[55] The primary challenge and drawbacks of

the material is the presence of different oxidation states of manganese. The inactive Mn^{3+} can undergo a disproportionation reaction towards Mn^{2+} and Mn^{4+}. While the latter remains in the cathodic solid phase, the Mn^{2+} dissolves in the electrolyte and precipitates at the anode. Therefore, it is crucial to maintain the average voltage below 3.58 V vs. Li/Li^+ to minimize the risk of dissolution.[64] Higher voltages, particularly at elevated temperatures, results in the formation of protons in the electrolyte solution and accelerate the aforementioned phenomena.

In 1997, *Amine et al.* substituted 25 % of the Mn-content with Ni, creating $LiNi_{0.5}Mn_{1.5}O_4$ (LNMO) or the so-called high voltage spinel class.[65] This material contains manganese in the more stable Mn^{4+} state, while Ni is oxidized from +III to the +IV state.[66] LNMO exhibits improved electrochemical performance, with an average operating voltage of up to 4.8 V vs. Li/Li^+ (compared to LMOs 4.0 V vs. Li/Li^+) and an usable specific charge capacity of 147 $mAh{\cdot}g^{-1}$.[67] The volumetric energy density of $\approx$ 635 $Wh{\cdot}kg^{-1}$ is approximately 1.4 times higher compared to LMO.[54] The expected oxygen release due to structural rearrangement of LMO/LNMO sets in at rather high potentials of $\approx$ 5.0 V vs. Li/Li^+. However, the commercialization of this material is limited as it currently operates close to the oxidative stability limit of the currently used carbonate-based electrolyte mixtures. The usage of rather high voltages results in the formation of protons within the electrolyte, which can then further attack the spinel-structure. Additionally, the synthesis of this material class is challenging due to the accompanied presence of $Li_xNi_{1-x}O_2$ phases.[68] In summary, this material can be used as active material, however it requires new high-voltage electrolytes. Currently it is estimated that the commercialization of this material class might occur in the late 2020s for the BEV market.[7]

At the same time of LNMO, the phospho-olivine phosphate $LiFePO_4$ (LFP) was discovered by *Padhi and Goodenough.*[69] This material clearly stands out from all other CAMs due to its low price (0.14 US \$ kg^{-1} for Fe),[51] environmental friendliness, and security. The covalent oxygen bondage results in a high level of safety, accompanied with a long-cycle lifetime. Hence no gas evolution, e.g. oxygen release from the lattice, during cell life is being expected.[70] However, the phosphate structure only provides 1D-channels for lithium diffusion, resulting in a rather low rate capability.[71] The relative low valence redox couple ($Fe^{2+/3+}$) results in an average operating voltage of 3.40 V vs. Li/Li^+. Its usable specific charge capacity is 160 $mAh{\cdot}g^{-1}$ resulting in a volumetric energy density of $\approx$ 544 $Wh{\cdot}kg^{-1}$. In recent years, significant effort has been made to increase the rate capability by using LFP-nanoparticles and conductive carbon agents.[72,73] Currently, LFP batteries are primarily used in applications where low costs and longevity are prioritized over high energy density, such as heavy-duty vehicles (buses & trucks), grid storage systems, and power tools.

However, contemporary amperex technology co. limited (CATL) has announced plans to release a commercial LFP battery pack in mid-2025 for the use in Tesla, BYD, MG, and Ora models.[74,75]To date, the spinel oxides and phospho-olivines have already reached their maximum achievable lithium extraction/insertion capacity ($1 > x_i > 0$) and no significant structural improvements can be expected. In contrast, the layered transition metal oxide (TMO)-class have not been fully delithiated during cycling so far.[76]

The most prominent class of CAM materials today are the so-called lithium-nickel-manganese-cobalt-oxides (NMCs).[76,77] *Liu et al.* substituted Ni in LNO with Co and Mn and reported on this material class for the first time.[78] These compounds are still based on the layered LCO structure with the general formula $Li[Ni_xMn_zCo_{1-x-z}]O_2$ (NMC_{xyz}) and represent the 3^{rd} generation of CAMs. The industrial benefits of those materials include a higher energy density and reduced environmental impact due to the reduction of cobalt, together with a decrease in costs ($\approx$ 50 US \$ kg^{-1} for NMC622[51]). Today, several different NMC materials, such as NMC111, -622, or -811, exist. Some general rules can be addressed to all of those. Firstly, manganese and cobalt are present in the Mn^{+4} and Co^{+3} oxidation states, while nickel can be found in either the Ni^{+2} or Ni^{+3} oxidation state. Secondly, although nickel offers a higher capacity, it has poor cycling and thermal stability. Thirdly, cobalt provides structural stability and enables fast kinetics, while fourthly, manganese is electrochemically inactive but stabilizes the structure, thereby improving cycle life and safety. Incorporating multiple metals into the LCO structure can therefore prevent the bulk-phase transition observed in LCO at high SOC.[79,80] The first commercialized and most studied material in this class is $Li[Ni_{0.33}Mn_{0.33}Co_{0.33}]O_2$ (NMC111). It provides a specific charge capacity of 160 $mAh{\cdot}g^{-1}$ with an energy density of $\approx$ 624 $Wh{\cdot}kg^{-1}$ and an upper cut-off voltage of 4.3 V vs. Li/Li^+.[79] NMC111 was also used in the first fully EV of BMW, the i3.[15] Increasing the nickel content led to 180 $mAh{\cdot}g^{-1}$ for NMC622,[81] and 210 $mAh{\cdot}g^{-1}$ ($\approx$ 798 $Wh{\cdot}kg^{-1}$) for NMC811.[79]

However, not only cobalt can be replaced. For instance, the replacement of manganese by alumina leads to the class of lithium nickel cobalt alumina-oxide (NCA) materials. Among these materials, $Li[Ni_{0.8}Co_{0.15}Al_{0.05}]O_2$ (NCA80) is the most prominent due to its well-developed status and its performance (220 $mAh{\cdot}g^{-1}$, $\approx$ 760 $Wh{\cdot}kg^{-1}$), as well as an operating voltage of 3.80 V vs. Li/Li^+.[55] It is worth noting that NCA80 has the same nickel content as NMC811, with similar metal costs.[76] The benefits lie in the improved kinetics of Li-diffusion due to the use of alumina instead of manganese. However, it currently suffers from lower thermal stability than NMC811. The material is already used in the battery pack of Tesla's Model S.[7,82] Even if there are many well developed NMCs and NCAs, all TMOs undergoes the same phase-transition during

lithiation (charging).[83] Note that also all NMCs and NCAs are synthesized in a lithiated state. NMCs have a hexagonal structure in their fully lithiated state, see Figure 2, which is referred to as H1-stage. As charging progresses and the TMO reaches ≈ 30 % delithiation, it enters the monoclinal (M)-phase, followed by the hexagonal (H2) and finally the third hexagonal (H3) phase. A detailed description of the phase-transition is given in chapter 5. The average volume contraction increases with the nickel content, ranging from approximately ≈ 1 % for NMC111 up to ≈ 5 % for NMC811.[84] This phenomenon is commonly known in the battery community as the 'breathing of the LIB'.[85]

Finally, at high levels of delithiation (SOC ≥ 80 %), NMCs materials release oxygen from their near-surface regions.[81,86] This causes the relatively unstable surface layer to gradually transform into a spinel or rock-salt-type material.[87] *Jung et al.* revealed that this reactive singlet oxygen subsequently reacts with the liquid electrolyte, forming CO and CO_2.[81,86] The repeated volume changes lead to continuous cracking of the NMC particles. The newly exposed surfaces can then, in the presence of singlet oxygen, react with the electrolyte and led to continuous side-reactions in form of steady gas evolution reactions within the cell. The oxygen release is also observed at high temperatures, making it a critical topic in battery development. Once released, oxygen can ignite the liquid electrolyte within the cell environment, contributing to the so-called thermal runaway of a LIB.[88,89] The release of oxygen was also investigated within this work as function of the electrode densification process. This process step can increase the volumetric energy, but can also lead to particle cracking and stress within the coating and hence might influence the gas evolution at high SOC.

Table 2: Selected electrochemical properties of the most common cathode active materials (CAMs) for the usage in lithium-ion batteries.[54,55,90] The electrochemical data refer to the material level. The operating potential is the midpoint voltage at a C/20 rate.

Cathode material	**Capacity$_{\text{theo.}}$ [mAh·g^{-1}]**	**Capacity$_{\text{pract.}}$ [mAh·g^{-1}]**	**Potential [V vs. Li/Li^{+}]**	**Stability**
$LiCoO_2$	274	190	3.80	medium
$LiNiO_2$	275	150	3.80	low
$LiFePO_4$	170	160	3.40	high
$Li[Ni_{0.8}Mn_{0.1}Co_{0.1}]O_2$	275	210	3.80	medium
$Li[Ni_{0.85}Co_{0.05}Al_{0.1}]O_2$	279	200	3.80	high
$LiMn_2O_4$	148	120	4.00	low
$LiNi_{0.5}Mn_{1.5}O_4$	147	135	4.80	high

Nowadays, research strategies are focusing on strategies to continuous increase the nickel content, e.g. NMC955. However, this approach is limited by the synthesis conditions that arise with higher nickel content. Increased nickel contents reduces the calcination temperature, promoting higher levels of surface impurities, such as carbonates.[79] These impurities can lead to increased gas evolution in form of CO_2 and a reduced cycling performance.

However, almost all electric vehicle manufacturers are intensifying their reliance on NMC-based LIBs. Other promising CAMs, such as LNMO or Li-and-manganese rich layered oxides (LMR-NMC), provide an astonishing energy density of up to $\approx$ 900 Wh·kg^{-1}.[55] However, they still suffer from poor energy efficiency, worse cycling stability, and low rate capability due to their low electrode density. The primary reason for using these materials is the significantly lower cost of manganese, which is currently priced at $\approx$ 2 US \$ kg^{-1} [52] compared to nickel's $\approx$ 16 US \$ kg^{-1}.[51] Manganese is also more abundant and widely distributed across many countries, reducing the risk of supply chain shortages. The global market for battery electric vehicles is continuously increasing, and meanwhile also the need for high energy materials, such as NMCs. The assumed global annual production of NMC material will therefore be increased from currently 0.5 up to $\approx$ 3 TWh, which is assumed will be more than half of the total global CAM production.[91] Hence, detailed insight´s on this material class will be given in the following.

Structural Properties of the Li[$Ni_xMn_yCo_z$]O_2 (NMC) Material Class

NMC materials belong to the family of layered transition metal oxides (LTO). Their crystal structure is based on the α-$NaFeO_2$-lattice, with alternating layers of transition metal ions (nickel, manganese, cobalt) and lithium ions, separated by oxygen layers. Figure 6 illustrates the crystal structure of the NMC-class.

The transition metal ions occupy octahedral sites, while the lithium ions occupy tetrahedral ones within the layers. Within the transition metal layers, the metal ions (Ni, Mn, Co) are coordinated by six oxygen ions in an octahedral arrangement. This arrangement provides structural stability and determines the oxidation state and coordination geometry of the transition metal, forming a network of corner-sharing octahedra. In addition to the octahedral coordination, NMC materials have tetrahedral sites within the transition metal layers. These sites are occupied by lithium ions, each surrounded by four oxygen ions in a tetrahedral arrangement. The tetrahedral coordination enables the intercalation of lithium ions during charge and discharge procedures. During this, the lithium ions are inserted and extracted from the lattice, occupying and leaving vacant tetrahedral sites, respectively. The crystal structure of the NMC material is three-dimensional, with layers of transition metal and lithium ions stacked on top of

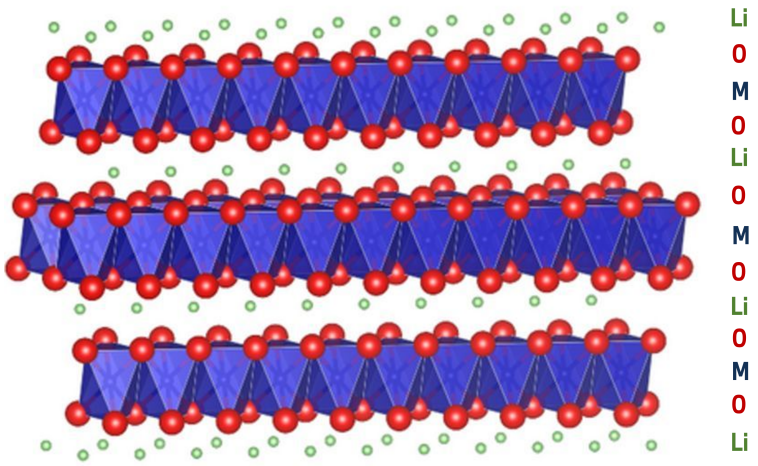

Figure 6: Crystal structure of the layered oxide class R(-)3m. $LiMO_2$ structure consist of alternating layers of lithium (Li, green), transition metals (M, blue) and oxygen (O, red); graphic was created using VESTA.[92]

each other. This lattice facilitates the insertion and extraction of lithium ions. NMC materials provide structural stability and facilitate ion diffusion. Crystal defects, such as vacancies or impurities, may be present. Vacancies occur when an ion is missing from its expected position in the crystal lattice. Impurities within the material can occur from the substitution of ions with different elements or be introduced during the synthesis process. The resulting crystal defects can affect the electrochemical properties of the material and hinder ion diffusion and charge transport within the crystal structure.[92,93]

The synthesis of NMC materials involves several steps. Firstly, precursor materials containing the desired elements (nickel, manganese, cobalt, and lithium) in the appropriate stoichiometric ratios are prepared. This can be achieved by mixing metal salts or oxides in a solvent or by using other chemical routes such as co-precipitation or sol-gel methods. The precursor materials are then thoroughly mixed and ground to ensure homogeneity and enhance the reactivity of the powders. Then, the mixed precursor powders are heated in a furnace under controlled atmospheric conditions. The calcination process involves heating the powders at a specific temperature for a certain duration. This step helps to remove any volatile components, drive off moisture, and initiate solid-state reactions to form the desired NMC compound. The temperature and duration of calcination depend on the chosen synthesis route and the desired properties of the NMC material. Following calcination, the resulting NMC powder is usually milled to decrease particle size and enhance the material's electrochemical performance. This process increases the surface area and improves the diffusion of lithium ions within the material. Subsequently, the milled powder may undergo annealing. This process involves heating the powder at a lower temperature to relieve any residual stress and improve the crystallinity of the material.[94]

Two types of crystallinity are available for NMCs: single crystalline (sc) or poly crystalline (pc). The structural differences of both types is shown exemplary in Fig. 7. Single crystalline NMC materials have a well-defined crystal structure with a continuous lattice arrangement throughout the entire material. This means that the material is composed of a single crystal with no grain boundaries or defects. Single crystalline NMC materials are typically synthesized using specialized techniques such as chemical vapor deposition or melt growth methods. These materials exhibit high crystalline perfection and uniform properties throughout the crystal. Poly-crystalline NMC materials are composed of multiple crystals with varying orientations and sizes, separated by grain boundaries. These materials are typically synthesized using solid-state reactions or solution-based methods as mentioned above. The grain boundaries can affect the electrochemical properties of the material, such as its capacity, rate capability, and cycling stability. The grain boundaries can also act as sites for surface reactions and can influence the material's surface chemistry.

Generally, single crystalline NMC materials demonstrate superior electrochemical performance and cycling stability compared to poly-crystalline NMC materials. This is due to the absence of grain boundaries, which reduces the likelihood of side reactions and enhances lithium ion diffusion within the material. However, synthesizing single crystalline NMC materials is more challenging and costly, and their properties can be highly dependent on the synthesis conditions. Poly-crystalline NMC materials are frequently used in commercial lithium-ion batteries due to their ease of synthesis and lower cost.[95]

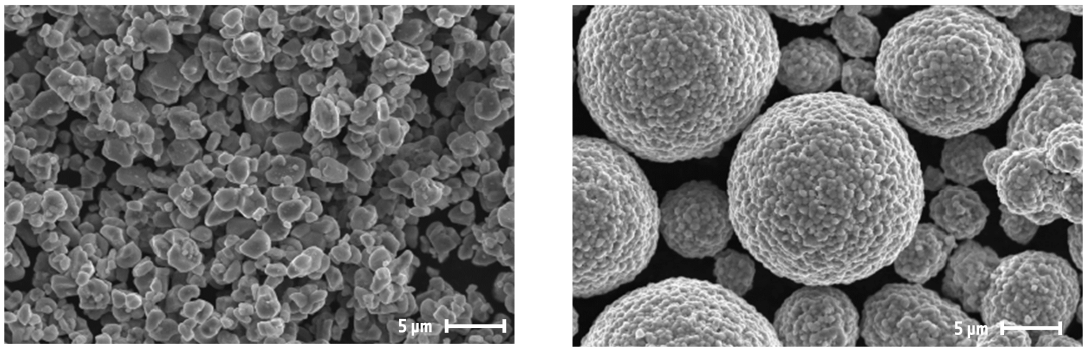

Figure 7: SEM image of NMC811 bulk material for single crystalline (left) and poly-crystalline material (right).

2.4 Electrolyte Solutions

The overall function of the liquid electrolyte is to enable the Li^+-ion transport between the electrodes. Besides its main function, the electrolyte faces also many technically, regulatory as well as economically hurdles. On one side, it has to be comparable with the used active and side materials, including current collectors, separator, and various plastic parts within the cell can. On the other side, a large liquid temperature range, low costs, safety as well as health and environmental aspects are required. As the voltage-range covers more than 4 V, exceeding the limit of aqueous electrolytes ($\approx$ 1.2 V), LIB electrolytes rely on non-aqueous, aprotic solvents and a dissolved Li-salt. However, due to the constant exposure towards voltage, the electrolyte components are also one of the main sources of gas evolution, due to their electrochemical breakdown over lifetime.[96] Table 3 and Figure 8 provide an overview of the typical used solvents and their physical properties, while Figure 8 shows the structure of the components.

State of the art electrolytes comprises at least one cyclic- and one linear-alkyl carbonate as solvent. The cyclic carbonate, e.g. ethylene carbonate (EC), fluoroethylene carbonate (FEC), or vinylene carbonate (VC) enables the dissociation of the conducting salt (typically $LiPF_6$) due to they relatively high dielectric constant. As the cyclic ones are typically solid at room temperature, the linear carbonates, e.g. diethyl carbonate (DEC), dimethyl carbonate (DMC), or ethyl-methyl carbonate (EMC) are being used to decrease the viscosity and freezing point of the mixture.[11,96] The physical properties of any electrolyte mixture can be easily tuned by changing the quantity of solvents and the ratio of cyclic to linear carbonates. In this way, various electrolyte mixtures regarding specific cell chemistry and applications can be created.

Table 3: Physical properties of conventional organic carbonate solvents. T_{melt} is the melting point, T_{boil} is the boiling point, respectively. The data are mainly adapted from[96,97] or are individual referred.

Solvent	$\mathbf{T_{melt}}$ **[°C]**	$\mathbf{T_{boil}}$ **[°C]**	**Viscosity** η **[cP]**	**Dielectric constant** [ϵ]	**Density** [$\mathbf{g \cdot cm^{-3}}$]
EC	36.4	248	1.90	89.8	1.32
FEC	18.0	212	4.10[98]	79.7	1.48
VC	19.0	162	-	126[99]	1.36
PES	96.0	-	-	3.5[100]	1.60
DMC	4.60	91.0	0.59	3.1	1.06
EMC	-53.0	110	0.65	3.0	1.01
DEC	-74.3	126	0.75	2.8	0.97

The current electrolyte mixtures offer a liquid temperature range from -20 to +60 °C and a sufficient electrochemical stability window of up to ≈ 4.5 V vs. Li/Li$^+$, while the reductive stability is limited to ≈ 0.8 V vs. Li/Li$^+$.[30] The electrochemical stability is reached by the formation of a passivation layer at the surface of the electrodes.[29] In particular, the use of EC is indispensable, as it is the crucial forming agent of the so-called solid electrolyte interface (SEI), see chapter 2.5 for a detailed description of the SEI formation process. The SEI serves as a protective film that blocks the electron transfer between the negative electrode and the electrolyte, thus inhibiting further electrolyte decomposition.[101]

Lithiumhexafluorophosphate ($LiPF_6$) is typically used as salt, commonly in concentrations between 0.8 - 1.5 M.[96] Of all known Li-salts, $LiPF_6$ provides so far the best trade off between conductivity, safety, hazardous, and costs.[102] However, the stability of the salt and therefore the usage of the cell is limited to +60 °C. Higher temperatures results in a disproportionation, forming LiF and PF_5. Furthermore, $LiPF_6$ is very sensitive towards water. Trace water contamination's, e.g. during cell assembling or cell-can leakage, can result in the formation of HF and POF_3.

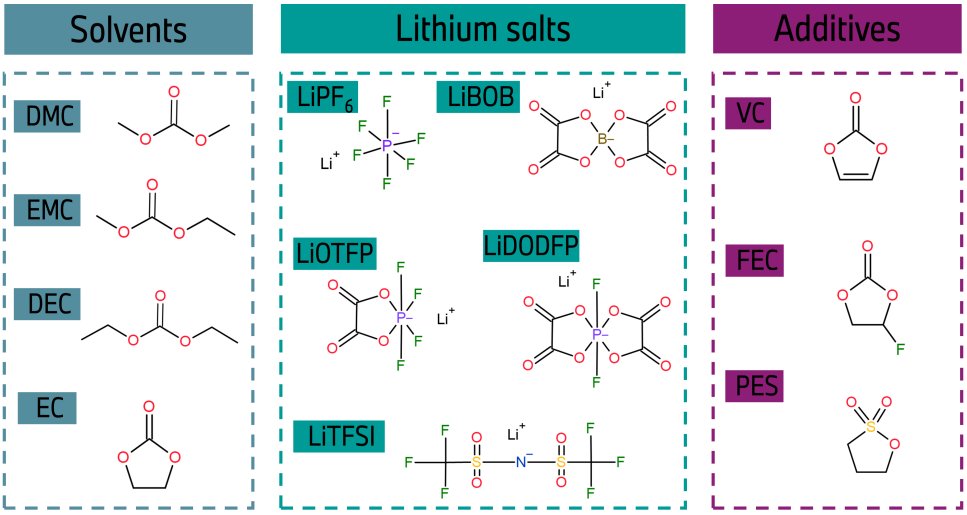

Figure 8: Chemical structures of electrolyte solvents (left), lithium salts (middle), and additives (right), commonly used in state of the art LIBs.

In search for alternative salts, the class of lithium borates, e.g. lithium-bis-(oxalato)borate (LiBOB)[103] and lithium-difluoro-(oxalato)-borate (LiDFBOB)[104] along with further lithium phosphate salts, e.g. lithium-difluorobis-(oxalato)-phosphate (LiDODFP)[105] or lithium-tetrafluoro-(oxalato)-phosphate (LiOTFP),[96] have gained a lot of attention from academia as well as industry. As the Li$^+$-ions comes along with a rather big solvation shell, the diffusion of the ions is naturally hindered within the liquid phase.

Therefore new lithium salts with rather large cations so-called weakly coordinated anions (WCAs) are needed, to decrease the ionic forces. Due to their spherical increased cations, these newly developed salts can provide better Li^+-conductivity and a better SEI forming ability.[106]

The ionic conductivity is hereby the most critical property in electrolyte development, as it is directly connected to the power of the cell. However, their long-term influence on the cell performance is still unclear. For example, it is known that $LiPF_6$ passivate the aluminum current collector, whereas this is not the case for the lithium-bis-(trifluoromethane-sulfonyl)-imide (LiTFSI)-salt.[96,107]

In order to improve the cycle and calendaric lifetime of LIBs, more and more so-called additives are developed and dosed to the base electrolyte mixtures, typically in concentration of < 10 wt. %.[108–111] The reduction potential of the additives is typically higher, than from the base electrolyte, in order to reduce them at the very beginning of the first charging cycle at the negative electrode. An early electrochemical triggered decomposition helps to form a more homogeneous and therefore stable SEI film. Typical used additives are FEC, VC or 1,3-propane sultone (PES).[112–114]

Solid-State Electrolytes

To enable safer and higher energy density batteries, solid-state electrolytes have emerged as a promising alternative to the traditional liquid electrolytes used in lithium-ion batteries. These solid-state materials offer several key advantages that could revolutionize battery technology.[115]

Firstly, one of the primary benefits of solid-state electrolytes is their enhanced safety profile. Unlike liquid electrolytes, solid-state electrolytes are non-flammable and do not suffer from issues such as leakage or thermal runaway. This improved safety can significantly reduce the risk of battery fires and explosions.[96] Secondly, solid-state electrolytes enable the use of lithium metal anodes, which have a significantly higher specific capacity compared to the graphite anodes, as shown in Figure 3. This can lead to a substantial increase in the overall energy density of the battery system, allowing for longer run-times and more compact designs. Thirdly, many solid-state electrolyte materials exhibit a wider electrochemical stability window, meaning they can be used with high-voltage cathode materials, as explained in Section 2.3. This expanded compatibility can further enhance the energy density and performance of solid-state batteries. Fourthly, solid-state electrolytes can potentially improve the cycle life of batteries by preventing the formation of lithium dendrites, which can short-circuit the battery and lead to premature failure.[18,19]

Currently, researchers are exploring various materials for (all)-solid-state electrolytes, including i.) ceramic electrolytes such as lithium garnet and lithium superionic conductors, ii.) polymer electrolytes like polyethylene oxide and polyvinylidene fluoride.[96,107] Both materials can provide solid-state ionic conductivity and stability. Hybrid solid-state electrolytes combine organic and inorganic components to leverage the advantages of both.[115,116]

While solid-state electrolytes hold great promise, there are still several challenges to overcome before they can be widely adopted. These include achieving high ionic conductivity, stable interfaces with electrodes, and developing scalable manufacturing processes. Ongoing research and development in this field are expected to address these challenges and pave the way for the widespread adoption of solid-state battery technology. Here, also OEMS has been used hitherto to analyze the degradation phenomena on these materials *in-operando*.[116]

2.5 Interfacial Processes in Lithium-Ion Batteries

In the previous sections, the basic concepts of the battery working principle (2.1), electrode active materials (2.2-2.3), and the liquid electrolyte (2.4) were explored and described separately. This section will delve deeper into the interfacial processes between the liquid electrolyte and the polarized electrode. The interface between the electrode and electrolyte can be seen as the most important part of a LIB, as ionic and electrochemical reactions occur here simultaneously.

In General

To fully utilize the potential of LIBs, they must operate beyond the thermodynamic stability window of the organic electrolyte. Achieving kinetic stability requires the decomposition of trace amounts of electrolyte and conducting salt on the negative electrode surface, forming the solid electrolyte interface (SEI) layer. The SEI is a complex, heterogeneous, and structurally disordered passivation layer, with a thickness of typically 10-100 nm.[117] The layer is formed in situ, primarily during the first reductive cycle of battery life, when there is an abundance of electrons available. Once a certain thickness is reached, the SEI acts as protective layer which effectively blocks the electron transfer between the vulnerable active material of the anode and the electrolyte. In comparison to that, Li-ion diffusion is essential for subsequent de-/intercalation processes on the anode side. Therefore, it is necessary to have a homogenous SEI layer on the anode surface to prevent further undesired electrolyte decomposition reactions. A poorly formed SEI increases cell resistance, leading to capacity fading and poor power density due to ongoing electrolyte consumption and active lithium loss.[117] To achieve an overall excellent performance, including long cycle life, high rate capability, safety, and other important aspects, the SEI should be thin, while having a high physical strength, including tolerance towards expansion and contraction due to the volumetric graphite/silicon expansion. Additionally, the SEI should be also insoluble in organic solvents and have a wide temperature and voltage stability.[118]

However, many factors are involved in forming a good and sufficient SEI layer. Since the layer is formed within the first cycles of battery life, it is directly coupled to the first irreversible capacity loss of the cell, which is approximately 10 % of the original capacity.[118] Extensive research has been conducted over the past 40 years to comprehend the function, composition, morphology, and formation mechanism. Until today, the formation and growth mechanism is less understood than the resulting chemical and physical properties and remains one of the most ambiguous issues in battery science. One of the major reasons is the thinness of the layer and its sensitivity towards oxygen and water, which limits the number of analytical techniques.

To further optimize LIBs, it is necessary to better understand and tune the growth mechanism of the SEI. This is especially important in modern large-format cells with a variety of chemicals, additives and materials within the cell can. Unfortunately, controlling the properties of the SEI is challenging as they are influenced by many factors, such as reactivity of the electrodes, electrolyte composition, electrochemical conditions, and temperature.[117]

The History of Understanding the Passivation Layer Formation

A general passivation layer on lithium metal surface was first observed by *Dey et al.* in the 1970s.[119] In 1979, *Peled* introduced the concept of SEI for alkali metals in non-aqueous battery systems.[29] He proposed a double layer SEI with a thin and compact solid-layer near the electrode surface and a second, thicker and more porous layer near the electrolyte interface, which consist of larger organic compounds, mixed with electrolyte molecules. *Nazri & Muller* soon detected Li_2CO_3 on lithium electrode surfaces as the main portion of the SEI.[120] *Aurbach* discovered lithium alkyl carbonates in addition to Li_2CO_3 due to electrolyte decomposition on lithium surfaces.[121] In 1990, *Fong et al.* described the general passivation layer formation on graphite for the first time.[30] *Kanamura et al.* later discovered that the compact part of the SEI layer also comprises Li_2O and LiF when using graphite as anode. In the same year, *Dahn et al.* highlighted the advantage of using ethylene carbonate (EC) for SEI formation on graphite. Based on these discoveries, *Peled*[122] introduced his widely accepted 'mosaic structure' of the SEI, which is schematically shown in Fig. 10. Based on the conventional electrolyte reduction processes on a graphite surface, *Aurbach et al.* proposed the first SEI formation process in 1999.[123]

Thermodynamic View

A widely used concept to explain the energetic formation of the SEI layer was proposed by *Goodenough and Kim* and is schematically shown in Figure 9.[12] According to this, the electrolyte stability window (E_g) is related to the energy difference between the lowest unoccupied molecular orbital (LUMO) and the highest occupied molecular orbital (HOMO). If the anode's chemical potential (μ_A) is higher than the LUMO, the electrolyte solution is being reduced. On the other hand, the electrolyte solution undergoes oxidation if the chemical potential of the cathode (μ_C) is lower than of the electrolyte´s HOMO level. As it was described in section 2.2, the intercalation potential of lithium in graphite ranges from 0.0-0.25 V vs. Li/Li^+, which falls below the reductive stability limit of organic carbonate-based electrolyte mixtures. This leads to the formation of SEI at the anode, unless the electrode is protected by an effective SEI layer.[124,125]

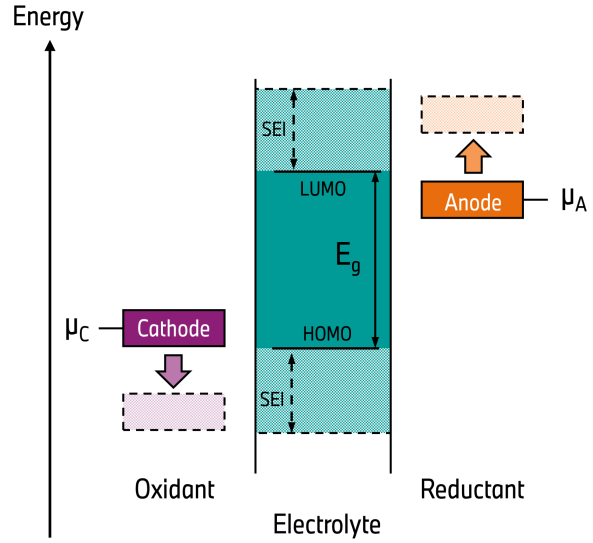

Figure 9: Energetics of the anode and cathode SEI layer formation under electrochemical reduction (LUMO) and oxidation (HOMO) conditions in a Li-ion cell. μ_A and μ_C refer to the lithium chemical potential at the anode/cathode, respectively. E_g represents the electrochemical stability window of the electrolyte system. Adapted and re-drawn from literature. [124]

The thermodynamic stability window of today´s conventional electrolyte systems ranges between ≈ 1.0 - 4.5 V vs. Li/Li^+. In order to further increase the energy density of today´s LIBs, the difference between μ_A and μ_C has to be as large as possible.

2.5.1 SEI Formation on Graphite Based Anodes

As graphite is the most important anode material nowadays and in near future, this section is mainly dealing with the formation process while using graphite-containing negative electrodes. From the liquid electrolyte perspective, almost every organic carbonate/Li-salt mixture can form a solid electrolyte interface. However, the most prominent SEI-forming agent is EC in a mixture with linear carbonates, as it was described in section 2.4.

In the battery community it is widely accepted that the SEI is being formed in two stages. [118] Once the charging of the cell and thus polarization of the graphite electrode begins, the electrolyte compounds in the near-electrode surface area undergo reductive decomposition reactions. This step happens under fast kinetics to form new species. In the second step, these species undergo precipitation processes and begin to form the actual SEI layer. This process continues until the entire fragile graphite surface is protected by a thin passivating film.

For example the use of EC and its one-electron reduction via Equation (2.4) or two-electron reduction via Equation (2.5) process results in the formation of gaseous ethylene or carbon monoxide and lithium-organo-alkyl-carbonate species.

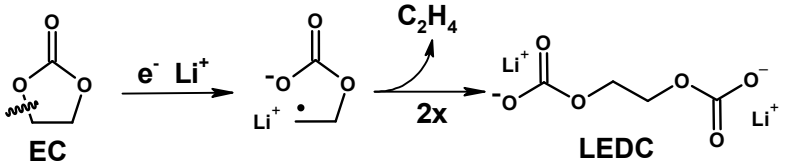

(2.4)

Latter one subsequently precipitates to lithium ethylene dicarbonate (LEDC) and Li_2CO_3. Both components are beneficial in forming a highly stable SEI with a network of organic Li-carbonates. Additionally, lithium carbonate is difficult to dissolve as it shows a high endothermic solvation enthalpy, achieving long-term stability. In practical applications, EC is always blended with linear carbonates to lower the viscosity and increase the liquid range of the mixture. The reduction of EC and DMC for example forms highly passivating surface films due to the precipitation of mainly $ROCO_2Li$ and $RO-Li$ species, which are linked and bridged together, resulting in a highly Li^+-ion conductive 3D network.[126] However, linear carbonates are less passivating than cyclic ones, e.g. EC as they get reduced at lower potentials into lithium alkyl-carbonates. Several possible reaction pathways, especially in large-format cells are shown and described in section 6.7.

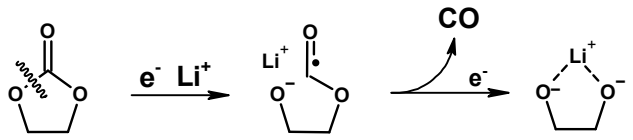

(2.5)

Simultaneously to the solvent reduction process and SEI layer built-up, the solvated Li^+ ions diffuse with a slower rate towards the graphite surface due to a concentration gradient in the liquid phase. The lithium ions are then intercalated between the graphite sheets, forming LiC_x moieties. This process prevents the formation and deposition of metallic lithium (dendrites) on the graphite surface.
In the past, solvent co-intercalation in-between the graphene sheets was a major issue, particularly when using propylene carbonate (PC). Solvent co-intercalation can result in the exfoliation of single graphene layers and the subsequent destruction of the graphite structure.[118] The choice of both, the solvent molecule, and the type of graphite are important factors to consider. In this context it is beneficial to use highly oriented pyrolytic graphite (HOPG) with a reduced specific surface area.[118] On the other hand, natural graphite comes along with a higher surface area and is known to co-intercalate solvent molecules due to its in-homogeneous morphology. However, a quick and effective SEI formation at potentials higher than those of the co-intercalation process can prevent any solvent molecule from intercalation into the graphite host structure.

The selection of the anodes material surface area involves a trade-off within the batteries final capacity. On one hand, less anode surface area results in less capacity loss during SEI formation. On the other hand, a higher surface area is needed for high power density (capacity at high C-rates). The latter one requires also additional SEI formation and hence more initial lithium-ions. Also safety plays an important role here. To prevent lithium plating or dendrite formation, the anode capacity is usually 10 % higher than that of the cathode.[118] This extra material must be also fully covered by a SEI surface. Therefore, optimizing the electrode ratio (negative to positive electrode surface area) is an incremental part of today's cell development.[117]

In general, various parameters and reduction processes compete with each other during the early SEI formation. The reactants include not only the electrolyte solvents, salts, and additives, but also impurities such as trace-air or -water, as well as structural side-groups, such as carboxy ($-COOH$), or hydroxy ($-OH$). Intrinsic parameters such as reductive potential, activation energy, and exchange current density, together with extrinsic parameters, such as temperature and applied current, makes the description of the exact formation mechanism (especially within large-format cells) challenging. In addition to that, the evolution/consumption of soluble intermediates, insoluble precipitates and gaseous species, such as C_2H_4, H_2, CO_2, and CO are taking place, simultaneously.[127] Therefore, the formation mechanism, onset, composition, properties, and stability of the resulting SEI are still highly debated. Despite this unclarity it can be stated that most reduction processes occur between 0.8 - 0.2 V vs. Li/Li^+.[118]

The Usage of Additives for SEI Formation

In order to enhance a faster and more stable SEI formation on the negative electrode surface, liquid additives are commonly mixed within standard electrolyte mixtures and can be classified into four groups: I.) The subclass of polymerizable additives is probably the most common one. This class includes VC, PC and FEC, and they are commonly used to form a polymeric network on the negative electrode during the early SEI formation. This network provides enhanced protection from further side reactions within the electrolyte solution and allows a long-term cycling stability and coloumbic efficiency.[118] Those additives are typically used in concentration of around < 10 %. Only FEC can be also used as co-solvent. All of those additives typically release CO_2 upon reduction. VC reduces the reductive activation energy by showing a higher reduction potential of $\approx$ 1.0-1.4 V vs. Li/Li^+ compared to EC ($\approx$ 0.6-0.9 V vs. Li/Li^+). PC as an additive is no longer used because it was found to easily co-intercalate with lithium into the graphene layers, which causes capacity fading and critical cell failure. II.) Surface film-forming additives are more reactive than the commonly used carbonates and react mainly on the anode surface area. An example of this subclass is the salt LiBOB, which has a lower thermal reactivity than $LiPF_6$ and effectively stabilizes the graphite structure. However,

its solubility in organic carbonate-based electrolytes is its major drawback. III.) Additives for shuttle mechanism are another sub-class. Typically, these are biphenyl- and aromatic compounds. Their aromaticity enables oxidation at the cathode side in case the voltage exceeds the upper cut-off voltage. The oxidized species, now a radical cation, can then diffuse to the anode and complete the shuttle mechanism. This mechanism prevents over voltage and further cell failures. IV.) The last sub-class of additives are known as H_2O and HF-scavengers. These are for example cellulose-based separators to prevent protic species, such as H^+, from causing cross-talk between the electrodes.[128]

The effectiveness of the additives could be measured by the amount of ethylene released, steaming from the reduction of EC, making OEMS a suitable technique for formation-cycle improvements. Other classical approaches to determine the effectiveness are long-term cycling or fast-aging procedures to describe the electrochemical performance with/without additives.

Side Reactions SEI has to Face With

Although the SEI protects the anode surface from decomposition reactions, it is susceptible to be damaged during long-term cycling. In this context the typically used salt $LiPF_6$ becomes critical. Lithiumhexafluorophosphate reacts in all kind of solutions to form lithium fluoride and phosphorus pentafluoride ($LiPF_6 \rightarrow LiF + PF_5$). Phosphorus pentafluoride is a potent Lewis acid and is being reduced at voltages > 1.5 V vs. Li/Li^+. However, PF_5 may also react with protic species within the cell environment to form HF and POF_3. The cell performance is mainly affected by the occurrence of HF, as it attacks the SEI through various reactions where some of them are shown in Figure 10. The in-situ formed HF reacts at the anode with ROLi and $ROCO_2Li$ to form LiF, ROH, and $ROCO_2H$ moieties, which significantly worsen the anode's passivation potential.[126] Hence, the time-resolved detection of gases, such as POF_3 via OEMS as shown by *Misiewicz et al.*[129] can help to precisely determine the circumstances of the very early SEI attack.

HF is additionally responsible for the dissolution of transition metals (TMs) on the cathode side. The dissolved TM then diffuses to the anode and precipitates there in form of metal clusters. Another side reaction within LIBs is the deposition of metallic lithium on the anodic surface as described in section 2.2. Therefore, the design of the LIB must ensure that the potential of the anode is always above 0.0 V vs. Li/Li^+ to prevent lithium plating. In order to ensure that all graphite particles reach the same potential at the same time, a high level of uniformity in both the graphite coating and SEI layer is necessary.[126]

Current Hurdles and Further SEI Optimization Strategies

A lot of effort was pushed into the development of stable & durable SEI layers since its discovery in the 1990s. As it was described in the former pages, an optimal SEI layer should be uniformly distributed, have a negligible electronically conductivity and strong electrolyte diffusion resistance, while having a high Li-ion permeability. Once formed, further decomposition reactions with salt/solvents should not occur. This is especially important, to keep the loss of cycle-able lithium as small as possible. In reality, the SEI thickens gradually over lifetime due to the exposure of electrons to the electrolyte or the diffusion of electrolyte towards the graphite surface. Both cases, cause ongoing Li-ion usage and continuous resistance growth. Hence, the following points are the key for further SEI optimization:

Firstly, improving the SEI-layer formation by the use of additives, which results in a better SEI architecture as well as faster film formation. To avoid any cracking of the SEI layer due to stress from volume change upon cycling, the molecular forces between graphite and the SEI should be as strong as possible. This is especially important, when using silicon blended carbon materials, as they show a profound volume change between the fully de-/lithiated state.[118,126] Secondly, modifying the anode surface structure, to enhance the exchange current density, charge & discharge reaction kinetics and wettability of the particles. Thirdly, development of new electrolyte mixtures, that result in less Li-loss during formation. Fourthly, optimize the charge & discharge cycle during first charging procedure that enhance a good SEI layer formation.[130]

The latter point has been found to be most important one for industrial battery cell production, as the optimization of the extrinsic parameters can be relatively easy implemented in existing production lines. It has been found, that the applied current density, cut-off voltage and cell temperature have a positive effect on the chemical and micro-structural properties of the resulting SEI layer. The SEI formation initially starts from $\approx$ 0.8 V vs. Li/Li$^+$ and thickens gradually to $\approx$ 0.3 V vs. Li/Li$^+$. Applying higher charging rates results in an increased anode potential and hence an increased electron availability. Following that, the electrolyte components get easier reduced and the resulting SEI will have a more porous character with loosely aggregated organic components, facing a higher electronic- as well as ionic-conductivity. On the other hand, a lower charging rate results in a much denser SEI with lower electron conductivity, but increased ionic conductivity.

This is the main reason why formation protocols have historically an extreme low charging rate, e.g. 10 h (C/10) or 20 h (C/20). Slow charging is beneficial for SEI formation, but slows down the cell production rate and increases plant size and therefore manufacturing costs.

Elevated temperatures during initial charging results in the formation of a more stable SEI. Temperature accelerates not only the diffusion, but affects also the final precipitation process. It was found that using accelerated formation temperatures, e.g. 40 °C results mainly in the precipitation of Li_2CO_3 and Li_2O, rather than $ROCO_2Li$ components.[118] Additionally, the electrode-stack wetting´s behavior is also affected by the temperature, which is highlighted more in section 2.6. In sum, optimized SEI formation procedures can safe a lot of time and space, resulting in lower costs during cell production and a better longevity of the cells itself.

The effect of temperature onto the SEI layer formation process within large format automotive prismatic cells was investigated during this work and presented in chapter 6. In here, the formation process was monitored via the gas release using OEMS as novel approach to examine when gas evolution and yet SEI formation is finished.

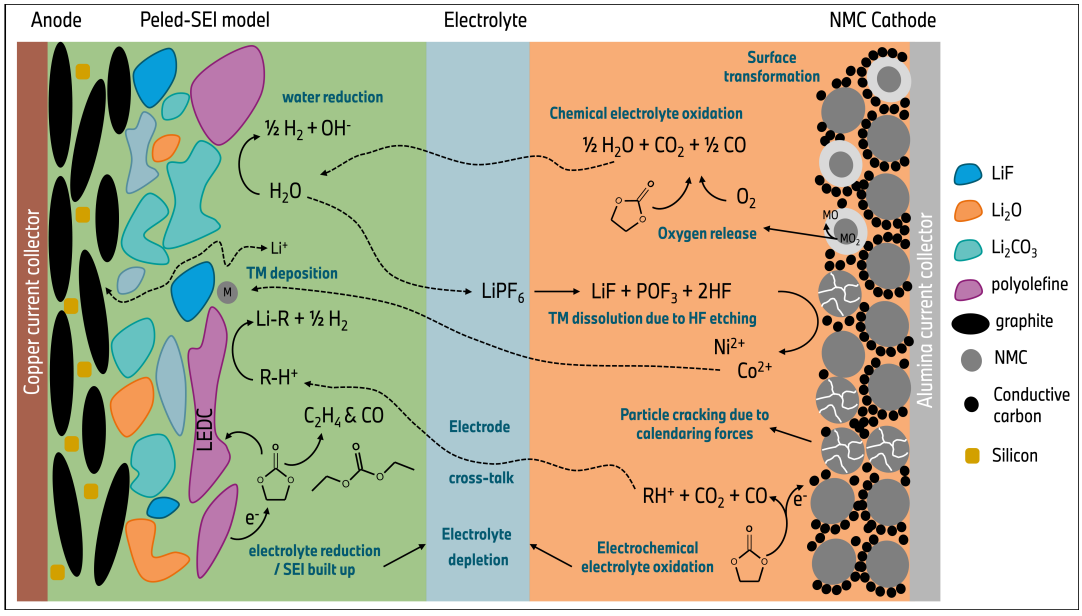

Figure 10: Schematic illustration of some undesired side reactions occurring in a Li-ion battery cell and which are investigated in this PhD project by the use of OEMS.

2.5.2 Aging Mechanism of Cathode Materials

There are much fewer studies available dealing with aging mechanism taking place on the cathode interface region, compared to the anode. One main reason is that cathode materials generally operate safer within the stability window of the electrolyte (see Fig. 9). However, also cathodes facing side reactions during cycling, which can be generally divided into fast- and long-term aging phenomena.

An irreversible capacity loss can occur during the 1st cycle, due to kinetic limitations as not all lithium-ions which were de-intercalated during charge process, can be re-intercalated into the host structure again. Reaching higher cell voltages more and more lithium-ions are extracted from the layered lattice. These ions need to be solvated by the polar alkyl carbonates, in order to be accessible by the bulk electrolyte. The carbonate based electrolytes are thermodynamically unstable towards this electrochemical oxidation, resulting in volatile and non-volatile by-products. This irreversible capacity loss within the first cycle is very similar to the SEI formation on the anode and especially NMC-based electrodes are prone to that issue. Therefore, this layer is often referred to cathode electrolyte interface (CEI), as counterpart to the SEI. However it´s present was debated for a long time and the CEI is believed to be rather thin and less efficient, than it´s counterpart. *Aurbach and Kanamura* detected similar species as on the anodic site, e.g. LiF, $ROCO_2Li$, and Li_2CO_3.[123]

Similar to the aging processes of the anode, the decomposition of $LiPF_6$-salt plays an important role, due to it´s hydrolysis with trace water or intermediately formed protic species. Besides the formation of the corrosive gases POF_3 and PF_5, also the formation of HF occur. Latter one will led to TM dissolution into the electrolyte. A subsequent diffusion of the TM towards the anode and a deposition (cross-talk) in form of metal clusters leads to loss of active lithium, capacity fading and dendrite growing, finally causing SEI-decomposition, short circuits and gas evolution reactions.[121,131]

As during charging, the lithium extraction continuous from the host structure, the diffusion of the TM into the less filled Li-slabs becomes more and more feasible. As the TM hinders in the subsequent cycles, the Li-ions from their re-intercalation into the host-structure, an increase in impedance growth and hence capacity fading can be monitored. This process is also called "cation-mixing". The similar size of Ni^{2+} (0.69 Å) and Li^+ (0.76 Å) facilitates cation mixing.[4,79] Displacing nickel from the structure, the material bonding characteristics can alter, forming a variety of phases and lowering the cells capacity. The tendency for the diffusion decreases in the order Ni > Co > Mn, which means that this process is very likely for CAMs with high nickel-content, e.g. NMC811. Due to it´s rather slow diffusion ability, manganese is supposed to stabilize the NMC structure in this crucial aspect.

In order to further increase the capacity of the cathode, and thus the cell capacity more and more attempts are carried out to increase the upper cut off voltage of the cell. As shown in Figure 4, the voltage profile of a NMC-based cathode exhibit a sloped potential profile. In this case, an increase of the upper cut-off voltage (> 4.3 V vs. Li/Li^+) would increase both, the specific capacity and the mean voltage of the cell. Hence a significant portion of the theoretical capacity of the CAM remains unused.

However, if the positive electrode potential increases and reach a certain point, the crystal structure of the NMC starts to collapse and a surface transformation of the layered oxide structure to a spinel / rock-salt type can be observed. Additionally, the diffusion of TM into the lithium slabs is also accompanied by lithium or TM diffusion into the tetrahedral voids of the Li-slabs, yielding a disordered spinel-structure, that might be further transform into the rock-salt structure. The structural rearrangement of the layered structure occurs hereby under the release of reactive oxygen. This typically sets in when approx. 80 % of the lithium ions are being removed. The onset of the oxygen release directly correlates with a significant drop in cycling stability due to impedance growth upon phase-transformation from the spinel-/rock-salt structure, as the surface has a significantly reduced Li-ion conductivity.[81,86]

The oxygen release does not only result in the decomposition of the cathodic surface structure, but also leads to electrolyte oxidation, as some of the oxygen is released as highly reactive singlet ($^1O_2$) as shown in Eq. (2.6).

$$\mathrm{Li}_x\mathrm{MO}_2 \rightarrow \mathrm{Li}_x\mathrm{MO}_{1+x} \; + \; (1-\mathrm{x}) \; {}^1\mathrm{O}_2 \tag{2.6}$$

This species causes chemical oxidation of the electrolyte and influences the long-term stability of the cell. In this context, the use of EC becomes problematic as $^1O_2$ causes the chemical oxidation, to which EC is vulnerable, see Equation (2.7). This reaction causes CO_2 evolution and has a distinct onset potential, which was analyzed in detail by *Jung et al.*[81] and has to be avoided in order to prevent the NMC particles from degradation and electrolyte breakdown.

$$4 \; \mathrm{O}_{\mathrm{lattice}} \; + \; \mathrm{EC} \rightarrow 2 \; \mathrm{CO}_2 \uparrow \; + \mathrm{CO} \uparrow \; + 2 \; \mathrm{H}_2\mathrm{O} \tag{2.7}$$

The formed singlet oxygen can however also react with another singlet oxygen species to form molecular oxygen, according to Equation (2.8).

$$2 \; \mathrm{O}_{\mathrm{lattice}} \rightarrow \mathrm{O}_2 \uparrow \tag{2.8}$$

The findings by *Jung et al.* further demonstrated that the layered structure is thermodynamically not stable during delithiation and will decompose exothermic towards the spinel and rock-salt type. Further findings by *Jung et al.* revealed the voltage dependence of the oxygen release from NMC. These findings were very useful in order to optimize the safety of today's battery cells.[81,86] This is especially important as it is assumed, that during a cell over-voltage or thermal runaway, the cell is generating its own oxygen, through the above shown Equation.

NMC particles does also change their volume during de-/intercalation, depending on their amount of nickel. NMC811 shows a volume change of up to 5 %, whereas NMC111 shows only a smaller volume change of approx. 2 %. However, a repeated volume change in every single particle during long-term cycling causes micro-cracking of the secondary particles (if pc-NMC is used). This leads to a worsen contact between primary particles and an increase of surface area. Latter one results in an acceleration of the before mentioned side-reactions, including electrolyte oxidation and hence gas evolution.
Above 4.85 V vs. Li/Li^+ the electrochemical electrolyte oxidation of today's used electrolyte mixtures occur. This phenomenon does not show a distinct onset potential, but increases exponentially with the cell voltage. Here, even low amounts of oxidized electrolyte (mainly CO_2) per cycle causes a continuous pressure increase and electrolyte loss up to end of life (EoL).

In order to further increase the capacity of the cathode, by increasing the upper cut-off voltage, it has to be done very carefully. However, even a voltage of 5 V vs. Li/Li^+ would be feasible in order to maximize the energy density of the cell. But this would lead to an fast cell aging, due to the before mentioned degradation processes.

Another important issue, which was addressed within this work and shown in chapter 5, is how the electrode densification process, also known as "calendering" - influences the gas evolution, especially the oxygen release under high voltage application. As the energy density must be increased, higher calendering pressure is being used, which might result in partial particle breakdown of the CAM material, again especially pc-NMC are vulnerable to it. The partial breakdown of some particles might be beneficial to increase the material accessibility (diffusion, exchange current density). However, it also carries the risk that more side reactions accompanied with gas evolution occur due to increased surface area and higher resistance due to more interface regions.

2.6 Automotive Lithium-Ion Battery Cell´s

A brief introduction into the basics of industrial battery manufacturing will be given in the following section. Furthermore, two process steps within the cell manufacturing process chain were investigated via OEMS and are therefore explored in more depth. Finally, the state-of-the art implementation of battery cells into electric vehicles is shortly described.

2.6.1 Cell Manufacturing

In general, a high level of precision, uniformity, and automation is necessary to produce LIBs in good quality and safety. This clearly differs from academia battery research, mainly dealing on a coin-cell basis or other smaller test cell setups. The overall battery cell manufacturing process chain is exemplarily shown in Figure 11 and covers more than 50+ individual steps, which can be divided into 3 main stages: i.) Electrode manufacturing, ii.) Cell assembly, and iii.) Formation and testing.[132–134]

Usually all production steps happen under dry-room atmosphere, with a dew point lower then -45 °C, until the cells are sealed and transferred to the test center. Merely, the anode coating can be processed within standard atmosphere, as the anode slurry is typically water-based.

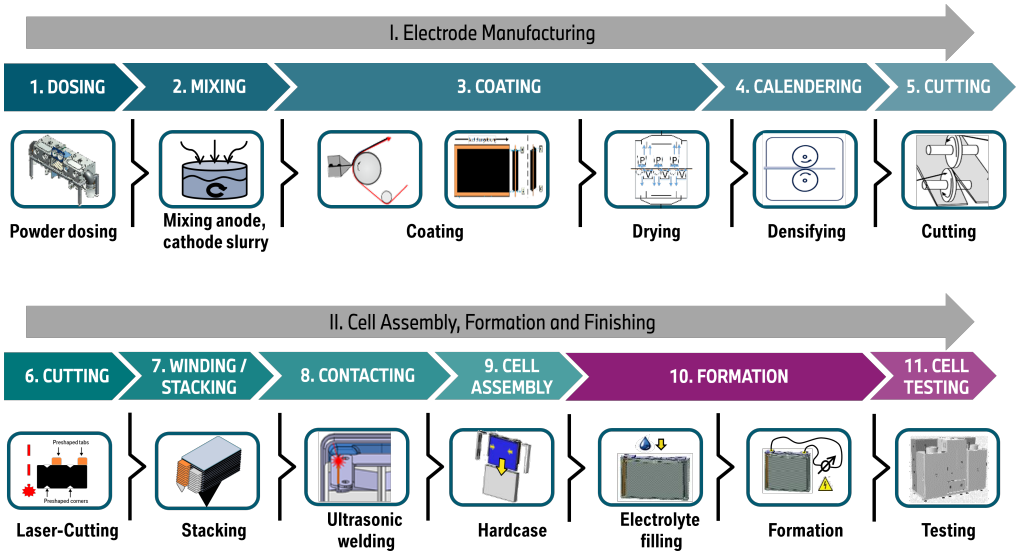

Figure 11: Schematic overview of the Li-ion battery cell manufacturing process chain.

Starting at the very beginning, the raw materials (1) are initially combined with the solvent to produce the anode/cathode slurry (2). A binder is added for improving adhesion between the particles and the current collector. Conductive agents increase the conductivity in between the particles. To achieve a stable and processable slurry,

the viscosity, density, solid content as well as mixing-steps and -times have to be optimized.[134] The air quality must be also strictly controlled to avoid dust particles or moisture (high Ni-cathode material) in the slurry. If desired, slurries can be also produced in vacuum mixing process, to avoid air and gas bubbles.[106]

Within the coating process (3) the slurries are being thinly coated on either alumina or copper foil. Slot die or double slot die are the common used techniques.[135] Both can be applied in either single side coating or double side coating processes. Fully automatic coating machines can operate at speeds up to 80 $m \cdot min^{-1}$.[134] The coating thickness, mass loading and line speed has to be precisely monitored on-line, to ensure high quality coatings. A subsequent drying process (100-150 °C) of the films is included in the continuous process step. Here, three competing physical processes taking place simultaneously: i.) Evaporation of the solvent, ii.) Diffusion of the binder, and iii.) Sedimentation of the AAM/CAM. Therefore, the drying speed and temperature heavily influences the final material distribution within the coating.[134]

In the calendering step (4; roll pressing) two rolls compresses the electrodes from both sides to achieve an even thickness and density of the electrode.[136] Hereby, the volumetric energy density is drastically increased. However, too harsh calendering results in particle cracking, increased tortuosity and an increased electrode resistance.[137,138] A deeper introduction into this process step will be given in the following pages. Subsequently, the electrode coil is vertically cut (5) into narrow sheets of the required size for the LIB. In a second step the so-called notching process (6) cuts-out a v-shape on the uncoated parts of the current collector, leaving just the corner of the current collector for later contacting. In this step usually optical inspections, tab peel strength measurements or electrical resistance measurements are being used, to identify not usable electrode sheets, e.g. burring or buckling parts.

Depending on the type of cell (cylindrical/prismatic/pouch) different methods for the final assembly exists (7-9). All processes combines the negative with the positive electrode, by the use of a separator in between. Pouch and prismatic cells are typically built by stacking the different layers on top of each other. The initially used jellyroll technique is not so often used anymore, as it results in too much mechanical stress on the bend side of the electrodes.[139] Cylindrical cells, now used by BMW and Tesla, are being produced using the winding method.[140] Finally, an alumina-tab is attached to the uncoated part of the cathode and a copper tab is applied on the anode side. Then, the electrode stack is insert into the cell casing and connected to the terminals.

In the last step of manufacturing the formation (10) and testing (11) is carried out. Here, the liquid electrolyte is filled in the cell and the cell is charged for the first time with electric energy. After SEI formation and accompanied gas evolution, the cells are sealed and relocated from dry-room. Finally, their robustness and safety is checked. The formation process step was under investigation during this PhD thesis and is therefore described in more detail below and further explored in chapter 6.

2.6.2 Electrode Calendering Process

Calendering is the mechanical processing step to increase the electrode´s density and uniformity, which are both crucial for the battery's electrochemical performance. Calendering typically follows the drying step of the electrode and is schematically depicted within Figure 12. A calendering machine typically consists of two or more hardened steel rolls that can apply a controlled amount of pressure (F_N) to the electrode sheet. The rolls can be adjusted to set the gap between them, which determines the final thickness of the electrode.

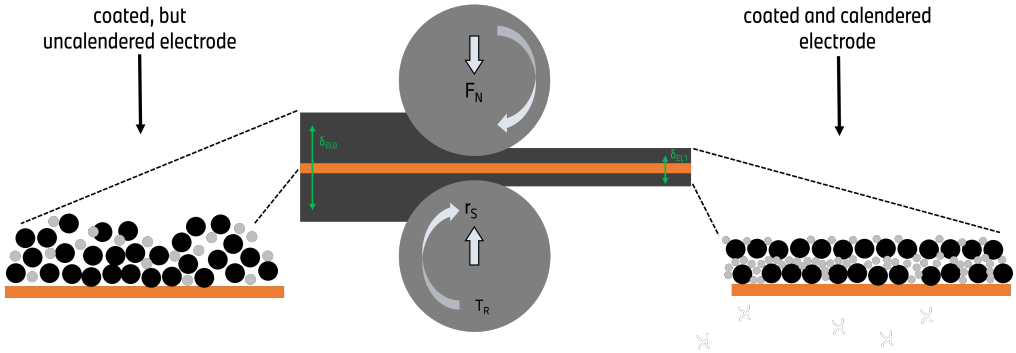

Figure 12: Schematic illustration of the calendering process during battery manufacturing and the accompanied relevant parameters. Left: uncalendered and hence uneven electrode, right: calendered electrode with high uniformity and evenness.

The following process parameters are crucial within the calendering process. The roll pressure (F_N) exerted by the rolls must be sufficient to compact the electrode material without causing damage. The optimal pressure depends on the material composition and the desired density. The applied calendering pressure is often described as line load (q_L), which is the ratio of the applied force (F_N) and the coating width (w_C). The roll gap (Δ) describes the slot between the two rolls and is based on the target thickness ($\rho_{El,1}$) and the thickness of the freshly coated electrode ($\rho_{El,0}$). This gap is usually slightly less than the desired thickness to account for the material's elastic recovery (spring-back effect) after compression. The roll speed (r_S) defines at which speed the electrode material passes through the rolls. A consistent speed is necessary to achieve similar contact-time and therefore area. The speed heavily influences the quality of the electrode coating and ones set, it ensures constant thickness.

The roll temperature (T_{R}) also has to be adjusted, as it influences the behavior of the binder within the electrode material. Temperature control can aid in achieving the desired compaction and surface properties.[138,141]

Throughout the calendering process, quality control measures are in place to monitor the thickness and density of the electrode. Advanced systems use laser gauges and other sensors to measure these parameters in real-time, allowing for immediate adjustments. However, in batch process or pilot plant dimension an altimeter is often used to determine the thickness throughout the electrode geometries (width w_{C}, and thickness δ_{El}).[142,143] The calendering process is not just about achieving the correct dimensions in terms of thicknesses; it also plays a significant role in enhancing the electrical contact between active material particles and improving the adhesion of the coating to the current collector. Both impacts the energy density of the cell. A denser electrode can store more active material in the same volume. It also ensures the structural integrity of the electrode during battery cycling. Uniform compaction of the electrode material can reduce mechanical stress during cycling, potentially extending the battery's cycle life. Calendering also reduces the internal resistance of the battery, which improves the power density. Thus allowing for faster charging and discharging rates.

Despite its importance, calendering presents also several challenges, as the process must be carefully optimized for different electrode materials and formulations to avoid damaging the electrode structure. Over-calendering can lead to decreased electrode porosity, hindering electrolyte infiltration and ion transport. Insufficient calendering can result in poor mechanical stability and lower energy density. In sum, calendering is a critical step in the production of battery electrodes, with a significant impact on the final battery's performance. The process requires precise control over multiple parameters to ensure that the electrodes meet the necessary specifications. As battery technology advances, the demand for more sophisticated calendering techniques will continue to grow, driving innovations in the manufacturing equipment and processes used in the industry. After calendering, the electrode may undergo additional treatments such as surface conditioning or slitting to the required width for cell assembly. These steps are crucial for ensuring the electrode's compatibility with the subsequent battery assembly processes.

The effects of calendering onto the micro-structural changes as well as the accompanied gas evolution due to the interfacial reactions between various densified electrode materials and electrolyte were in-depth studied within this work, using OEMS as the method of choice. The results of this work are shown in chapter 5.

2.6.3 Cell Formation Process

The formation step usually covers the electrolyte filling into the assembled cell, followed by the first charging procedure to form the SEI. Section 2.5 described hereby in detail, the necessarily of a good and uniform SEI-layer, within the entire anode. In the following a deeper understanding into this process step will be gained.

The formation protocol usually includes slow charging and discharging procedures, which can last for several hours to days and runs typically in batch processes. However, the former shown cell production process chain (see Fig. 11) is operating in a continuous production of e. g. electrode coils. To tackle this bottleneck, either large investment in charging equipment (e.g. formation chambers) is necessary, or the size of the dry-room has to be adapted. Hence, the formation process can occupy up to 25 % of the floor space in dry rooms. In addition to the large amount of needed electricity, the formation step is leading to significant manufacturing costs.[144,145]

Technically, the process can be divided into three steps: i.) Wetting, ii.) Formation, and iii.) Aging. Each of these steps is crucial for ensuring high quality LIBs and are a well kept secret of each cell manufacturer. A general workflow is schematically shown in Figure 13.

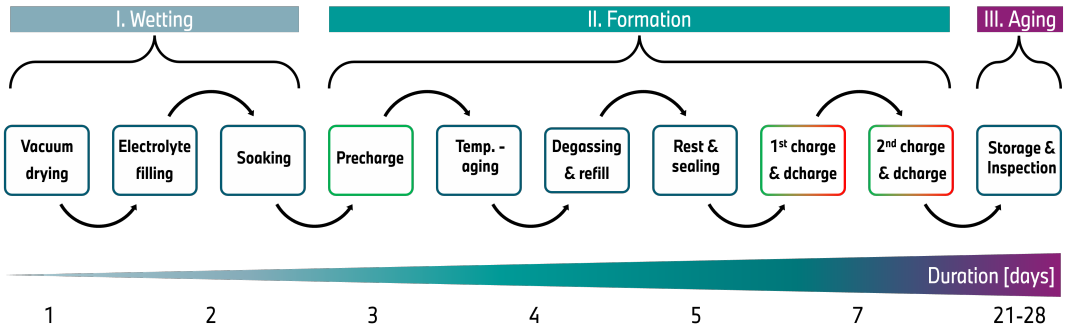

Figure 13: Typical workflow of Li-ion battery cell formation, including a former electrolyte wetting procedure and a latter accompanied aging step.

I. Wetting: The wetting step allows the electrolyte to come in close contact to the active material macro- and micro-pore structure. The electrolyte is filled into the cell by applying a pressure profile, which consists of an alternating procedure of over-pressure and vacuum, to activate the capillary effect within the active material (soaking). Finally, the amount of electrolyte is gravimetric determined (balance) or volumetric within the filling machine. Elevated wetting temperatures of usually 40-60 °C reduces the surface tension of the electrolyte.[132,134] Time, pressure and temperature profiles can differ for cell types and chemistry's and are the key knowledge of this production step.

Without excellent wetting, a complete and homogeneous SEI formation will not occur. To ensure a dry environment before the electrolyte is filled into the cell casing, the cells are usually dried again under dynamic vacuum within dry-room conditions.[146,147]

II. Formation: In this step, the cell is charged with electrical energy for its 1st time. In consequence of that, the electrolyte is electrochemically reduced on the polarized anode, forming gaseous, such as hydrogen (H_2), ethylene (C_2H_4), carbon monoxide (CO) and carbon dioxide (CO_2),[129,148] liquid, and solid products, among which only a few of the solid products are desired to constitute the SEI layer on the negative electrode. Currently, no standard formation procedures have been established, as each manufacturer has their own recipe for optimizing the process based on specific LIB configuration and intended applications, such as high power or high energy and represent the core knowledge of each cell manufacturer. However, the formation procedure and the technical steps are rather similar.

Many parameters, such as temperature, current rate, cycle numbers influences the exact composition of the SEI and are a well kept manufacturers secret.[132] The SEI is critical in ensuring optimal lifetime of the LIB and multiple reviews have examined the impact of SEI composition on the overall cell performance.[118,149–151] Hence, investigations of so-called fast formation procedures have been intensified in order to enable affordable cell production in Europe.[152] Several publications have shown that higher current rates can decrease the formation time without sacrificing the efficiency of LIBs.[146,147] Dividing the initial charging process into sections is another feasible approach. Splitting the first part of the formation process, i.e. when the cell needs to be opened to release the formed gases, from the rest, i.e. when the cell might as well be sealed, time and space could be further optimized. This procedure was also examined within this work in chapter 6 and is exemplarily shown in figure 14.

After sufficient reduction of the electrolyte, most gas generation should stop. Following that, the cell can be degassed (vacuum), eventually refilled with fresh electrolyte, sealed, and relocated from expensive dry room environments to complete the formation protocol elsewhere. Once the formation is completed, the cells are relocated to the storage and inspection area.

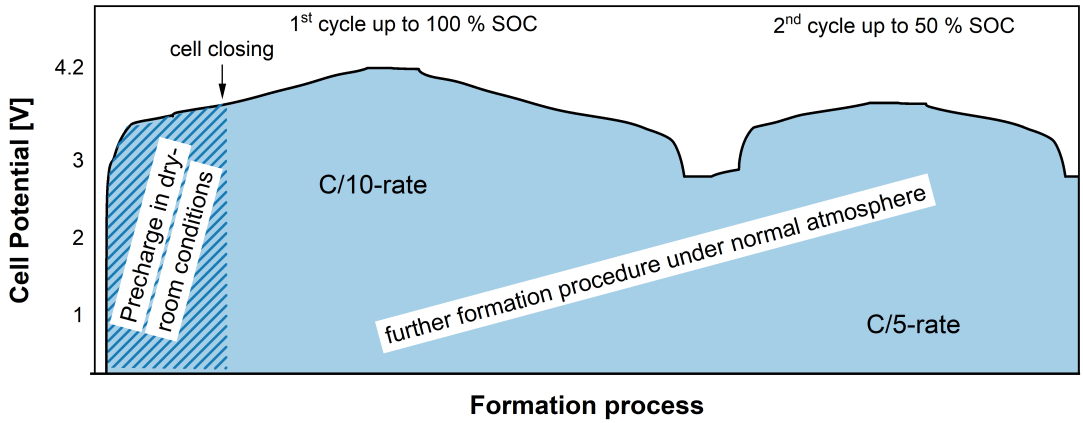

Figure 14: Voltage profile during automotive cell formation procedure, including one cycle with C/10 and one with C/5. The formation is split into a precharge process with accompanied gas evolution within dry-room atmosphere and a further formation procedure with the sealed cell under normal atmosphere.

III. Aging: The aging and inspection procedure is the last step in cell production. During this step, the open circuit voltage (OCV) is regularly measured to determine the self-discharge rate of the cell. Typical loss-rates are in order of $\approx$ 1 mV/day. Furthermore, the internal resistance of the cell is determined. Within this procedure the cells are also stored at different SOC in so-called aging towers. Here, different conditions can be applied to the cell. Usually, the cells run through a high temperature (30-50 °C) and low temperature (20-25 °C) aging procedure, last for two or three weeks. Besides the performance determination of each cell, it is also necessary for safety and quality assurance, before the cells are shipped to the customer.[134]

Finally, the cells are discharged to their shipping state of charge, combined with an optical inspection, pulse test and leakage testing. The cells might be sorted according to their performance data (grading).[134] The duration and exact procedure strongly depends on the cell manufacturer, the used cell chemistry, and represents also an additional cost factor for manufacturing.

2.6.4 Cell Formats for Automotive Application

The current global market for automotive battery cells is highly heterogeneous, with numerous cell manufacturers. Each of them producing their own cells, based on their individual production line and according to the specifications of their main (automotive) customers. This results in a huge variety of cell sizes, interior & exterior design as well as material combinations. The overall cell shapes however, can be classified in prismatic soft-case (pouch), prismatic-hard case, and cylindrical format. [153]

Pouch cells consist of several stacked layers of electrode within a flexible casing. These cells were typically used for laptops, cell phones or e-bikes. However, due to their reduced weight and flexibility they have also become interesting for BEV applications. [154] Chevrolet, Renault and Nissan are currently using pouch cells, as they provide a maximum of flexibility, module design and capacity. Nevertheless, the flexible pouch casing makes it hard for EV applications, e.g. in case of a fatal car accident. Also their temperature and pressure has to be precisely controlled. [155]

In consequence of that, the prismatic-hard case cells were developed, as their casing is much stronger and withstand much higher external forces. They are being produced in a similar way, by stacking several dozens of electrode/separator sheets on top of each other. Both, BMW and Volkswagen uses this cell format in their current EVs architecture, as they are more compact and easier to cool. However, there are many process steps involved to make sure, the alignment of each layer is perfect. If one electrode layer does not achieve its perfect position, short circuits or lithium-plating can occur. Also the required tap-welding of each layer is time and cost intensive and prone to failures. Additionally, this cell format suffers from low energy density due to unused space within the cell can and problems with large numbers of charge and discharge cycles due to swelling and thus cell-can deformation. [155]

In the past, there was a high pressure on the side of the car manufacturer to produce EVs at all. Therefore the basic car concept with combustion engine was typically straight-forward replaced with battery packs, see Fig. 15 for inspiration. Here the effort was more on the general concept and the implementation of series production of EVs. This resulted in a large quantity of unused space within the car/high-voltage battery pack. However, those first EVs cars allowed sufficient ramp-up time for OEM to further improve battery pack design and system optimization as it can be seen in the BMW iX3 model (right part of Fig. 15). Nowadays, more effort is being used for the cell-to-module or cell-to-pack integration in order to extend the km-range and the limits of the specific cell chemistry.

Figure 15: Technical illustration of the rather simple high voltage battery integration into a BMW i3 (left) and a more advanced integrated HVS-package in a BMW iX3 (right). Figures provided by BMW Press Club.[156]

In consequence of this development, a new type of cell format re-emerged in the last years, the cylindrical cell.[157] The main advantage of this cell format is their ease of production, as they were already being produced since 1994 from Panasonic, e.g. in the 18650 cell format.[158] Mainly the diameter and height had to be adapted to the processing machines, to produce this cell type for EVs.

Due to the internal structure of cylindrical cells, the electrodes are winded under high stress/tensile forces and the complex stacking and tab-welding process is eliminated. The final electrode coil is inserted in the stainless-steel can. One of the head-sides represents the positive terminal, whereas the cell can itself represents the negative terminal. Cylindrical cells have the additional benefit of resisting much more internal pressure, occurring due to gas evolution and electrode swelling. Prismatic cells where often swollen during charge/discharge with makes it difficult to implement them in a vehicle, as enough space have to be left, allowing space for cell swelling that each cell can swell several millimeters.

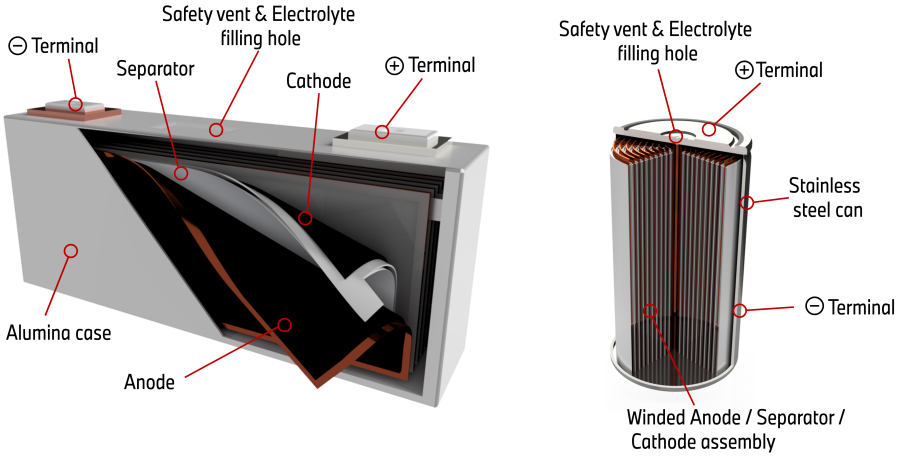

Figure 16: Internal architecture of a prismatic (left) and a cylindrical (right) battery cell. Both design's were used within this work and studied regarding their gas release; drawn by author.

2.7 In-Operando & In-Situ Characterization Techniques

To meet the growing market and customer demands, new LIBs with increased power and extended lifespan are being developed. This requires the use of even more demanding compositions of active materials and liquid electrolyte formulations, as formerly described in section 2.2 - 2.4. However, to fully utilize the potential of future LIBs, it is essential to do not only consider their performance, but also their aging in more depth. Thus, continuous developed of new and powerful analytical methods with a special focus on battery degradation components is necessary.

Until today, battery research even in industry still relies on well established techniques and cycling protocols, such as cyclic voltammetry (CV), electrochemical impedance spectroscopy (EIS), incremental capacity analysis (dQ/dV) (ICA), or differential voltage analysis (dV/dQ) (DVA). Currently, state-of-the-art LIBs exhibit a coloumbic efficiency (CE) of over 99.97 %, indicating that only 0.03 % ($\approx$ 300 ppm) of all electrochemical reactions within the cell are irreversible processes.[159] Hence, the focus must set on the understanding of these minor side reactions during cycling and their impact on the battery cell performance. Nevertheless, many analytical techniques come to their limit as they can usually only measure battery components after disassemble procedure and mostly also air contact. This ends in the loss of information of the analyte during cell operation.

2.7.1 Overview and Necessity

The interface between the electrode and electrolyte, as well as the electrode surface, is the most crucial and least understood region in a LIB. Numerous complex reactions involving gaseous, liquid, and solid intermediates/products occur, such as SEI formation and redox reactions. An in-depth understanding of these interfacial reactions, down to the micro-structure, is key to developing new battery materials, optimized cell chemistry´s, and operating conditions.[160]

This understanding can be gained through the use of in-operando[1]/in-situ[2] characterization techniques. Therefore, the development and adaptation of non-destructive, advanced analytical techniques with high selectivity, sensitivity, and resolution has experienced a significant increase in recent years. Those powerful techniques can bridge the gap between conventional ex-situ measurements and costly synchrotron measurements, to unravel the internal behavior of LIBs, in real-time .[161]

[1] in-operando is referred to: acting like in the original state
[2] in-situ is referred to: in the original place

Various in-operando/in-situ methods exist and are specialized in detecting degradation processes of the anode, cathode, interface or electrolyte with either solid, liquid or gaseous compounds. Table 4 provides an overview of the most common methods used in the field of LIB research.[162]

Table 4: Advancement of in-operando/in-situ methods for examining batteries and battery materials. References for the individual method can be found within the text.

Technique	Product	Location	Battery configuration
OEMS	gaseous	all	coin, pouch, automotive
XPS	solid	electrode surface	↓
XRD	↓	in the electrode	↓
SEM	↓	↓	coin, (ASSB[115])
SECM	↓	↓	coin
Raman[163]	solid, liquid	↓	coin, pouch
FT-IR	↓	↓	↓
NMR[164]	↓	↓	coin

In-operando methods offer the advantage of observing even transient processes and detecting thermodynamically unstable intermediates. However, they also come along with some hurdles. Firstly, they are more complex to set up, secondly the operation relies usually on self-defined and controlled measure principles, and thirdly the interpretation of the collected data is more time intensive and requires a lot of experience by the operator. The latter one is mainly due to the presence of all other cell components, which often results in overlapping signals. In comparison, for ex-situ measurements the sample must be prepared in accordance to the specific requirement of the analytical method, e.g. liquid chromatography (LC) or inductively coupled plasma-mass spectrometry (ICP-MS).[162]

2.7.2 Development of OEMS- and DEMS-Techniques

One of the most widely used analytical techniques is mass spectrometry (MS), as it can be interfaced to several neighboring analytical and electrochemical techniques.[165–167] This feature makes online electrochemical mass spectrometry (OEMS) by far the most established in-operando method, capable of monitoring volatile compounds, due to electrochemical reactions, in a variety of cell configurations. The development of those setups has already a history of almost 45 years (see Fig. 17). The obtained gassing data allow to draw conclusions about the processes in all three phases within a LIB.

OEMS is capable to monitor the temporary evolution and consumption of gaseous species within the cell headspace. Most of these side-reactions occur due to electrolyte degradation, as it was shown within Figure 10. Obtaining real-time information during

cycling on these thermal & electric-potential triggered reactions inside a LIB, and their consequences, e.g. swelling and impedance growth give new insights to optimize the overall performance of batteries and their materials, as well as to guarantee operational & storage safety.

For most operando methods, the connection principle presents a major challenge. It must provide the analytical technique access to the battery environment, such as a capillary connection towards MS for gas analysis, or the implementation of a quartz window to allow electromagnetic waves interactions with the LIB. On the other side, it should have only a minor influence onto the LIBs natural state. Regarding OEMS, this means developing a gas-tight cell housing that allows for gas sampling from the cell to the MS while preventing interference with gases from the outer atmosphere. Additionally, the gas sampling should be as low as possible, to do not remove the volatile electrolyte. For latter reason, differential electrochemical mass spectrometry (DEMS) was developed.

It has been the main goal of this PhD thesis to set-up a new OEMS system and to develop several connection strategies for coin-cell, prismatic and cylindrical cell format to study the gas evolution reactions within automotive battery cells.

From the Past to the Current State of the Art OEMS

The first time that MS was used to determine volatile products from electrode reactions, was in early 1971. Back then, *Gadde and Bruckenstein* monitored the temporary evolution of O_2 from a $HCLO_4$ solution.[168] In 1984, *Wolter and Heitbaum* presented their first DEMS setup and its application in the field of electro-catalysis.[169] The equipment comprised an electrochemical cell, a membrane inlet system, and a mass spectrometer. The products formed at the porous working electrode were drawn through the pores into the ion source of the mass spectrometer. The feasibility of the setup and the combination of CV were described. The term differential was added to point out, that the gaseous products were immediately transferred into the MS via a differential pumped gas inlet system.

In 1998, *Imhof and Novak* applied DEMS to LIBs for the first time.[127] They demonstrated the temporary evolution of ethylene and hydrogen due to SEI formation, the electrochemical electrolyte oxidation (evolution of CO_2 and CO), the release of lattice oxygen from metal oxides (O_2, CO_2), and the reduction of protic decomposition compounds and trace water (evolution of H_2).[170] In 2005, *Novak et al.* developed a cell setup with an open-headspace configuration.[171] This allowed the evolved gases to be immediately transported to the MS via a continuous flow of argon, used as a carrier gas. The benefit of this setup was a significantly lower electrolyte-induced background.[172]

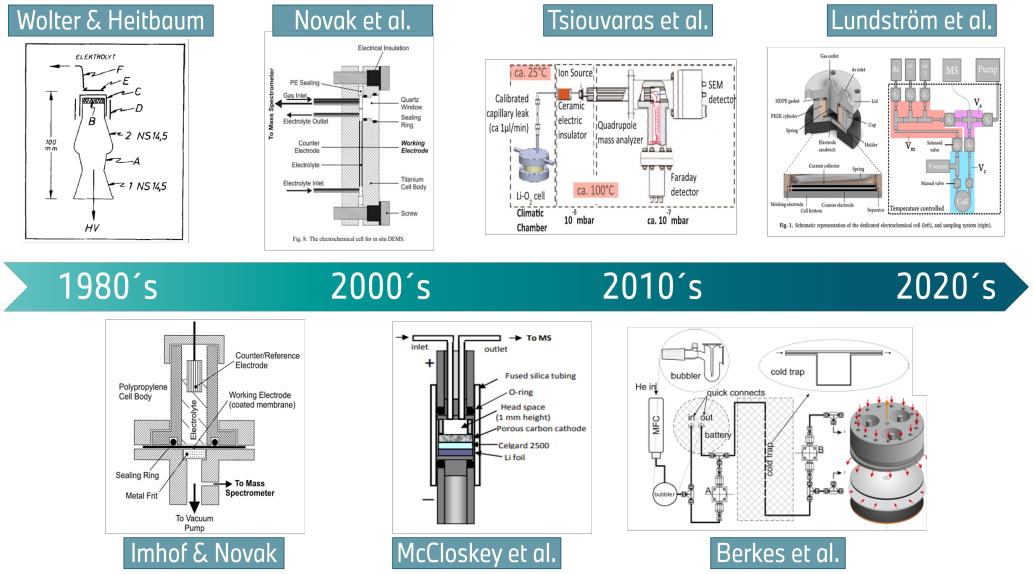

Figure 17: Some of the most important milestones in the field of time-resolved mass spectrometry coupled with electrochemistry between 1980 and today. References are given in the text.

In 2010, *McCloskey et al.* developed a DEMS based on a set of gas valves.[173] This allowed a semi-closed headspace that was only probed by MS at discrete intervals. By avoiding a continuous flow of carrier gas through the cell, less depletion and higher sensitivity was achieved as the gases could accumulate in between the sampling interval. *Berkes et al.* optimized the DEMS setup by including a cold trap to remove volatile electrolyte compounds before entering the UHV of the MS.[174] They also used infrared spectroscopy (IR) within the setup to further improve the sensitivity for carbon monoxide.

He et al. later developed a semi-closed approach with a larger cell volume and a different valve arrangement, but with comparable performance.[175] The size of the cell has a significant impact on the sensitivity and resolution of the collected mass spectra.
Lundström et al. continued the work of He and McCloskey by implementing a DEMS setup with an online partial and total pressure measurement unit for LIBs, connecting a pressure sensor to the electrochemical cell to provide direct insight into the gassing behavior of the cell.[159] This allows to detect all gaseous species, even if there mass traces are not monitored within the MS.

On the other side, *Tsiouvaras et al.* made a similar journey and developed a so-called online electrochemical mass spectrometry (OEMS) system in 2011.[176] The system uses a closed cell headspace that is directly connected to the MS with a crimped stainless-steel capillary, without the flow of a carrier gas. The leakage rate, of the capillary is defined for each capillary individually and is typically around 1 µL·min.$^{-1}$.[177] This leads to a continuous drop in cell pressure, which limits the experimental time.

2.7.3 The Journey of Developing Gas Analysis Techniques on Large-Format Automotive Cells

Monitoring gas evolution and consumption in large-format cells has been rarely seen in the past, but is a strongly growing research field due to the ever-increasing usage of LIBs. The main challenge is hereby the interface between the analytical techniques and the large-format cell, e.g. custom-made cell housing. This is particularly true because large-format cells have to be pierced/opened in order to extract the gases while cycling, which presents a series safety hazard. The development path is illustrated within Figure 18.

First experiments on larger cell´s were carried out on single layer and multi-layer pouch cells. In 2014 *Aiken et al.* developed an apparatus based on *Archimedes'* principle to measure gas evolution after formation.[178,179] This principle was further optimized within *J.R. Dahn's* group, who combined this setup with the option of a single-time gas measurement by piercing pouch cells with a syringe. This approach can be considered as the first combination of electrochemical cycling of larger cells and gas measurement.[180]

On the side of cylindrical cells *Matasso et al.* designed a test chamber to examine gas evolution during cycling of 26650 (2.6 Ah, $LiFePO_4$/graphite) cells.[181] They used a pressure sensor to detect all gaseous species contributing to the overall cell pressure. *Schmitt et al.* (2020) later developed an in-vitro pressure sensor-setup for monitoring gas pressure inside prismatic LIBs (34 Ah; NMC111/graphite) during operation and extensive cycling procedures.[85] However, just few studies have been conducted on either pouch cells or larger cell format while using a pressure sensor.

In 2020, *Schmiegel et al.* designed a gas sampling method that was incorporated post-production into 240 mAh (NMC811/graphite) pouch cells.[182] This approach allowed multiple-time measurements of the headspace and bridged the gap towards online gas analysis for LIBs under commercially relevant conditions. Furthermore, it can be seen as the first combination of electrochemical cycling and gas analysis via MS in an semi-online approach.

DEMS or OEMS measurements, as they are known today, had not been possible until recently, due to the reasons explained above. However, in 2020, *Mattinen et al.* made a significant step by developing an open flow OEMS for 18650 cylindrical (1.5 Ah NMC/graphite and LMO/graphite) cells.[183] The study examines the effect of cell voltage and C-rate on gassing behavior and reports on a capability that was previously unattainable.

In 2023, *Misiewicz et al.* developed a dedicated adapter for prismatic 48 Ah PHEV2 cells (NMC/graphite chemistry).[129] This adapter can be screwed on different sizes of prismatic cells, which were carefully penetrated with a drilling machine within glovebox atmosphere. It allowed them to monitor pressure and gas evolution on an intermittently closed electrochemical mass spectrometry (ICEMS) setup. They used this setup to conduct an in-depth study on the gassing behavior within two cycles with low C-rate. The study observed even small effects on gas evolution, pressure behavior, and graphite stage-formation.

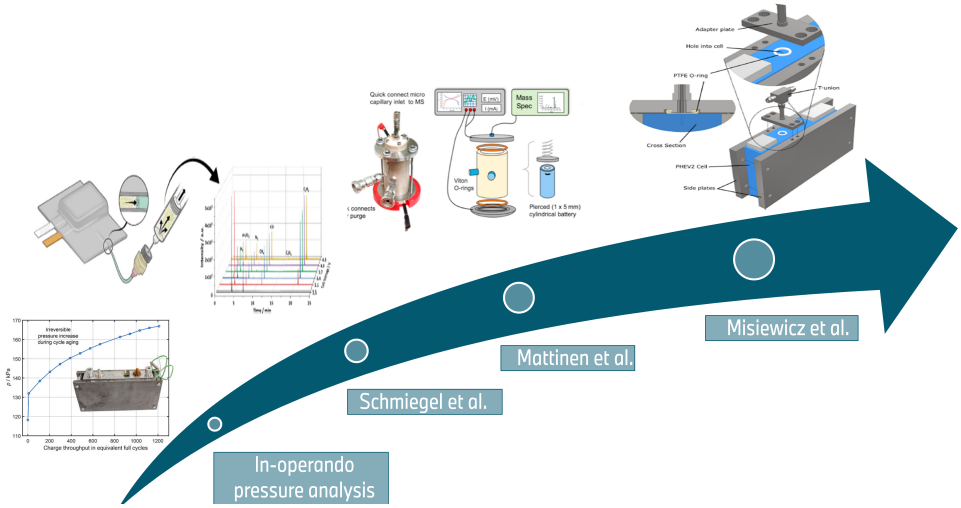

Figure 18: Some of the most important milestones in the field of in-operando analysis of large-format lithium-ion cells, starting from pressure analysis up to complex mass spectra evaluation in a real-time approach.

Investigating the gassing behavior of commercially battery cells has gained a lot of interest in research. Recently published studies have analyzed prismatic[129] and cylindrical cells (18650 cell type).[183] An interesting aspect of studying these considerably larger cell formats are the altered gas pathways that arise from the modified configuration of the electrodes. While the electrodes are horizontally aligned in the typically used model cell (see Figure 17) and gases can therefore simply escape, the electrodes in cylindrical cells, are wound-up and have a significantly larger geometry. This means that any gases that are produced have to diffuse much longer distances through the battery cell system. This presumably increases the time it takes to detect the gases. Furthermore, the possibility of "commercial in-operando cell analysis" allows investigation at every stage of their operational life, e.g. after use in BEVs.

Based on these rich and fundamental developments, this work presents the implementation of a novel concept for prismatic cell as well as a cylindrical cell housing for BMW in-house produced 4695 cells, as well as commercially available cylindrical cells in similar format. The development process is described in section 3.1.5, and the application is discussed in section 7.1.

Experimental Methods

This chapter provides an overview of the used analytical- and electrochemical characterization techniques, with a special emphasis onto the deployed OEMS system. Furthermore, the working steps for electrode- and electrolyte manufacturing, as well as cell preparation for the in-operando gas analysis of Li-ion batteries are described.

3.1 Online Electrochemical Mass Spectrometry (OEMS)

OEMS is an analytical technique that combines electrochemistry with MS to study and characterize electrochemical processes within battery cells. This is done, by the time-depended combination of the electrochemical data with the recorded mass traces of the individual gaseous components. These gas species can occur as intermediate- or side products or can be even provided as reactant. OEMS is therefore a powerful technique to investigate the true behavior within a realistic cell environment. The electrochemical cell and the mass spectrometer are coupled in an online configuration, allowing a real-time analysis of the electrochemical processes within the battery cell. OEMS setups are individual custom-made and not yet available on the mass market. In consequence of that, the time resolution of the setup is an important parameter, as it strongly depends on the developed setup. Determining the time resolution helps to correctly interpret the measured data and to compare one setup with others. Hence, the time-resolution was studied within this work, see chapter 4 for the in-depth study. The time resolution of the herein implemented setup was found to be in the order of 10-100 seconds, depending on the gas species. As the usually applied charging/discharging protocol is typically in the range of hours, e.g C/10 = 20 h for one full cycle, the term "online" seems to be justified.

An OEMS is very similar towards the earlier described DEMS system. The difference between both setups is basically the time interval in between each measurement point. Within an OEMS, the cell headspace is directly connected towards a mass spectrometer and the sampling rate of the mass trace depends on the scan-speed of the MS. In contrast to that, the cell within a DEMS setup is usually closed and intermittently purged with carrier gas, which transports the evolved gasses from the headspace of the electrochemical cell to the mass spectrometer. Consequently, the data within an

OEMS setup represents quantities of evolved/consumed gasses ($nmol$), whereas DEMS approaches typically represents evolution/consumption rates ($nmol\ min^{-1}$). Hence, OEMS provides good detection limits and time resolution as the gases of interest are not diluted by the carrier gas. On the other side, DEMS approaches offer theoretically unlimited measurement time due to continuous head space refilling and the well sealed battery cell represents a more realistic approach.

Following that, OEMS is a technique to gain deeper understanding of complex electrochemical systems and processes and MS is used as a tool which provides the time-resolved information about the gaseous components and the underlying parasitic side reactions.

3.1.1 Basics of Mass Spectrometry

A mass spectrometer is essentially an instrument used to identify ionized molecules based on their mass to charge ratio (m/z). Today, several different kinds of MS techniques exist. However, the principle of using electric and magnetic fields to accelerate and establish the trajectories of ions inside the spectrometer according to their mass/charge ratio is common to all of them. MS is widely used in various fields, including chemistry, biology, physics, and environmental science, for the identification, quantification, and structural elucidation of molecules.[184]

History

The origins of mass spectrometry can be traced back to the late 19$^{\text{th}}$ century, with the pioneering work of several scientists who laid the foundation for this analytical technique. In 1898 *Wilhelm Wien*,[185] a German physicist, developed an apparatus that could separate charged particles based on their mass-to-charge ratio, laying the groundwork for mass spectrometry. Based on that, *Francis Aston*,[186] a British chemist, developed the first mass spectrograph, which was able to separate isotopes of neon and measure their masses with high precision. In the following 20$^{\text{th}}$ century several advancements had become reality towards MS. In 1918 *Arthur Dempster*,[187] an American physicist, constructed the first modern mass spectrometer, which used a magnetic field to separate ions based on their mass-to-charge ratio. In the 1940s *Alfred Nier*,[188] an American physicist, made significant improvements to mass spectrometers, including the development of the first high-resolution mass spectrometer.

However, to that time it was very difficult to achieve stable and spatially uniform magnetic fields, especially with permanent magnets. These difficulties lead to low mass resolutions and drifts in the calibration curve of the instrument. In addition, the presence of stray magnetic fields affected other instruments that may be used in conjunction with a mass spectrometer, e.g. a potentiostat.

In 1953 *Wolfgang Paul*,[189] a German physicist, recognized that the use of magnetic fields could be eliminated by a clever design of alternating quadrupolar electric fields rather than magnetic fields, hence the name quadrupole mass spectrometer (QMS) was born. Until today, quadrupole mass analyzer became one of the most widely used mass analyzers in the field of mass spectrometry. The working principle of a QMS is therefore explained in the following section and shown within Figure 19.

In the 1960-70s the development of soft ionization techniques, such as electron ionization (EI) and chemical ionization (CI), allowed the analysis of larger and more fragile molecules. Also in the 1970s the concept of tandem mass spectrometry (MS/MS) was introduced, enabling the fragmentation and structural analysis of selected ions.[190] Since the 1980s MS has become additional attention due to the development of electro-spray ionization (ESI) and matrix assisted laser desorption/ionization (MALDI). These soft ionization techniques revolutionized the analysis of large bio-molecules, such as proteins and peptides. Additionally, the development of time of flight (TOF) mass analyzers provided high-resolution and high-mass capabilities, expanding the applications of mass spectrometry, once more.[191,192]

The coupling of mass spectrometry with separation techniques, such as gas chromatography (GC-MS) and liquid chromatography (LC-MS), has greatly expanded the analytical capabilities of MS. The continuous advancements in ionization techniques, mass analyzers, and hyphenated techniques, such as OEMS have made mass spectrometry an indispensable analytical tool in a wide range of scientific disciplines, from chemistry and biology to environmental science and forensics.[191,192]

In terms of OEMS the MS can be rather simple designed, as only distinct molecules, e.g. H_2, C_2H_4, CO, CO_2 or O_2 are being studied. Therefore, a rather simple QMS with a focus on small molecules (low mass) is the device of choice and explained in the following.

Working Principle of Quadrupole Mass Spectrometry (QMS)

A quadrupole mass spectrometer typically consists of an ionizer unit (e.g. by electron bombardment from a hot filament), an ion accelerator, and a mass filter. Latter one consist of four parallel metal rods arranged in a square configuration. A cross-section of the used QMS as well as the principal of the quadrupole mass filter is shown in Figure 19.

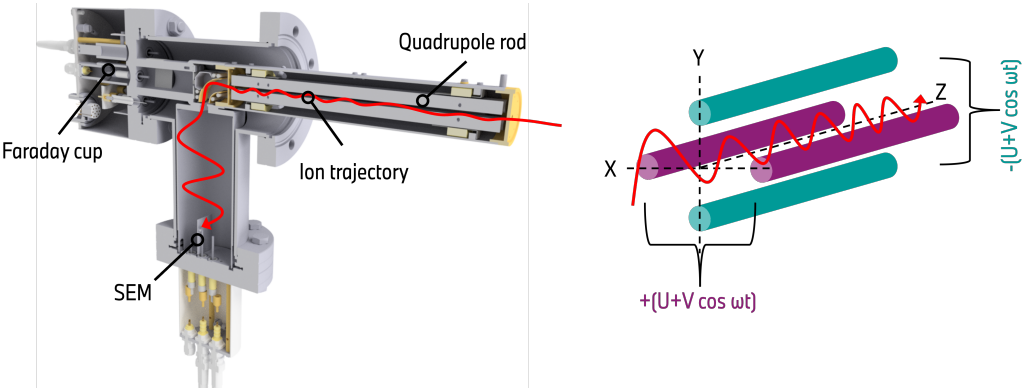

Figure 19: Left: Cross-Section of the used quadrupole mass spectrometer. Right: Schematic drawing of the quadrupole mass filter principle. The ion trajectory while using the secondary electron multiplier (SEM) is shown as red line in both figures.

Two opposite rods of the QMS have a potential of (U+V·cos(ω t)) whereas the other two rods have a potential of -(U+V·cos(ωt)). Here, U is a direct current (DC) voltage and V·cos(ωt) is an alternating current (AC) voltage, creating a dynamic electric field within the analyzer. A mass spectrum is obtained by monitoring the ions passing through the quadrupole filter as the voltage on the rods is varied. Two options are available: Varying ω and holding U and V constant, or varying U and V with (U/V) fixed for a constant angular frequency (ω). The stability of the ion trajectory within the quadrupole is determined by the m/z-ratio of the ion. Only ions with a specific m/z-ratio will have a stable trajectory and will reach the end of the rods. All other ions will have an unstable trajectory and be ejected from the analyzer.

In order to achieve higher sensitivities, a secondary electron multiplier unit is often used, to increase the electrical signal from the ions. Therefore, the SEM is usually placed in a 90 ° angle towards the quadrupole mass filter in order to get rid of neutral particles, as they are not influenced by the electric field of the QMS. This configuration is highly stable and provides excellent mass resolution. Nowadays, QMS is one of the most widely used mass spectrometric techniques due to its simplicity, cost-effectiveness, robustness, and versatility to measure ionized atoms/charged particles quickly within a wide mass range including rapid data acquisition and analysis. Additionally, it allows an easy compatibility with hyphenated techniques, such as GC-MS, LC-MS, or OEMS, providing powerful analytical capabilities.

3.1.2 Setup Specifications and Working Principle

The installed OEMS setup within BMW is depicted in Figure 20. The figure presents the overall setup, whereas the important parts are labeled and described at the bottom of the figure itself. The main intention of developing this OEMS setup was to especially optimize it towards the adaption of large automotive cells. Therefore, the setup had to be robust, fulfill high demands on technical cleanliness, and mobile in order to relocate it e.g. within safety rooms, in case of risky investigations, e.g. overcharge or high temperature experiments.

The principle hardware of the used setup was mainly inspired and adapted from *Tsiouvaras et al.*[176] which is being used at the technical university of Munich. Also the data analysis procedure was adapted from this chair, mainly inspired by *Metzger et al.*[28] The cell design for model cell application was meanwhile adapted from *Lundström et al.*[193] from the university of Uppsala, Sweden.

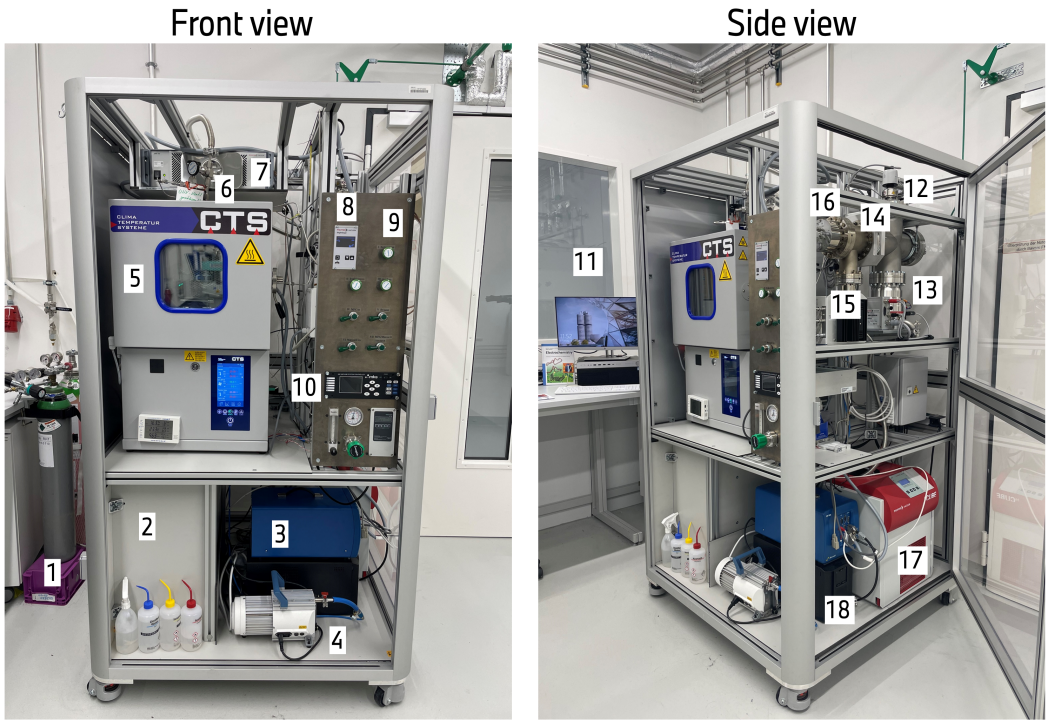

1 = argon supply
2 = calibration gas cabinet
3 = potentiostat
4 = oil pump
5 = climate chamber
6 = interface section
7 = QMA-400 unit
8 = pressure gauge
9 = gas supply / control board
10 = mass flow control unit
11 = computer
12 = cross beam ionization source
13 = HiPace 300 turbo pump
14 = quadrupole mass analyzer
15 = SEM detector
16 = faraday cup
17 = rough pump
18 = uninteruptable power supply

Figure 20: Photograph of the OEMS setup, launched during this work at BMW. The most important parts are labeled and described on the bottom. The setup is fully movable, within operation due to an installed uninterruptible power supply (UPS) unit.

The individual electrochemical cell (see section below) is placed within a climate chamber (5; Series S CTS, Germany) and connected via crocodile clips to the potentiostat (3; SP-300 Biologic, France). In addition, the cell is connected via the interface section (6) to the MS inlet. The interface consist of a crimped capillary leak open (CLO) (Vacuum Technology Inc., USA) which is screwed onto the electrochemical cell within a glovebox. The interface region further consist of a series of valves and metal hose to connect the cell to the mass spectrometer (14, HiQuad QMA410, Pfeiffer Vacuum, Germany). A ceramic insulation (Swagelok type: VCR-FF-KR13-SST64, Germany) is located within the walling of the climate chamber, which isolates the MS from the electrochemical cell and avoids parasitic currents.

Before opening the valves between cell and the ultra high vacuum (UHV) of the MS, a rough pump (17) is being used to reduce the gas ballast within the interface region. An argon gas supply (1) is available, which is used to purge the interface in between the rough vacuum procedure and to purge the cells headspace before the electrochemical protocol is being applied. Several gas pipes are available for flushing the setup either with argon or calibration gas (2). For daily usage the gas bottles are stored outside (1), but a gas cabinet (2) is available for fully independence and mobility. The control board (10) allows to precisely control the volumetric flow, using mass flow controller (MKS Instruments, Germany).

The MS itself consist of a cross beam ionization source (12), a quadrupole mass analyzer (14), a Faraday cup (16), and a SEM (15) for detection. The vacuum is provided by a turbo pump (13; HiPace300, Pfeiffer Vacuum, Germany) and is measured by a pirani cold cathode (8; Pfeiffer Vacuum, Germany). The vacuum reaches $< 10^{-10}$mbar when the interface is closed and $\approx 10^{-7}$mbar when the interface is open and an electrochemical cell is connected. Furthermore, the setup includes a MS control unit (7; QMA-400, Pfeiffer Vacuum, Germany), a high frequency generator and a second rough-pump (17; HiPace 80 Pfeiffer Vacuum, Germany) to evacuate the lines before the turbo pump can operate.

An uninterruptible power supply (UPS) (18; APC Smart UPS, SMT1500IC) allows the former mentioned mobility of the complete setup for at least 20 minutes, which is enough to allocate the setup from a standard lab room towards a safety room in case of serious experiments on large format cells. The complete setup is built into a wheel-based frame of Item profile bars. The side walls are either closed with aluminum sheets or transparent Plexiglas. The nearby computer (11) is then being used to start/stop data acquisition (MS, potentiostat and pressure sensor).

3.1.3 Basic Principles of Operation

The within a glovebox (O_2 & H_2O < 1 ppm) assembled cell is subsequently transferred towards the climate chamber of the OEMS. The detailed cell design is described separately in the next section, whereas the exact cell components as well as the type of electrolyte and cycling procedure is given separately in each study in the results part. The assembly of the model cell is similar to a procedure used in coin-cells and shortly described here. The electrode assembly typically comprises a counter electrode on the bottom of the cell, a porous separator (poly-olefin or glass fiber), a working electrode and 100-300 µL of electrolyte. Typically a stainless-steel mesh wire was used as current collector. The narrow aperture of the mesh ensure a sufficient conductivity, while having a maximum of porosity and hence unhindered gas evolution into the cell´s headspace. Therefore the coating of the upper electrode had to face upwards.

The typical measurement routine of a single OEMS experiment is schematically depicted in Figure 21. After connecting the cell to the MS and the potentiostat, the interface section is flushed with argon and the gas ballast is reduced with an oil-pump, before the valves are opened towards the UHV region. Hence all ion currents should exponentially decay and achieve a stable plateau. After that, the cell is purged with argon for 5 min with a fixed flow rate of 10 mL per minute, allowing a five-times headspace refreshment and the removal of volatile organic compounds, introduced through the glovebox atmosphere.

The used CLO provides a single step pressure reduction with a calibrated leakage rate of $\approx 1 \cdot 10^{-5}$mbar*L*s^{-1}. Since the OEMS is otherwise a closed system with a headspace volume of several milliliters, depending on the type of electrochemical cell, the continuous gas sampling decreases the headspace pressure within the cell. This limits the measurement time to 40-50 h in total for the model cell. However, the measurement time could be increased by intermittent purging the cell headspace with argon. This would enable consecutive cycles. However, also this procedure might be limited by the evaporation of electrolyte portions, unless the argon gas stream is pre-wetted with the used electrolyte.

Following that, the electrochemical cycling protocol can be started by simultaneously record the mass traces, the cell´s potential and inlet pressure. During the procedure the m/z-signals 1-240 are measured with a dwell-time of 200 ms for each mass channel. Pressure and cell potential was usually recorded each second. In order to study the potential dependent gassing behavior of the individual material, rather slow charge/discharge protocols, e.g C/10 were employed.

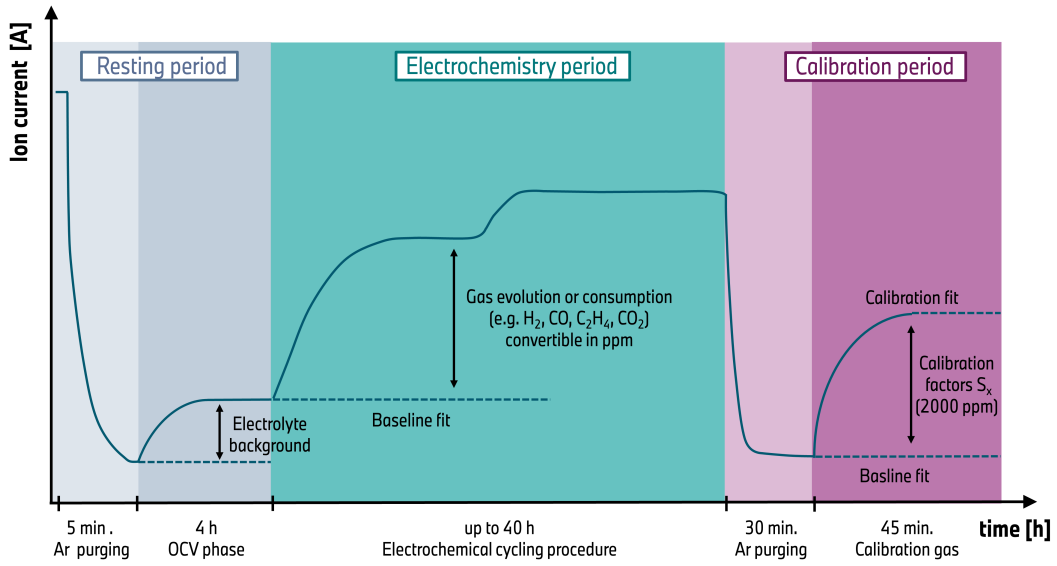

Figure 21: Typical measurement routine of an OEMS experiment, as initially described by *Metzger et al.*[28] The cell is initially purged with argon, followed by an OCV rest-phase for signal equilibration. Consequently, the electrochemical procedure is carried out, up to 40 h. For quantification of the evolving gases, a calibration procedure is followed.

Prior the charging procedure, a 4 h rest period is taking place under OCV conditions. This is necessary, to achieve stable background signals due to gas phase rearrangement and temperature equilibration of the cell. The equilibrated background signals are either fitted with a second order exponential decay function or a combined exponential/linear function (baseline fit). This function is then extrapolated to the actual electrochemical measurement and subtracted from the normalized signals to correct for the electrolyte background.

3.1.4 Data Treatment and Calibration Procedure

To obtain the evolving gas amount in dependence of the electrochemical applied protocol, one need to follow a complex data treatment and calibration procedure, which is represented step by step in Figure 22.

Firstly, the ion currents of interest (I_x) are normalized towards the signal of the ^{36}Argon-isotope (I_{36}^{Ar}). This procedure minimizes the influence of minor temperature and pressure fluctuations during the rather long measurement time. ^{36}Argon is chosen because of its unique mass and its almost non-changeable high concentration in the cell headspace. The normalized data are then background corrected for each signal, due to the rather strong influence of the electrolyte to each individual mass trace.

In order to quantify the detected ion currents, a calibration of the setup including the complex battery matrix is necessary. To do so, the cell is purged with argon after the electrochemical procedure for 30 min (see Fig. 21). The argon flushing removes the accumulated gases and is used to interpolate the remaining electrolyte background by a second order exponential decay function. Then, the cell is purged with a calibration gas mixture, containing H_2, O_2, CO_2, CO, and C_2H_4 each in a concentration of 2000 ppm in argon (Westfalen, Germany). From that, the individual calibration factor (S_x) for each gas can be determined by a linear fit of the baseline-corrected signal and the calibration fit.

For further evaluation the signals are smoothed with a Savitzky-Golay function. The signals are then translated into moles (n_x) using the cell volume (V), pressure (p), temperature (T), molar gas volume (R) and a calibration factor (S_x), as shown in Equation (3.1).

$$n_x = \frac{pV_{cell}}{RT} \cdot \left(\frac{I_x}{I_{36}^{Ar}} \right) \cdot S_x \tag{3.1}$$

For comparing the gas evolution of different materials, coatings, and even other setups, it is commonly used to express the evolved/consumed moles of gas in regards to the active material (AM) amount or surface area, e.g. $\mathrm{nmol} \cdot \mathrm{g}_{\mathrm{AM}}^{-1}$ or $\mathrm{nmol} \cdot \mathrm{m}_{\mathrm{AM}}^{-2}$ terms by using the loading of the individual electrode or their active surface area, obtained by brunauer-emmett-teller (BET) measurement. In a last step, the electrochemistry is time resolved plotted within the obtained gassing behavior of the conducted experiment.

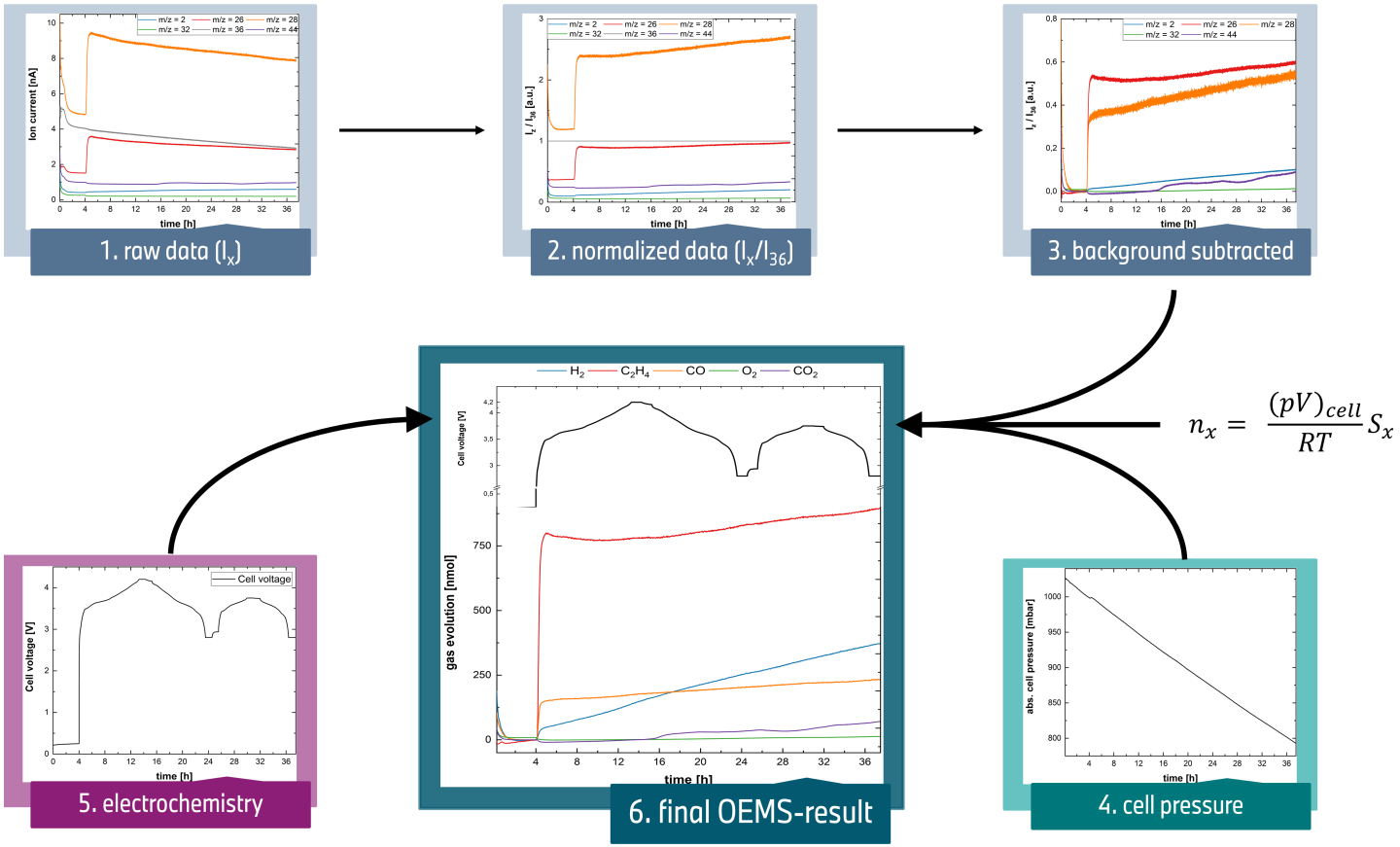

Figure 22: Detailed view on the OEMS data treatment. 1) raw data received from MS for mass traces of interest. 2) mass traces are then normalized to the ^{36}Ar signal. 3) Next, the electrolyte background after 4 h OCV phase is subtracted. 4) during the experiment, the cell pressure is continuously measured. 5) electrochemical data from the potentiostat. 6) the last step is the combination of all data. This is achieved by using the ideal gas law and the data from 3 and 4, together with the overlay of the electrochemical data shown in 5). If necessary the molar gas evolution can be convert in units of [µmol*g^{-1}] or [µmol*m^{-2}] if the electrode loading and BET surface area are known. Additionally, gas evolution rates can be calculated by calculate the first derivative.

3.1.5 Electrochemical Cells for In-Operando Application

The unique strength of *in-operando* methods, is the possibility to investigate battery cells in a non-equilibrium stage to observe transient processes or thermodynamic unstable intermediates. However, in order to do so, the electrochemical cell must fulfill the specific requirements of the analytical technique. In the case of OEMS the cells must have a connection port towards the MS, while providing excellent tightness towards the outer atmosphere. Latter one is important, as the existence of other gases, e.g. air (O_2, CO_2) and H_2O influence the electrochemical triggered reactions and the background of each mass channel. Additionally, the cell must be adapted towards the electrochemical source (Potentiostat), while on the same time preventing electronic interactions towards the sensitive MS. In sum, the development of electrochemical cells for *in-operando* applications provides a serious hurdle.

In this section, the developed electrochemical cells for OEMS application, will be presented. First, the model cell approaches (swagelok type cells) are described. Following that, an unique adaption principle for large format prismatic cells, was designed within BMW´s prototype battery production and is explained in detail. Based on those two pathways, a novel housing for large format cylindrical cells was developed too.

I. Model Cell Approaches

The model cells described within here or in literature are all based on the idea, to represent a perfect swagelok cell, which are commonly used to study the electrochemical behavior on material level. The first approach of a self-developed model cells, is presented in Figure 23 and 24. The cell body was made out of a polychlortrifluorethylene (PCTFE or kel-F) cylinder. The bottom and top, respectively where made out of stainless-steel cylinders. Latter ones had an engraving for hosting O-rings. Both, bottom and top steel- cylinder where manually pressed into the kel-F cylinder for each experiment. This prototype had with 22.5 mL a rather large inlet volume. The used electrodes had an diameter of 40 mm for the anode as well as for the separator. The cathode had an diameter of 38 mm respectively. On top of the electrode sandwich was a stainless-steel spring, which connected the top lid with the upper electrode (usually cathode) and the bottom cylinder with the negative electrode (usually anode). Within the top´s lid, three swagelok connections where integrated. One was used as gas inlet, e.g. for argon flushing, and one as gas outlet, combined with a t-union to adapt the pressure sensor. The other swagelok adapter was being used as the inlet to the MS. Initially a peak capillary was being used between cell and MS. Later, the peak capillary was replaced by the stainless-steel crimped capillary leak open, due to clocking issues.

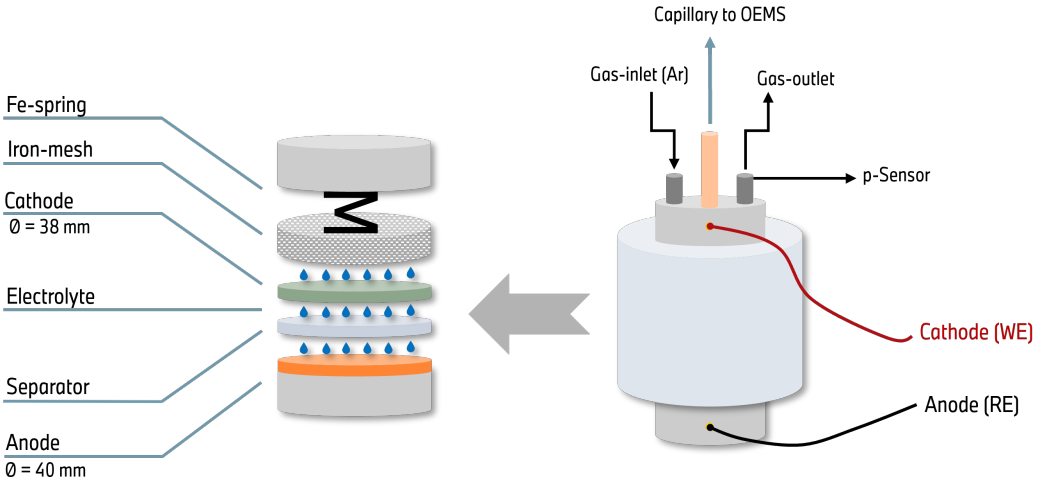

Figure 23: Schematic representation of the first model cell prototype cross-section (left) and full view (right), developed within this work.

In a later development step, also flat gaskets where used in-between the steel and kel-F cylinder and an external mechanism wit the principle of a screw clamp was being used to press the parts together, for better sealing. A photograph of this prototype can be seen in Figure 24. This model cell type was being used within the first year of this work and provided the basis for the data, used to determine the setup´s specific response-time. See chapter 4 for further information's.

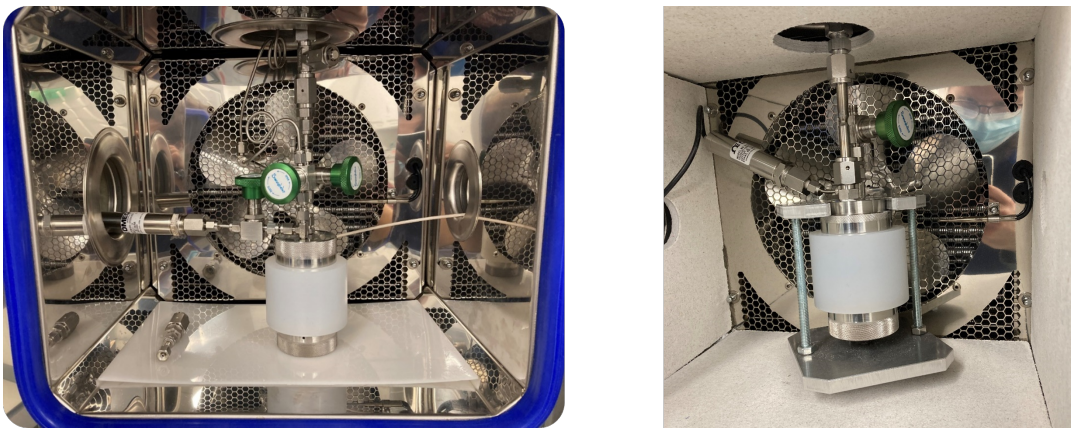

Figure 24: Photograph of the first model cell prototype (left) and an further developed sealing mechanism, based on the screw clamp principle (right). In both cases the prototype was placed within the climate chamber and being already connected to the OEMS.

The second approach of a model cell design, was mainly inspired by the work of *Lundström*[193] from the university of Uppsala. The herein developed cell is consistently made out of stainless-parts, with welded swagelok glands. The cell body itself is located on a polyoxymethylene (POM) ground plate. The inner part of the stainless-steel cup consist of an polyether ether ketone (PEEK) cylinder, within the cell body itself. The sealing between body and lid is achieved by flat polytetrafluoroethylene (PTFE) gaskets. The lid is secured with four screws, which allows an even pressure distribution along the gasket and excellent tightness. The total cell volume is with 9.5 mL, rather small, compared to the first prototype. However, most OEMS cells are in the range of $\approx$ 10 mL of head space volume. Smaller volumes provide a higher sensitivity towards the monitored gasses. However it also comes along with higher hurdles regarding the accurate sealing of the cell. The used electrodes within this model had a diameter of 16 mm for the anode as well as for the separator. The cathode had an diameter of 14 mm respectively. On top of the electrode sandwich was a stainless-steel spring, which connected the top lid with the upper electrode (usually cathode) and the bottom cylinder with the negative electrode (usually anode).

The cell´s lid comprises of four connection pathways. Two glands serve as gas in- and outlet, while the other two are connected to the pressure sensor or provide access to the UHV system, via the crimped capillary. The left part of Figure 25 shows the diffusion path of the released gasses from the electrode sandwich through the CLO towards the MS. This type of model cell was used within the studies, shown in chapter 5 and 6 as well as for comparison reason towards cylindrical cells and other cell setups.

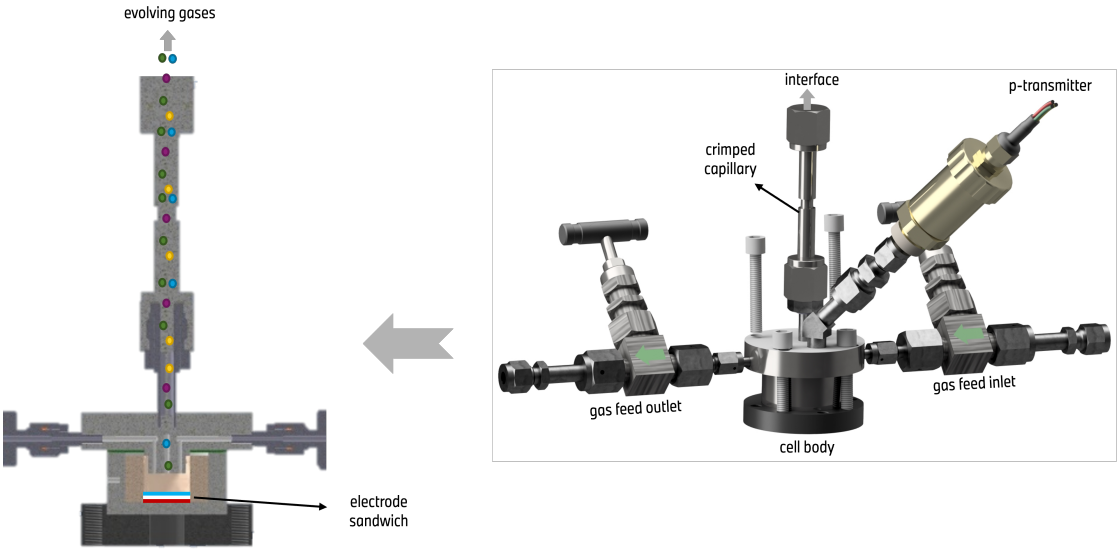

Figure 25: Schematic representation of the second model cell prototype cross-section with gas diffusion path (left) and full view (right), developed within this work.

II. Prismatic Automotive Cell Concept

Until today only few works can be found in the literature, dealing with in-operando measurements on prismatic automotive battery cells, as already described in section 2.7. All of those methods had to deal with the fact, that the cell is well sealed and already underwent charge/discharge protocols. Hence, a delicate opening procedure has to be done, in order to apply the specific measurement with a second dedicated adapter.

Following that, the in-house production of the herein used battery cells, provided a rare opportunity, to integrate the connection adapter within the battery cell, before the cell is assembled and sealed. Additionally, a more realistic cell setup is obtained. Figure 26 provides a glimpse onto the production process of the adapter integration into the cells lid, as well as the final prismatic battery cell. The individual working steps, for the integration of the adapter into the cell´s lid, are shown and explained in the appendix of this work, see Figure 79.

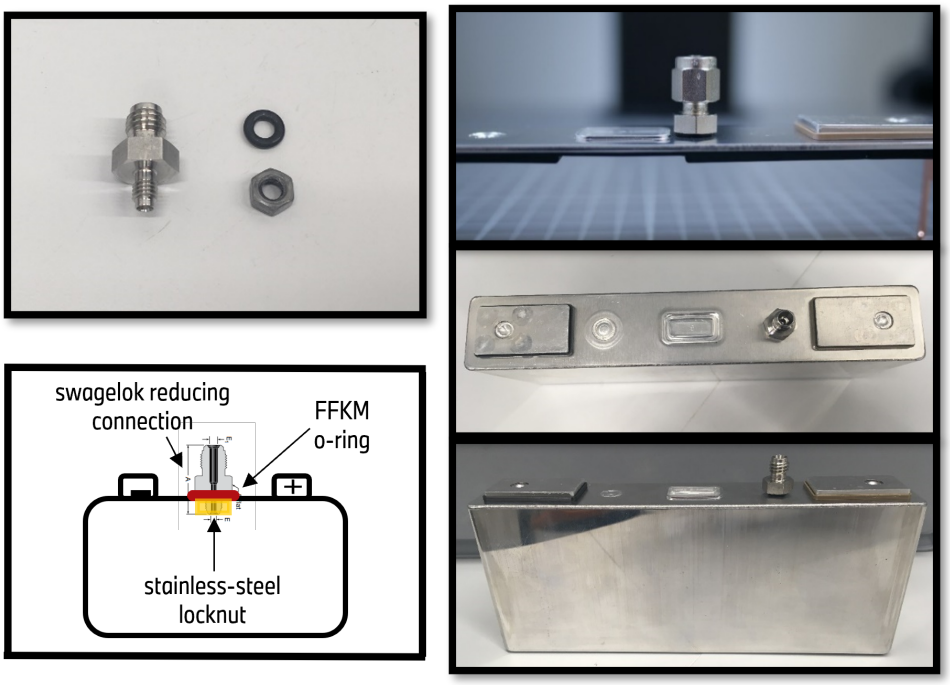

Figure 26: Various pictures illustrate in detailed the connection principle of large-format prismatic cells and the used sub-components.

The lid of a prismatic battery usually consist of the negative and positive terminal, a safety vent in case of a fatal pressure increase, and a electrolyte filling hole. In this work, a second hole was drilled into the lid on the opposite side of the electrolyte filling hole and a swagelok adapter (reducing unit) was inserted. The individual parts are shown on the left side of Figure 26. The adapter was secured with a bolt nut from the inner side of the lid and an o-ring was used for proper sealing.

Preliminary experiments were conducted, if i.) the sealing provides sufficient enough, ii.) if the inserted adapter/bolt-nut does not interfere with the inner parts of the cell. Therefore CT-scans were taken in order to make sure, that no electric connection between bolt-nut and electrodes occur. This would end in a short-circuit when the cell is charged for its first time, and had to be avoided under all circumstances. The requirements were also necessary, as the modified cells/experiments were performed within BMW´s prototype production facility, including automatic cell filling and formation procedures. Therefore it was necessary, to check if the adapter causes any problems with the used machines.

After the adapter integration into the cell´s lid, the lid was combined with the cell casing by laser-welding, see right side of Figure 26. After that, the cells were vacuum dried and underwent the usual battery production process, by filling up the cell with electrolyte (see section below) and preparing the cell for the individual formation procedure. The integrated adapter than allows to connect the cell via the inlet-interface to be connected directly towards the mass spectrometer of the OEMS system for in-operando gas analysis.

III. Cylindrical Automotive Cell Housing

The cylindrical cell housing should fulfill more challenging requirements, in comparison to the concept for prismatic cells. First, the concept should provide the gas analysis of in-house produced cylindrical cells, where the electrolyte filling opening is not yet sealed. This is comparable to the approach within prismatic cells, but with the premise that no additional connector had to be adapted to the cell itself. The second requirement should allow the analysis of already sealed and cycled cells, e.g. EoL cells or commercially available ones. Therefore, the cells must be re-opened again and insert in the OEMS cell housing. The re-opening of cells might be a safety issue and has to be done within glovebox conditions. The re-opening of cells was done with another developed tool, described at the end of this section in Fig. 34. As cylindrical cells newly appeared on the market, a proof-of concept of this setup/format was the major milestone within this work.

The designed housing chamber for cylindrical cells is illustrated within Figure 27. The housing is composed of an outer stainless-steel (SS) container for accommodation of a 46*95 mm cylindrical cell. Different containers with larger length dimension were available, in order to host even larger or smaller cylindrical cells, e.g. 46*110 mm. The container is isolated by a POM insulation plate to the bottom steel-part. An inner PEEK cylinder between battery cell and container avoids short circuits. The outer stainless-steel cylinder acts as negative terminal and is electronically isolated from the positive terminal (lid). Isolation is achieved using a single-use flat high density polyethylene (HDPE) gasket. The housing parts are sealed with threaded rods that are screwed into the base and pass through holes in the lid, on top of which they are secured with bolt nuts. The electrical connection of the cell is ensured by a spring (outside diameter: 46 mm, length: 60 mm, wire gauge 2.5 mm, spring rate: 1.845 N/mm; TH-MINI, Germany) that is placed between the battery cell and the housing cover. To improve contact and minimize corrosion, the spring was sputtered with gold. A guide ring (HDPE) attached to the cover ensures the correct positioning of the spring and avoids contact between the spring and the base body of the housing. This is necessary due to the contacting of the positive terminal of the battery cell with the base body of the housing. The cover and the bottom are therefore on the negative potential. Sockets for banana plugs in the base body respectively in the lid-part enable electrical contact to the potentiostat. Four welded-on glands on the lid allow the connection of two bonnet needle valves, a pressure sensor (PAA-33X, Keller Druckmesstechnik, Germany), as well as the connection to the MS via the crimped-capillary leak open. Swagelok VCR metal gasket face seal fittings are used for all connections.

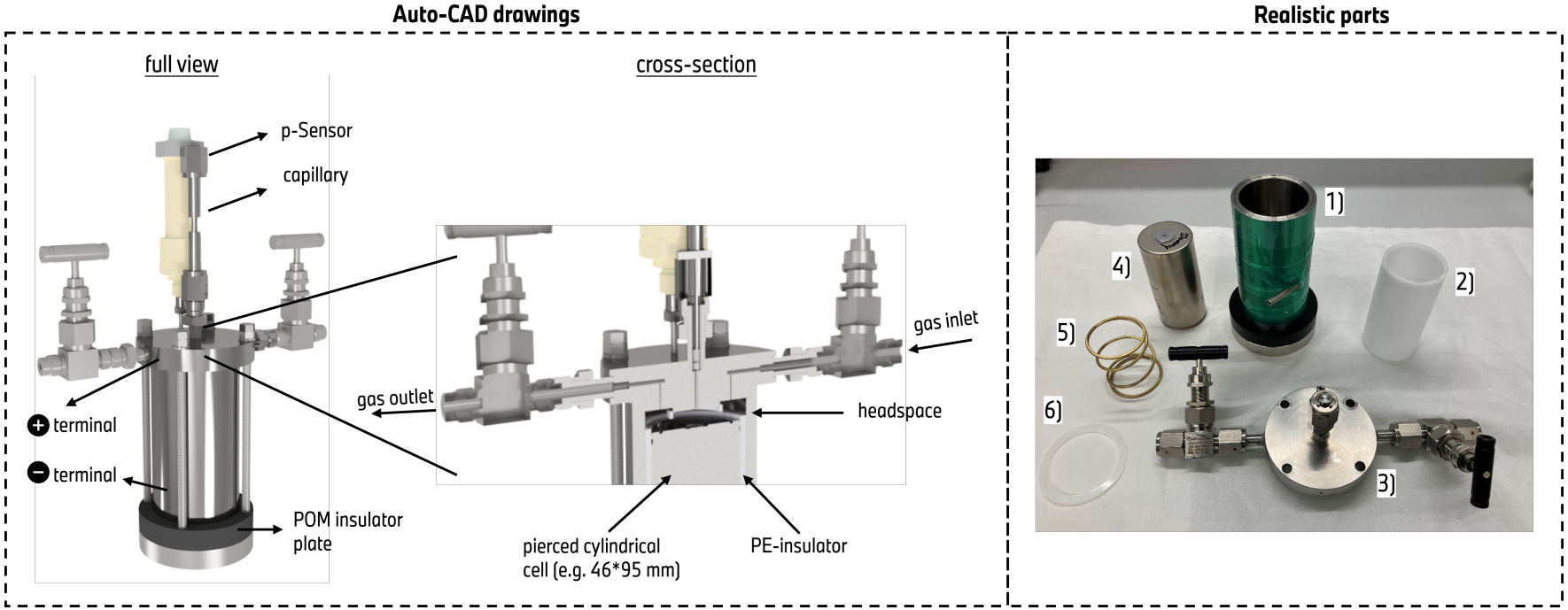

Figure 27: Left: Schematic CAD-drawing of the cylindrical cell housing in full view and cross-sectional view. Right: Realistic view of the original parts. The metal cylinder (1) represents the negative terminal. An additional PEEK-cylinder (2) avoids short circuits. The lid-compartment (3) works as positive terminal. A pierced cylindrical (4) is inserted and electrical contact between the terminal is achieved using a gold-sputtered spring (5). Lid and cylinder are electrically isolated by using a PE-flat sealing (6). To avoid any short-circuits during assembling, the outer cylinder was additionally wrapped in Kapton-tape. Electrical contact towards potentiostat was achieved by using clamps.

The headspace volume of the chamber was calculated based on computer-aided designs of the components to be 179.5 mL respectively 24.98 mL when a cylindrical cell (46*95 type) of BMW's internal test production is inserted and confirmed by using an in-house pressure test-bench. As for all other electrochemical cells, the sealing of the container is essential. A pressure drop resulting from a leakage may lead to misinterpretations and might influences the gas generation reactions. The leakage rate determination is meanwhile shown in the appendix, within Figure 82. However, the headspace volume to cell capacity is drastically reduced within this setup, as compared to the model cell approaches.

Nevertheless, the exact volume is necessary for the calculation of the molar fractions of the analyzed gasses, see Eq. (3.1). Due to the much higher ratio between the gas volume that emerges during initial charging and the headspace volume of the chamber, compared to the model cell, a gas burette (100 mL) is mounted on one of the bonnet needle valves of the chamber, see Figure 80 in the appendix. As the gas burette can be closed after the measurement, it is possible to transfer it to carry out further analyses like offline GC. This technique is employed for all measurements involving cylindrical cells during the initial charging process. Furthermore, the gassing during normal charging of a commercial cell (46*95 type) is analyzed. During this, the chamber is not connected to a gas burette due to the expectantly small amount of gas to be produced.

Within this work the cell housing was used mainly to study the cell formation. Also the different behavior in terms of gas release in dependence of the cell geometry, and the varying cell chemistry were investigated. For further information see chapter 7.1. The housing was also used, to study the gassing of cylindrical cells during normal cycling. Therefore, the cell had to be pierced with a specially designed tool and subsequently transferred into the OEMS cell housing. For further information about the cell piercing and transferring, see section 3.4.

Gas Inlet Interface

Besides the variation in the used electrochemical cells, they all using the same kind of gas inlet interface. The inlet provides a defined gas flow from the electrochemical cell to the MS in a one-step pressure reduction. Hence, a detailed look on this component is given in the following.

Figure 28 visualizes the used crimped capillary inlet. The component is made out of stainless-steel, whereas the gas inlet region is made out of a porous metal filter (sintered metal). The use of this calibrated leak allows a one-stage pressure reduction from 1.0 bar in the electrochemical cell to 10^{-7}mbar in the MS. The use of a porous metal flow restrictor is meanwhile beneficial as the gases diffuse uniformly through the porous metal part, with minimal friction and a laminar flow.[177] On the other side, the use of a conventional orifice (lower right part of Fig. 28) causes non-uniformly gas velocity, pressure and heat increase due to the single opening.[194] Additionally, the complete steel based interface makes it reliable especially under harsh conditions, e.g. battery environment and toxic or corrosive gases e.g. HF, POF_3, PF_5.

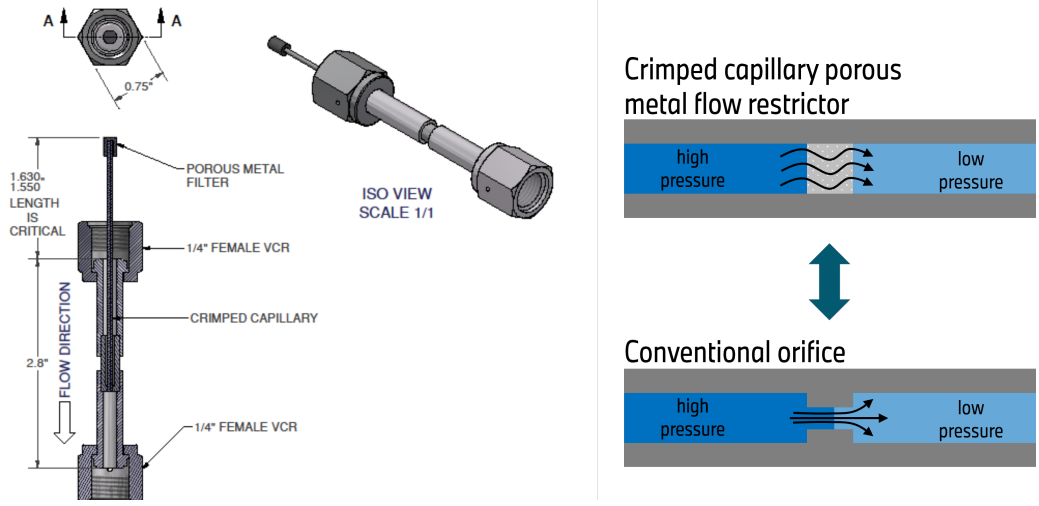

Figure 28: Left: Technical drawing of the used crimped capillary leak open (CLO). Thankfully provided by vacuum technology Inc.[177] Right: Basic principle of porous flow restrictor vs. conventional orifice used in gas flow application.

The CLO provides therefore a continuous gas flow towards the cell. However the time gases need to be detected by the MS strongly depend on the overall OEMS configuration and was therefore investigated within chapter 4. Furthermore, the continuous gas removal led to a continuous pressure drop within the cell, limiting the overall measuring time to approximately 50 hours.

3.2 Used Electrochemical Techniques

Several electrochemical techniques were used for cycling of lithium ion battery cells and are shortly explained in the following. The techniques were applied by the usage of a BioLogic SP-300 potentiostat with an integrated high current/high voltage option board (up to 10 A & 48 V). Further details to the specific experimental conditions are described separately in each result chapter.

I. Chronoamperometry (CA) is a widely used fundamental analytical technique due to its relative ease of implementation. The general working scheme is shown in part 1 of Figure 29. CA is commonly used to study the electrocatalytic activity of materials. Although it´s sensitivity it has poor selectivity.[195] The electric potential of the working electrode (WE) is stepped from a potential where no electrode reaction occurs to a much higher potential that triggers electrochemical reactions, e.g. start of electrolyte decomposition. The resulting current from faradayic processes is then monitored as a function of time. The electrochemical active species spontaneously diffuse to the surface of the WE, which causes an increase in current. The concentration of the active species subsequently decreases with distance from the electrode and the reduction/oxidation of new species at the electrode surface becomes diffusion-limited. As a result, the faradayic current decays over time due to limited mass transport, exhibiting exponential decay. CA can be used to measure the current-time dependence for diffusion-controlled processes. The great benefit lies in the fact, that CA delivers a clear starting point of the induced reactions.[196] This technique was used to determine the response time of the herein described OEMS system, see chapter 4.

II. Galvanostatic cycling with potential limitation (GCPL) allows a constant current to flow through the electrochemical cell, until the predefined cut-off potential is reached. The general working scheme of GCPL is illustrated in sub-figure 2 of Figure 29. The resulting galvanostatic cycling curve is a plot of the cell voltage against time. This technique provides fundamental electrochemical information about the electrode, such as capacity and overpotential. Additionally, it closely mimics the practical working conditions of a LIB. The current used to charge or discharge the cell is often denoted as C/t, where C is the capacity and t is the time in hours required for a full charge. For example, C/10 means that the current is adjusted so that the cell is fully charged within 10 hours in accordance to its theoretical capacity.[195,196] The capacity of an electrode (anode or cathode) can be calculated using Equation (3.2).

$$C/t\ [mA] \ = \ \frac{m_{El.} \cdot \mathcal{X}_{AM} \cdot C_{AM}}{t} \tag{3.2}$$

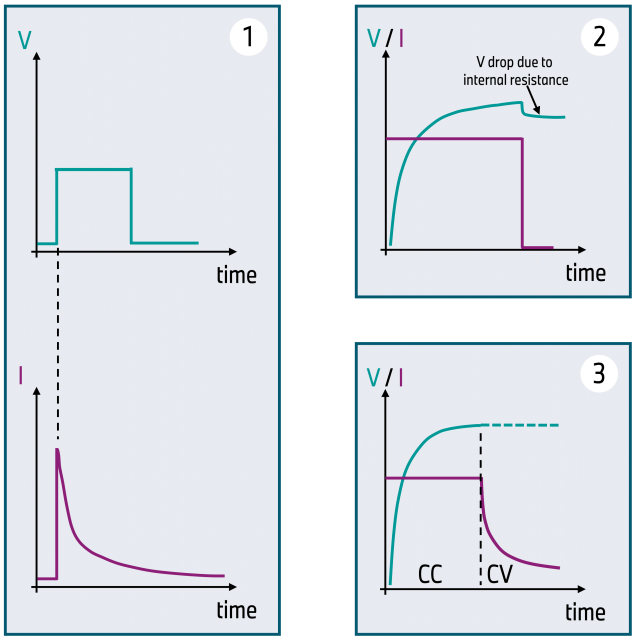

Figure 29: Schematic representation of the standard electrochemical techniques, which were used within this work. 1.) Chronoamperometry (CA); 2.) Galvanostatic Cycling with Potential Limitation (GCPL); 3.) Constant-Current-Constant-Voltage (CCCV) method.

with:

I = charge / discharge current
C_{AM} = specific discharge capacity of the active material
$\mathcal{X}_{\mathrm{AM}}$ = ratio of the active material in the electrode
$m_{\mathrm{El.}}$ = weight of the electrode
t = time for desired full charge / discharge

III. Constant current constant voltage (CCCV) is illustrated in part 3 of Figure 29 and charges the cell with a constant current, which is often higher than in GCPL mode, until the upper cut-off voltage is reached. Then, a switch to constant voltage mode prevents over-voltage of the cell. The current drops exponentially, usually as long as it exceeds 10 % of the initial current used under CC mode. The CV mode enables the cell to be charged to 100 % SOC and get rid of the internal resistance, which causes a potential drop (indicated in part 2 of Figure 29).[197]

3.3 Electrode & Electrolyte Preparation

Various active materials and other electrode components were used within this work for electrode & electrolyte preparation and are listed in Table 5. For the positive electrode (cathode) either NMC811 or NMC946 were used. The negative electrode (anode) was based on graphite or metallic lithium. In case of the cylindrical automotive cell format the anode was based on silicon-graphite composite material (BSO-L). Super C65 and LiTXHP were used as conductive carbon additives. Polyvinylidene difluoride (PVDF) was used as polymer binder. Therefore, the materials of the electrodes of the model cell do not differ from those of the electrodes of the prismatic/cylindrical automotive cells, which were investigated within this work. Both electrode-slurry's were usually prepared, using NMP as solvent. Further information's are provided in the experimental section of each manuscript, shown in the results part of this work.

Table 5: Electrode materials for Li-ion batteries used in this work.

Material/Name	**Supplier**	**Notes**
Anode		
SMG-A5	Hitachi, Japan	$\theta_{\mathrm{BET}} = 2.5\ \mathrm{m^2 \cdot g^{-1}}$
BSO-L	BTR New Material, China	silicon content: 7.4 %
Cathode		
NMC811	Umicore, Belgium	pc, $\theta_{\mathrm{BET}} = 0.75\ \mathrm{m^2 \cdot g^{-1}}$
NMC946	B&M, China	pc, $\theta_{\mathrm{BET}} = 0.53\ \mathrm{m^2 \cdot g^{-1}}$
Carbon		
Super C65	IMERYS, Switzerland	$\theta_{\mathrm{BET}} = 61.9\ \mathrm{m^2 \cdot g^{-1}}$
LITXHP	Cabot Corporation, USA	$\theta_{\mathrm{BET}} = 102.6\ \mathrm{m^2 \cdot g^{-1}}$
Polymer binder		
PVDF	Solvay, Belgium	tradename: Solef 5140
Counter Electrode		
Metallic lithium	Albemarle, USA	disc diameter: 15 mm thickness: $\approx$ 750 µm
Solvent		
NMP anhydrous	Sigma Aldrich	distilled & dried in-house

Electrode Preparation for Model Cell Application

For the study of Li-ion batteries on material level, electrodes were generally prepared by using a table coater machine and are manufactured individually, adapted to the required properties. For the cathode production, all of the following steps had been carried out in a dry room atmosphere. The processes of producing an anode/cathode are otherwise similar. For both electrodes, initially the binder solutions of poly-vinylidene fluoride (PVDF) in n-methyl-2-pyrrolidone (NMP) (anhydrous, 99.5 %, Sigma Aldrich, USA) was prepared by stirring them for at least 12 h on a stirring plate.

Active materials and conductive additive´s are then mixed into the solution using a planetary mixer (Thinky Are-250, part one within Fig. 31). The resulting slurry is coated on a stainless steel mesh (mesh size 0.212 mm / wire gauge 0.090 mm, Spoerl, Germany) with a film applicator (TQC Sheen,Germany; part two within Fig. 31). Alternatively, solid foils or laser-perforated current foils were used within this work. The difference between the current collectors, is basically their porosity and therefore the degree of gas permeability. The various substrate are schematically depicted within Figure 30. Solid foils were used within chapter 4 and are similar to the foils used for large-format prismatic cells. Laser-perforated current collector foils were specially designed and handmade, see chapter 5.

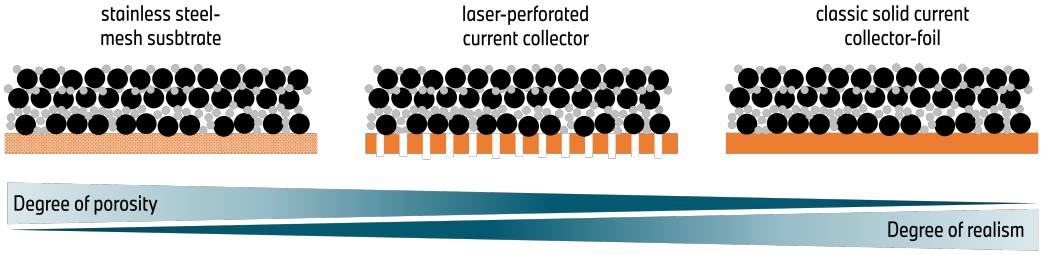

Figure 30: Schematic representation of the different substrates, used within this work as current collector for experiment within model cell approaches. Left: highly porous stainless-steel mesh; middle: a classical solid-foil which was manually laser-perforated to achieve a porosity; right: classical solid foil current.

After drying in a ventilated oven (100 °C) for 1 h, the electrodes are punched out into discs with a diameter of 16 mm for the anode and 14 mm for the cathode (part three within Fig. 31). Subsequently, the discs are dried under dynamic vacuum at 120 °C (glass oven B-585, Buechi, Switzerland; part four within Fig. 31). Before assembly for the OEMS measurement, the individual disc was weight and the mass loading was determined, according to Equation (3.3).

$$m\,[AM] \;=\; \frac{m_{\mathrm{El.}} \cdot \mathcal{X}_{\mathrm{AM}} - m_{CC}}{A_{\mathrm{disc}}} \tag{3.3}$$

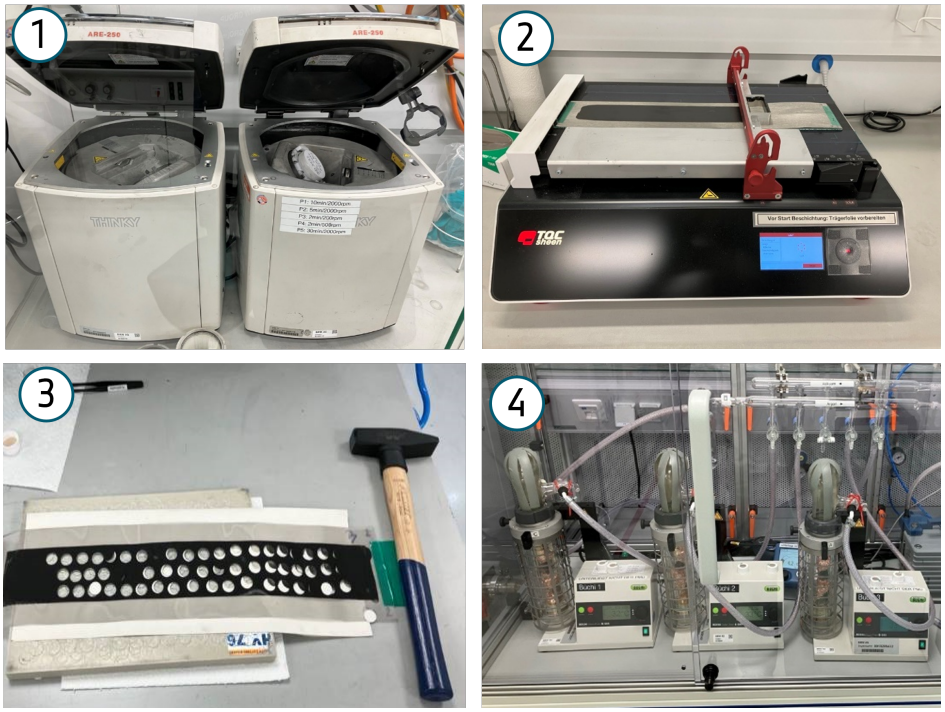

Figure 31: Workflow of electrode preparation for OEMS measurements; 1.) Slurry preparation within planetary mixer; 2.) Slurry coating on either mesh or (laser-perforated) current collector foil. 3.) Disc separation; 4.) Drying within dynamic vacuum oven. The procedure is completed by active mass loading determination.

After relocating the discs from dry-room into glovebox, they were dried again for 12 h at 100 °C within the heated evacuation chamber of the glovebox.

Electrode Porosity

Porosity of the single electrode disc was determined according to Equation (3.4),

$$\varepsilon = 1 - \frac{m_{\mathrm{El}} \cdot [(\chi/\rho)_{\mathrm{NMC}} + (\chi/\rho)_{\mathrm{CB}} + (\chi/\rho)_{\mathrm{PVDF}}]}{V_{\mathrm{El}}} \tag{3.4}$$

where χ is the mass fraction in the electrode and ρ the density of the CAM (NMC), carbon black (CB), and binder (PVDF). The symbols m_{El} and V_{El} correspond to the electrode mass and volume.[136] The latter one was calculated using the disc diameter and the measured thickness before and after compression. Using the above-shown formula assumes the incompressibility of the current collector. The assumption is not fully justified as it is known, that single particles penetrate into the current collector while using high line loads, as shown by literature.[198]

Hydraulic Compression of Electrodes to Mimic the Calendaring Effect

In order to mimic the calendaring effect onto the electrodes within single OEMS measurements, an uni-axial hydraulic compression was carried out. After coating and cutting the collector foil in squares, they were placed between two stainless-steel metal plates (roughness = 0.2 Ra; parallelism = ± 5 µm). The gap between the plates was sealed with Kapton tape and the arrangement was placed in a ventilated oven at 120 °C for 1 h. Subsequently, the sandwich was compressed within a 2-column manual lab press (type: PW 40; P/O/Weber, Germany) for 60 sec., according to the desired pressure. The procedure is exemplary shown in Figure 32. The electrode thickness of each sample was determined before and after compression, using an altimeter (Interapid, Switzerland) with a resolution of ± 1 µm. The results of this work is meanwhile described in Chapter 5.

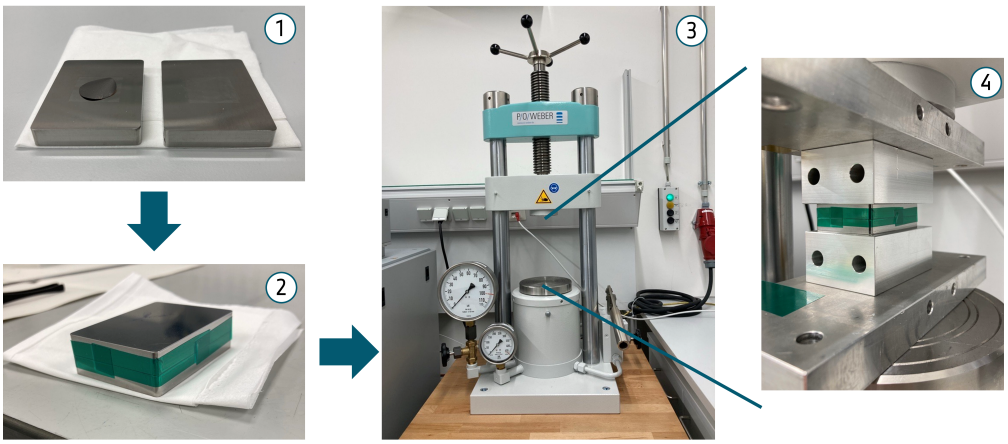

Figure 32: Working steps for the static cathode compression. 1.) a 15-mm diameter cathode disc is punched out and placed between two stainless-steel metal plates (surface roughness <5 µm); 2.) the metal plate/electrode-sandwich is sealed with tape and placed for 1 h in a ventilated oven at 120 °C; 3.) the sandwich is statically compressed to mimic the calendaring step. The pressure is applied for 1 min. Step 1 and 2 occur in dry-room conditions. After compression the sandwich is relocated in dry-room, vacuum dried, relocated to glove-box and further prepared for the OEMS measurement.

Electrolyte Mixtures

Table 6 lists the used solvents and salts, used within this work for various electrolyte mixtures. All ingredients were purchased in battery grade and used, as received. All solvent mixture ratios were based on the mass of the solvent components. Self-made mixtures were prepared in argon-filled gloveboxes (H_2O and $O_2 < 1$ ppm), in pre-cleaned alumina vessels, to protect them from UV radiation and stored consequently under glovebox conditions. Vessels were dried under dynamic vacuum for at least 12 h. During preparation, the salt was first weight and filled into the vessel, followed by the liquid component. The mixtures were then stored for 12 h prior usage, to allow the salt to be dissolved.

Table 6: Organic electrolytes for Li-ion batteries used in this work. All solvent mixture ratios are based on the mass of the solvent components.

Solvent		**Salt**	**Comment**	**Applied**
Cyclic	**Linear**			**in**
EC (50 wt %)	DEC (50 wt %)	1.0 M $LiPF_6$	so-called LP40	4&6
EC_{only}	/	1.5 M $LiPF_6$	mixed inhouse	4&5
FEC_{only}	/	1.5 M $LiPF_6$	mixed inhouse	7
EC (17-23 %)	DMC (21-27 %)	1.0 M $LiPF_6$ +WCA-2[1]	official	7
FEC (8-14 %)	EMC (27-33 %)	+ WCA-3[1] (0.1-6 %)	BMW supplier	

LP40 was used in Chapter 4 and 6, especially for the large format cells, whereas the self-made EC_{only} electrolyte was used for Chapter 5. Due to the use of silicon within cylindrical cells, a state of the art electrolyte had to be used, where the exact formula of the WCA[2] can not be shared. All electrolyte mixtures usually underwent Karl-Fischer titration and had a water content of less than 10 ppm. The mixtures were replaced every 6 months.

[2]weakly coordinated anion, exact formula can not be shared

3.4 Handling and Preparation of Large-Format Automotive Cells

The large-format cells used within this work were produced in-house in accordance to the general working-scheme, shown in Figure 11. However the cells were produced and stored in a dry-state, which means without electrolyte. In this configuration the cells can be easily stored for longer time and if needed the cells were then filled with electrolyte manually.

Filling of Prismatic Cells

In order to connect the prismatic cells to the mass spectrometer, a dedicated adapter was integrated into the cell casing, before assembly (step 9 in Figure 11). After combining the cell case with the modified lid, the general formation procedure shown in Figure 13 was used as standard workflow. This means, the cells were vacuum dried and transferred into a glovebox. Here, the electrolyte filling was carried out manually while using the integrated adapter, as it is shown in Figure 33.

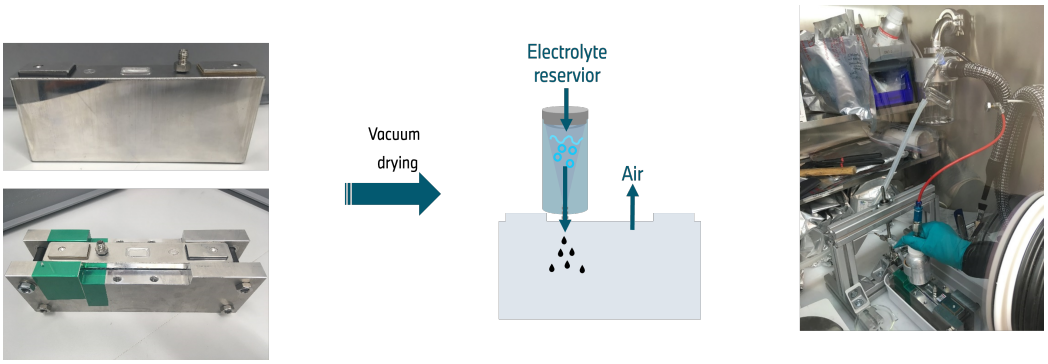

Figure 33: Workflow of handling and preparation of large-format prismatic cells prior OEMS measurement. Left: Large format cells with an integrated adapter were produced in-house. After vacuum drying, the cells were filled using the designed adapter. The usually used electrolyte filling (recognizable on the left upper side of the cell) hole was used to allow air to come out. After filling, the cell underwent wetting, temp-aging and sealing of the original designed electrolyte filling hole.

An aluminum can with an additional integrated adapter in the bottom, served as electrolyte reservoir. This allowed a connection between the cell adapter (male thread) and the electrolyte reservoir (female thread). Subsequently, the electrolyte was filled into the cell, while the remaining air was pushed out through the original designed filling hole of the cell. In between the cell was weight on a balance to monitor the amount of electrolyte within the casing.

After temperature aging (45 °C) for 12 h within the glovebox, the cell´s electrolyte filling hole was sealed via laser-welding within dry-room production environment. Then, the cell was relocated into the glovebox and the peripheral swagelok adapters were screwed onto the cell. Finally, the assembly was relocated onto the mass spectrometer setup and charging was carried out. Detailed information's about this procedure are described within chapter 6.

Handling of Cylindrical Cells:
While the construction process for prismatic cells was interfered with the integrated adapter within the lid, cylindrical cells should be measured without additional adapter unit. Furthermore, the OEMS system should be optimized towards the possibility to measure any cylindrical cell at any period of lifetime, e.g. end of life. These ambitions made it necessary to use other strategies.

To measure those cells and also any commercial cylindrical battery cells on the OEMS, they must be pierced to allow the gases produced during charge/discharge to escape. This was done with a special designed piercing tool, shown within Figure 34. It basically consist a stainless-steel mandrel, which can be screwed into the cell (part A of Fig. 34). For piercing, the cover and housing are first tightly screwed together once the cell has been added (part B of Fig. 34). The mandrel is then screwed in to a defined depth adapted to the cell type. As the cell would be exposed to the ambient air during this process, it has to be carried out in a argon-filled glovebox (MBraun, Germany; H_2O & $O_2 < 0.5$ ppm).

Therefore, cells of the 4695 type that have undergone the complete in-house manufacturing process, including electrolyte filling and sealing were utilized for the investigation of gassing during initial charging. In detail this means, that the cells were filled with electrolyte, rest to allow electrolyte wetting (24 h) sealed, transported to the dedicated glovebox and pierced to get prepared for the OEMS analysis.

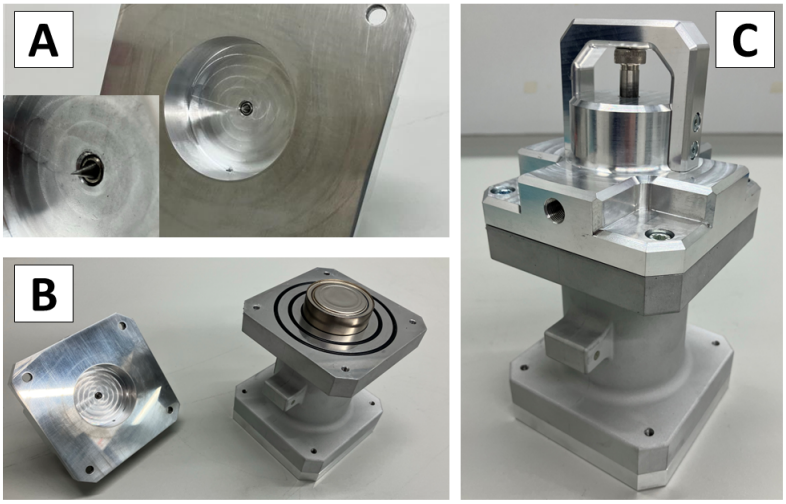

Figure 34: Battery piercing tool for cylindrical cells. A: Mandrel that is pierced in the battery cell, B: Battery cell (4695 type) inside the piercing tool; C: Assembled piercing tool.

A high level of safety was considered, prior initial charging at the OEMS, as any defect within the cell could lead to a thermal runaway and had definitely be avoided. In order to inspect, if the piercing process was successful without any damage to the cell computed tomography (CT) was used as a safety precaution. Computed tomography (CT) is a non-destructive analysis method that is well established in the field of battery cell analysis. During the measurement, several X-ray images of the test object are taken from different directions at a specific position in the beam path. This enables a digital reconstruction of the battery cell as a 3D object, e.g., to detect contact defects (short circuits) within the cell. In this work a phoenix v|tome|x m, CT from Waygate Technologies was used.

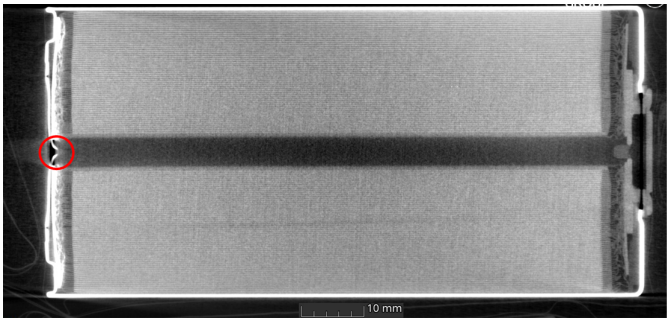

Figure 35: Cross section CT-scan of a cylindrical battery cell (4695 type) with puncture (red circle) to allow the gases to escape during formation for measurement at the OEMS.

3.5 Further Techniques (GC, BET, XPS, HPLC, SEM)

The following section provides a brief introduction to each methodology/used system in this work, and the specific sample preparation. These additional offline or*post-mortem*-studies were used in addition to the developed OEMS system, to either verify the OEMS results or gain additional knowledge about the complex processes monitored within LIBs by OEMS.

Offline Gas Composition via Gas Chromatography

To verify the quantified gasses, measured via OEMS on large-format cells during formation, the gases were collected and stored in a gas buret (see Appendix or Figure 36). The buret was then transferred and the collected gasses were measured offline using a gas chromatography (GC) system.

GC is an analytical method used to separate and analyze volatile or gaseous compounds without decomposition. The method can provide both qualitative (based on retention time) and quantitative results. The chromatography column (stationary phase) is the central component of a GC. The column is a long, thin tube densely packed with adsorbents, such as silica. A carrier gas, typically He, Ar or N_2, provides the mobile phase, which continuously passes through the column. A mixture of several components is injected into the column and separated based on their different affinities to adsorb on the stationary phase. Each component behaves independently in terms of adsorption.[199]

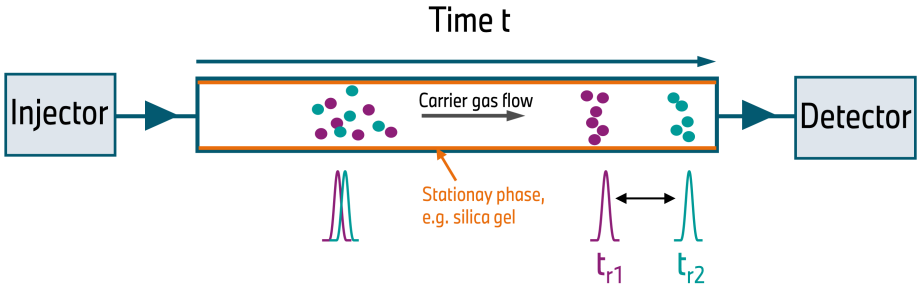

Figure 36: Basic principle of gas chromatography, drawn by the author.

A weaker adsorption affinity results in a stronger transport by the carrier gas, leading to earlier eluation (faster t_r). To account in for the temperature-dependent nature of this interaction, the column is typically placed in a climate chamber. The separation of individual species depends then only on the following facts: i.) flow rate of the carrier gas = length of the column; ii.) the boiling point of the species and iii.) the polarity. The first point has to be optimized in regards to the instrument and to the general nature of mixtures, which will be separated.

As in this work the GC system was used to investigate the composition of permanent gases (C_2H_4, H_2, CO_2, and CO), the only variable is the polarity of the individual gases. Therefore a two-channel gas chromatography system (990 micro GC, Agilent Technology, Santa Clara, USA) with a thermal conductivity detector (concentration range: 0.1 % - 100 %) was used. The first channel was equipped with a 10 m, 5Å molecular sieve column operated with argon as the carrier gas, while the second channel had a pora plot U column (10 m, 10 µm fused silica film, ∅ = 0.32 mm) and operated with helium. Prior to measurement, the connection pipe was flushed and evacuated three times with argon to minimize contamination from the atmosphere. The data were corrected by subtracting the nitrogen content, and the oxygen value was recalculated by assuming a nitrogen to oxygen ratio of 78:21. This is justified due to the minor leakages and transportation of the buret from the OEMS to the GC, that could only introduce air. All measurements were conducted three times. A photo of the data acquirement and measurement routine can be found in the appendix (Fig. 81).

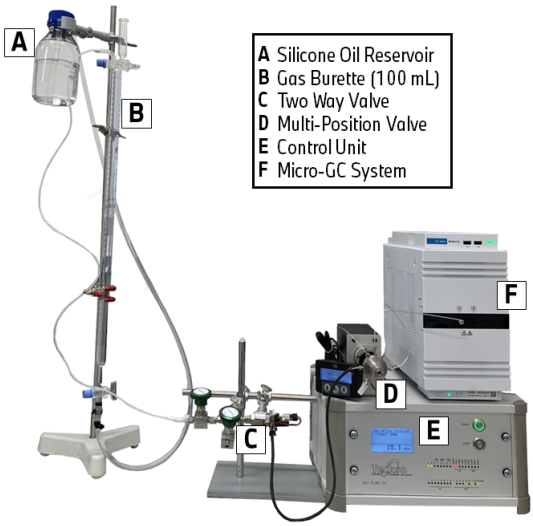

Figure 37: Photograph of the used GC system and its connection towards a gas buret, to measure and to verify the gasses, released during the formation of large format automotive cells. Description of the individuals parts are shown within the figure.

Surface Area Determination via BET-Theory

A precise method for determining surface area and pore volume is required as both are linked to the activity and stability of all types of heterogeneous catalysts and active materials. It is also common to present OEMS results by referring to the released amount of gas in terms of surface area ($\mu mol \cdot m_{BET}^{-2}$), as both surface area and pore volume are important factors in terms of gas release.

The brunauer-emmett-teller-theory serves today as an important analytical method for determining specific surface area through gas adsorption.[200] The materials surface and morphology can be quantified by adsorbing a specific volume of gas (usually N_2). An adsorption isotherm of the gas near its condensation point, at saturated vapor pressure, is then recorded. Adsorption isotherms describe the relationship between surface coverage and pressure at a constant temperature. As the BET theory is simply another derivation of the general isotherm equation for the case of multi-molecular adsorption, the general assumptions based on Langmuir's theory of an uni-molecular layer remain valid.[201]

In both theories, gas molecules are physically adsorbed onto an infinitely solid layer. There is no interaction between different adsorbent layers. Furthermore, the occupation of adsorption sites is not related to the occupation of neighboring sites. Due to this independence, both monolayer and multilayer adsorption can be described relatively well with Equation (3.5).[190]

$$\frac{p/p_0}{(1-p/p_0)\cdot V_a} = \frac{1}{V_m \cdot B} + \frac{(B-1)}{V_m \cdot B} \cdot \frac{p}{p_0} \tag{3.5}$$

with:

V_a = Volume of gas adsorbed at pressure p
V_m = Volume of gas required to form monolayer
B = BET-constant (related to energy of monolayer adsorption)
p/p_0 = relative pressure of adsorbate

The BET adsorption isotherm is obtained by plotting (p/p_0) / $(1-p/p_0)$ vs. (p/p_0). By linear regression of Equation (3.5) the BET-constant B and the monolayer gas volume V_m can be obtained. The specific BET-surface S_{BET} can be determined from Equation (3.6).

$$S_{BET} = \frac{V_m \cdot N_A \cdot \sigma}{V \cdot m} \tag{3.6}$$

Herein is N_A the Avogadro-constant, σ is the molecular cross section of the adsorption species, V is the molar Volume and m the mass of the adsorbate gas.[190,202] The cross section for nitrogen is referred to 0.43 nm^2.[203]

In the context of this work, a double determination of the active materials was carried out on a Micrometrics ASAP 2020 machine. Therefore, typically 1 g of substance was filled into a BET-flask and was measured according the typical measuring procedure, which typically involves a 12 h drying step, followed by the adsorption measurement with nitrogen. Typically values for the used CAMs in this work were $\approx$ 0.5 - 1 m^2g^{-1}, $\approx$ 2.5 m^2g^{-1} for carbon (AAM) material and $\approx$ 60 m^2g^{-1} for conductive carbon materials.

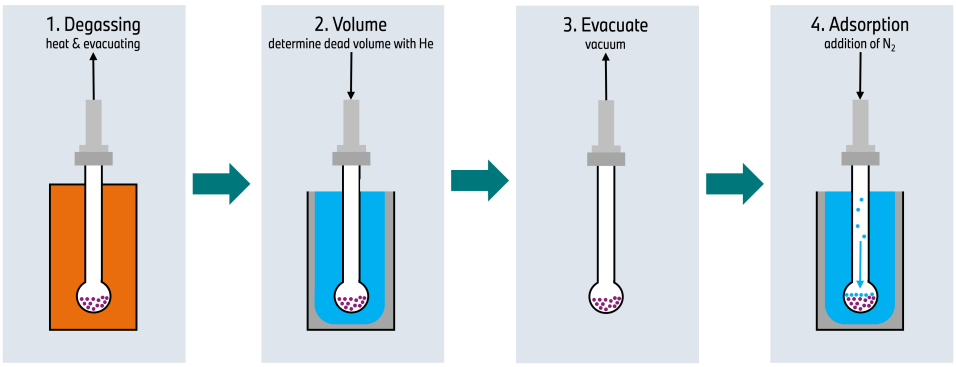

Figure 38: Basic principle of BET surface measurement routine, drawn by the author.

Anode Characterization via XPS

X-ray photoelectron spectroscopy (XPS) is a surface-sensitive analytical technique to investigate the elemental composition and chemical state of materials. The method involves irradiating a sample with X-rays, leading to the emission of photoelectrons from the material's surface. By measuring the kinetic energy of the emitted photoelectrons, XPS enables the determination of the elements present on the surface, their relative concentrations, and their chemical states.[190]

After cycling, model cells were usually disassembled in an Ar-filled glove box and harvested anodes were rinsed three times with DMC. The electrodes underwent X-ray photoelectron spectroscopy (XPS: PHI Versa Probe II, KAlpha) using a focused monochromatic Al Kα radiation beam (hν = 1486.6 eV, 70.6 W) under ultrahigh vacuum with a beam diameter of 100.0 µm. The electrode samples were transferred from the Ar glove box to the XPS chamber via an air-free transfer vessel. The spectra were adjusted to the hydrocarbon peak at 284.8 eV and fitting was performed using the MultiPak software (Physical Electronics). All electrode sheets were measured in three different positions. Results of the investigation of the electrodes surface via XPS can be found within chapter 6.

Electrolyte Analysis via HPLC-Orbitrap

Identification of thermally produced formation products within the electrolyte, was performed on a Vanquish™ Flex UHPLC system (Thermo Scientific™, USA) hyphenated to a LCMS-Orbitrap exploris 120 (Thermo Scientific). Reversed phase chromatography was carried out on a ZORBAX Eclipse plus-C18 column (50x2.1 mm,1.8mm; Agilent Technologies,USA) maintained at 45 °C and a flow rate of 0.4 mL*min^{-1}. The mobile phase gradient comprised of water (A) and acetonitrile (B), both containing 0.02 % formic acid. The optimized gradient started with 2 % B from 0 to 1.0 min and gradually increased to 100 % within 10.0 min. The mobile phase was kept constant at 100 % for 3 min. before the column was equilibrated at 2 % B for 4 min. The sample solution for injection was obtained by disassembling the large-format cells in a glove box atmosphere, followed by separating one negative electrode sheet and cutting it into small pieces. The pieces were subsequently transferred into a centrifuge tube with 5 mL acetonitrile, which was then left to rest for 45 min. before a second dilution step (1:100) with acetonitrile was done. We analyzed 1 µL of this solution by HPLC in positive ESI mode, with the mass range set to m/z = 40–200 amu in MS1 and m/z = 150–1500 amu in MS2 mode for the low and high mass windows, respectively. Compound Discoverer 3.3 software (Thermo Scientific) was used for structure elucidation.

Study of the Response Characteristics of an OEMS System Using Chronoamperometry

4.1 Motivation

In this section the article "Study of the response characteristics of an OEMS system using chronoamperometry" will be presented. As it was shown in section 2.7, there were several OEMS setups developed over the last decades. However, besides all these custom-made systems and their proof-of-concept studies, a clear definition or description of the setup-specific response-time, as well as the reaction time of the electrochemical cell is still missing. In the context of this chapter, the response-time will be defined as the time, which is needed from the electrochemical triggered gas evolution within the model cell until they are detected in the MS. As there are different OEMS and DEMS systems exists and each strongly depends on the custom-made setup, the response-time can be seen as a setup specific key parameter and will further help to interpret the generated data on that specific setup. Especially in regards to measurements on large-format cells, where a delayed gas detection due to the cell geometry is expected.

This chapter has been published in: Scharf, J., Matysik, FM., Study of the response characteristics of an online electrochemical mass spectrometry system for gas analysis of lithium-ion cells using chronoamperometry. Monatsh Chem, **154**, 1025-1033 (2023) (DOI: 10.1007/s00706-023-03094-z)

Keywords: Electrochemistry • Lithium-ion cell • Mass spectrometry • Material science • Gas analysis • Response time

4.2 Abstract

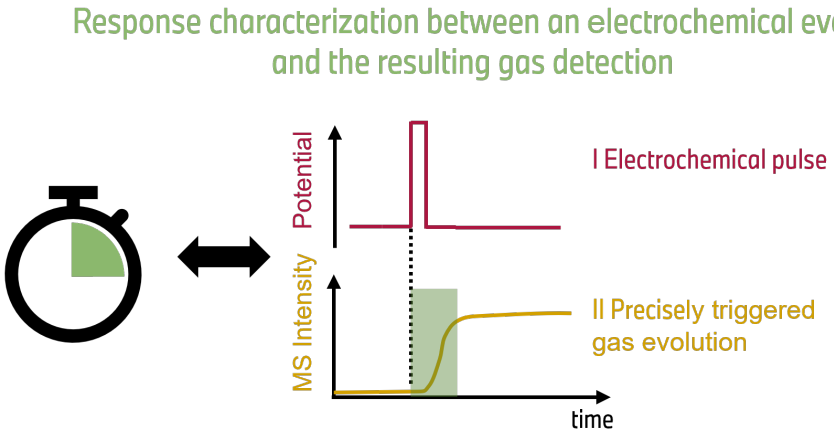

Figure 39: Graphical abstract for the embedded chapter in this work dealing with the response time characterization of the developed OEMS system.

OEMS is a promising analytical technique to monitor minor side reactions with gaseous species, taking place while charging and discharging a lithium-ion battery cell. However, besides the manifold examples of these custom-made systems and their application, a clear analytical view on the origin of the evolving gasses and their manifold interactions within the cell environment is missing and therefore given in this work. To get a better understanding of the complexity of gas evolution associated with electrochemical reactions in lithium-ion battery cells, the use of chronoamperometry as an analytical method was chosen. This led to a precise variation of the applied voltage and voltage-pulse length and enabled therewith a clear starting point of the electrochemically triggered reactions. It was found that chronoamperometry can be used to precisely trigger those reactions with gaseous products. Additionally, it was found that the release of gaseous species depends on many parameters including the cell configuration, the current, and the gas species. The response time determination showed that a custom-made highly porous electrode configuration had an overall better response behavior within minutes with differences for the respective gasses of interest, compared to a standard foil configuration cells. The herein presented methodology shows how an electroanalytical approach can help gain further insight into advanced hyphenated methods, such as OEMS in the context of studies of lithium-ion battery cells.

4.3 Introduction

To fulfill the ambitious CO_2 targets within the Paris climate protocol, the need for LIBs has grown exponentially within recent years. Mainly the demand for automotive and further public transportation purposes, such as busses and ferries, leads to a growing amount of cell factories around the globe.[204] However, to use the full potential of

future LIBs, their aging must be understood in more detail.[159,183] One growing aspect is the gas evolution during the very first charge. Hereby, the liquid electrolyte is partially decomposed into hydrogen (H_2), ethylene (C_2H_4), carbon monoxide (CO), and carbon dioxide (CO_2), while forming the SEI on the negative electrode.[129,205–207] To track these gaseous byproducts, advanced analytical techniques with high selectivity and sensitivity are needed. A sophisticated approach is made by the combination of electrochemical cycling procedures with MS.[165–167,208]

Imhof and Novak,[127,171,172] as well as *McCloskey et al.*[173] pioneered the use DEMS to observe the gas evolution during SEI formation. Their setup allowed a discrete sampling of the gas species from a semi-closed cell headspace probed by MS. Alternatively, *Gasteiger et al.*[176] developed an OEMS system. A closed cell headspace is directly connected to the MS with a crimped stainless steel capillary. However, despite all these custom-made setups and their proof-of concept studies, a clear and critical analytical description of the overall interactions of the complex processes taking place in a LIB and their influence onto the response behavior is still missing. In the context of this work, the response-time (τ_R) is defined as the time between the electrochemical event (EC Event) and the recording of the gas species in the MS, schematically shown in Fig. 40.

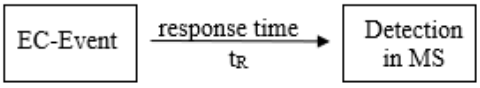

Figure 40: Schematic representation of the response time description of an OEMS system, used in this work.

In this report, the electrochemical response behavior of a model cell for the usage of electrochemically coupled mass spectrometry is described. CA as a simple electroanalytical method was used to generate a well-defined stimulus for a short time interval to follow the response characteristics of the respective experimental configuration. The two parameters, namely the applied potential and the pulse duration, were used to precisely trigger the electrochemical reactions, when charging a cell for the first time. The simultaneously recorded mass spectra were used to evaluate the responding gassing behavior of the cell. The study was carried out with two different electrode cell configurations. First, a model system with standard foil coating was used. Then, a more detailed investigation was carried out using a highly porous and gas permeable mesh coating.

4.4 Experimental

I. Setup

For mass detection, a HiQuad QMA410 crossbeam MS from Pfeiffer Vacuum® with a continuous secondary electron multiplier detector was used. The MS had a m/z scan range of 1–128 amu. For electrochemical investigations, a Biologic® VSP300 potentiostat and the software EC-Lab® (version V11.43) were used. Data assignment between the MS ion current signal and the electrochemical recording was done using origin® (version 2019) and the local time in both text files. The electrochemical cell can be seen in Fig. 41. All connections are made by using stainless steel Swagelok connectors (Swagelok®, USA). The cell is connected via a stainless steel crimped CLO (Vacuum Technology Incorporation®, USA) to the MS.[177,194] The crimped capillary provides a leak rate of 10^{-5} mbar dm^{-3} s^{-1} and has a 0.5 µm stainless steel cup filter, which provides a continuous laminar flow from ambient pressure to the UHV regime.

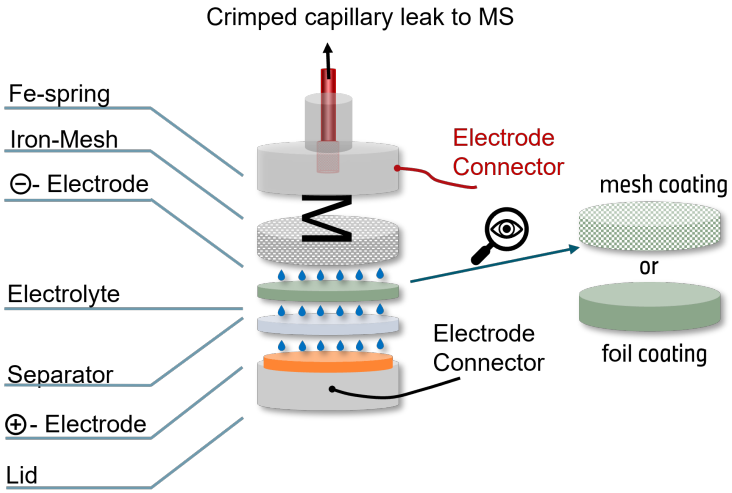

Figure 41: Scheme of the electrochemical model cell and the two different cell configurations used for the response characterization.

II. Materials

The negative electrode was prepared by stirring a 5.0 wt. % solution of PVDF (Solef® 5140, Solvay Belgium) together with NMP (anhydrous, 99.5 % Sigma-Aldrich) for 12 h at room temperature. Then, 2.0 % super C65 (IMERYS®, Switzerland) was added and the mixture was stirred for 30 min. in a planetary orbital mixer with 2000 rpm (Thinky Are 250, USA). Subsequently, 93.0 wt. % graphite powder (SMG-A5, Hitachi, Japan) was added and the solution was mixed for 10 min. with 2000 rpm. The slurry was coated on either a stainless steel mesh (0.212/0.090 mm, Spoerl KG, Germany) using a 150 µm gap applicator or on a copper foil (10 µm thickness Iljin, South Korea). In both cases, an automatic film applicator (TQC Sheen) was used. The coating was first

dried in a ventilated oven at 100 °C before punching out in 16 mm disks. The positive electrodes were produced using 96.0 wt. % NMC811 (Umicore, Belgium), together with 0.2 wt. % BM-730H (Zeon, Japan), 1.8 wt. % Solef 5140 and 2.0 wt. % LITXHP (Cabot Corporation, USA). The NMP containing slurry was coated on a aluminum foil (15 µm thickness Hydro, Norway). The dried electrodes were punched out in 14 mm disks. Positive and negative electrodes were separated using a Whatman separator (Whatman PLC, United Kingdom), which was soaked with 200 µL electrolyte. The liquid electrolyte was a mixture of EC and DEC in 1:1 ratio (w/w) together with 1 M of $LiPF_6$ (Sigma Aldrich, Germany).

III. Cell Preparation and Electrochemical Procedure

For all described experiments, the cell parts and electrodes were dried within a drying cabinet (Büchi oven) at 120 °C for at least 12 h and subsequently transferred into an argon filled glovebox (MBraun®; O_2 and $H_2O < 1$ ppm). Cells were built by placing a positive electrode on the bottom of the cell, followed by the separator, and adding 200 µL electrolyte. Finally, the sandwich was covered with the negative graphite containing electrode sheet (either foil or mesh) and an additional iron mesh for contacting the electrode stack. The cell was sealed and connected via the crimped capillary leak towards the MS. Due to the high vapor pressure and gas phase equilibrium rearrangement, the cell was rested for 4 h under OCV (mesh electrodes) or 11 h (foil electrodes). Then, chronoamperometry was carried out. For the time variation of the mesh-coated positive electrodes, the following procedure was carried out: A potential of 4.2 V was applied for 1 s, 2 s, 3 s, 4 s, and 5 s, respectively. After each potential pulse application, the electrode system was kept under OCV conditions for one hour, while MS recording was done. The procedure for foil coated electrodes was as follows: 1 s (0.5 h OCV), 2 s (0.5 h OCV), 3 s (0.5 h OCV), 4 s (0.5 h OCV), 5 s (1 h OCV), and 7.5 s (1 h OCV). For the potential variation with a four second pulse duration, the following procedure was carried out: 2.0 V (45 min. OCV), 2.5 V (45 min OCV), 3.0 V (45 min OCV), 3.5 V (45 min OCV), 4.0 V (45 min OCV), and 4.5 V (45 min OCV).

IV: Data Processing

To avoid signal fluctuations due to minor pressure and temperature changes, the collected raw MS data were divided by the signal intensity of the ^{36}Argon (m/z = 36) isotope and further labeled as I_x/I_{Ar}^{36}. Furthermore, a background correction was carried out by subtracting the value for each gas species at the end of the OCV phase. As some gasses may overlay with the signals from the gasses of interest, the following equations for the calculation were used. Hydrogen was measured using the m/z = 2 trace, whereas ethylene was measured using the m/z = 26 trace. Carbon dioxide used the m/z = 44

values and oxygen used the m/z = 32 value. Carbon monoxide had to re-calculated as ethylene and carbon dioxide showed a strong contribution on the same mass channel. The intensity of CO was recalculated using the formula: $I_{28}^{CO} = I_{28}^{tot.}-(0.14*I_{44}^{CO_2}) - (1/0.63*I_{26}^{C_2H_4})$.[209] The formula accounts for the typical fragmentation contributions of carbon dioxide (0.14 of the base peak current) and ethylene (1/0.63 of the base peak current) to the mass channel 28. By subtracting both contributing components, the corrected signal intensity due to CO evolution can be estimated.

4.5 Results and Discussion

I. Challenges in Online Gas Analysis for LIBs

In this chapter, the most important parameters, which have an influence on the response behavior and therefore onto the definition of online gas analysis are described. The response time of a LIB to the applied electrochemical stimulus in terms of gas generation will depend mainly on the setup itself and on the cell configuration. Usually, LIB electrodes are coated on either copper or aluminum foil, which are impermeable for the evolving gasses. An alternative to this configuration is a gas permeable electrode, where the active material is coated on a mesh substrate. See the experimental section and Figure 41 for a detailed illustration of the two configurations used in this study.

The mesh provides a regular spacing in the order of micrometers, which results in a highly porous and gas permeable electrode. Using standard foil coated electrodes, the formation of gas bubbles and a possible bubble entrapment in the porous active material can be assumed. The microscopic bubble formation will depend on the quantity of formed gasses (massive vs. small gassing). Hence, it is a function of the interval of the passing current, the surface area of the active material, the gas species as well as the overall cell chemistry. After formation, a partitioning of the gasses between the active solid material, the liquid electrolyte phase, and the gas phase will take place. Each of these phases allows several degrees of freedom for interactions.

Therefore, the individual properties for each gas, in each phase must be considered on its own. Another important parameter is the reactivity of the produced gasses within the electrochemical surrounding of a LIB. The gasses have also different solubility properties in the liquid phase.[210,211] Especially, carbon dioxide shows an increased solubility in common electrolyte components, such as ethylene carbonate. Due to their higher solubility, evolving CO_2 molecules tend more likely to dissolve in the liquid phase and delays in the MS detection might occur. Further important properties are the molecule size, pressure, temperature, conductivity, and viscosity. In addition, the interaction between the gasses and all other LIB components has to be considered.

In this context, the liquid electrolyte plays a crucial role. A solution of lithium hexafluorophosphate in organic carbonate blends represents the state-of-the-art electrolyte. However, especially the conducting salt, e.g., $LiPF_6$ shows a strong sensitivity towards water impurities and forms reactive by-products, e.g., hydrofluoric acid (HF). These compounds may react with the evolving gasses or the organic carbonates, to produce even those gasses of interest, e.g., hydrogen or carbon monoxide. Some carbonates meanwhile have a high vapor pressure and produce MS signals with high intensity, which may overlay with the signals from the gasses of interest.[209] To reduce this influence, the LIB is usually hold at OCV conditions for several hours to obtain a stable background signal for each mass channel. In case of high vapor pressures or complex electrolyte mixtures, the background signal does not converge, and a more complex calculation routine (exponential fitting routine) has to be used to differentiate between electrochemically produced gasses and the ongoing increase of degradation-related gasses.

After their formation and manifold interactions within the material mix, the formed gasses diffuse into the cell headspace. In a mesh configuration, the diffusion length is in order of micrometers, whereas for a foil configuration, the distances are much longer (order of millimeters). The retention of the gasses in this configuration will strongly depend on their exact place of origin within the electrode assembly. The gasses which are formed on the outer side, can diffuse fast into the cell headspace, whereas gasses formed in the center of the electrode diffuse through the electrode until they reach the outer edge of the electrode. The diffusion for each species is mainly a function of solubility, molecule size, and temperature, and can be expressed by the diffusion coefficient of each gas species. The cell headspace itself provides a diffusion length in the order of centimeters. However, the diffusion in the gas phase is comparatively fast. The molecules can than easily enter the UHV regime where they are recorded by the MS. In our case, the barrier between cell headspace and UHV regime is made of a crimped capillary, where a porous metal filter allows a one-stage pressure reduction.[194] This flow restrictor provides a uniform gas flow with minimal friction. However, the dwell time within this restrictor strongly depends on the viscosity of the gas and the size of the gas molecules.

All herein described phenomena provide only a short summary about the most obvious factors, which must be considered, when it comes to online gas analysis within LIBs. All these factors strongly interfere with each other and are not taking place separately. Therefore, a clear definition or separation of these processes is challenging. While using typical cycling protocols, e.g., galvanostatic cycling with potential limitation, it also has to be considered, that the hereby monitored current is associated with a higher transient response, where even the starting point of the gas evolution can't be clearly defined. Rough estimation only based on the diffusion length implies that the evolving gasses

can be detected within minutes. To answer the analytical question of the response behavior between the electrochemically triggered gas evolution and the corresponding detection in the MS, a clearly defined starting point of the electrochemical reaction itself, is needed first. This is usually not the case, when cycling LIBs with standardized, e.g., galvanostatic methods. The use of CA allows to instantly step the potential of the working electrode to a well-defined potential and therefore having a clearly defined starting point (t_0) of the electrochemical reaction. Furthermore, CA allows a precise variation of the applied potential and pulse length of the applied potential.

II. Study of the Influence of the Applied Potential

At first, investigations concerning the influence of the applied potential regime were carried out by using the mesh configuration LIB only. A starting potential of 2.0 V and an upper cut-off voltage of 4.5 V were chosen as the potential window of interest. The potential was held for four seconds in each experiment, whereby the potential was step wise increased by 0.5 V for each measurement. The applied CA protocol and the resulting current data are depicted on the left side of Fig. 42. The simultaneously recorded mass spectra, for the individual gas species are depicted on the right side of Fig. 42.

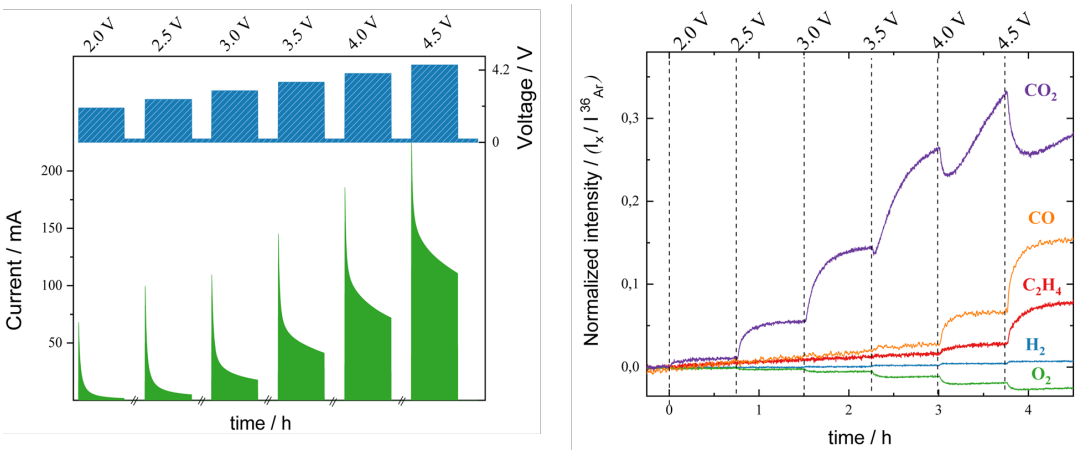

Figure 42: Left: Applied potential (top, blue) and recorded current (bottom, green) during the applied voltage variation under chronoamperiometric conditions with a pulse length of four seconds each. **Right:** Corresponding gassing-response behavior, recorded by the mass spectrometer for the gasses of interest. For better comparison, the intensities were normalized to the ^{36}Ar isotope (denoted as I_x/I^{36}_{Ar}).

The vertical dashed lines indicate the times for the application of short potential pulses for the CA measurements. As it is out of the scope of this manuscript to exactly describe the different chemical processes which occur in a LIB, only the general behavior for each configuration will be discussed briefly. For the use of the lowest potential of 2.0 V, already a slight increase in the CO_2 (purple) signal can be seen. In this potential region,

the decomposition of various impurities is expected.[212,213] The increase of the applied potential to 2.5 V and 3.0 V results in a further sharp and significant rise of the CO_2 mass trace. This indicates that the amount of released gasses strongly depends on the passing current. The use of the nominal potential of 4.0 V reveals the expected gassing behavior during the first charge of the cell. Note, that an expected gas evolution is determined as the point, where a response of all here shown mass traces can be seen.

The application of a potential of 4.5 V would normally lead to a decomposition of most cell materials. But as these processes are relatively slow and therefore, the applied potential sequence was probably too short to result in that kind of decomposition as this would result in a higher amount of CO_2 evolution.[81] The MS signals for the gasses ethylene (red) and carbon monoxide (orange) already start to increase, using lower potentials. It is most likely that some electrochemical reactions are already been triggered earlier. For example, it is known that impurities, like water or HF, trigger the decomposition of the electrolyte in an early stage if the cell is only assembled and not charged, as only the SEI protects the cell components from further degradation.[212,213] These degradation processes most likely end up, by producing ethylene and carbon monoxide. No obvious change in the hydrogen (blue mass trace) can be seen. The stepwise decrease in the oxygen mass trace (green) is most probably the result of a minor amount of oxygen, which is reduced shortly after the potential is applied. However, this series shows clearly how the CA approach can be used to trigger specific electrochemical reactions and to monitor their consequences on the gassing behavior. It is important to note that even in the context of a simple CA experiment, differences concerning the response behavior for the formation, release, and detection of various gasses can be seen.

III. Investigation of the Influence of the CA Pulse Length

As second part of this study, the variation of the pulse length was investigated. In this chapter both cell configurations, namely the mesh configuration as well as the foil configuration, were used to investigate how the pulse length effects the overall gassing behavior for different configurations. According to the former experiments, where a significant gassing behavior was observed for potential pulses between 4.0 and 4.5 V, a cut-off potential of 4.2 V was used in this study. The potential pulse duration and the recorded chronoamperiometric currents are depicted in Figure 43. The pulse length ranged from one second up to four seconds for the mesh configuration and up to seven seconds for the foil configuration. The latter parameter setting was applied in order to generate a similar amount of gas (signal intensities) as for the mesh configuration. The recorded currents ft to the earlier performed potential variation series. Here, the potential variation was also performed for the mesh configuration and showed a similar current behavior in the potential regime between 4.0 and 4.5 V.

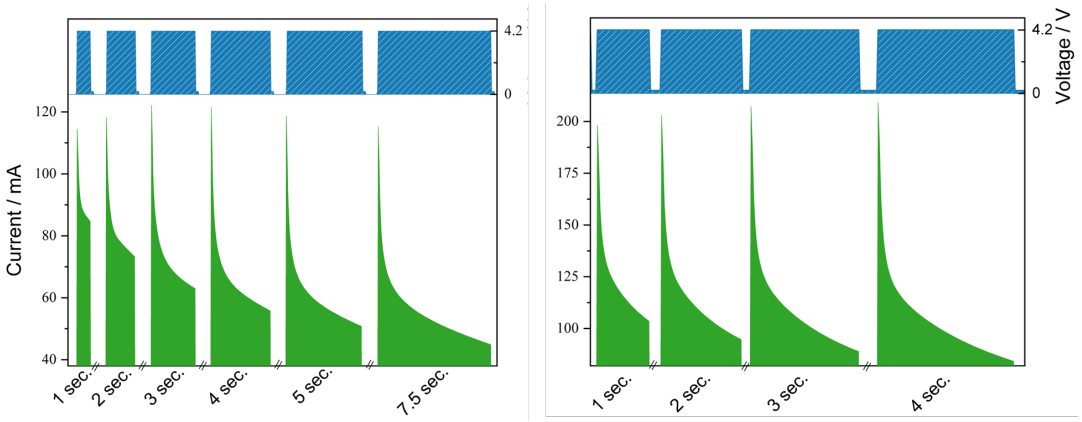

Figure 43: Applied potential pulses (top, blue) of varying durations and recorded currents (bottom, green) for chronoamperiometric measurements using a foil configurated LIB (left) and a mesh configurated LIB (right).

The simultaneously recorded mass spectra, for the individual gas species are depicted in Fig. 44. For the foil configuration (left), no sufficient gas evolution can be assigned to the CA pulse until a pulse length of five seconds is reached. However, an apparently linear increase of the intensities assigned to CO and C_2H_4 can be seen for shorter pulse lengths and might be attributed to early formed reactive by-products.[159]

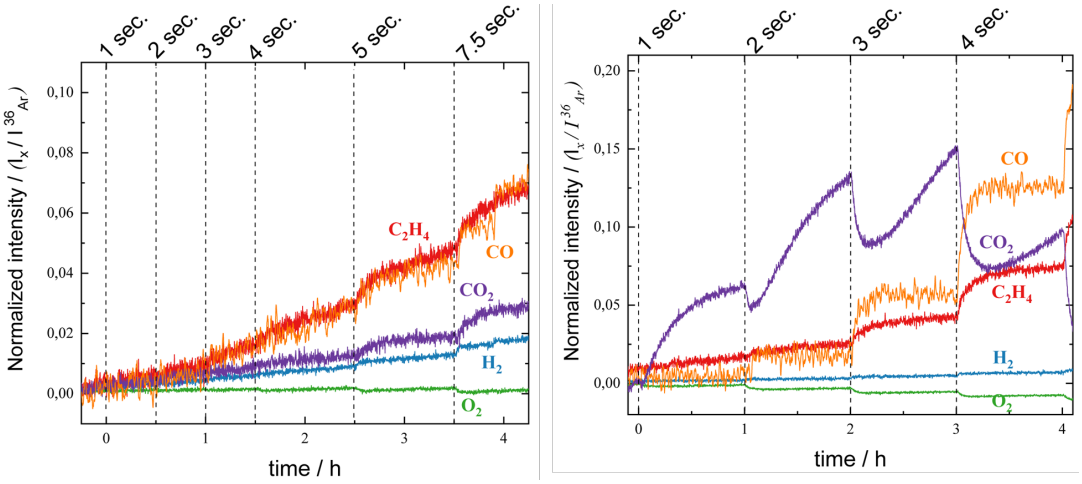

Figure 44: Detected gas species during pulse length variation for either foil configurated LIB (left), or mesh configurated LIB (right). Note the different y-axis scale.

In case of the mesh configuration LIB (right part of Fig. 44), a shorter pulse length of three seconds is already sufficient to produce the expected gaseous species in a significant amount. Even the shortest applied pulse length of one second reveals a direct influence on the CO_2 intensity. The CO_2 behavior is special in several aspects. It is the only mass trace which shows an increasing as well as a decreasing behavior, directly related to the performed CA experiment.

This behavior points out that besides gas evolution, the assumed gas consumption or dissolution processes must also be considered. However, besides the CO_2 behavior, the linear increase of ethylene and carbon monoxide can be seen here. This suggests the assumption that ethylene is already been formed at shorter pulse sequences.

By comparing both configurations, it can be concluded that the overall response behavior for each configuration differs from each other. For the foil configuration, a longer pulse length is needed to produce the same amount of gas as in the case of the mesh configuration. For the latter configuration, the response behavior is more pronounced, meaning that higher sensitivity (amount of gasses formed) and a faster response is achieved. Consequently, the pulse length can be kept rather short.

The gassing behavior in the foil configuration can be distinguished into two processes. First, an abrupt increase of the MS signals due to the CA stimulus can be seen for all mass traces, which is similar as for the mesh configuration, but much less in terms of absolute intensities. Then, the signal increase lowers its slope and changes to a more linear function. One explanation for this behavior could be that under these circumstances, the produced gasses are entrapped in the electrode assembly. The gasses, which are formed on the outer side of the electrode, can access the gaseous headspace faster as their diffusion distance is rather short. This results in the abrupt increase of the MS signals. Gasses which are generated close to the center of the electrode must diffuse through the laterally aligned electrode stack until they reach the outer part of the electrode. This results in a linear increase of the MS signals. For the mesh configuration, the produced gasses can easily diffuse through the highly porous material and are detected by the MS, as most active material seems to be accessible to the head space. Consequently, the mesh configuration provides more pronounced signal intensities and reveal even fast changes in the gaseous head space composition.

IV. Evaluation of the Response Time Characteristics

Finally, a precise evaluation of the response time was carried out. Thus, a detailed view of the individual mass traces in a rather short time interval after the application of the potential pulse is useful. Due to its more pronounced response characteristics regarding the CA stimulus and the MS signal increase, the mesh configuration, with a pulse sequence up to 4.2 V and four seconds, was chosen (see left part of Fig. 45). To describe the response time, the following procedure was performed. First, the initial intensities, before the CA procedure, were read out (I_0). The intensities after 20 min. (I_{20}) were used as final value (100 %). The response time was determined analog to time constant definition typically used in the context of sensor characterization.[214]

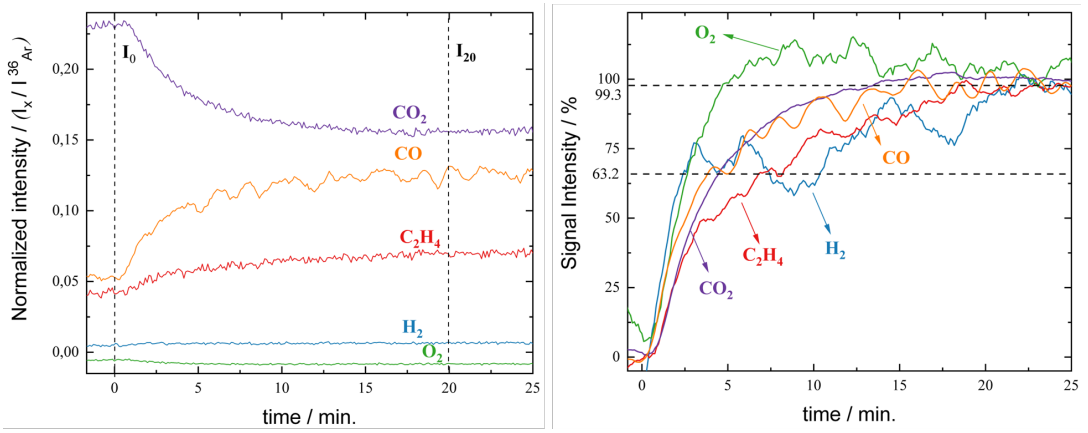

Figure 45: Left: Detailed view of MS intensities of various gasses after one CA experiment, using a pulse length of four seconds and a potential of 4.2 V, using a mesh configurated LIB. **Right:** Relative mass signal intensities to determine the response time for either 63.2 % or 99.3 % (dashed lines).

Two values for each mass channel were determined. The first value corresponds to 63.2 % and the second to 99.3 % of the final intensities. The relative signal intensity for the mass channels of interest are plotted in Fig. 45. All response time data are furthermore depicted in Table 7. The focus was first set on the 63.2 % benchmark. The fastest response is achieved for hydrogen, followed by oxygen, and carbon dioxide. Ethylene and carbon monoxide show the slowest response characteristics. This behavior can be explained with the origin of the evolved gas species. It is necessary to differentiate between directly consumed (oxygen) and produced gasses (hydrogen) or the gasses which are formed due to the SEI formation. These gas species are only the by-product of a cascade of several electrochemically triggered reactions at a certain potential inside the LIB. So, the origin and the response behavior of those produced gasses (ethylene, carbon monoxide, and carbon dioxide) are different from those of the gasses hydrogen and oxygen. However, all gasses reach the benchmark within seven minutes, after the CA experiment was performed. The response time to achieve 99.3 % of the final value is much longer for all gasses, taking up to 22 min.

Table 7: Response time values for a four second chronoamperiometric pulse measurement with a mesh configurated LIB.

Benchmark %	**H_2**	**C_2H_4**	**CO**	**O_2**	**CO_2**
			sec.		
63.2	141	404	229	156	262
99.3	1304	1116	924	294	808

Hydrogen shows a special behavior. It has the fastest response time to achieve 63.2 % of the total signal intensity but takes the longest time to achieve the 99.3 % signal intensity. This indicates that besides gas evolution also, gas consumption is a part

which has to be considered. Hydrogen is quickly formed but can be consumed fast within the cell environment. Furthermore, it has to be considered that hydrogen is challenging to measure within the MS due to its permeating properties. The results discussed above show that from an analytical point of view, the response time for each gas can be differentiated. However, the reason for the differences in response characteristics depends on many intrinsic parameters, and on the cell configuration itself. In addition, the cell chemistry has an important influence. Chemical processes, like the SEI formation are relatively slow processes.

As the SEI is a fundamental key factor for the overall cell lifetime as well as for the performance of the cell, its correct formation is a crucial and cost-intensive part of every LIB manufacturing process. The usually applied very first cycling protocol is most likely in the range of hours up to days to form an ideal and homogeneous layer of this slowly formed SEI. Therefore, the presented response time characterization can be summarized toward a general response time which is for both cases in the range of several minutes. This estimation is strongly influenced by the amount of the released gasses. A further aspect is that under the described experimental conditions, the amount of gas evolution was sometimes close to the lower detection limit of the overall setup. When cycling a cell, a much higher gas release is expected, which will further affect the response time toward a faster response behavior.

4.6 Conclusion

In this work, the response characteristics of a custom-made online electrochemical mass spectrometry system for gas analysis in lithium-ion battery cells are presented. The results were achieved using CA to trigger electrochemical reactions within a cell under the release of gaseous compounds. As the gassing is a very complex interaction of gas evolution as well as gas consumption within a manifold environment, e.g., solid active material and liquid electrolyte components, a variety of parameters, such as diffusion, solubility, viscosity, and reactivity of the individual gas species, play an important role when it comes to online measurement techniques of those gasses. CA was used as it provided a clear starting point of the electrochemical reaction itself to reduce the uncertainty in comparison to typically used cycling protocols. The advantage of short voltage pulses during the CA experiment was that all formed gaseous species can clearly be assigned to the rather short interval of the applied electrochemical stimulus. While investigating first the potential range from 2.0 to 4.5 V and the corresponding effect on the gassing behavior, it was found that the CA technique can be used to trigger specific electrochemical reactions, e.g., water splitting and to investigate the dependency on the applied potential toward the individual underlying chemical reactions. In addition, the effect of the pulse length of the potential jump on the gassing behavior was investigated

for two typical LIB configurations. It was found that the adapted highly porous mesh configuration LIB provides much faster response characteristics towards the applied potential pulse. The foil configuration LIB showed an overall similar behavior, but much less pronounced. Furthermore, it was found that in case of the foil configuration LIB, delays of the transport of the formed gasses occurred by trapping them inside the foil electrode assembly. However, the foil configuration LIB is more representative for the typical LIB situation. A more detailed investigation of the overall response characteristics for a mesh configuration LIB revealed the complexity and challenge of pointing out a defined response time for the overall system. This study demonstrated the intricate nature of online gas analysis of LIBs using a simple electrochemical stimulus through a chronoamperometry experiment. The relevant gasses were detected within minutes, although with individual variations in response characteristics. The findings imply that the interpretation of more complex LIB experiments conducted through an online electrochemical mass spectrometer system is in principle possible, but must be approached with critical care to ensure proper identification of gas species and their corresponding electrochemical phenomena and time of formation.

Impact of Electrode Densification on the Electrochemical Performance & Gassing Behavior of NMC955

5.1 Motivation

In this chapter the model cell is used in a half-cell configuration to investigate the effect, calendaring has onto the structural stability of NMC cathode materials. As explained in section 2.5.2, the structural stability of NMC materials is crucial for long-term function of the battery cell. Parasitic side-reaction can occur due to an increase of the upper cut-off voltage, but also depends on the morphology of the active material. Here, the calendering process step (explained in section 2.6.2) has a profound impact on the particles morphology. Calendering is needed to improve the electrical contact and reducing the thickness of the electrode. However, it causes also particle cracking and hence a higher probability of those unwanted parasitic side reactions, causing ongoing gas evolution reactions.

Within this section, positive electrodes containing NMC955 were produced on different substrates, and were calendered with varying calendering force, to investigate the impact of this mechanical process step in more depth. Besides thickness measurement and REM cross-sectional analysis, OEMS was used as novel technique, to gain further insight into the electrochemical performance of those electrodes. Especially, to investigate the different gassing behavior of those electrodes. The use of OEMS allowed to draw conclusions on the intrinsic behavior of those electrodes and the parasitic side reaction, while measuring the occur/absence of typical gasses, e.g. CO_2 and CO.

Keywords: Li-ion batteries • NMC Cathodes • Gas evolution • Online electrochemical mass spectrometry • Calendering • Electrode structure

5.2 Abstract

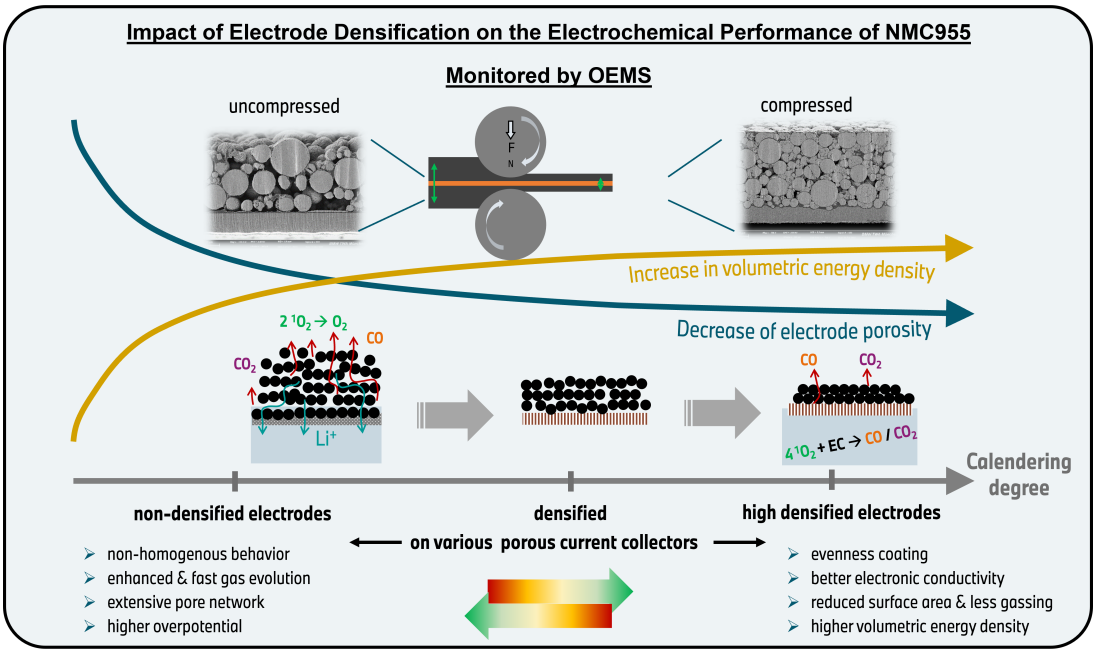

Figure 46: Graphical abstract for the following chapter dealing with the impact of electrode densification on the electrochemical performance of NMC955 material.

Calendering is a crucial process step during electrode manufacturing and enhances the volumetric energy density of the electrode. However, critical care has to taken into account as the densification influences many other parameters, e.g. electrical & ionic conductivity, adhesion strength, porosity, as well as effective surface area. Beyond a certain point of densification the long cycle life and rate capability can be negatively effected, e.g. due to particle breakdown. Hence, the calendering should be optimized in regards of the material and posterior application. Herein we present how the calendering step influences the electrochemical performance of NMC955-Li-half cells during delithiation up to 5.0 V vs. Li/Li^+. Online Electrochemical Mass Spectrometry was used to study the simultaneous gas release due to decomposition reactions and structural rearrangement of the NMC material. Experiments were carried out on highly porous mesh or laser-perforated current collector using EC_{only} (1.5 M $LiPF_6$ + EC) electrolyte. It was found that the cells´ capacity, the amount of released gas and the release of lattice oxygen, strongly depend on the degree of compaction. SEM was used as supporting method to visual inspect the differently compacted electrodes and identified extensive pore network for non-compressed electrodes.

5.3 Introduction

In recent years, lithium nickel-manganese-cobalt oxide (NMC) has emerged as material of choice for lithium-ion battery (LIB) cathodes due to its optimal blend of energy density, capacity, and stability. However, the quest for an enhanced battery performance has led to a continuous refinement of NMC materials, with a particular focus on their structural stability. NMC materials typically adopt a layered crystal structure, known as the α-$NaFeO_2$ -type. This type of structure consists of alternating layers of transition metals (nickel, manganese, cobalt) and lithium ions, separated by atomic oxygen layers. The layered structure allows for the insertion and extraction of lithium ions during charge and discharge cycles. It also provides structural stability and facilitates Li^+-ion diffusion within the bulk material.[215] The stability is paramount, as it influences the performance, longevity, and safety of the battery cell.[5,76]

Single-crystalline NMC (sc-NMC) materials have a well-defined crystal structure with a continuous lattice arrangement and uniform properties throughout the entire material. On the other hand, poly-crystalline NMC (pc-NMC) materials consist of multiple crystals with different orientations and sizes, separated by grain boundaries.[78,93] The grain boundaries can affect the electrochemical properties of the material, such as capacity, rate capability, and cycling stability. Additionally, they act as sites for interface reactions and influence the material's surface chemistry, leading to electrolyte decomposition. However, sc-NMC materials are more challenging to synthesize and thus more expensive, as their properties can be highly dependent on the synthesis conditions. Poly-crystalline NMC materials are more commonly used in commercial LIBs due to their ease of synthesis and lower cost.[216,217]

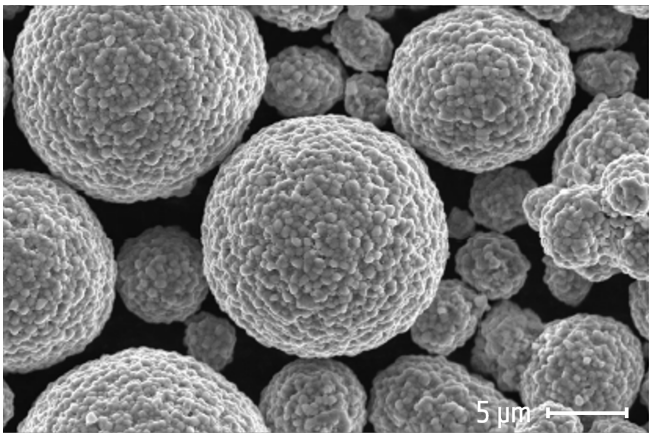

Figure 47: SEM figure of the used NMC poly-crystalline material with a median diameter of $D_{50}<$ 15 µm, figure provided by supplier.

The structural integrity of NMC materials is not solely contingent on their intrinsic properties, but is also significantly affected by the electrodes manufacturing process. Among these, calendering —a mechanical pressing process applied to increase the volumetric electrode density[218] and for improvement of the inter-particle electrical contact[216]— is known to exert a profound impact on the material's microstructure.[136,138] Figure 48 depicts a general calendering-process scheme. While the densification achieved through calendering can enhance the electrical conductivity[137,216] and mechanical robustness of the electrode, it may also induce stresses[219] and defects that compromise the structural stability of the material. In particular, cracked particles causing larger surface area, which is then exposed to the electrolyte and hence more electrolyte degradation reactions can take place. Furthermore, the electrodes´ porosity and tortuosity are being influenced, which are both crucial for high performance LIBs.[216,220]

A critical issue that has garnered attention in terms of degradation, is the release of oxygen due to lattice rearrangement, during the discharge process at high degree of delithiation ($>$ 4.3 V vs. Li/Li^+).[221] The structural changes from a layered towards a rock-salt type releases highly reactive singlet oxygen ($^1O_2$)[221,222] and is schematically shown in Equation (5.1).

$$Li_xMO_2 \rightarrow Li_xMO_{1+x} \; + \; (1-x) \; {}^1O_2 \tag{5.1}$$

The release of lattice oxygen induces the formation of a resistive oxygen depleted surface layer around the NMC particles, causing poor cycling stability and continuous electrolyte degradation.[81,217,223–225] This degradation phenomena undermines the importance of proper electrochemical testing procedures. Preventing the in-situ formation of oxygen, due to a cell over-voltage scenario, is an important safety aspect in terms of inducing and accelerating the thermal runaway in large-format cells.[222,226]

The voltage-resolved detection of oxygen release within cathode materials requires specialized techniques, such as OEMS systems. Several groups investigated the onset of the oxygen release by the use of OEMS and its dependence, e.g. on the nickel-content,[81] temperature,[86] crystallinity,[217] coating strategies,[226] cycling conditions,[221,227] as well as other characteristics.[222,228,229] *Jung et al.*,[81] reported that the NMC materials exhibit a good cycling stability and capacity retention, when the material is charged up to the point before O_2-release ($\approx$ 80 % state of charge). However, the state of the art OEMS-configuration does not represent a realistic battery configuration, yet.

OEMS approaches often uses stainless-steel mesh electrodes, which allow an excellent analysis of the electrochemical applied condition, e.g. voltage in regards of the degradation phenomena in terms of gas evolution. However, industrial coin-cell arrangement comes typically along with foil-coated electrodes and their production involves several critical steps, which additionally have an impact onto the gas evolution, e.g. densification.[137]

Using solid foils as current collector (CC) might carry the risk of trapping the gases between electrode and separator and hence provide more time for interference of the evolved gases within the liquid/solid interface. Hence, the time resolution & degree of information's from the OEMS might be reduced.[230] On the other side, it is not possible to investigate the calendering effect on mesh-coated electrodes, as no realistic material compaction can be carried out due to the geometry of the mesh, as shown below. Also calendering first on foil-current collectors and coating secondly onto mesh substrate is assumed to influence the electrochemical behavior, as binder particles may migrate within the NMC-structure while preparing a second slurry in between both steps. In sum, the interplay between oxygen release and calendering presents a complex challenge that requires a new approach.

This work aims to dissect the relationship between the structural stability of NMC materials and oxygen release, with a particular emphasis on the dependence of the calendering process with adapted laser-perforated current collector foil to allow rapid exchange of gases and lithium ions within the interfaces. By scrutinizing the effects of calendering on the micro-structural integrity and oxygen evolution kinetics of NMC cathodes, we seek to illuminate the pathways through which the manufacturing process influences the material's behavior during battery operation. Our investigation will provide insights that could inform the optimization of calendering parameters, with the goal of mitigating oxygen release and enhancing the overall performance and safety of NMC-based lithium-ion batteries.

In this chapter, we studied the impact of the electrode density due to calendering onto the electrochemical properties as well as the accompanied gas evolution of a polycrystalline transition metal oxide ($Li[Ni_{0.9}Mn_{0.04}Co_{0.06}]O_2$) so-called NMC955. The active material was delithiated up to 5.0 V vs. Li/Li^+ on two different types of current collectors while using OEMS half-cell configurations. First, the active material was coated onto a micro laser-perforated aluminium current collector foil, to allow gas evolution and lithium diffusion throughout the current collector. Second, the same material was dispersed on a porous micrometer mesh, which allows fast gas diffusion and excellent electric contact to the active material. The appearance of oxygen release was found to strongly depend on the compaction pressure and the configuration.

5.4 Experimental

I. Electrode Manufacturing

The positive electrode was created within dry-room atmosphere by preparing a 1.35 wt. % solution of polyvinylidene fluoride (PVDF, Solef 5140, Solvay Belgium) mixed with n-methyl-2-pyrrolidone (NMP, anhydrous, 99.5 % Sigma-Aldrich) for 12 h at room temperature. Then, 1.50 wt. % LITXHP (Cabot Corporation, USA) were added and the mixture was stirred for 30 min in a planetary orbital mixer at 2000 rpm (Thinky Are 250, USA). Finally, 97.0 wt. % NMC955 (B&M, Tianjin China) was added in two portions including a 30 min stirring time in-between with 2000 rpm. Additional information of the individual materials are also given in Table 8. The slurry with a solid content of 70 % was applied to a laser-perforated aluminum current collector or a stainless-steel mesh (0.212/0.090 mm aperture, Spoerl KG, Germany) using a 150 µm gap applicator. The laser perforated current collector provides a regular spacing of six holes per mm^2, with a diameter of 65 µm per hole, see Figure 56 for additional information. The coating was first dried in a ventilated oven at 100 °C before being punched into 15 mm discs (mesh coating) or 20 mm edge-length squares (collector foil). The mesh electrodes and separator (10 µm, ⌀=16 mm, Shenzhen Senior Tech., China) were further dried for 24 h under dynamic vacuum (Büchi, Switzerland) at 120 °C and 60 °C, respectively. The laser-perforated squares were further processed according to the procedure described below.

Table 8: Characteristics of the used materials within this work.

Material	**Share (χ)** [%]	**Density (ρ)** [g·cm^{-3}]	**Surface (BET)** [m^2· g^{-1}]
NMC	97.1	4.87	0.534
CB	1.50	1.80	61.91
PVDF	1.35	1.75	not relevant

II. Fundamentals: Calendaring

In an industrial environment, the applied calendering pressure is often referred as line load (q_L) and is the ratio of of the applied force (F_N) and the coating width (w_C), represented via Equation (5.2).

$$q_\mathrm{L} = \frac{F_\mathrm{N}}{w_\mathrm{C}} \tag{5.2}$$

In order to convert the line load to uni-axial static compression values, typical calendering parameters were used as starting point of our investigation. Today's cathode materials are being compressed with a line load up to ≈ 1200 N·mm^{-1}.[138,141] As NMC

particles are much harder than graphite, subsequently higher forces have to be used to effectuate particle deformation, particle-particle rearrangement with particle friction and particle breakdown, than for the compression of graphite-based anode flakes. [142,143]

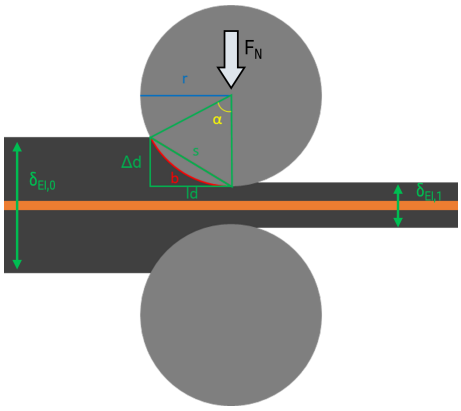

Figure 48: Schematic illustration of the calendering process. F_{N} is the roll force, electrode thickness before ($\delta_{\mathrm{El},0}$) and after ($\delta_{\mathrm{El},1}$), the roll radius (r), the arc (α), and the arc length (b).

The arc length (b) defines the compaction zone and depends on the rolling diameter (r_{D}), the gap (δ_{R}) and the electrode geometry (width w_{C}, and thickness δ_{El}). By using a typical roller radius of 300 mm, an average cathode thickness of ≈ 170 µm before and 120 µm after calendering (compaction of ≈ 30%). The resulting angle (α) can be determined, via Equation (5.3).

$$\alpha = \arccos\left[1 - \frac{\delta_{El,0} - \delta_{El,1}}{r_D}\right] \tag{5.3}$$

b can be subsequently calculated as the product of α and r. Following this, an areal pressure p in terms of N·mm^{-2} is obtained through Equation (5.4)

$$p\left[N \cdot mm^{-2}\right] = \frac{q_L}{b} = \frac{q_L}{\alpha \cdot r} \tag{5.4}$$

The herein used electrode sheets (squares) had an area of 4 cm^2, which results in an areal pressure of 120 kN (30 kN·cm^{-2}), using the above-given parameters. Based on these considerations, compaction pressures between 0 - 50 kN·cm^{-2} were investigated within this work. The value of 50 kN·cm^2 represents a deliberately "over-calendering" in order to mimic the effect of mechanically induced particle cracking.

Static Compression of Electrode Samples

Following coating and cutting the electrodes in 4 cm^2 squares, they were placed between two stainless-steel metal plates (roughness = 0.2 Ra; parallelism = ± 5 µm). The gap between the plates was sealed with Kapton tape and the arrangement was placed in a ventilated oven at 120 °C for 1 h. Subsequently, the sandwich was compressed within a 2-column manual lab press (type: PW 40; P/O/Weber, Germany) for 60 sec, according to the desired pressure. The procedure is shown in Figure 32. The thickness of each electrode sample was determined before and after compression, using an altimeter (Interapid, Switzerland) with a resolution of ± 1 µm. A 15 mm disc was punched out of the electrode square. The sample was weighed and subsequently transferred into a glovebox were further drying and OEMS preparation was carried out.

Calculation of Electrode Porosity

Porosity of each single electrode disc was determined according to Equation (5.5), where χ is the mass fraction in the electrode and ρ the density of the CAM (NMC), carbon black (CB), and binder (PVDF).

$$\varepsilon = 1 - \frac{m_{El} \cdot [(\chi/\rho)_{\mathrm{NMC}} + (\chi/\rho)_{\mathrm{CB}} + (\chi/\rho)_{\mathrm{PVDF}}]}{V_{El}} \tag{5.5}$$

where χ is the mass fraction in the electrode and ρ the density of the CAM (NMC), carbon black (CB), and binder (PVDF). The symbols m_{El} and V_{El} correspond to the electrode mass and volume.[136] The latter one was calculated using the disc diameter and the measured thickness before and after compression. Using the above-shown formula assumes the incompressibility of the current collector. The assumption is not fully justified as it is known, that single particles penetrate into the current collector while using high line loads, as shown by literature.[198]

III. Electrode Characterization via SEM

In order to evaluate the quality of the static compression-approach, SEM images of the individual compression steps were taken. The images were acquired with a Gemini SEM-450 Zeiss Crossbeam Neon 40 with a Gemini 2 electron module, using a voltage of 3 kV (cross-section) or 20 kV top view and a 200 pA sample current. For cross-section images the electrodes underwent ion milling to obtain a smooth edge. To that end, an ArBlade 5000 ion milling system (Hitachi, Japan) device was used, which provides a convergent broad beam of Ar^+ on a static tungsten carbide mask. The image segmentation was performed through the zoom stereo binocular (corresponding to CCD camera). Ar-etching was performed for 1.5 hours with an Ar-supply of 0.12 $cm^3 \cdot min^{-1}$. The acceleration voltage was 6.0 kV and the disc voltage was set to 1.8 kV.

IV. Online Electrochemical Mass Spectrometry

OEMS was used for the electrochemical cell testing and simultaneous gas detection. The setup´s principle operation and design was already described in our recent publication.[231] Before assembly, all pieces of cell hardware, electrode, and separator discs were dried at 120 °C within the heated glovebox evacuation chamber (MBraun, with H_2O & O_2 < 1 ppm), for 12 h. Two different OEMS cell configuration were used within this work. Both differentiate in terms of the used current collector. Either the active material was coated onto a laser-perforated aluminum current collector, where the coating is facing downwards to the separator interface to mimic a more realistic half-cell setup (see upper part of Figure 49) or the coating was applied onto a highly porous mesh as current collector, facing the coating partially upwards towards the cell´s head space, to improve gas diffusion and sensitivity (see lower part of Figure 49).

Assembling Procedure for the Closed Half-Cell Configuration

A lithium metal counter electrode disc (⌀=15 mm) was placed at the bottom of the cell cup, followed by a separator (Whatman glass-fiber, ⌀=16 mm). Then, 100 µL electrolyte (1.5 M $LiPF_6$ in EC) was added. The positive (working) electrode was placed in such a way that the coated side was facing downwards to the separator layer. Subsequently, 100 µL of the same electrolyte was added again. The half-cell sandwich was then covered with a virgin mesh disc (⌀=16 mm). Electrical contact of the electrodes was established by using a stainless-steel spring (Sodemann Industrifjedre, spring constant: 1.86 N/mm). After sealing under glovebox atmosphere and connecting to the MS, the cell was purged with Argon (Riessner Gase, Germany, >99.999%) for 5 min and then held at open circuit voltage (OCV ≈ 3.2 V vs. Li/Li^+) for 4 h. Subsequently, a constant current constant voltage (CCCV) formation was applied with a dis-/charge rate of C/5 using a SP-300 potentiostat (BioLogic, France). Cycling occurred according to the practically achievable discharge capacity of 222.1 $mAh \cdot g^{-1}$, determined at a formation step of C/10.

Assembling for the Mesh and Open Half-Cell Configuration

The cell was initially built and connected similar to the former described procedure (coating facing downwards) and the positive electrode was delithiated with C/20-current according to the theoretical capacity of 277 $mAh \cdot g^{-1}$, until 3.95 V vs. Li/Li^+ including a rather long CV step (I < 1 mA). Then, the cell was transferred into the glovebox and the positive electrode was flipped in a way, that the coating was facing towards the cell head space. 50 µL electrolyte (1.5 M $LiPF_6$ + EC_{only}) was added again and the cell was sealed and rest again for 4 h while connected to the MS. The NMC material was then delithiated with a C/200 step until 5.0 V vs. Li/Li^+, followed by an 5 h CV step.

In order to allow such a long measuring time, the cell head space had an initial pressure of 1.5 bar due to argon flushing. In case of the mesh-coated electrode, the mesh was insert in the cell cup with the coating facing towards the cell head space and delithiated up to 5.0 V vs. Li/Li^+ with C/5 in a single step.

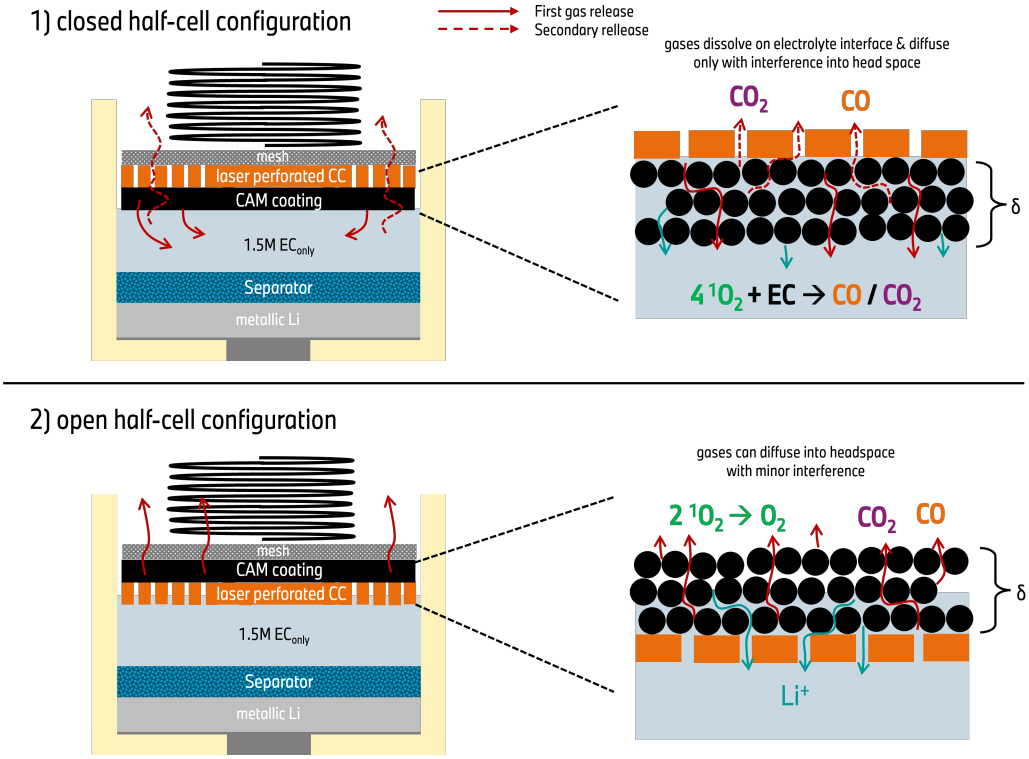

Figure 49: Schematic illustration of gassing related processes for 1) Closed half-cell configuration with laser-perforated current collector, to mimic the industrial configuration with foil-coated electrodes. 2) Open half-cell configuration with laser-perforated current collector to mimic the common used mesh-setup. In the lower case the released gases (CO, CO_2, and O_2) can easily enter the gaseous head space and are being detected by the MS, while in the upper configuration the gases mainly diffuse within the CAM/electrolyte interface. Here, further interaction with Li^+ and electrolyte (EC) occur. Especially, oxygen is assumed to be reduced to form CO_2. The gases must finally master to diffuse through the laser-perforated holes until they are accessible by the MS.

5.5 Results and Discussion

The results are categorized into three sections. Firstly, the physical electrode data are presented and qualitatively compared with ex-situ SEM images (top figure & cross-section) to evaluate the micro-structural changes as a consequence of the compaction process. Secondly, the electrochemical performance and gassing behavior within the closed half-cell configuration was analyzed as function of the electrode density. Thirdly, the gas evolution within the open half-cell configuration was studied in detail. Both configurations were compared to the gas evolution of the mesh substrate.

I. Analysis of the Compaction Pressure on the Electrodes Microstructural Properties

Calendaring Process

Figure 50 visualizes the electrode porosity, density, and thickness of the coating as function of the applied compaction pressure. All data are additionally depicted within Table 9. In general, as it had to be expected, coating-layer thickness and porosity decreases with increasing compaction pressure, while the coating density increases. These general trends were already described in several other publications.[138,141,219,232,233]

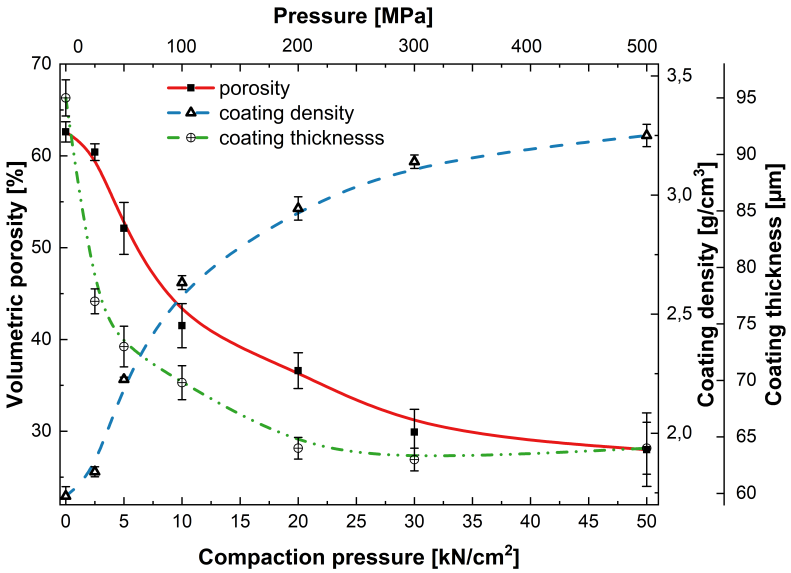

Figure 50: Electrodes porosity (red), coating density (blue), and -thickness (green) as a function of the applied pressure. Lines are drawn to guide the eyes.

The average tap density of the active mass is 3.53 g·cm^{-3}, which corresponds to an porosity of 63 % for the non-compressed and most likely also for the mesh coated electrode. Applying relatively small pressure to the laser perforated electrode samples, already results in a strong compaction of the material. The porosity and coating thickness exhibit an exponential decay and are therefore in accordance with *Schmidt et al.*[219]

and *Meyer et al.*[141] who proposed an exponential decay model for anode and cathode electrodes. However, it has to be noted that both groups used different material ratios and coating thicknesses, in comparison to our work. *Schmidt et al.*[219] reported slightly lower porosities (≈ 5 % less), while using higher pressures, but also more binder and CB were used in their work (8 % in total). In our study, only 1.5 % conductive carbon and 1.35 % binder were used in order to keep the impact of those additives as low as possible. A thicker coating can withstand higher applied pressures, due to load displacement, also called spring-back effect.[234] In particular, when a higher binder content is being used, significant differences may arise from the distinct bulk materials employed, which are primarily influenced by the composition of the coating, as well as the particle morphology and size distribution. As these parameters exhibit considerable variability across the various studies, only the general behavior of the electrodes can be comparatively evaluated.

Table 9: Compaction pressure, active mass layer thickness after compression and related volumetric porosities and capacity density for the investigated samples, including standard deviation (±).

Compaction pressure $[\mathrm{kN \cdot cm^{-2}}]$	**Coating thickness** [µm]	**Thickness reduction** [%]	**Porosity** [%]	**Coating density** $[\mathrm{g \cdot cm^{-3}}]$	**Capacity density** $[\mathrm{Ah \cdot L^{-1}}]$
0	94.6 ± 1.6	00.0	62.6 ± 1.1	1.74 ± 0.04	447.0
2.5	76.5 ± 1.1	11.7	60.4 ± 0.91	1.84 ± 0.02	/
5	73.0 ± 1.8	17.9	52.1 ± 2.8	2.23 ± 0.01	/
10	69.5 ± 1.5	26.5	41.5 ± 2.4	2.63 ± 0.03	607.3
20	64.0 ± 0.96	24.6	36.6 ± 1.9	2.94 ± 0.05	679.1
30	63.0 ± 1.0	23.7	29.9 ± 2.5	3.14 ± 0.03	688.0
50	64.6 ± 2.3	32.4	28.0 ± 3.0	3.25 ± 0.05	658.2

Applying a pressure of 30 $\mathrm{kN \cdot cm^{-2}}$ (300 MPa), the density of the electrode reaches 3.14 $\mathrm{g \cdot cm^{-3}}$ and a porosity of $\approx 29 \pm 2\%$. Cathodes with porosities >25 % are classified as moderately compacted. Electrodes with porosities <25 % are often described as highly compacted. The achieved results in terms of coating density using an applied pressure of 30 $\mathrm{kN \cdot cm^{-2}}$ was found to be in good agreement for what is typically found in automotive cells.[218,232,234]

Further applied pressure up to 50 $\mathrm{kN \cdot cm^{-2}}$ (500 MPa) seems not to affect the porosity, within the given failure range. However, the electrode density under these conditions was calculated to be 3.25 $\mathrm{g \cdot cm^{-3}}$, which fits very well with the theoretical achievable density of the material mix (see Table 10). The slight increase of the coating thickness between 300 and 500 MPa sample could again indicate, that the high applied pressure results in

a stronger spring-back effect of the coating. However, applying infinite pressure onto the electrode, would result in the density of the solid fractions, following extremely low porosity and ionic transport.

SEM Based Considerations

Figure 51 shows the SEM images from top view and cross-section view of several different compacted electrode samples. In general, the NMC poly-crystalline particles used herein have a spherical shape. The particle size distribution according to the supplier shows a $D_{10} < 6$ µm, $D_{50} < 14$ µm, and $D_{90} < 28$ µm, which means that 10 % of the particles are smaller than 6 µm, 50 % smaller than 14 µm, and 90 % of all particles are smaller than 28 µm. Both, mesh-coated and non-compacted laser-perforated electrode sample possess a distinct surface roughness and numerous gaps indicating an extensive pore network (white circles), even in deeper layer thicknesses at the interface between coating and CC. The mesh coating still shows the underlying mesh wire, which seems equally covered with an active material film.

However, the cross-section of the mesh coating reveals that under those coating conditions, which are conventional used for OEMS experiments, a considerably portion of particles is loosely aggregated and the electrical contact to the mesh-wire is only achieved due to weak inter-particle connections. The surface gets progressively flattened with increasing compaction, and parts of the large pore network disappear with increasing densification. With higher compaction pressure (30 kN·cm^{-2}) the electrode surface achieves a respectable plateau of a homogeneous compressed cathode. For better comparison, a sample of an automotive cell cathode is added in this comparison (see sub-Figure 4I). Validation of the calendering pressure onto cathode compaction using SEM was also done by several groups and showed overall similar effects.[136,138,198,219,233,235] Nonetheless, a calendering pressure of 30 kN·cm^{-2} already causes mechanically induced particle cracking, mostly visible on small and medium sized particles. The same was observed by *Schmidt et al.*[219] and *Kuchler et al.*[236] The highest applied compaction pressure (50 kN·cm^{-2}) results in a thinner electrode and enhanced particle cracking even at larger particles. In addition, it becomes visible that the NMC particles start to penetrate into the Al-current collector, as also observed by *Tran et al.*[198] Both phenomena could explain the rather high standard deviation within the thickness of those samples. Several groups additionally determined the porosity via mercury intrusion and found it always well comparable with the volumetric one.[219] However, they showed that up to a porosity of ≈ 30 %, most of the inter-particular pores are closed.[233] Pores with $\varnothing \approx 1$ µm and intra-particular pores are only closed at very high densification, as it is assumed to be the case for the 50 kN*cm^{-2} compressed-electrode. During this high densification also the binder material and other additives access the molecular pore system.[143,235]

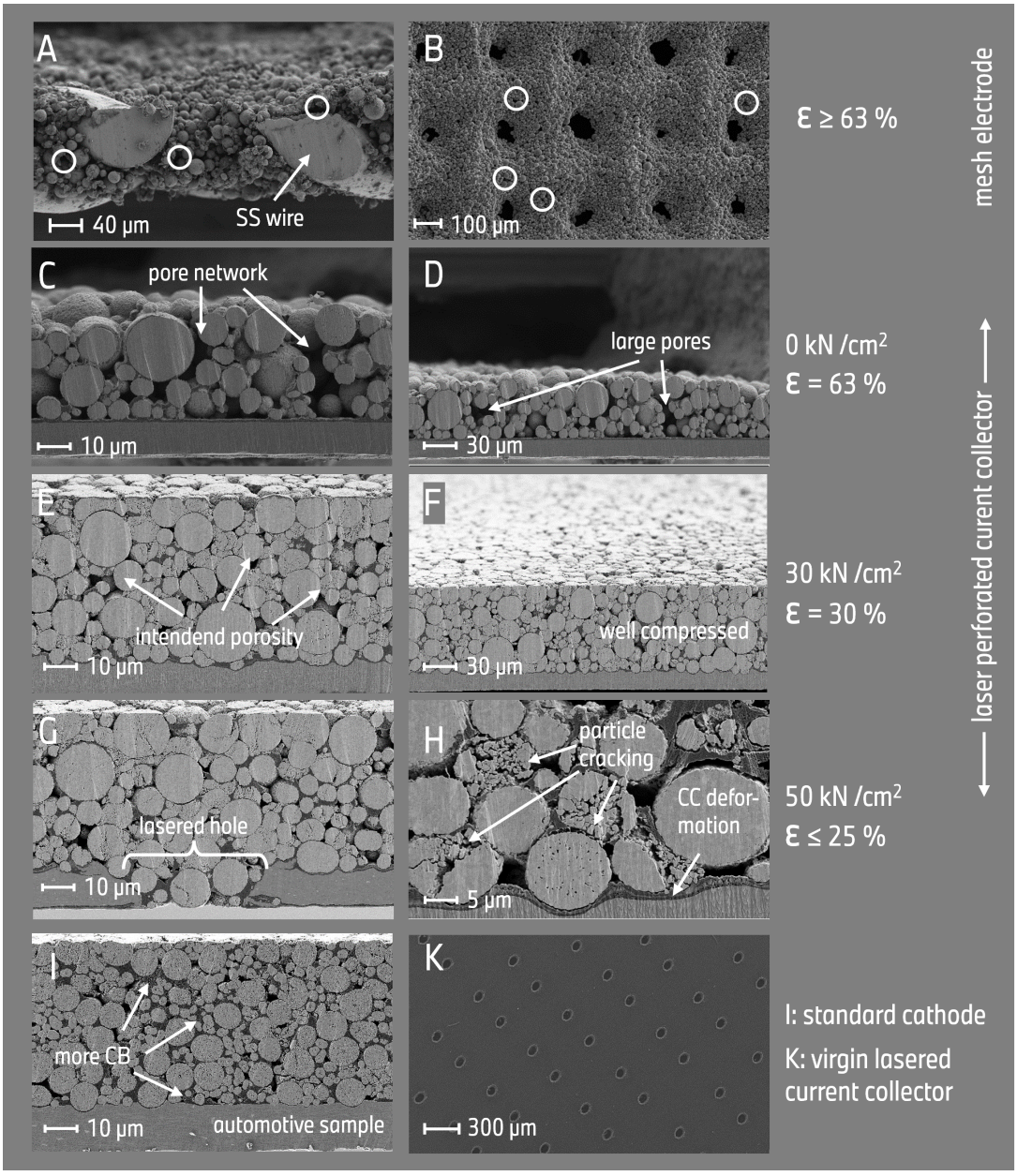

Figure 51: SEM-Images for various cathodes and current collectors, used within this work. A) cross-sectional image of the mesh coated electrode with a 250x magnification. B) Top view with 80x magnification of the same mesh coated electrode with pore network (white circles). C/D) cross-section of a laser penetrated aluminum foil coated sample without calendering (0 kN*cm^{-2}), 750x and 350x magnification. E/F) cross-section of a coated laser perforated aluminum foil sample with an applied calendering pressure of 30 kN*cm^{-2}, 750x and 350x magnification. G/H) cross-section of the same laser perforated samples with an applied calendering pressure of 50 kN*cm^{-2} with 750x and 2500x magnification. I) cross-section of a various NMC811 electrode harvested from an automotive cell, 1k magnification. K) top view of the used laser-perforated aluminum current collector with a 50x magnification.

In sum, the micro-structural analysis shows that with increasing compaction pressure a decrease in the pore network and pore sizes occur. Sufficient porosity is however necessary for the electrolyte to access active material throughout the electrode. With decreasing porosity an increase in tortuosity and hence kinetic limitations can be expected. Both phenomena might result in a high ionic resistance.[237] On the other hand, a higher compaction results in a thinner electrode which effectively reduces the diffusion path for the lithium ions. The observed particle cracking will also reduce the diffusion length within the solid-state phase, as the pressure induced cavities serve as electrolyte reservoir. Both factors will have a positive effect on the ionic transport within the electrode material.

Influence of Compaction Degree on Charge Capacity & Capacity Retention

Figure 52 shows the specific charge capacity and capacity retention for various compacted electrodes versus electrode density and porosity, respectively. The very left values represents the mesh coated electrode. Note that the electrode density and porosity of this electrode is not exactly known, but must be higher as the non-compacted one (second data point from left). However, the mesh electrode exhibit a specific charge capacity of 264 mAh·g^{-1}, which is close to the theoretical value of 276 mAh·g^{-1} and provides a coloumbic efficiency of 91.98 % within the first full cycle.

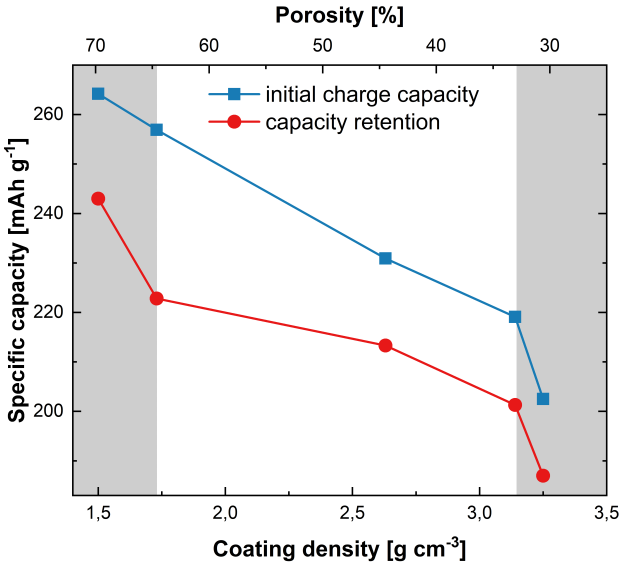

Figure 52: Capacity density of the various densified cathodes in half-cell configuration for first charge (blue) and discharge (red) versus electrode density (bottom x-axis) and electrode porosity (top x-axis) dis-/charged with C/5 at 30 °C. The gray shaded area indicate, where the capacity loss is higher, then the volumetric win due to a higher volumetric electrode density. Very left value represents the mesh coated electrode, where the density and porosity can not be clearly determined.

Switching solely to the laser-perforated current collector without compaction results in a specific charge capacity of 256.9 $mAh \cdot g^{-1}$ and a rather low coloumbic efficiency of 86.7 %. This decay can be explained due to the fact that for the mesh electrode the particles are very well covered around any stainless-steel wire, whereas for the non-compacted foil electrode the current must flow from the aluminum current collector foil throughout the porous coating until they reach each single microscopic NMC particle. The coloumbic efficiency is improved as soon as the material gets slightly compressed with an efficiency of 92.4 % for the 10 $kN \cdot cm^{-2}$ electrode. With increasing compaction the specific capacity of the material is continuously decreasing while the capacity retention stays rather constant. This can be especially seen for the very strongly compacted electrode, which results in a rather strong capacity decay. However, even this strong compaction shows a coloumbic efficiency of 92.3 %. In sum, a value of ≈ 3.2 $g \cdot cm^{-3}$ and a porosity of ≈ 32 % seems to be a preferred trade-off value between available capacity and volumetric gain due to electrode compaction.

II. Influence of Electrode Densification within a Closed Half Cell Configuration

First, the electrochemical data of the first two cycles with a charge-/discharge rate of C/5 within 3.0-4.8 V vs. Li/Li^+ are presented and discussed. Secondly, the gas evolution is described in relation to the compaction pressure. These experiments were carried out in such a way that the coating was facing towards the separator (downside), see Figure 49 for additional information.

Electrochemical Data

The specific charge and discharge capacities for the first full cycle are presented in part A of Figure 53. The curves show a dependence on the underlying compaction pressure, considering that the dis-/charge capacities decreases with increasing electrode density, as already described within Figure 52.

Starting with the delithiation process, the mesh and non-compressed electrode sample show a very similar behavior. Both electrodes consist of loosely aggregated particles, with a large pore network as identified within the SEM analysis. Additionally to those findings, the zoom-in area of Figure 6A reveals a clear and straight potential increase for the mesh electrode, followed by a similar behavior of the non-compacted perforated electrode sample. Latter one shows a rather small overpotential peak at 3.8 V vs. Li/Li^+, possibly introduced due to Li_2CO_3-impurities (see zoom-in area of Figure 6A) as discussed later in Figure 6C. NMC particles are not good electronic conductors when the active mass is not properly compressed; some parts are not accessible to the electron transfer from the current collector.[238] Hence, non-compressed electrodes usually come

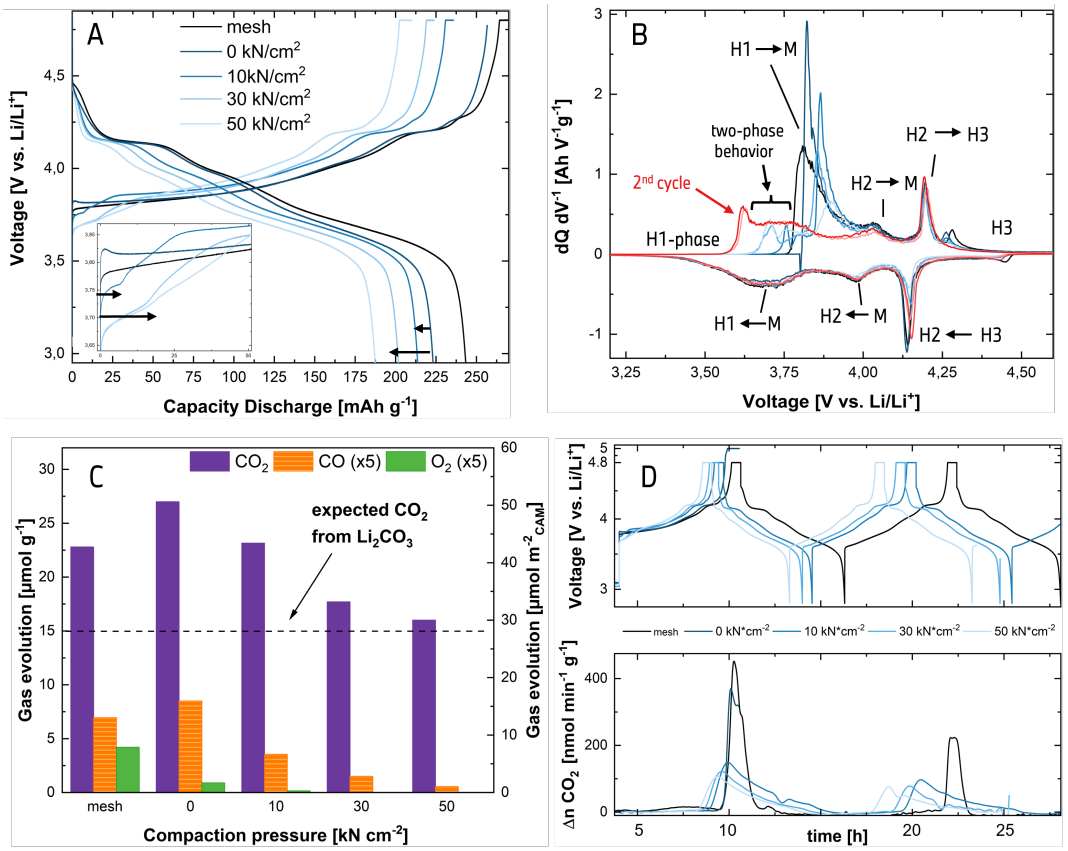

Figure 53: A) Charge and discharge capacities for the first cycle of various compacted electrodes with a charging current of C/5 at 30 °C in EC_{only}-electrolyte. B) Differential voltage analysis ($dQ \cdot dV^{-1}$) for the same electrodes during the first cycle (bluish) and second cycle (red) exemplary for 30-&and 50 $kN \cdot cm^{-2}$ C) Sum of the evolved gases (CO_2, CO, and O_2) after the first charge process, depicted at an cell voltage of 5 V vs. Li/Li^+ for the different compacted electrodes in terms of $\mu mol \cdot g^{-1}$. D) Voltage profile for the first two full cycles and the time resolved evolution of carbon dioxide in terms of nmol $min^{-1}g^{-1}$ (CO_2).

along with slower kinetics, lower volumetric capacity density, higher impedance, and thus a more pronounced cell overvoltage.[219,232] As in this case a reduced portion of the NMC particles participate in the current distribution, it can be anticipated that a pronounced particle polarization will ensure. With increasing compaction the material is better compressed and electronically connected. Thus, particle polarization becomes less feasible and a homogeneous dis-/charge behavior is obtained. This is represented by the rather similar electrochemical behavior of the medium compaction range, of 10 to 30 $kN \cdot cm^{-2}$. When the material gets even more compressed (>50 $kN \cdot cm^{-2}$), ionic resistance becomes more feasible, within the electrode. The compression might block the Li-ion diffusion into the active mass. With increasing compaction, especially when smaller pores < 1 µm are being closed by binder and conductive carbon, also the free electrolyte volume (pore volume) decreases, and less contact area is left, which results in impedance growth. Here, it can be assumed that there are electronically well connected regions next to rather poor connected ones, e.g. due to particle cracking

(see SEM images), resulting in a particle-by-particle delithiation process. On the other side, a reduction of porosity shortens the Li-ion diffusion path length and lowers the concentration gradient within the coating.[232,238] All phenomenons together result in a rather different (non-/homogeneous) delithiation process, indicated through the varying slopes within the zoom-in area of Figure 6A.

Nevertheless, even if the depicted data in terms of electrode densification negatively impacts the electrochemical performance during the first charge, the active mass volume is reduced when using higher compaction values. As long as the reduction in capacity is overcompensated by the volume reduction, an overall increase in the capacity density from 447 $Ah{\cdot}L^{-1}$ (non-compressed) up to 679 $Ah{\cdot}L^{-1}$ (30 $kN{\cdot}cm^{-2}$), is achieved. Further compression does not lead to an increase (658 $Ah{\cdot}L^{-1}$) for 50 $kN{\cdot}cm^{-2}$. Here, the capacity loss due to particle cracking and kinetic limitation overcompensates the volume reduction. The volumetric capacity densities are additionally depicted in Table 9. The optimum porosity and electrode density with regards to the specific capacity is described in Figure 52. However, a rate performance determination or any other discussion about the performance of those electrodes is out of the scope of this work. The reader is therefore referred to the following literature.[142,218,219,232,237,238]

In order to further investigate the impact of the compaction pressure onto the structural and electrochemical changes within the material during de-/lithiation, differential capacity vs. voltage profiles ($dQ{\cdot}dV^{-1}$) were obtained and are depicted in Figure 53B. In general, the used $Li[Ni_{0.9}Mn_{0.04}Co_{0.06}]O_2$ is quite similar to $LiNiO_2$ / Ni-rich materials,[81,215,239] respectively and is known for several phase transformations during de-/lithiation. The characteristic oxidation and reduction peaks are denoted within the graph. The first phase transformation during delithiation (anodic peak) from the hexagonal to the monoclinic-stage (H1 $\rightarrow$ M) occurs in the voltage region of 3.8-4.0 V vs. Li/Li^+. Here, the non-compacted electrode on laser-perforated current collector substrate shows the highest and sharpest peak intensity. The peak intensity is decreasing as soon as the electrode is being densified. This behavior can be attributed to the Li_2CO_3 introduced overpotential, as described in Figure 6A. On the other side, the mesh-coated electrode shows a more sluggish H1 to M transformation, as reported earlier by *Jung et al.*[81] Here, particles which are well connected towards the mesh and particles which are less connected result in a more inhomogeneous delithiation process. Hence, a broader peak is formed. Also the geometry of the current collector (3d round steel-wire vs. 2d flat aluminum foil) and hence charge transfer limitations might play a role here.

As the densification increases, the formation of accompanied shoulder peaks in the lower anodic voltage region of 3.65-3.9 V vs. Li/Li^+ can be observed and might be attributed to a two-phase delithiation process of the layered oxide. The apparent two-phase

behavior has been described in several publications.[240–243] *Park et al.*[244] believed that the interfacial exchange current is being influenced resulting in a spatial inhomogeneity in the electrostatic potential caused by the limitations in electrical conductivity, due to an incomplete coverage of the particle by carbon black. However, we believe that the resulting two-phase behavior is due the occurrence of Li_2CO_3 impurities on the surface of the NMC particles. The carbonate represents an activation barrier for the Li-ions to be extracted from the NMC-lattice, resulting in a higher overpotential within the 1st cycle. Indeed, the second performed cycle of all electrodes show lower potentials, see Figure 57. As soon as the material gets compressed, the electronic conductivity between the NMC, CB and Li_2CO_3 particles is improved. It might be also the case, that some portions of the Li_2CO_3 is scratched off during compaction and lowering the activation barrier. The comparison between first cycle and second cycle (red curve) confirm our assumption, as the H1 to M transformation is drastically reduced in intensity. This indicates that the activation barrier introduced by Li_2CO_3 is drastically reduced within the first cycle of Ni-rich materials.

The kinetics for the strongly densified electrode seem to be more kinetically hindered, again as peak potentials during lithiation continuously shift by 86 mV to higher values for the H1 to H1+M[239] Here it might be the case that some pores are closed off, resulting in solid state diffusion regimes. Additionally to that, the overall decreased capacity enables more current to be available for the well-connected NMC particles, enhancing an ever increasing imbalance between good and poor connected phases. Indeed, the composite volume resistivity (see Figure 58) shows an increased resistance for the strongly densified electrode sample. All in all these phenomenons are playing together and result in a rather individual particle delithiation process for strongly compacted electrodes.

A second and rather small peak at 4.05 V vs. Li/Li$^+$ indicates the transformation from the H2-stage $\rightarrow$ M. At 4.2 V vs. Li/Li$^+$ the phase transformation from hexagonal H2 to hexagonal H3 occurs (H2 $\rightarrow$ H3).[245] The latter one causes abrupt volume contraction within the unit cell of the NMC material, and several studies have shown that this phase transformation is responsible for capacity fading of nickel-rich materials under high voltage applications due to the irreversible release of singlet oxygen[79,81,215] Both phase-transformation seems not to be influenced by the electrode densification process. On the negative scan, a clear redox peak at 4.15 V indicates the reverse phase transformation from H3 to H2. Here, again a decreasing intensity with increasing electrode densification can be clearly seen and might be attributed due to the decreasing capacity and increasing resistance as peak potentials are continuously shifted by 10 mV. Additionally, the phase transformation from M to H2 and M to H1 are clearly visible and unchanged from the densification process.

Gas Evolution as a Function of Electrode Compaction

Figure 53C summarizes the released gasses after the first charging process, depicted at the end of the charge phase at a cell voltage of 4.8 V vs. Li/Li^+ from the various compacted electrodes in terms of released gas per gram material ($\mu mol \cdot g^{-1}$). Carbon dioxide is the main evolving gas, accompanied by CO and O_2, when charging a half-cell to such high potentials. *Freiberg et al.*[246] and others[223] have shown that the decomposition of Li_2CO_3 occurs at 4.6 V vs. Li/Li^+ in the presence of protons or other protic species like HF, as depicted in Equation (5.6). The active material used within our work comes along with impurities of 0.12 % wt. Li_2CO_3, which causes $\approx$ 15 $\mu mol \cdot g^{-1}$ of CO_2. The expected amount of CO_2 due to electrochemical breakdown of the carbonate is indicated by the vertical dashed line within the bar graph.

$$Li_2CO_3 \ + \ 2\ H^+ \rightarrow 2\ Li^+ \ + \ CO_2 \uparrow \ + H_2O \tag{5.6}$$

Alternatively, the electrochemical oxidation of Li_2CO_3, shown in Equation (5.7), has been described in several reports.[223,246,247] However, the gas analysis within these studies found exclusively CO_2/CO and the evolution of O_2 had not been observed. Our studies provide no indication that this reaction is taking place either, as the release of O_2 was only detected within non-compacted or lower-compacted electrodes.

$$Li_2CO_3 \rightarrow 2\ Li^+ \ + \ 2\ e^- \ + \ 1/2\ O_2 \uparrow \ + CO_2 \uparrow \tag{5.7}$$

On the other side, the formed water within Equation (5.6) can be electrochemically reduced ($2\ H_2O \ + \ 2e^- \rightarrow H_2 + 2\ OH^-$)[39] and the resulting hydroxide ion reacts subsequently with the ethylene carbonate to form CO_2, see Equation (5.8).

$$OH^- \ + \ EC \rightarrow \ CO_2 \uparrow \ + EG^- \tag{5.8}$$

Indeed, all measurements revealed a H_2 content of $\approx$180 nmol. The formed water within Equation (5.6) can furthermore react with the NMC material and cause carbonate formation, which subsequently reacts again, according to Equation (5.7).

Reaching higher cell voltages, the release of highly reactive singlet oxygen ($O_{lattice}$) due to the NMC phase transformation becomes more feasible, as shown by *Jung et al.*[81] The structural transformation from a layered towards rock-salt type (see Equation (5.1)) causes the electrochemical oxidation of ethylene carbonate (EC), as shown in Equation (2.7).

$$4\ O_{lattice} \ + \ EC \rightarrow 2\ CO_2 \uparrow \ + CO \uparrow \ + 2\ H_2O \tag{5.9}$$

The formed singlet oxygen can however also react with another singlet oxygen species to form molecular oxygen, according to Equation (5.10).

$$2\ O_{lattice} \rightarrow O_2 \uparrow \tag{5.10}$$

In general, the mesh electrode and non-compacted sample provide most O_2. The total amount of released gas (CO + CO_2 + O_2) increases from 25.0 µmol·g^{-1} (95 nmol mA·h^{-1}) for the mesh electrode up to 28.9 µmol·g^{-1} (113 nmol mA·h^{-1}) while simply using the laser-perforated current collector with no compaction pressure. A compaction with 10 kN·cm^{-2} results in the release of 23.9 µmol·g^{-1} (104 nmol mA·h^{-1}). Further compaction results in the complete loss of the former detected O_2 and a general lower amount of the detected gases (CO_2 and CO). A compaction of 30 kN·cm^{-2} results in 18.0 µmol·g^{-1} (82 nmol mA·h^{-1}), while a compaction with 50 kN·cm^{-2} provides 16.1 µmol·g^{-1} (80 nmol mA·h^{-1}).

The depicted data clearly show that with increasing electrode density and hence decreasing charge capacity, less gas is being released. With higher coating density, less surface area and subsequently fewer side reactions between the CAM and electrolyte interface might occur. The data also indicate that assuming a well-distributed amount of Li_2CO_3 in each electrode sample, with higher compaction, the amount of gaseous side-products is reduced, probably due to the fact, that some portion of the Li_2CO_3 is being closed off in inaccessible pores. In line with that is the evolution of CO as this species is exclusively formed according to Equation (5.9). Hence, with increasing electrode density and an assumed reduced surface area, less electrolyte decomposition due to reactive oxygen attack via Equation (5.9) occurs.

Part D of Figure 53 shows the voltage-resolved evolution of CO_2 for the different electrode samples, already described in Figure 6A. The depicted data clearly shows, that with increasing compaction, the release of CO_2 needs longer, as the gas diffusion is probably hindered by the compaction of the material. For the mesh coating and non-compressed sample, a relatively sharp peak up to 430 nmol·min^{-1}g^{-1} ($\approx$ 10.8 nmol $\cdot$ min^{-1}) can be observed, which is very similar to the 10 nmol $\cdot$ min^{-1} detected by *Kaufman et al.*[223] For higher compaction pressures an ever increasing smearing out effect can be observed. Hence, the gases need longer to evolve from the coating, when the compaction is being increased. The SEM sub-Figure G within Figure 51 visualizes these circumstances, where the coating and a laser-perforated hole are depicted to imagine the rather long diffusion distance within the coating.

As the gases are trapped within the electrode sandwich, longer reactions times and hence subsequent reactions, like Equation (5.6 or 5.8), become more feasible. Additional reactions might also produce CO_2, as it always serves as thermodynamic sink. Addi-

tionally, the data indicate, that some portions of the CO_2 might be exclusively released during the discharge process, i.e. when the NMC materials get lithiated again. Here, the re-intercalating Li-ions might push out the gas molecules from the lattice structure. Analyzing the CO_2-peak during the second cycle, it can be concluded that less CO_2 is evolving for all samples. This strengthens the assumption that the majority of CO_2 within the first cycle stems from Li_2CO_3 decomposition or other, e. g. rock-salt surface reconstruction reactions.

The Release of Oxygen, Influenced by the Degree of Compaction

As it was described in the above paragraph, the diffusion path and therefore the time release of the gases strongly depend on the current collector and degree of densification of the electrode. This is particularly important for the release of single lattice oxygen at high degree of delithiation ($>$ 4.3 V vs. Li/Li^+). Figure 6C already showed that molecular oxygen (O_2) was detectable for the mesh configuration and tremendously reduced for the foil-coated electrode.

Figure 54 provides a detailed time- and potential-resolved view of the O_2-release for the differently compacted electrodes. Firstly, it is visible that the release of oxygen appears due to the H2→H3 phase transformation as explained in Figure 6B. Secondly, and more important, the nature of the substrate (mesh or foil) and the degree of densification influence the amount and the response of the O_2-release from the electrode. Here, the mesh sample shows the highest amount (0.8 µmol g^{-1}) of released O_2 and exhibit a well-pronounced gassing behavior according to the electrochemical protocol and underlying phase-transformation, as indicated through the dashed lines in Figure 54.

The non-compacted laser-perforated sample results in a decay of 75 % (0.2 µmol g^{-1}) of the amount of O_2, compared to the mesh sample, as also shown the bar graph in Figure 6C. Further compaction results in an ever weaker rising oxygen value over time. However, it is assumed that the O_2, as well as other gases, might be trapped within the electrode sandwich and CAM coating, respectively as it was discussed for the CO_2 mass-trace in Figure 6D. The mass-traces for each measurement were carefully analyzed to ensure, that no oxygen diffusion from the outer atmosphere was leaking in. As it can be seen in the time slot between 8-10 hours, all mass-traces were either decreasing or rather constant ensuring proper tightness of the setup. In the case of a moderately compacted electrode (10 kN $\cdot cm^{-2}$), the particles seem electronically well connected, but the electrode is still porous enough to allow O_2 and other gases to escape easily.

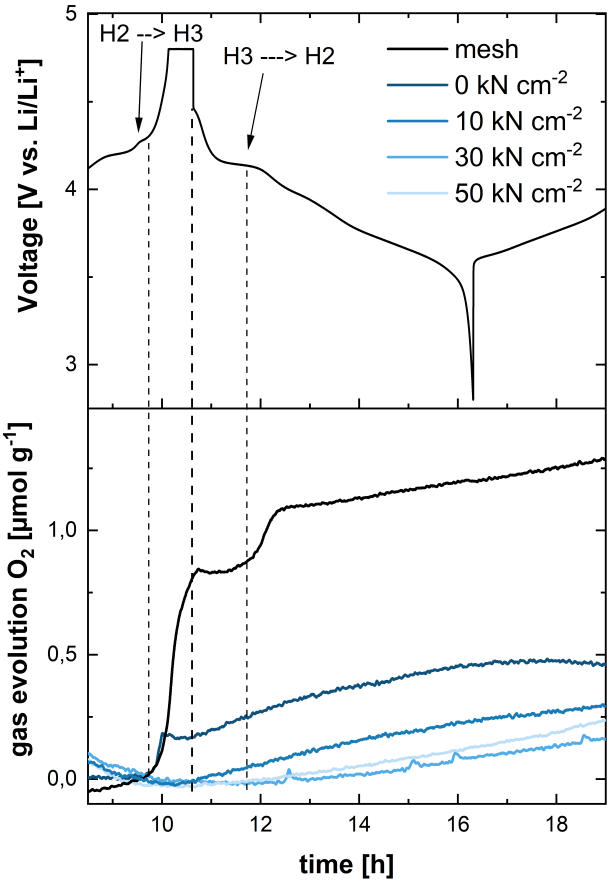

Figure 54: Top: Cell voltage within the first charge cycle (C/5) at 30 °C. Bottom: Gas evolution of O_2 for different compacted electrode samples. The horizontal dashed lines indicate the NMC phase transformation from H2 → H3 and vice versa, as well as the end of the CV phase (middle line), which was used for the data shown in sub-figure C of Figure 6.

In order to prove how the gas evolution depends on the diffusion within the differently compacted electrodes, similar experiments were carried out while flipping the electrode into the so-called open head-space configuration, which is presented in the following part.

III. Influence of Electrode Densification within an Open Half Cell Configuration

Figure 55 shows the time- and potential resolved gas evolution of O_2, CO and CO_2 between 4.2 - 5.0 V vs. Li/Li^+ for a non (0 kN*cm^{-2}), medium (10 kN·cm^{-2}), and strongly (50 kN·cm^{-2}) densified electrode. A rather slow charging procedure (C/200) was carried out, as the Li^+-transport through the laser-perforated Al current collector is limited by the perforation, while the active material is facing towards the cell head space. Consequently, the current has to be transported from the spring to the particles themselves.

Degradation Behavior $<$ 4.7 V vs. Li/Li$^+$

In the voltage regime between 4.2-4.7 V vs. Li/Li$^+$, the electrodes behavior looks quite similar and is therefore referred to section 3.2.1. Besides the electrochemistry, a linear increase of all gases can be seen and can be assigned to the continuous breakdown of Li_2CO_3, as shown in Equations (5.6 & 5.7). The non-compressed electrode shows significantly higher amounts of all analyzed gases, specifically that of CO_2 and CO, likely formed via Equation (5.9). This might be the result of the high porosity and hence increased amount of accessible carbonate impurities, which are then decomposing. The other electrodes have a significantly reduced porosity compared to the non-compacted one. Furthermore, a higher O_2 value is detected for the non-compacted electrode, which again suggests that a strong particle polarization causes the release of O_2 at certain domains within the coating.

Degradation Behavior $>$ 4.7 V vs. Li/Li$^+$

In the voltage region $>$ 4.7 V vs. Li/Li$^+$, some differences can be clearly seen in the electrochemistry regarding to the electrode densification. Here, the medium compression seems to promote a more pronounced voltage plateau and hence phase transformation, respectively, than the non-compacted or strongly compacted one. The $dQ \cdot dV^{-1}$-analysis (see Figure 59 in SI) exhibit a well pronounced peak for the medium-compacted sample at 4.85 V vs. Li/Li$^+$.

When the cell voltage reach 4.7 V vs. Li/Li$^+$, the earlier described electrochemical oxidation of ethylene carbonate starts. Indeed, above this threshold, a simultaneous and exponential increase of all gases can be seen. The electrochemistry shows that this happens in accordance to the NMC phase transformation, where the release of oxygen from the NMC lattice occur. The order of detected molecular O_2 follows hereby the same order as the intensity of the high-voltage plateau. A moderately compressed electrode shows the highest amount of released O_2 and the strongest high voltage plateau. Furthermore, the slope of the oxygen mass trace is clearly enhanced in case of the medium compacted one, in comparison to the other compressed electrodes.
The non-compacted electrode shows less pronounced characteristics regarding O_2-release and high voltage plateau. It is likely, that due to particle polarization, some domains release their reactive oxygen at lower potentials, confirmed through the higher background signal. The densified electrodes meanwhile, have a lower O_2-threshold in lower voltage regions. However, their strong increase of molecular oxygen, indicates that the gas is formed relatively quickly, and a large portion of the reactive oxygen atoms will react via Equation (5.10) forming molecular oxygen. This might be an indication, that less EC is available under these circumstances.

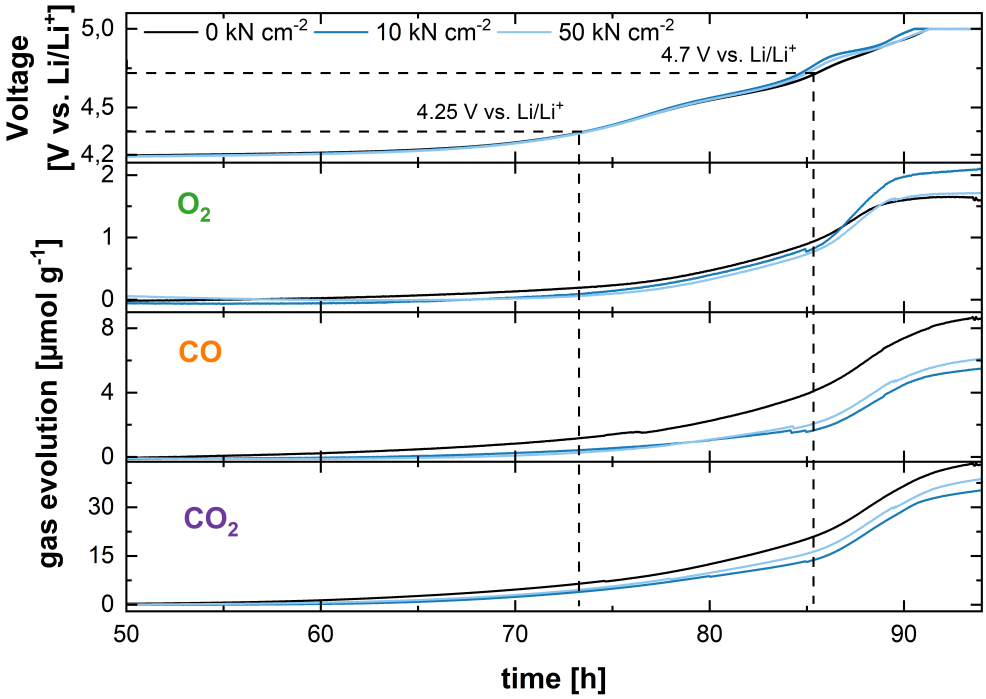

Figure 55: Time-and potential-resolved view of the partial gas evolution of O_2, CO, and CO_2 for non-(black), medium-(dark blue), and strong-(light blue) densified electrodes. Delithiation in the range of 3.95 up to 5.0 V vs. Li/Li^+ was performed at 30 °C with a rate of C/200, first 50 h and the delithiation up to 3.95 V vs. Li/Li^+ wit C/20 are not shown here. The dashed lines indicate a cell voltage of 4.25 and 4.7 V vs. Li/Li^+, respectively.

In terms of CO- and CO_2 evolution, the non-compressed electrode shows a significantly higher amount of both gases (51 µmol·g^{-1}), while, the compressed electrodes release more gas in the higher voltage region (stronger slope > 4.7 V vs. Li/Li^+). Especially CO is nearly halfed when the electrode is being compressed. The medium-compressed electrode releases less gas (40 µmol·g^{-1}), than the higher-densified electrodes (45 µmol·g^{-1}). This might be an indication that due to the applied pressure, more particles are cracked, as confirmed by SEM, and hence there is more exposed surface area that can facilitate side reactions. However, the differences are small, as one would expect significantly more gas after particle cracking. The behavior of both gases and their relation towards densification led to the conclusion that for densified electrodes Reaction (5.9) plays a crucial role. This particular makes sense, as within a highly densified electrode, where all pores are filled with electrolyte (EC), the reactive oxygen has a high probability to react in accordance with Equation (5.9). The strong kink in the oxygen evolution as observed in Figure 55, is mirrored by the form and shape of both other gases, indicating that their evolution has the same origin, as described by *Jung et al.*[81,86]

In conclusion, it can be said that the gas evolution increases with increasing electrode density. The evolution of CO_2 was found to correlate linearly with the applied pressure, indicating that due to compression the most parasitic reaction can be stopped. The

reaction, shown in Equation (5.10) is unlikely, as somehow two oxygen from nearby have to directly meet without any other interference, whereas the 4 $O_{lattice}$ reaction (Eq. 5.9) is more likely as oxygen diffuses within the EC_{only}-electrolyte and rather stable intermediates are formed.

5.6 Conclusion

Herein, the influence of electrode densification of poly-crystalline NMC955-electrodes onto their electrochemical behavior was studied by the use of online electrochemical mass spectrometry. Analysis was applied using laser-perforated current collector foils, to investigate the effect of calendering, while allowing proper gas and Li^+-diffusion. OEMS Li-half-cells were built in two configurations were the CAM coating was either facing towards the separator interface or the head space of the model cell to mimic a realistic setup or enhanced gas evolution. Analysis and comparison was also applied to common used mesh-coatings.

Static compression of the foil-coated electrodes revealed the expected behavior in terms of decreasing porosity and electrode thickness, while an increase in the coating density with increasing compaction pressure was detected. The electrodes microstructure was thereupon characterized using SEM. Here, non-compacted foil- and mesh-electrodes revealed a loosely bonded coating film with an extensive pore network. Applying moderate pressure was found to reduces the pore size and extent of the pore network. Larger applied pressure revealed the begin of particle breakdown of smaller and medium NMC particles and the penetration of larger particles into the current collector.

Analysis of the electrochemistry within a closed half-cell configuration, while delithiating the NMC up to 4.8 V vs. Li/Li^+ revealed a strong dependence of the cells capacity on the degree of compaction. It is assumed that particle polarization, diffusion and therefore resistance are influenced by the degree of compaction. The online measured gas evolution showed reduced amount of gas for densified electrodes, as the porosity is getting reduced, while compacting the electrode. A large portion of the released gases stems from Li_2CO_3 impurities. Nevertheless, especially for porous electrodes significant amount of other gases were detected. The detection of molecular oxygen, formed due to the NMC phase transformation was possible for mesh- and non-compacted electrodes. Hence, electrode compaction seems to impact the degradation reactions as the pores are filled with electrode and hence reactive oxygen starts a degradation cascade on the ethylene carbonate, rather then to evolve as molecular oxygen.

Studying the NMC-phase transformation in an open half-cell configuration, while delithiating up to 5.0 V vs. Li/Li^+ revealed that the non-compacted electrode results in more CO and CO_2 -release, while a moderate compression seems to promote the formation of molecular oxygen, while forming a minimum on other gases. This rather low degree of compaction revealed a relatively similar behavior in terms of response characteristics and gas release, than the highly porous mesh coated electrode showed. Hence, the inter-particle contact seems to be well established, while the high porosity still allows the formation of molecular oxygen due to excellent gas diffusion.

Apart from novel insight into the compaction dependent gas evolution within electrodes, our approach provides unique opportunities to further optimize LIB´s production processes and improvement in regards of safety. Additionally, it was shown that OEMS as novel in-operando technique, can be used to investigate the impact of even single process steps within LIB production and their time-resolved impact onto the electrochemical degradation behavior.

5.7 Extra material

A) Laser Perforated Current Collector

A manually laser perforated current collector foil was used, in order to study the impact of the calendering on the cell performance. Holes were needed in order to allow gas diffusion in to the cell head space as well as to allow lithium ions to diffuse within the bulk liquid electrolyte. Perforation was done using a 5 W laser marking system (AI0 G+ 532 nm, Östling, Germany) with the laser set to 70 % power; 10,000 shot frequency and a scan speed of 100.

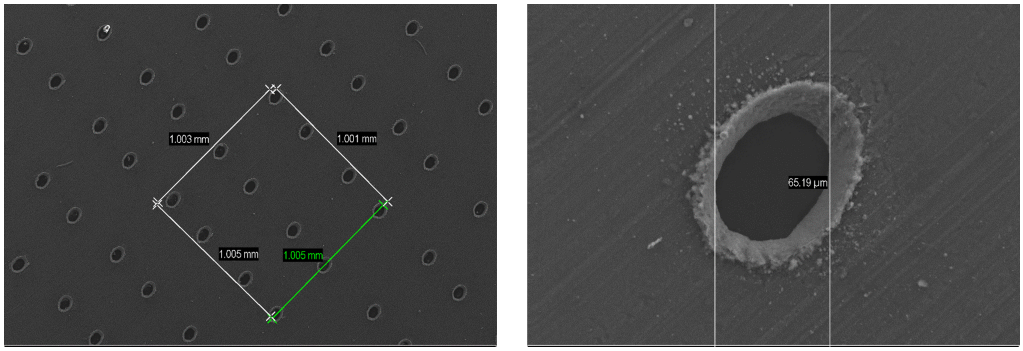

Figure 56: SEM top view image of the laser perforated current collector, used within this work. The current collector is coated with a carbon layer, to allow the absorption of the laser beam for perforation. Following that, the CAM coating can be done.

The holes had an average diameter of 65 µm and the current collector had an equal distribution of 6 holes per mm^2. In order to find an adequate charging current, the hole to surface area ratio was determined, see Equation (5.11)

$$\frac{\mathrm{A_{surface}}}{\mathrm{A_{hole}}} = \frac{1mm^{\ 2} - 0.0205mm^{\ 2}}{0.0205\ mm^2} = 47.7 \approx 50 \tag{5.11}$$

B) Voltage Profiles for the First two Full Cycles for Various Compacted Electrode Samples

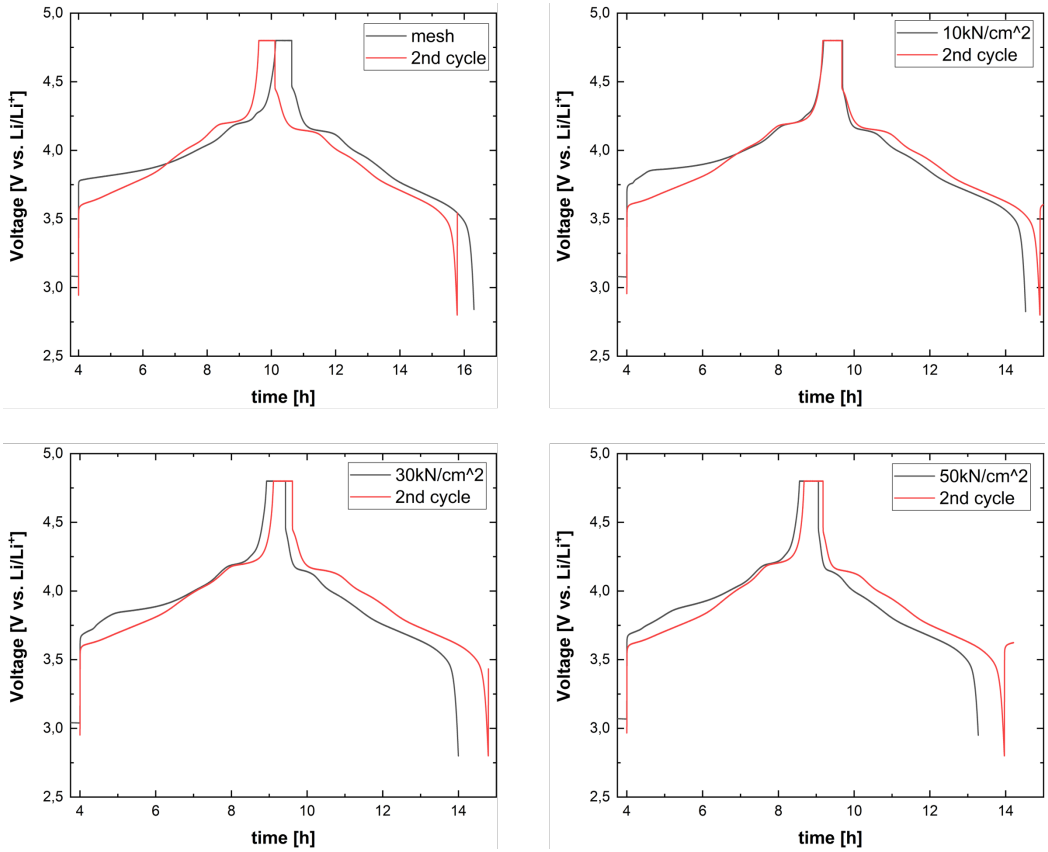

Figure 57: Voltage profiles for the first (black) and second (red) full cycle with a charging current of C/5 at 30 °C in EC_{only}-electrolyte. Shown for mesh current collector (top left); laser-perforated current collector densified with 10 kN·cm^{-2} (top right); 30 kN·cm^{-2} (bottom left), and 50 kN·cm^{-2} (bottom right).

C) Composite Volume Resistivity

The resistivity of the electrode coating was determined post-mortem. Therefore, an electrode resistance measurement system RM2610 (Hioki E.E. Coperation, Tokio) was used. In order to do so, the electrodes were carefully extracted from the OEMS cell after the electrochemical experiment within glovebox conditions. Next, the electrodes were washed with DMC within the glovebox and dried within the evacuation chamber of the glovebox for 1 h. For the resistivity measurement, the electrodes were then transferred into the dry-room. The device differentiates between the resistance in the coating volume and the contact resistance between the electrode coating and the current collector foil. For this purpose, a constant current is applied to the electrode and the voltage distribution is measured at 11 different points on the surface.

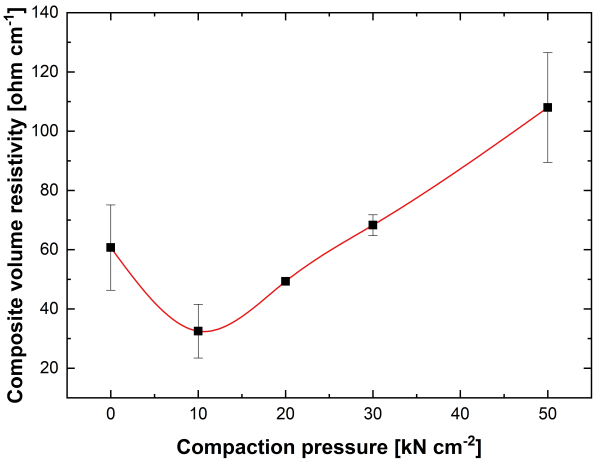

Figure 58: The composite volume resistivity for the different compacted electrodes. Line is drawn to guide the eyes. Each electrode was measured on six randomly chosen point within the individual electrode disc.

D) Differential Voltage Analysis Within the Open-Cell Configuration

Figure 59 shows the differential voltage analysis (dQ dV^{-}1) for the experiments under open cell configuration. Same characteristics as shown in the sub-figure C of Figure 53. The rather small peak at 4.0 V vs. Li/Li^{+} is due to phase transformation from hexagonal (H2) to mono-clinic phase (M). The main peak within this diagram occurs at 4.2 V vs. Li/Li^{+} and indicates the H2 to H3 phase transformation. Surprisingly, the peak at 4.85 V vs. Li/Li^{+} shows something for an applied compaction pressure, while so significant changes can be seen for the non-compressed sample. The 30 kN sample shows the appearance of a shoulder at a half-cell voltage of 4.2 V vs. Li/Li^{+}.

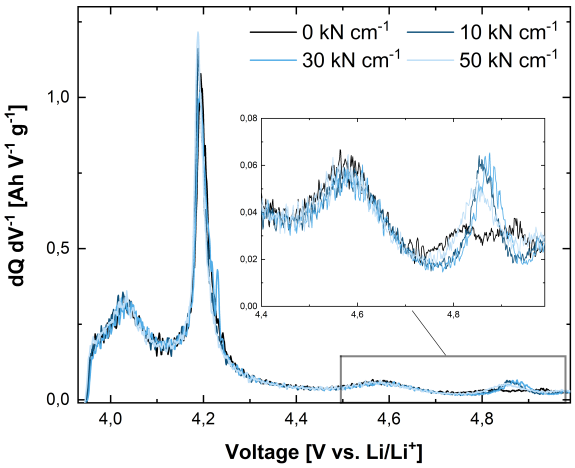

Figure 59: Differential voltage analysis (dQ dV^{-}1) within the closed-cell configuration while using different compaction pressures.

Gas Evolution in Large-Format Automotive Lithium-Ion Battery during Formation: Effect of Cell Size and Temperature

6.1 Motivation

In this section the article "Gas evolution in large-format automotive lithium-ion battery during formation: Effect of cell size and temperature" will be presented. As it was shown in section 2.7, there were several OEMS setups developed over the last years, dealing with the challenge of in-operando investigations on large-format cells . However, besides all these custom-made connection systems and their proof-of-concept studies, the investigated cells were always purchased from a supplier and occasionally the composition of the battery materials was even unknown. Besides, the uncertainty of the used materials, the gas evolution within one cycle under normal cell operation is assumed to be rather low. On the other side, the gas evolution during first charge, when the SEI is being formed is accompanied by a large gas evolution. This procedure is typically carried out by the battery supplier and is therefore of great interest for the academia society. Within this section, the formation of prismatic 72 Ah cells was carried out on our OEMS system and presents therefore the first ever known reported time-resolved gas evolution due to SEI formation within large format cells. Further studies on the liquid electrolyte as well as the negative electrodes where used to complete the found trends.

This chapter has been published in: J. Scharf, C. von Lüders, F.-M. Matysik, C. Misiewicz, J. Wandt, E. J. Berg, Gas Analysis of Large-Format Automotive Lithium Ion Battery Cells during Formation: Effect of Cell Size and Temperature, J. Power Sources, 603, 234419, **2024**.

Keywords: Li-ion batteries • Automotive cells • Gas evolution • Online electrochemical mass spectrometry • Cell formation

6.2 Abstract

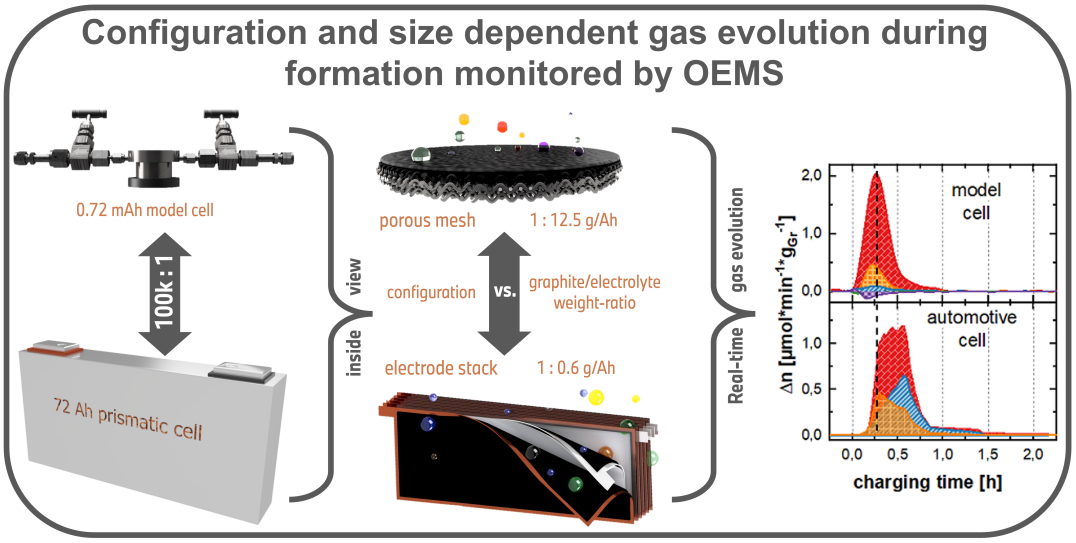

Figure 60: Graphical abstract for the embedded chapter in this work dealing with the in-operando gas analysis on large-format prismatic cells during formation and the effect of cell size and temperature.

Optimization of cell formation during lithium-ion battery cell (LIB) production is needed to reduce time and cost. *Operando* gas analysis can provide unique insights into the nature, extent, and duration of the formation process. Herein we present the development and application of an online electrochemical mass spectrometry (OEMS) design capable of monitoring gas evolution and consumption in both model coin-cells (Q = 0.72 mAh) with a graphite/electrolyte weight-ratio of 1:12.5 and large-format Li-ion cells (Q = 72 Ah) with a graphite/electrolyte weight-ratio of 1:0.63 during operation. Although the composition and amounts of gas are highly comparable, even when validated against *ex-situ* analysis, the gas release rate is lower from the larger cell size and likely limited by gas bubble transport through the electrode stack of the cell during formation. Higher temperatures accelerate the formation process, but also alters the composition and extent of gas released. Apart from providing novel insights into the formation processes of large-format Li-ion cells, our OEMS setup offers an opportunity for the battery manufacturing and automotive industry to explore the impact of battery formation and/or operating conditions on gas evolution in next-generation Li-ion batteries of any size.

6.3 Introduction

Meeting the climate goals of the Paris Agreement within the European Union requires significant reductions in CO_2 emissions from the transportation sector.[248] One important solution is the use of LIB based electric vehicle (EV)). However, the LIB is currently the most expensive single component integrated in an EV.[204] Considerable progress has been made towards LIB optimization through active material development, as well as electrode- and battery pack design in recent years.[144,249] As consequence, numerous gigafactories are announced or already being constructed to meet the demands of the market for environmentally sustainably produced LIBs for next-generation EVs.[250] Despite this progress, primary challenges remain in reducing the manufacturing cost of each LIB.

One of the most cost intensive process steps during production is the time each LIB spends under dry room conditions, that relying on energy intensive dehumidification processes. Unfortunately, these conditions are indispensable due to the presence of water-sensitive components, such as electrolyte and active materials.[159,212,251] The major bottleneck within dry room production steps is the initial charging process, known as formation, during which the liquid electrolyte is filled into the cell casing and the cell galvanostatic dis-/charged to form the solid electrolyte interface (SEI). In this process, the electrolyte is electrochemically reduced forming gaseous (such as hydrogen (H_2), ethylene (C_2H_4), carbon monoxide (CO) and carbon dioxide (CO_2)[129,212]), liquid, and solid products, among which only a few of the solid products are desired to constitute the SEI layer on the negative electrode.

The SEI is critical in ensuring optimal lifetime of the LIB and multiple reviews have examined the impact of SEI composition on the overall cell performance.[118,149–151] Currently, no standard formation procedures have been established, as each manufacturer has their own recipe for optimizing the process based on specific LIB configuration and intended applications, such as high power or high energy. The formation protocol usually includes slow charging and discharging procedures, which can last for several hours to days and involve electrolyte wetting and aging steps. Consequently, the formation process can occupy up to 25 % of the floor space in dry rooms, leading to significant manufacturing costs.[144,145] Hence, investigations of so-called fast formation procedures have been intensified in order to enable affordable cell production in Europe.[152] Fortunately, several publications have shown that higher current rates can decrease the formation time without sacrificing the efficiency of LIBs.[146,147]

Additionally, dividing the initial charging process into sections is another feasible approach. Splitting the first part of the formation process, i.e. when the cell needs to be opened to release the gases formed, from the rest, i.e. when the cell might as well be

sealed, time and space could be further optimized. After the electrolyte is sufficiently reduced and most gas generation has halted, the cell is sealed and relocated from expensive dry room environments to complete the formation. The study presented herein therefore investigates how this processes can be further improved, namely by studying the impact of temperature on gas release during formation. Temperature effects gas evolution because of its influence on physical characteristics like gas solubility,[211] reaction kinetics and molecular transport properties.[252] Tuning temperature is one of the most technically feasible options as the design space is very limited in cell production.

In this perspective, a time-resolved examination of voltage related gas evolution is valuable. Apart from determining when the formation gassing stops and the extent of it, the gases released during the initial stages of a battery's lifespan also offer crucial insights into internal molecular processes. Gas analysis of batteries is a proliferate field of research with numerous developed methodologies, such as combining Li-ion cells with pressure sensors,[116] cell buoyancy tests,[180] external force measurements,[253] and more advanced techniques like online electrochemical mass spectrometry (OEMS).[159,174,176]

OEMS has hitherto been proven most powerful to determine not only the onset and extent of gas evolution, but also the internal composition under *operando* conditions. Regardless of the gas analysis methodology, most investigations have focused on small model Li-ion coin-cells containing only a few milligrams of battery materials. These allow the investigations even down to a single electrode material level, without the interference of any extraneous gases, e.g. oxygen.[159,174,176] In this scenario, the gas evolution usually falls within the micro-litre range, while using small electrodes (diameters of a few millimeters). Additionally, the electrolyte is often used in excess amounts, with a ratio of m_{Ely} to $m_{Gr} \approx 1{:}0.1$.[251] This contrasts with automotive cells, where much less electrolyte m_{Ely} to $m_{Gr} \approx 1{:}3$ is typically employed.[114,254]

Therefore, *Schmiegel et al.*,[182] *Misiewicz et al.*,[129] and *Mattinen et al.*[183] have developed OEMS for gas analysis during cycling of larger cells, including pouch, prismatic, and cylindrical ones. However, in the above mentioned publications, the large-format cells already underwent formation, hence a minor gassing is being expected during the normal cell operation. On the other hand, the formation process generates a significant amount of gas over a short period of time. To our knowledge, the gas evolution during the formation of large-format cells has not been reported before and is therefore of significant interest.

Herein, we present an OEMS system that can be deployed with both model coin-cell and large-format automotive cell arrangements in order to monitor gas evolution, especially during initial cell formation. By using the same cell chemistry to compare both cell setups, we highlight the extent to which results from coin cells correspond with gas evolution in practical cells. Furthermore, we validate the setup by employing an established offline gas chromatography (GC) system to analyze the collected gases from large-format cells. From an industrial perspective, temperature is identified as a critical factor influencing the gas release of large-format cells. The influence of cell temperature (ranging from 10 °C to 40 °C) during formation is investigated in order to understand its impact on gas evolution rate and composition. Our study contributes towards utilizing OEMS as an advanced *operando* technique in industrial battery research on large-format LIBs.

6.4 Experimental

I. Setup

The herein described OEMS system is mainly inspired by the work of *Tsiouvaras et al.*[176] and is primarily composed of three main components, that are schematically depicted in Figure 61.

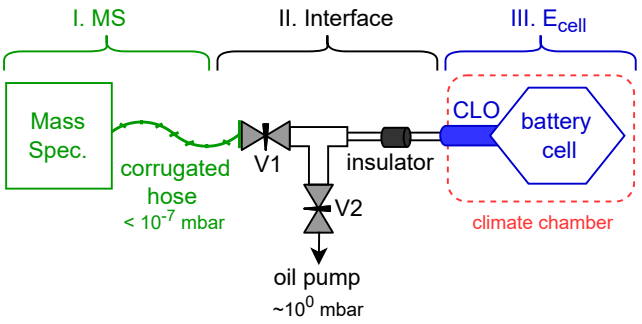

Figure 61: Schematic representation of the OEMS setup used within this work.

The first component is a quadrupole mass spectrometer (MS; QMA-400, Pfeiffer Vacuum, Germany) equipped with a Faraday detector and a scanning electron microscopy (SEM) to identify species with a mass-to-charge ratio of 1-200 amu. Molecules undergo electron ionization (EI) which uses 70 eV ionization energy. The second component, known as the interface region, connects the ultra high vacuum (UHV) region of the MS to the cell (3rd part). The interface comprises a 1/4" VCR-T-union (Swagelok®, USA), a ceramic electric isolator (VCR-FF-KR13, 132 mm, U_{max}= 13 kV, Vacom Messtechnik, Germany) and two 1/4"-VCR-valves (SS-4BK-VCR). The isolator prevents electrical

interactions between the cell and the sensitive MS environment. The electrochemical cell is connected to the electric isolator via a calibrated crimped-capillary leak open (CLO; Vacuum Technology Inc., USA). The crimped capillary leak open (CLO) enables a single-stage pressure reduction, resulting in a defined gas flow of ≈ 1 µL*min^{-1} (leakage rate = 1*10^{-8} mbar*L*s^{-1}) from the headspace of the cell, which then flows to the MS ionization chamber. Both, the CLO, and electrochemical cell function within a controlled climate chamber (Type: T-40/25/S, CTS GmbH, Germany), where they are situated. The working pressure in the UHV-regime is achieved by utilizing a turbo-molecular pump (HiPace300, Pfeiffer Vacuum). Pressure is measured using a pirani cold cathode gauge (PKR-360, Pfeiffer Vacuum), which records a pressure of lower than 1*10^{-10} mbar when V1 is closed, and roughly equal to 1*10^{-7} mbar during measurements.

II. Model Cell

The model cell used in this study is designed in a coin cell configuration and represented on the left-hand side of Figure 62. The required cell components were sourced from *Lundström et al.*,[159] although modifications were made to the fittings between the cell body and the MS, as well as to the gas inlets. To flush and calibrate the cell, two 1/4"-VCR needle valves (SS-3NBVCR4, Swagelok®, USA) were used as gas inlets and outlets. Additionally, two glands on the lid's top face were incorporated to allow for a connection to a pressure transmitter (PAA-33X, Keller Druckmesstechnik, Switzerland) and for the CLO to probe the headspace of the cell. All components were welded or made of VCR-Swagelok face seal fittings.

Electrode Manufacturing

The negative electrode was created by preparing a 3.70 wt. % solution of polyvinylidene fluoride (PVDF, Solef 5140, Solvay Belgium) mixed with N-methyl-2-pyrrolidone (NMP, anhydrous, 99.5 % Sigma-Aldrich) for 12 h at room temperature. Super C65 (IMERYS, Switzerland) was then added (1.20 %) and the mixture was stirred for 30 min in a planetary orbital mixer at 2000 rpm (Thinky Are 250, USA). Following this, 95.1 wt. % graphite powder (SMG-A5, Hitachi, Japan) was added and mixed for 10 min at 2000 rpm. The slurry (solid content: 50 %) was applied to a stainless-steel mesh (0.212 / 0.090 mm, Spoerl KG, Germany) using a 150 µm gap applicator. For the positive electrode, a slurry with a solid content of 70 % was created by mixing 96.0 wt. % NMC811 (Umicore, Belgium), 0.20 wt. % BM-730H (Zeon, Japan), 1.80 wt. % Solef 5140 (Solvay, Belgium) and 2.0 wt. % LITXHP (Cabot Corporation, USA). The slurry was applied to a 15 µm aluminum foil (Norsk Hydro, Norway). Both coatings were first dried in a ventilated oven at 100 °C before being punched into 16 mm (negative electrode) or respectively 14 mm (positive electrode) discs. The electrodes and separator (10 µm, ⌀ = 16 mm, Shenzhen Senior Tech., China) were further dried for 24 h under dynamic

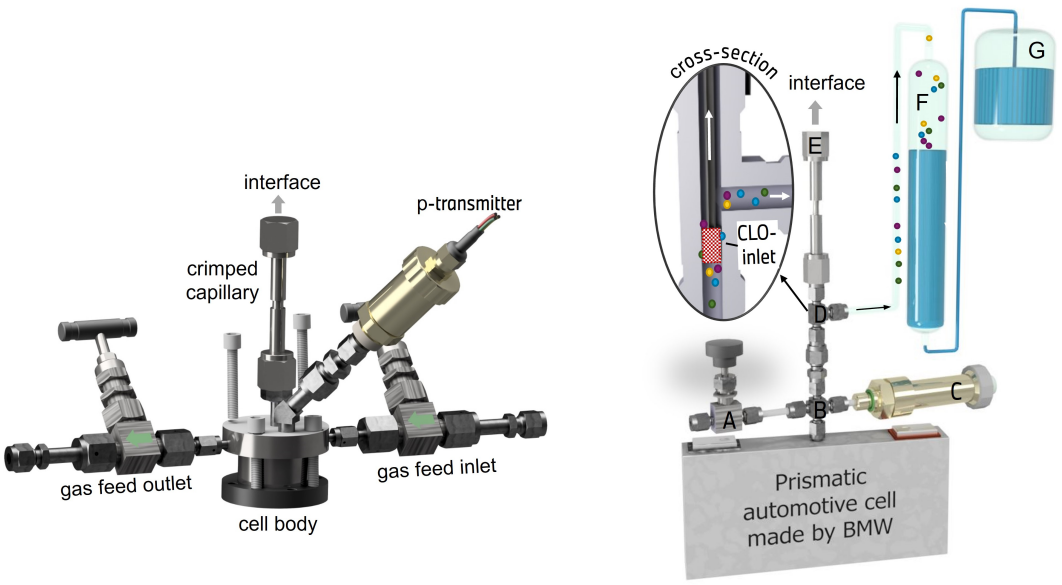

Figure 62: Left: Schematic representation of the model cell used within this work, consisting of a cell body and an electrical insulated lid part. Latter one has two valves for gas feed in & outlet and two welded glands for the connection of a pressure transmitter and a crimped capillary. **Right:** Schematic representation of the automotive cell setup. A) Swagelok vent for flushing the headspace before F is connected. B) VCR-cross union sealed with a FFKM-O-ring towards cell. C) p-transmitter. D) VCR-T-union with connection towards a 500 mL gas buret (F) and the embedded CLO (E). The gas buret is initially filled with silicon oil and connected towards an oil reservoir (G) for isobaric conditions.

vacuum (Büchi, Switzerland) at 120 °C and 60 °C respectively. The electrode loadings were $m_{Gr} = 10.36 \pm 0.13$ mg*cm^{-2}($\equiv$ 3.85 mAh*cm^{-2}) for the negative electrode and $m_{NMC} = 18.9 \pm 0.03$ mg*cm^{-2} ($\equiv$ 3.82 mAh*cm^{-2}) for the positive electrode. Considering the different first cycle irreversible capacities of the active materials, these area capacities results in a N/P ratio of slightly above 1.00.

Assembling

Before assembly, all pieces of cell hardware were dried at 110 °C on a heatplate in a glovebox atmosphere (MBraun, with H_2O & $O_2 < 1$ ppm) for 12 h. Once cooled, a positive electrode was placed at the bottom of the cell cup, followed by the separator and the negative electrode. A total of 200 µL electrolyte (ethylene carbonate / diethyl carbonate 1:1 + 1 M $LiPF_6$, Sigma Aldrich) was added between the layers. This results in a electrolyte to graphite weight-ratio of 1:12.5 (36 g/Ah). The cell lid and bottom were electrically separated using a flat 1 mm PTFE-gasket (Resogoo GmbH, Germany). Electric contact of the electrodes was established by using a stainless-steel spring (Sodemann Industrifjedre, spring constant: 1.86 N/mm). The cell was sealed by attaching the lid, pressure-transmitter, and CLO to the cell body. The cell was then carefully transferred from the glovebox to the OEMS setup. The volume of the model cell was determined to be 6.7 mL.

Operation & Calibration

The model cell is connected to the MS through the insulator-/ CLO-interface. An oil pump (via V2) is used to minimize the gas ballast before opening V1 towards the MS. After evacuation, the cell headspace was flushed with argon (99.999 %, Rießner Gase GmbH, Germany) for 3 minutes with a flow rate of ≈ 50 mL*min^{-1} to eliminate any residual gases. The cell was then left under open circuit voltage (OCV) for 4 hours to achieve a stable background signal for each mass channel. galvanostatic cycling with potential limitation (GCPL) was then conducted using a SP-300 potentiostat (BioLogic, France), controlled by EC-Lab software. The cell was charged at a C/10-rate, corresponding to the theoretical capacity of the negative electrode.

To eliminate any signal fluctuations due to minor pressure and temperature changes, all mass signals (I_z) were normalized to the ^{36}Ar isotope and denoted as (I_z/I_{36}^{Ar}). Ion currents were then converted to concentrations using calibration factors (S_x) for hydrogen (m/z = 2), ethylene (m/z = 26), carbon monoxide (m/z = 28), oxygen (m/z = 32) and carbon dioxide (m/z = 44).[209] Therefore, the model cell was initially flushed with Ar and subsequently with a calibration gas mixture (2000 ppm each in Ar) until a stable signal was attained (≈ 45 min). Carbon monoxide had to be recalculated, as ethylene and carbon dioxide both demonstrated a strong contribution on the same mass channel. In this study, the signal intensity of CO arising from gas evolution was estimated using the following formula: $I_{28}^{CO} = I_{28}^{tot.}-(0.14*I_{44}^{CO_2})$ - $(1/0.63*I_{26}^{C_2H_4})$.[209] This formula takes into account the standard fragmentation contributions of carbon dioxide and ethylene to the mass channel 28. The molar gas evolution was then calculated based on ideal gas law using equation (6.1). The molar gas evolution rate Δn was obtained via the first derivative of formula (6.1).

$$n_x = \frac{pV_{cell}}{RT} \cdot \left(\frac{I_x}{I_{36}^{Ar}}\right) \cdot S_x \tag{6.1}$$

III. Automotive Cell

For the second and main part of this study, a 72 Ah prismatic cell with a similar composition to the model cell experiments was used. The cell comprised 40 stacked layers of double-sided coated anode (1.73 m^2) and cathode (1.60 m^2) electrodes, with electrode loadings of $m_{Gr} = 129.7 \pm 2.5$ g*m^{-2} (≡ 4.58 mAh*cm^{-2}) and $m_{NMC} = 202.3 \pm 1.0$ g*m^{-2} (≡ 4.08 mAh*cm^{-2}), respectively. The electrode thickness (double sided) is 202 ± 2 µm for the anode and 157 ± 2 µm for the cathode, respectively. The thickness of the anode current collector foil is 10 µm, whereas the thickness of the cathode current collector foil was 12 µm. Prior manufacturing, a 1/8"-fitting (type: SS-400-6-2, Swagelok, USA) was integrated into the lid compartment. The connection was secured with a locking nut from the inside of the lid and sealed on the outside with a perfluoroelastomeric (FFKM) O-Ring (4*2 mm from COG Pinneberg, Germany).

Cell Preparation and Measuring Principle

After being produced in a dry room atmosphere, the cell was transferred to an argon-filled glovebox and dried on a heat plate for 24 h at 45 °C. Then, 135 g of electrolyte were introduced manually through the swagelok connector, and the cell was left to rest for another 24 hours on the heat plate at the same temperature. The electrolyte to graphite weight-ratio is in this case 1:0.63 (1.8 g/Ah). To ensure the consistency of the filling and resting procedures, a computer tomography (CT) scan was conducted for validation, comparing the manual process to the prototype production line's filling and wetting protocols. The cell was sealed by connecting a 1/8"-VCR-cross (see part B of Figure 62), equipped with a valve (A) and a pressure sensor (C). The CLO (E) is embedded into a 1/4"-VCR-T union (D) in such a way, that the gases evolving from the cell must go around the CLO´s orifice before being collected in a 500 mL gas buret as depicted in the highlighted cross-section of Fig. 62. Stack pressure was applied via two twin stainless-steel plates on either side of the prismatic cell and screwed together, that a lateral movement is prohibited, see[129] for a detailed illustration. After connecting the cell setup to the MS, the headspace was purged with argon through A until stable background signals were obtained. Subsequently, the swagelok tube was connected to the buret before A was closed. The buret was filled with silicone oil, supplied by a reservoir (G), before each experiment. After a resting period of one hour, the cell underwent GCPL with 7.2 A ($\equiv$ C/10) for 4 h, resulting in $\approx$ 60 % state of charge (SOC). The dead volume between the electrode stack and cell can was estimated to be 65.4 mL by using CT-scans. The total dead volume, including the gas pipe and gas buret was adjusted by controlling the volume of argon flushed in, so that it was set to 100 mL. Once gas evolution began, the gases accumulated in the gas buret and were read-off, once an engraved line was reached. The evolving moles of gas (Δn) were obtained from Equation (6.1), using ΔV from the gas buret as variable.

Offline Gas Chromatography

A two-channel gas chromatography system (990 micro GC, Agilent Technolgy, Santa Clara, USA) with a thermal conductivity detector (concentration range: 0.1 % - 100 %) was used to analyze the collected gases within the gas buret offline. The first channel was equipped with a 10 m, 5Å molecular sieve column operated with argon as the carrier gas, while the second channel had a Pora PLOT U column (10 m, 10 µm fused silica film, $\varnothing$ = 0.32 mm) and operated with helium. Prior to measurement, the connection pipe was flushed and evacuated three times with argon to minimize contamination from the atmosphere. The data were corrected by subtracting the nitrogen content, and the oxygen value was recalculated by assuming a nitrogen to oxygen ratio of 78:21. This is justified due to the minor leakages and transportation of the buret from the OEMS to the GC, that could only introduce air. All measurements were conducted three times.

6.5 Results and Discussion

The results are categorized into three sections. Firstly, the electrochemical data and online monitored gas evolution of both cell sizes are presented. Secondly, the gassing behavior of the large-format cell is analyzed in detail, focusing on the impact of temperature. Thirdly, an overall comparison of the gas evolution in both cell formats is conducted while taking into account their respective sizes. In addition, *ex-situ* measurements of the negative electrodes, as well as the extracted electrolyte were used to support the conclusions drawn from the gas analysis and are available in the supporting information.

I. Electrochemical Characterization

Figure 63A displays the cell voltage typical for NMC811/ graphite cell plotted against time during the 1st galvanostatic charge step (C/10-rate), for both the model cell (solid line) and the large format cell (dashed triangle) configuration at a temperature of 25 °C. The voltage profiles for both cell sizes are virtually identical, except for the minor but visibly higher overpotentials for the model coin-cell likely resulting from its lower electrode stack pressure. The voltage curve shows a plateau-shaped feature (1st vertical dashed line) emerging within 20 minutes at a full cell voltage of ≈ 3.0 V, which indicates that the negative electrode has reached the electrolyte reduction potential of about 0.8 V vs. Li/Li$^+$, which is well-known to correspond to SEI formation along with the associated gas evolution.

II. Gas Evolution as a Result of Cell Format

Model Cell: The solid lines in Figure 63B shows the integral gas evolution for the model cell. The gassing behavior represents that of a typical NMC811/graphite cell, as already reported in literature.[28,81] The gases evolving due to SEI formation and electrolyte reduction comprises mainly C_2H_4 (≈ 77 %), followed by CO (≈ 19 %) and H_2 (≈ 4 %). C_2H_4 and CO are the most consistently observed gases evolving as a result of EC reduction in an acid-catalyzed ring-opening reaction via either a one electron or two electron process. Each pathway produces a different radical anion as an intermediate product.[255,256] The one-electron pathway (Eq. (6.2)), proposed by *Aurbach et al.*,[257] leads to a disproportionation reaction with another EC molecule, producing lithium ethylene dicarbonate (LEDC), and ethylene as gaseous by-product. LEDC has been identified in many publications as a crucial component of the SEI.[118,149]

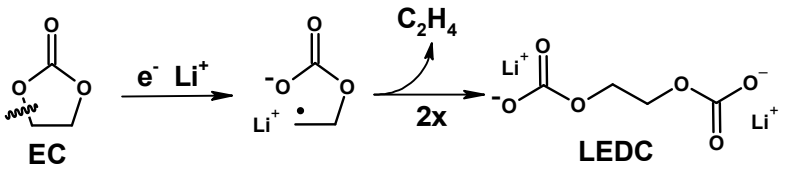

(6.2)

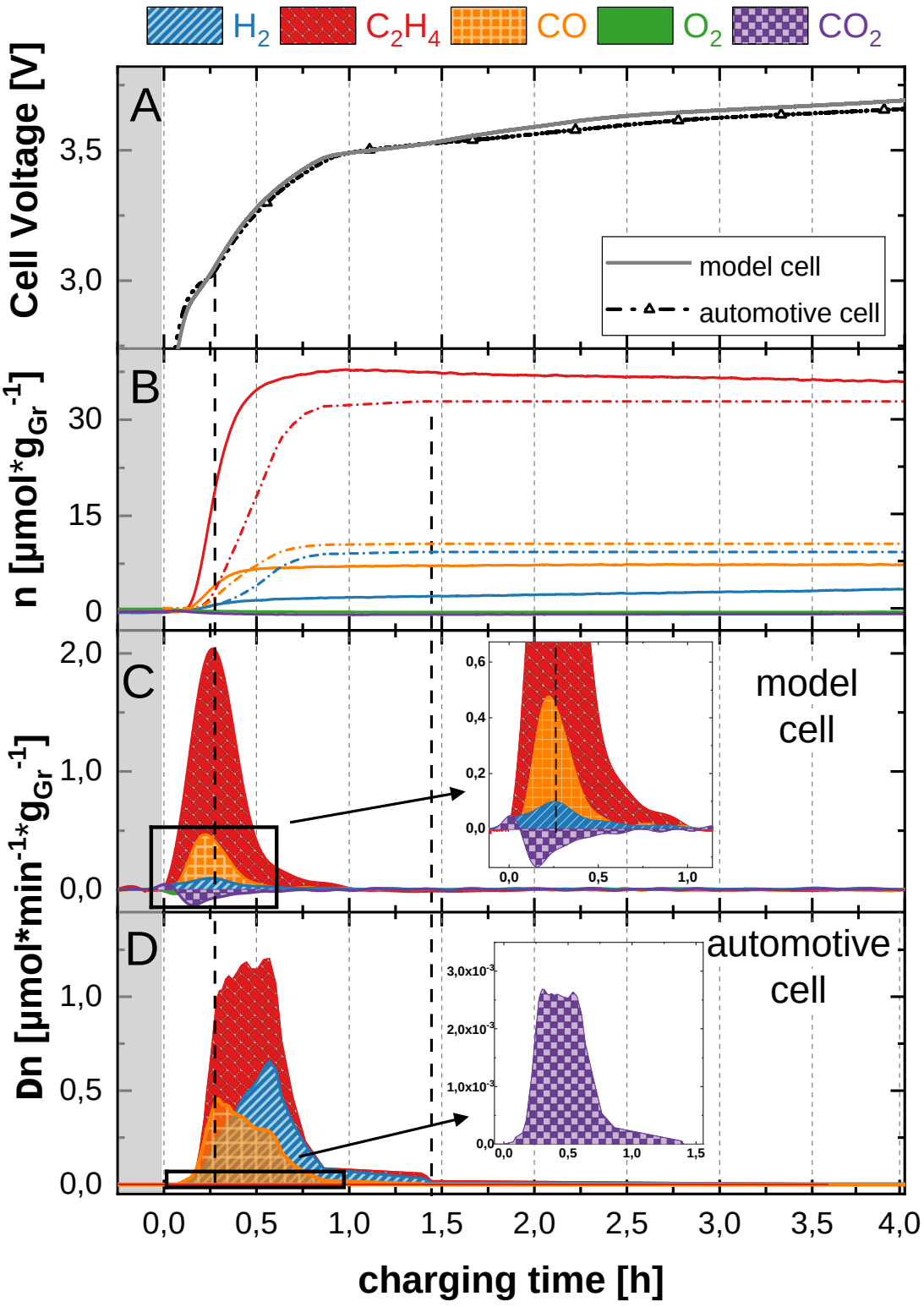

Figure 63: A: Electrochemical data for the applied GCPL with C/10-rate. B: gas evolution for model cell; C: gas evolution rate per gram carbon for model cell; D: gas evolution rate per gram carbon for automotive cell; exemplary chosen for 25 °C.

On the other hand, formation of the doubly deprotonated ethylene glycol component (Eq. (6.3)) via the two-electron pathway requires additional electrons and produces CO as a gaseous by-product.[131,258]

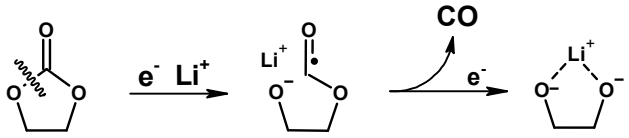

(6.3)

As the charging progresses, the concentration of C_2H_4 slightly decreases, and it is possible that C_2H_4 is reduced at the anode to form $Li(C_2H_4)_n$ polymeric compounds via subsequent reactions.[180] In contrast, the concentration of CO remains relatively constant, indicating an initial formation without further reactions.

Molecular hydrogen is also generated throughout the formation, mainly from the reduction of water impurities, shown in Equation (6.4).

$$H_2O + e^- \longrightarrow OH^- + {}^1/_2\, H_2 \uparrow \tag{6.4}$$

In Figure 63C, the molar gas evolution rate (i.e. the time-derivative of Δn) for the model cell is presented. Clearly, the ethylene peak overlaps as expected with the voltage plateau of the SEI formation, thus demonstrating the reasonable temporal resolution of the gas data for the model cell, as previously published.[230] Upon charge, H_2 sets in first as H_2O is reduced already at 1.8 V vs. Li^+/Li (Eq. (6.4)) and continues to evolve with an increasing rate until the SEI presumably passivates the surface. Both C_2H_4 and CO evolve at the same time and display similar evolution profiles, even though C_2H_4 peaks later as C_2H_4 relies on a slower 2nd order reduction process (Eq. (6.2)). Although to a very minor extent, CO_2 evolves already from the very start of the experiment, e.g. as a result of the dissolution of Li_2CO_3 residues on the cathode and hydrolysis of the organic carbonate solvents. Subsequently within the formation procedure, a consumption of CO_2 at the negative electrode[180,259] can be seen (inset of Figure 63C). The subsequent reaction of CO_2 is discussed later within this section. The results are in good agreement with *Metzger et al.*, who additionally showed, that a higher cell temperature leads to higher gas evolution of the above mentioned gases.[28]

Large-Format Cell: The dashed lines in Figure 3B equally shows the integral gas evolution data from the large-format cell, generally displaying the same behavior to the model coin-cell. However, the gas release is more "sluggish" for the large-format cell with a bit less C_2H_4 and more H_2/CO. Despite the sluggishness, the large format cell revealed a remarkably similar gas evolution profile during formation. The gas phase mainly consist of C_2H_4 ($\approx$ 71 %), followed by CO ($\approx$ 16 %), and H_2 ($\approx$ 14 %). Figure 63D shows the molar gas evolution rate for the large-format cell. Although the

cell design is completely different, the onset of the gas evolution is largely unaffected compared to the model cell. It can be assumed, that gas molecules formed near the outer edges of the electrodes can diffuse rapidly into the cell headspace and are responsible for the very similar onset time. However, the obtained gas evolution rate for C_2H_4 is reduced by approx. one-third to 1.25 µmol*min^{-1}g$_{Gr}^{-1}$, whereas the concentration of CO with 0.50 µmol*min^{-1}g$_{Gr}^{-1}$ seems nearly independent of the cell size, indicating similar processes in both cells leading to CO-formation. The H_2-evolution rate is drastically increased up to 0.60 µmol*min^{-1}g$_{Gr}^{-1}$. Based on Equation (6.4), residual water is assumed to be the primary source of hydrogen during the initial charging process.[39] As the drying procedure of the large-format cell (see section XXX) is not as thorough as for the model cell, traces of water will react with the conducting salt, once the electrolyte is introduced into the cell, represented by Equation (6.5).[260]

$$H_2O + LiPF_6 \longrightarrow LiF + 2\ HF + POF_3 \tag{6.5}$$

The freshly formed HF is then reduced earlier at about 2.2 V vs. Li^+/Li, as shown by Equation (6.6).[193]

$$HF + e^- + Li^+ \longrightarrow LiF + 1/2\ H_2 \uparrow \tag{6.6}$$

The detected CO_2 evolution (zoom-in Fig.: 63D) in the large-format cell may be attributed to the much longer wetting time, which enables the reaction of the freshly formed HF from Equation (6.6) with lithium carbonate, which is always present as minor impurity due to material production, as shown in Equation (6.7).[261]

$$2\ HF + Li_2CO_3 \longrightarrow H_2O + LiF + CO_2 \uparrow \tag{6.7}$$

The shapes of the gas evolution peaks (Figure 63C,D) are differently skewed. Carbon monoxide shows an early peak maximum with a flattening curve towards longer charging times, whereas it is the opposite trend for H_2. The C_2H_4 onsets immediately, at the same time as CO, and shows three maxima in total. Both CO and C_2H_4 are a result of electrolyte EC solvent reduction and are not limited by EC transport to the graphite electrode surface. On the contrary, H_2 evolves at a higher rate the higher the cell voltage and the H_2 evolution only declines once the SEI sufficiently blocks H_2O diffusion to the graphite electrode surface. Furthermore for the large-format cell, all peaks show an increased peak broadening compared to the model cell, resulting in an active gassing period of up to ≈ 0.7 h of charging time. Here, it can be expected that gases formed within the center of the electrode stack are being released. Assuming an average diffusion length of 3 cm within the cell stack, the time gases need to enter the cell headspace can be calculated using the Einstein-Smoluchowksi equation: $\Delta x = \sqrt{2D\Delta t}$. For C_2H_4 (D = 1.8*10^{-5}cm^{2}s^{-1} [262]) an average diffusion time of nearly 70 h would be expected. The fact that the gas release happens mainly within 45 minutes results in an

average diffusion distance of ≈ 3 mm. This result indicates, that the gases might be formed within the electrode pores (coating thickness of 200 µm) and diffuses then to the electrode/electrolyte interface. Here, the mass transport is likely governed by another process, e.g. gas bubble formation and subsequent convective flow. Indeed, evidence of gas bubble formation within the electrode stack was obtained by computed tomography (see SI for further details) scan of the cell after the completed cell cycling. Gas bubbles appeared to form between individual electrodes throughout the entire electrode stack. After 0.7 h of charging, the gassing rate of C_2H_4 and H_2 drops significantly to ≈ 0.1 µmol*min^{-1}g$_{Gr}^{-1}$, indicating that the active gas flow out of the cell headspace has stopped. Following that, the reduced flux of the evolving gasses can be seen up to a total charging time of ≈ 1.5 h (2 ndvertical dashed line).

For both cell formats, carbon monoxide evolves during the shortest time period, hence indicating fast initial formation without subsequent reactions leading to additional CO evolution. Hydrogen exhibits the broadest peak in both cell formats. The full width at half maximum (FWHM) almost doubles upon switching from the model cell arrangement (25 minutes) to the large-format cell (45 minutes) and is likely due to more limited transport of H_2 through the electrode stack to the headspace of the cell. H_2 can also be temporarily trapped in the microstructure of the conductive carbon material, resulting in a slower desorption rate.[260]

III. The Effect of Temperature on Gas Formation in Large-Format Cells

In this section the influence of cell temperature on the gas evolution and composition within the large-format automotive cells are described in detail.

The Total Gas Evolution Monitored by Gas Buret

Figure 64 shows the cell voltage as well as the total gas evolution rate during formation of the large-format cells as a function of time and temperature. Increased temperature leads to both stronger gas evolution and greater amounts of generated gases. The gassing time is also influenced by the temperature with the use of 10 °C showed evolving gases up to 120 minutes of charging, whereas 40 °C nearly halves the gassing time span (≈ 60 min). Interestingly, the temperature does not appear to significantly affect the time of the maximum gas evolution rate (indicated by dashed line). In addition to that, the overall shape of gas evolution peaks look rather similar for all temperatures, including a broad base, sharp maximum and the appearance of a shoulder with longer charging time. The presence of the shoulder in the gassing data during longer charging times is likely caused by the transport-limited H_2 release. Generally, gas evolution as observed by monitoring the buret agrees well with observation in Fig. 63.

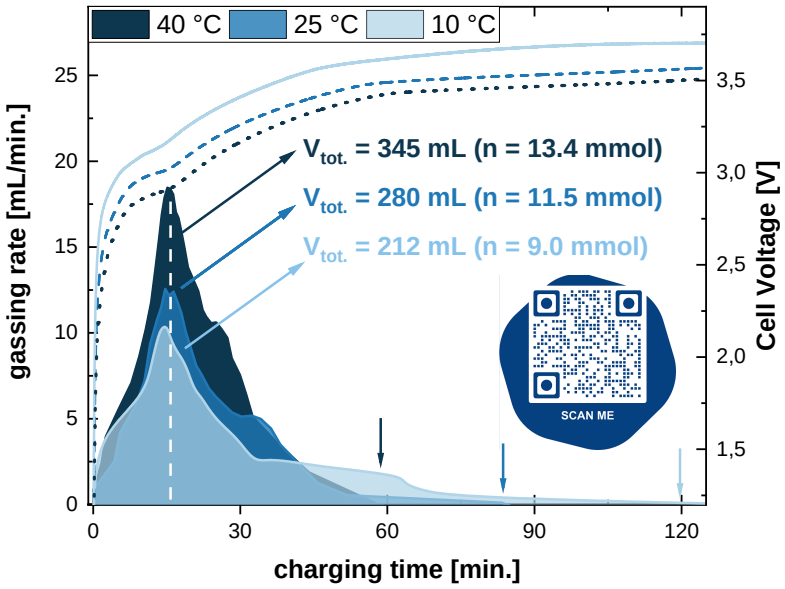

Figure 64: Cell voltage (dashed) and total gas evolution (filled area) versus time collected from the gas buret while charging automotive cells at different temperatures. The white dashed line indicates the maximum of the gas evolution. The downwards pointing arrows indicate the end of gas evolution. A live video of gas collection is online available via the embedded QR-code.

The obtained voltage profiles (right y-axis of Fig. 64) show a more well-defined reduction plateau ($\approx$ 3.0 V) with increasing temperature. The higher temperatures enhance the kinetics of electrolyte reduction with a more clearly defined SEI formation voltage plateau and more electrolyte being reduced before a fully passivating SEI is formed. In line with that, the thermogravimetric investigations (see SI) showed higher mass loss for lower charging temperatures. In combination with the reduced amount of released gases, it can be concluded that a more dense SEI-layer is being formed. This can be explained, with the stoichiometry of both EC reduction pathways (Eq.(6.2) and (6.3)

Offline Resolved Gas Composition by GC

Table 10 displays the gas phase composition obtained via GC after the complete charging procedure at various temperatures. The data suggest that the H_2 content increases steadily with higher cell temperatures, which can be related to faster diffusion of H_2O to the graphite before the surface is passivated by the SEI. EC reduction and the formation of C_2H_4 respectively CO is also influenced. A higher temperature favors the 2 EC reduction pathway (Eq. (6.2)). *Sloop et al.*[255] demonstrated that the opening of the EC-ring is an endothermic process, meaning that this pathway (Eq.(6.2)) should be favored at higher temperatures. Furthermore, a higher temperature increases mobility of the intermediate, which in turn increases the likelihood of two reduced EC to meet and generate C_2H_4 and LEDC. In any case, both effects lead to more ethylene with elevated temperatures.

Table 10: Gas composition of the released formation gases, measured after complete charging procedure. The gases were stored in a gas buret and subsequently analyzed via GC.

Temperature [°C]	H_2	C_2H_4	CO [%]	O_2	CO_2
10	13.4	53.1	32.6	0.75	0.09
25	14.4	67.5	17.5	0.18	0.02
40	17.3	67.9	14.7	0.31	0.16

On the other side, *Ota* and colleagues have shown that cleavage of the CO-group on the radical in Eq. (6.3) is an extremely exothermic process.[263–265] Calculations by *Leung et al.*[265,266] showed that reaction (6.3) exhibit a lower energy barrier, and is therefore the preferred product at lower charging temperatures, which is also supported by our gassing data. The lower mobility of reduced EC at lower temperatures may rather lead EC to accept two electrons before leaving the electrode surface (Eq. (6.2)). These findings are consistent with the data presented in section 3.3.1. and CO release should dominate during electrokinetically controlled SEI growth.[255] Neither O_2 nor CO_2 exhibit any clear trend with respect to the employed temperature. The presence of O_2 may be attributed to the fact that the larger cells were produced in dry room conditions. Although the cells were thoroughly purged before being filled with electrolyte, obtaining a completely O_2-free electrode stack prior to filling the cell is challenging.

Comparison of Online and Offline Approach

Figure 65 shows that total gas amounts and the respective compositions from the two analytical techniques, OEMS and GC, largely agree. Elevated temperatures result in the formation of more gas per gram carbon during SEI formation on the negative electrode side. The gas evolution increases from 40.1 µmol/g_{Gr} at 10 °C to 51.3 µmol/g_{Gr} at 25 °C, and 59.8 µmol/g_{Gr} at 40 °C, meaning that the total gas amount increases by 50 % for 40 °C in comparison to 10 °C. Furthermore, a higher temperature promotes both the H_2-evolution and C_2H_4-formation, while lower temperatures rather favor CO-formation. Although both OEMS and GC analysis display the same trend, the GC method detected higher H_2-content with a maximum deviation of ± 5 % observed in the 40 °C experiment. Conversely, the OEMS method shows higher values for C_2H_4, with a maximum deviation of ± 9 % for the 10 °C formation. There is no clear trend for the CO-values in the OEMS or GC values, although the maximum deviation of ± 7 % is observed in the 10 °C formation experiment.

Any discrepancy between the two OEMS and GC methods can be clarified through their respective measurement principles. The rapid gas evolution within a short period of time likely reduces the extent of mixing of evolving gases, especially with argon in the cell headspace, before the gas is pushed to the buret. Since a normalization towards argon is carried out, a dilution of the evolving gasses is necessary and guaranteed in the model cell case, where argon is the main gas fraction. However, the ratio of headspace volume to active material is much lower in the large-format cell. The predominant gas fraction is C_2H_4 with a volume already twice as much as the cell headspace volume, we expect less argon remain in the cell headspace, which is sampled by the MS. Consequently, the primary gas (C_2H_4) is being overestimated, and minor fractions, such as H_2 and CO, are being underestimated. The overall agreement is reasonable and the same trend is observed, which in turn supports our observation from the online measurements.

Another temperature related trend was observed exclusively by the use of OEMS for the CO_2-evolution (see Table 13). The stepwise increase in temperature results in the evolution of 0.13 %, 0.24 %, and 0.50 % CO_2 at a formation temperature of 10 °C, 25 °C, and 40 °C respectively, see Table 13 in the supporting information. It is known, that the EC hydrolysis towards ethylene glycol (EG), as shown in Equation (6.8), is thermally triggered.[267]

$$H_2O + EC \longrightarrow EG + CO_2 \uparrow \tag{6.8}$$

Dissolution of Li_2CO_3 residues on the cathode might as well be promoted at higher temperatures. However, the simultaneous CO_2-addition of the glycol (from Eq. (6.3)) or the steady breakdown of LEDC (from Eq. (6.2)) are also in accordance with the observed CO_2-behavior. Both pathways, described in Eq. (6.9) can form lithium ethylene monoxide (LEMC),[131] which is as well a commonly known SEI component.

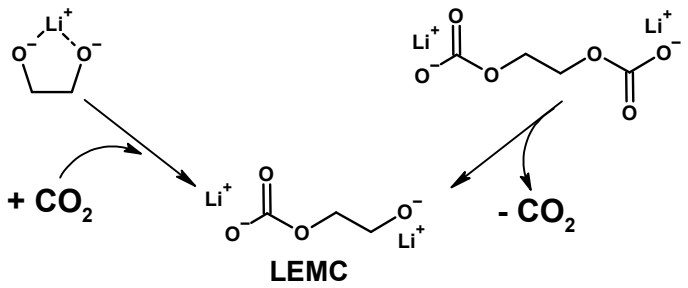

(6.9)

Cell Format

In order to investigate the relationship between gas evolution and cell size, the results obtained from experiments carried out on the model cell and the large-format cell at 25 °C need to be compared (see 3rd and 7th bar from left in Figure 65). The model cell generates a maximum of 47.1 µmol/g_{Gr}, while the large-format cell produces a total of 51.3 µmol/g_{Gr}. The key difference lies in the amount of hydrogen generated, with the large format cell producing 4.9 µmol/g_{Gr} more than the model cell. Considering only the water reduction shown in Eq. (6.4) as possible hydrogen source and using a cell weight of 675 g (530 g of AM + 145 g of electrolyte) the amount of residual water for the large-format cells is ≈ 85 ppm, which seems reasonable. Despite the difference in active material amount with a scaling factor of 1:100000 between the cell formats, the experiments conducted suggest that the gas evolution profiles display only a minor dependence on cell size itself and that model coin-cell experiments are representative also for larger commercial cell formats.

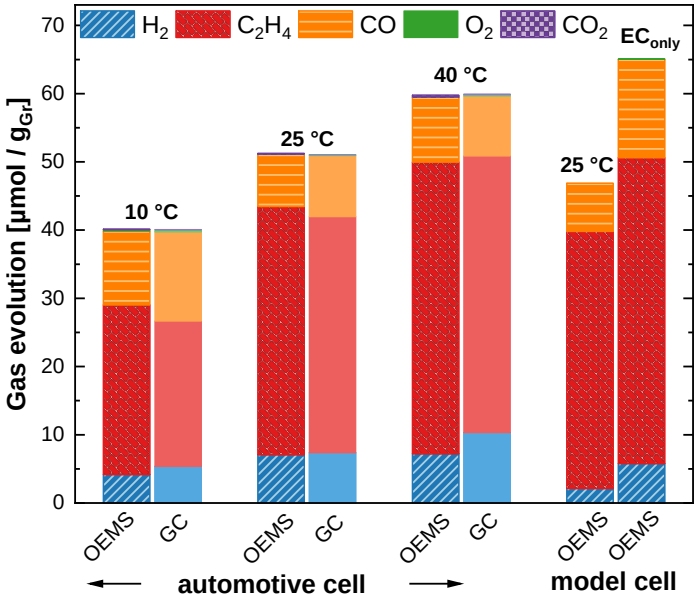

Figure 65: Gas evolution after formation for automotive cells (left) and model cell (right). The automotive cell gas composition was measured and was compared online via OEMS (hatched colors) and offline via gas buret + GC (full colors). All experiment were carried out, using EC:DEC (50/50 wt. %) electrolyte. The very right model cell one, was performed using 1.5 M $LiPF_6$ in EC_{only}, and a cell temperature of 25 °C.

IV. Validation of Reaction Mechanisms

Since EC accounts for only 50 wt % of the electrolyte mixture, additional investigations were carried out to determine whether the gases were released from EC or DEC. Experiments were conducted using EC_{only} electrolyte (EC + 1.5M $LiPF_6$) and are shown on the very right hand-side of Figure 65. The C_2H_4 / CO ratio for EC_{only} (3.2 :1) was found to be in good quantitative agreement with the ratio reported by *Solchenbach*

el al. (3.4:1).[212] However, the experiment revealed that even more gas per gram carbon is produced using this electrolyte. EC is more polar than DEC and likely dissolves more of the solid reduction products and needs more time to form a passivating SEI compared to when DEC is present. The addition of DEC as solvent results in a lower CO content, which can be explained by the resulting lower electrolyte viscosity that increases EC mobility and the likelihood that an EC moves away from the surface and meets another reduced EC and generate C_2H_4. In this context, both electrolyte viscosity and temperature appears to have the same effect on EC mobility and reactivity. Furthermore, these results indicate that the gases C_2H_4 and CO are exclusively formed by EC, and that EC accesses both reduction pathways (Eq. 6.2 & 6.3), as described by *Onuki et al.*[264]

6.6 Conclusion

Herein, the development and application of an Online Electrochemical Mass Spectrometer setup designed to monitor gas evolution and consumption in Li-ion batteries during operation are presented. Analysis is applied to batteries of two sizes, a model coin-cell and a prismatic large-format automotive cell with identical chemical compositions, and demonstrates the adaptability and scalability of the setup. Gas evolution during battery formation results primarily from the reduction of the electrolyte solvent ethylene carbonate in two competing processes, either triggering C_2H_4 or CO evolution depending on a 1e- or 2e- reduction reaction pathway. These results were validated with an EC-only electrolyte displaying nearly identical gas evolution profile as for the electrolyte with mixed solvents. Minor amounts of H_2 and CO_2 evolve predominantly from water impurity reduction. The influence of cell temperature on gas evolution during formation is furthermore explored. Although the gassing time is shortened, a higher temperature induces stronger evolution of C_2H_4 and H_2 gas and indicates that a more organic and porous SEI is formed. Although the overall gas evolution rates and compositions are similar in both cell formats, gas release needs more time ($\approx$ 0.3 h more) in the large-format cell due to longer gas transport distances through the electrode stack. Our data suggests that gas transport in large format cells mostly rely on convection as a consequence of bubble formation rather than on diffusion, as the latter process is orders of magnitude too slow to account for the observed gas amount and evolution rate. We can therefore conclude that gas analysis experiments based on model coin-cells, which are commonly applied in academic research labs, offer comparable results to what is expected from large-format commercial Li-ion cells. Apart from novel insights into the formation processes of large-format automotive cells, our developed setup provides unique opportunities to further optimize and accelerate LIB production, ultimately reducing the cost of each cell.

6.7 Extra Material

The Role of Lithium-Ethoxide (EtOLi)

Although DEC does not appear to actively participate in the gas evolution process, it is believed to interact within the acidic environment of a LIB. The formation of lithium alkoxide species, attested by Sasaki and colleagues,[268,269] is crucial for a prolonged elongation. Furthermore, the reaction of DEC can iteratively occur n times, yielding EtOLi along with the corresponding lithium ethyl carbonate each time, as shown equation (6.10).

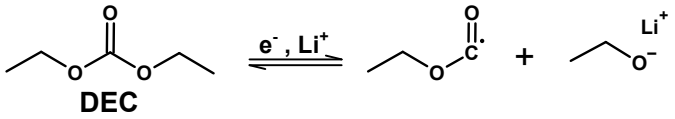

(6.10)

Formation Process of Accompanied Oligomers

According to literature LEMC reacts with the species formed in equation (6.10) to form polyethylene oxide (PEO)-like polymers.[255,270] The carbonyl groups incorporated into the polymer chain can arise from EC and DEC, but the termination of polymerization always involves DEC, signifying it as the final step in the chain-growing reaction.[271] In our electrolyte analysis (see Table 12 in SI), we identified three oligomeric products, which were also observed by *Henschel et al.*, who conducted an extensive study on the thermal aging and formation processes using ^{13}C-labeled EC/DEC electrolyte.[272,273] The general scheme is depicted in equation (6.11).

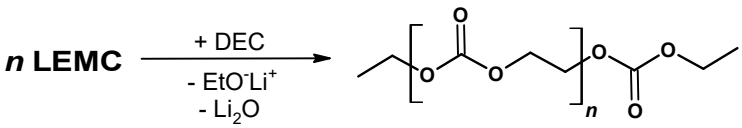

(6.11)

Our findings suggest that these species are significant byproducts that affect the cell performance since they were already formed within the initial 4 hours of battery operation. The shorter oligomer ($C_{11}H_{18}O_9$) was favored at lower temperatures, such as 25 °C, while the longer oligomer ($C_{14}H_{22}O_{12}$) was formed at higher temperatures, such as 40 °C. The MS-MS spectra for the individual species are shown in the supporting information (Figure 66) and demonstrate the $[M+H]^+$ proton adduct pattern for the oligomers, which bear a close resemblance in terms of their structure.

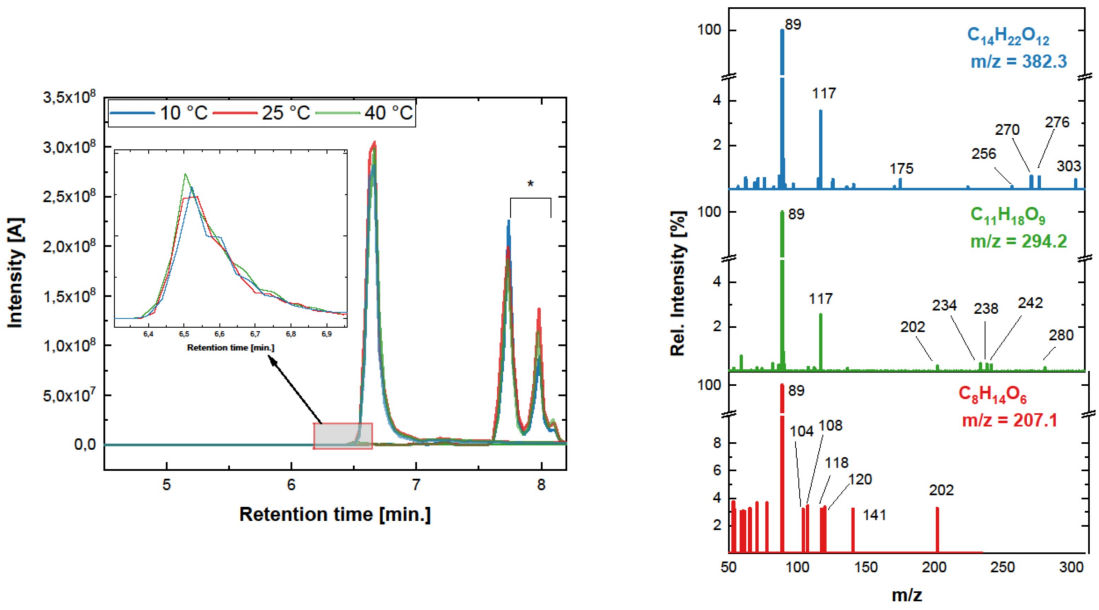

Figure 66: Left: LC-Chromatogram obtained from extracted electrolyte samples of large-format automotive cells, after first charging procedure at different temperatures. The area ratio of the very right peaks (marked with *) are 2.6 (10 °C), 2.0 (25 °C), and 1.93 (40 °C). Right: Obtained MS-MS spectra of the individual separated species, further described in Table 12.

Supporting Information

A) Evidence of Gas Bubble Formation

Evidence of gas bubble formation was obtained by computed tomography (CT) scan after the conducted electrochemical experiment. The CT scan (left part of Fig. 67) shows the bubble formation due to electrolyte reduction and SEI formation as dark gray spots, distributed along the electrode as well as in the entire electrode stack (cross-section CT). The cell was subsequently disassembled in glovebox and the evidence of gas bubble formation can be seen visual in the right Figure of 67. However, these Figures do only provide clear evidence of bubble formation. The assumption of an acceleration of gas bubble transport relies on the fact that gases leak out from the cell much faster than possible due to mere diffusion of dissolved gases though the cell stack, as discussed in the manuscript.

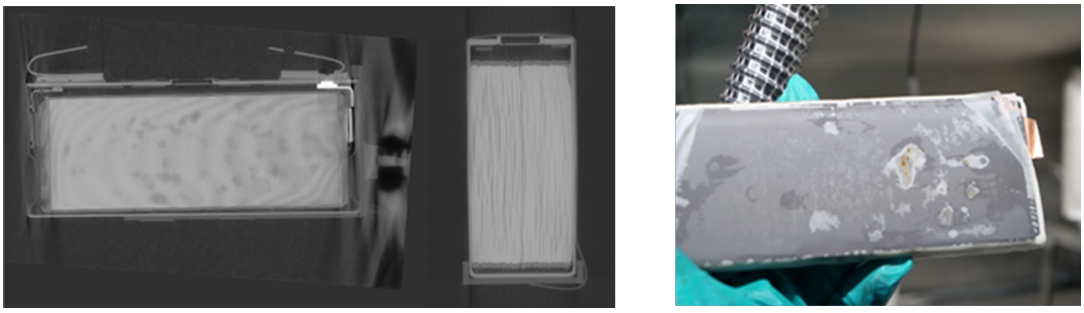

Figure 67: Left: Computed tomography scan of a prismatic large-format cell after formation. Gas bubbles can be seen as gray spots along the entire cell, and also within the stack (cross-section CT scan). Right: Evidence of bubble formation within the disassembly process of the cell. Gas bubbles are being formed and trapped between electrode and the separator.

Table 11: Overview of the electrode and electrolyte parameters for both cell sizes used within this work.

Parameter	Unit	Model cell	Large-format cell
Coated area anode	cm^2	2.01	17,300
Mass loading (graphite) anode	$mg*cm^{-2}$	10.36	12.32
Specific capacity anode	$mAh*g^{-1}$	372	
Areal capacity anode	$mAh*cm^{-2}$	3.85	4.58
Coated area cathode	cm^2	1.54	16,000
Mass loading (NMC811) cathode	$mg*cm^{-2}$	18.9	20.2
Specific capacity cathode	$mAh*g^{-1}$	202	
Areal capacity cathode	$mAh*cm^{-2}$	3.82	4.08
N/P ratio	/	1.01	1.12
Electrolyte loading	$g*Ah^{-1}$	36	1.8

B) Further Electrochemical Data for Large-Format Automotive Cells

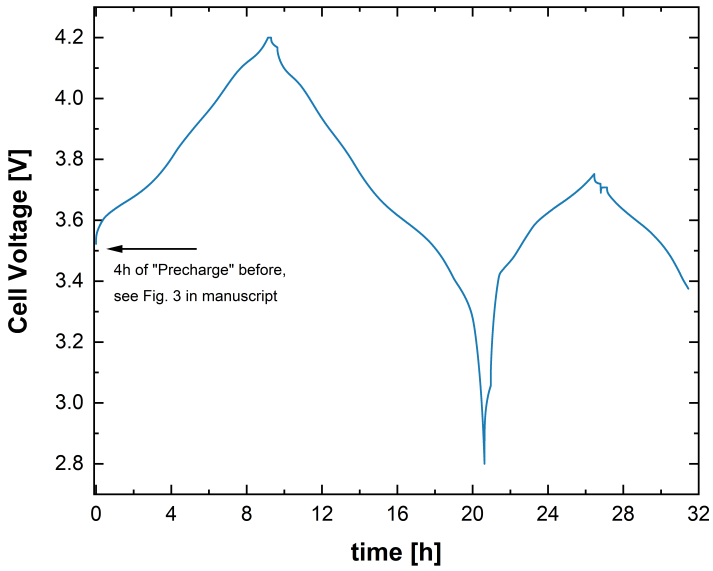

Figure 68: Cell voltage over time for the complete formation cycle of a prismatic 72 Ah graphite/NMC811 cell with 1M $LiPF_6$ EC/DEC (50/50 wt-%) -electrolyte.

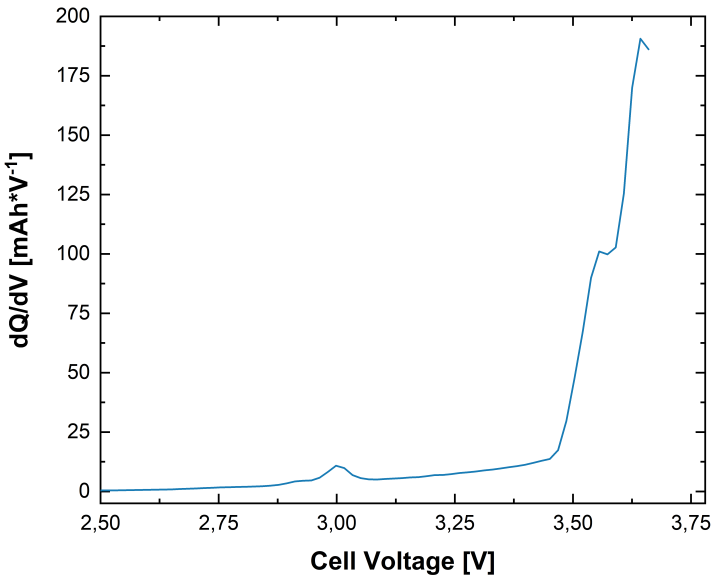

Figure 69: Differential voltage analysis (dQ/dV) for a large-format prismatic cell during formation at 25°C.

C) Simultaneous Thermal Analysis-Mass-Spectrometry

After formation, cells were disassembled in an Ar-filled glove box and harvested negative electrodes were rinsed three times with DMC. The graphite containing active material of the washed electrodes was scratched off under air and mortared until an evenly sized powder was obtained. Due to this procedure we believe, that all lithium-containing species reacted towards lithium carbonate. The mortared powder was analyzed by using a simultaneous thermal analysis-mass spectrometry (STA-MS) system (449 F1 Jupiter, Netzsch Instruments, Germany) coupled with a MS-unit (QMS 403 Aëolos, Netzsch Instruments). The samples were heated with a heating rate of 10 K^*min^{-1}. All samples were measured twice.

The thermogravimetric investigations of the harvested negative electrode material are presented in Figure 70. The analysis indicates that higher mass loss occur at lower charging temperatures. The mass loss for a pristine negative electrode is set to 0.0 %, as the thermal investigation was only carried out up to a temperature of 1000 °C at which only the decomposition of lithium-containing species, e.g. Li_2CO_3 and binder material occurs. The pristine negative electrode had no contact to electrolyte prior and was investigated via STA-MS, right after fabrication. Based on the obtained data, it can be concluded that a greater number of (inorganic) species are deposited on or within the surface of the negative electrode when lower charging temperatures are used. The mass loss difference between 40 °C and 25 °C, and 25 °C and 10 °C almost doubles (factor 1.9), indicating that more material is deposit on the negative electrode surface at lower temperatures, compared to higher temperatures.

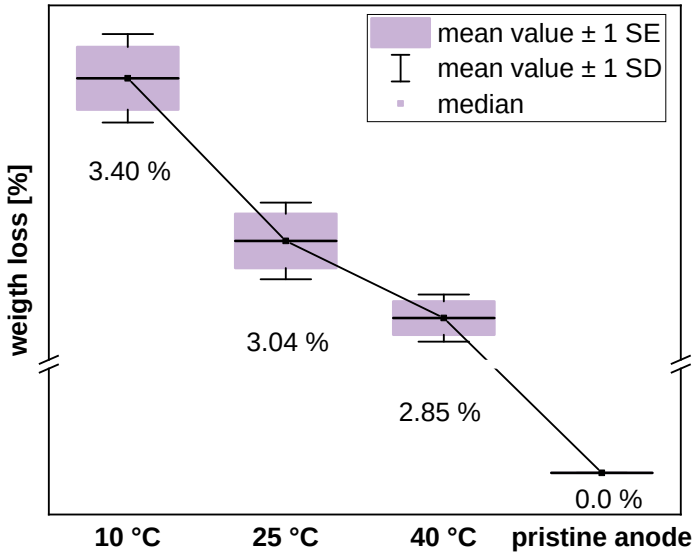

Figure 70: Mass loss of the negative electrode obtained from large-format cells after formation cycle for various temperatures.

D) Surface Composition of Partial Lithiated Negative Electrodes

Additional analysis was conducted on the harvested electrodes from the large-format cells immediately after the formation cycle. At this point, the negative electrodes had a state of charge (SOC) of approximately 40%. To investigate the correlation between temperature and the resulting SEI composition of the graphite electrodes, XPS spectra were obtained after cell formation. Furthermore, simultaneous thermal analysis mass spectrometry (STA-MS) were carried out, which underlined the XPS findings. The XPS fitting results, including C1s, F1s, O1s, and Li1s, as well as STA-MS results are depicted in the supplementary information. The obtained surface compositions of the electrodes are displayed in Figure 71. The C1s core peaks consist of peaks associated with graphite (284.4 eV) and hydrocarbons/binder (287.0 eV).[274] After being charged, the peak at 287.0 eV is no longer visible, suggesting the formation of a surface layer known as SEI. At lower charging temperatures, a characteristic peak for Li_2C_2[275,276] is observed at 282.65 eV. Conversely, the CO_3-peak (288.2 eV) is observed at higher temperatures.

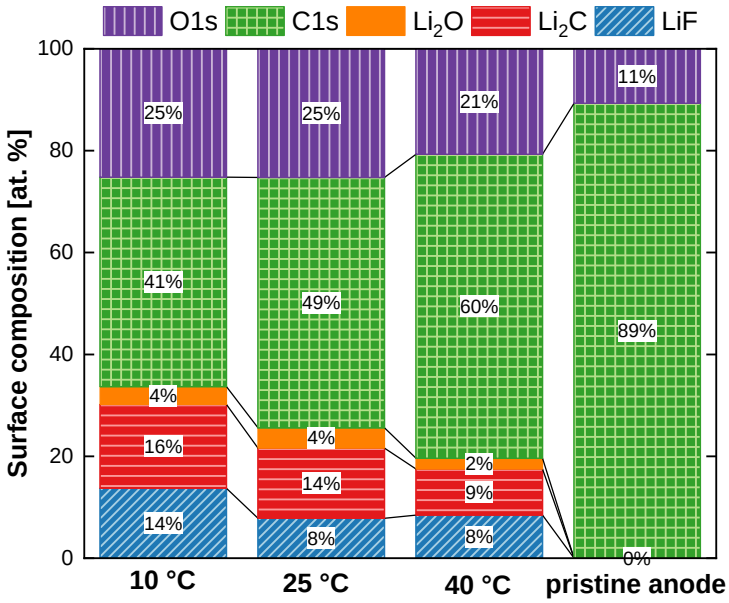

Figure 71: Surface composition obtained by XPS, of various negative electrodes, harvested from automotive cells, after formation cycle.

No fluorine was detected in the pristine anode; however, for all other samples, F1s core peaks were observed for LiF (684.71 eV) and $LiPF_6$ (686.72 eV). A significantly higher LiF-content was detected for the electrode charged at the lowest temperature. Peaks of the binder material dominate the O1s core peaks of a pristine anode at 531.2 eV and 533.1 eV. During initial charging, the peaks slightly shift to higher binding energies,

and the intensity of the C=O/C-O-Li peak (531.2 eV) increases, consistent with the deposition of species containing C=O on the graphite surface. A decreased amount of Li_2CO_3 was detected at 533.1 eV for the sample charged at 40 °C, indicating a thinner film formation, and in accordance with our gassing and electrochemical data. In general, analysis of the different charging experiments reveals that lower charging temperature result in the deposition of more lithium-containing inorganic species on the surface of the negative electrodes.

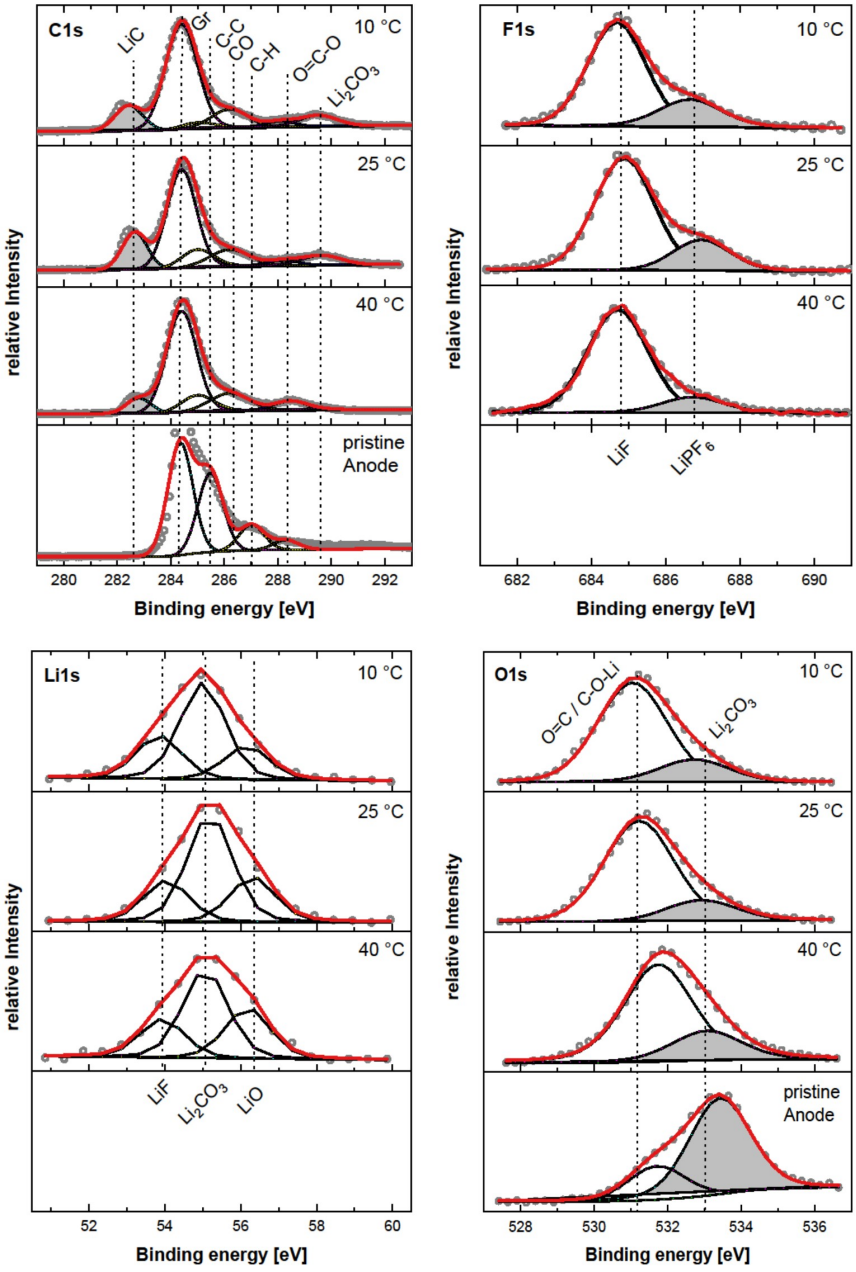

Figure 72: C1s, F1s, Li1s and O1s core peaks of fresh and charged graphite electrodes while using different temperatures during initial charging cycle of automotive cells. Electrodes were charged with C/10 with LP40 electrolyte.

Gas Evolution in SiO_X-containing Battery Cells

7.1 Motivation & Background

This chapter investigates the gas evolution behavior in silicon oxide (SiO_x)-containing battery cells, which is a critical issue for the commercialization of high-energy density lithium-ion batteries. As described in chapter 2, the need for ever increasing energy density and fast charging requires new electrode and electrolyte formulations. Hence, the usage of silicon-alloys and-oxides is one of the most promising opportunities in the near future, to tackle both needs. However, the usage of SiO_x-electrodes comes along with larger volume expansion during charge/discharge procedure. The following chapter is structured into several key sections.

The first section examines the gas evolution characteristics of model battery cells containing SiO_x-based anodes, under the usage of different electrolyte compositions. The goal here is to understand the fundamental mechanisms driving gas release in these systems. The second part focuses on the study of automotive cylindrical cells (type 4695). This includes an analysis of the gas evolution during the formation cycling, with a particular focus on the influence of temperature on the gas release behavior. As a proof of concept, this section also presents a comprehensive study of gas evolution in a standard 4695 cylindrical cell, demonstrating the applicability of the developed time-and potential-resolved gas analysis techniques for any kind of battery cell at any kind of cell life.

The findings from this thesis provide critical insights into the gas evolution mechanisms in SiO_x-based battery cells, which can inform the development of strategies to mitigate this issue and enable the commercialization of high-energy density lithium-ion batteries for automotive and other applications.

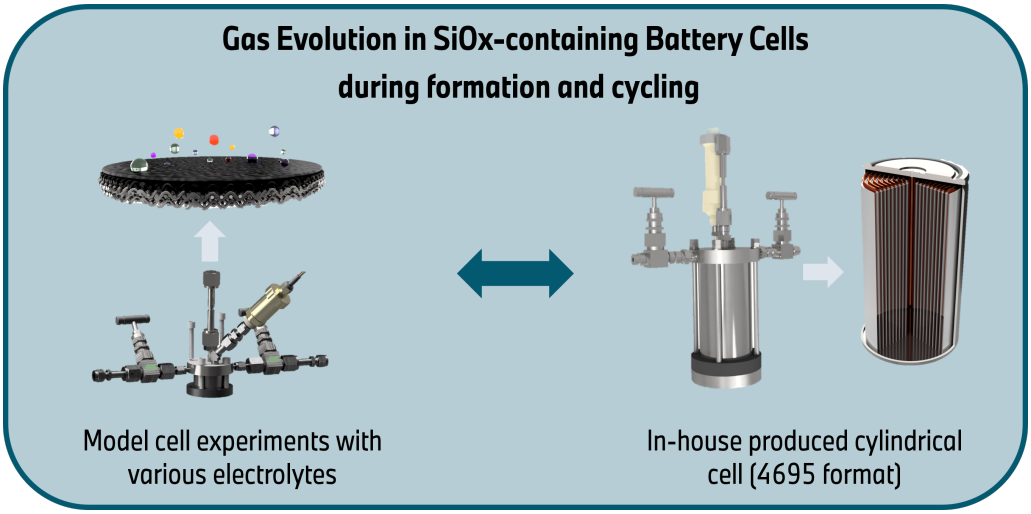

Figure 73: Graphical abstract for the embedded chapter in this work dealing with the in-operando gas analysis on silicon containing electrodes either in model cell arrangement or large-format cylindrical cells.

7.2 Model Cell Experiments with Various Electrolytes

Experiments with the model cell approach were conducted, to gain deeper knowledge about the electrochemical processes in silicon-containing electrodes. Similar to the investigations on large-format prisma-tic cells, those model cell experiments should provide a profound knowledge base about the reduction processes on the material level. Especially as the implementation of silicon within the negative electrode of cylindrical cells, comes along with rather complex electrolyte mixtures (see next section). Therefore, simple model cell experiments with rather simple electrolytes were conducted, to understand the gas evolution processes, prior experiments on cylindrical cells.

I. Experimental

Setup and Model Cell

The herein described measurements were conducted on the same setup, as the model cell experiments, described in the prior chapter (see chapter 6). Only other materials were used for electrode production and hence other electrolyte mixtures were used due to the different cell chemistry. To investigate the gassing behavior of SiO_x-containing electrodes, three different electrolytes were used. Either FEC_{only}, a commercial one with two unknown additives and a self-made replicate of the latter one, without the additives. In general, 200 µL of the individual electrolyte were used in a single model cell experiment. For further details on the individual electrolyte mixture see Table 6.

Electrode Manufacturing

For both electrodes, a binder solution of PVDF (0.20 wt.%; BM-730H, Zeon, Japan) in NMP is prepared in advanced by stirring them for at least 12 h. Active materials and conductive additives are then mixed into them with a planetary mixer (Thinky Are-250). The materials that were used are NMC811 (96.0 wt.% of the solid content; Umicore, Belgium). 1.80 wt.% binder (Solef 5140/1001, Solvay, Belgium) and carbon black as conductive additive (2.0 wt.%; LITXHP, Cabot, USA). For the anode, PVDF (3.0 wt.%) was used as binder, carbon black as conductive additive (2.0 wt.%; Super C65, Imerys, Switzerland) and SiO_x (moderate content; BSO-L, BTR New Material, China), respectively graphite (84.5 wt.%; SMG A5, Resonac,Japan) as AAMs. The resulting slurry was coated on a stainless steel mesh (mesh size 0.212 mm / wire gauge 0.090 mm, Spörl, Germany) with a film applicator (TQC Sheen,Germany). After drying in a ventilated oven (100 °C), the electrodes are punched into discs with a diameter of 16 mm for the anode and 14 mm for the cathode. Subsequently, the discs are again dried under dynamic vacuum at 120 °C (glass oven B-585,Büchi, Switzerland). For the cathode, all of those steps have been carried out in a dry room atmosphere. In sum, the materials of the electrodes of the model cell do not differ from those of the electrodes of the in-house produced cylindrical automotive cells (see next section below). Except for the binder and the solvent used for the anode. For these, a water-based carboxymethyl cellulose (CMC)-binder (CMC by Daicel Miraizu, Japan and Aquacharge SW100 by Sumitomo Seika) was used.

II. Results: Gas Evolution Behavior During SEI-Formation

The time- and potential-resolved gas evolution of the model cell experiments are shown in Figure 74 and can be divided into three parts. Firstly, the gassing behavior of the electrode was studied by the use of a FEC_{only}-electrolyte (left sub-figure of Figure 74). Secondly, a replicate of a commercial available electrolyte was used and was studied (middle part of Figure 74). Thirdly, the commercially available electrolyte with two unknown additives was used and was studied. The findings of all experiments are summarized in the following.

Starting with the FEC_{only}-electrolyte the main evolving gases are CO_2 (up to 2.2 nmol/s) and H_2 (0.15 nmol/s). Hereby, CO_2 is emitted once the cell potential exceeds 2.0 V vs. Li/Li^+, while H_2 is formed at slightly higher potential. The results are in accordance with the literature and can be explained by the reduction of FEC, as shown in Equation (7.1).[277,278] The evolution of H_2 can be traced back to originate from the reduction of water impurities within the cell environment, respectively the

HF which was formed by the reaction of the conductive salt with the trace water, see former chapter 6 for more information about this process.

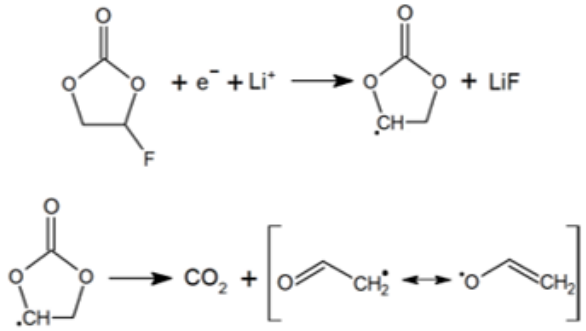

(7.1)

However, H_2 can be also originate from FEC and its accompanied reduction towards VC, as shown in Equation (7.2). The formation of VC might be beneficial, as it is well known, to built a cross-linked SEI layer, due to the reactivity of the sp^2-hybridized C-atom.[278–280] Other gaseous species, like CO or C_2H_4 cannot be observed within this experiment.

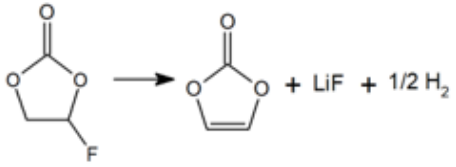

(7.2)

Switching solely to the replicated electrolyte containing EC, EMC, DMC, FEC and $LiPF_6$ (see table 6), the online monitored gas evolution changes. The evolution of comparatively larger amounts of CO_2 (up to 1.9 nmol/s) at the beginning and the subsequent parallel formation of C_2H_4 and CO (maximum with 0.29 nmol/s respectively 0.1 nmol/s) can be observed. It can be assumed that the major peak of CO_2 at the beginning is again caused by the reduction of FEC as shown in the former experiment (see Eq. (7.1)). The subsequent detection of C_2H_4 and CO is most probably caused by the decomposition of EC since it is more likely to be reduced compared to the other linear carbonates DMC and EMC (see also the result part in chapter 6). It is known that the one-electron reduction path leads to the formation of C_2H_4 as can be seen in Equation (6.2). In contrast, the formation of CO can be attributed to the two-electron reduction of EC as highlighted in Equation (6.3).

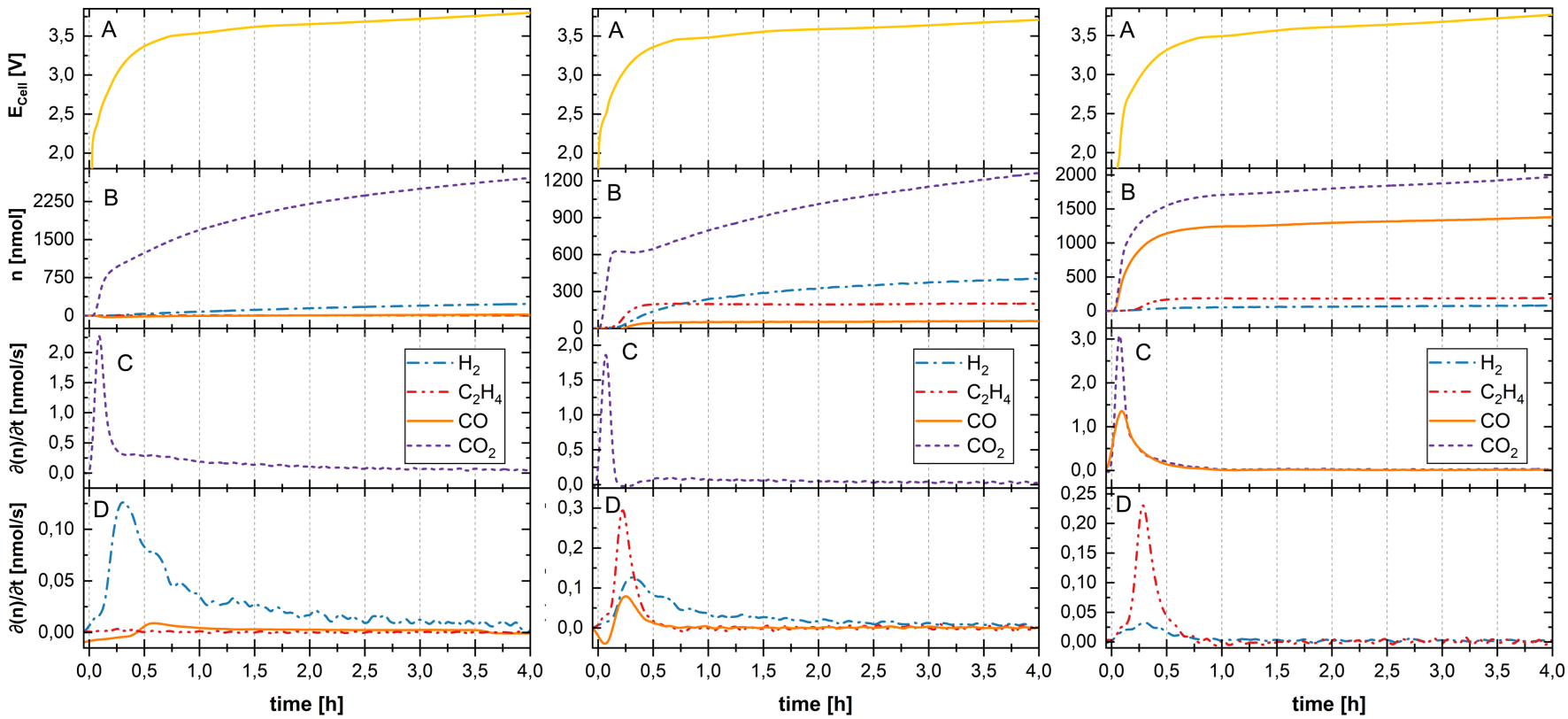

Figure 74: Summary of the conducted experiments with various electrolyte mixtures. Left: Experiment with FEC_{only} electrolyte. Middle: Experiment using a replicate of the electrolyte which is typically used in cylindrical cells, containing EC, DEC, DMC and EMC as carbonate component. Right: Experiment conducted with the commercial electrolyte, where the exact formulation is not known. Experiments were carried out with SiO_x containing negative electrodes and NMC811 as positive electrode. A charging current of C/10 was used and cell temperature was kept at 30 °C. A) cell potential; B) absolute gas evolution in terms of nmol; C & D) gas evolution rate in terms of nmol/s.

Hydrogen arises at the same time as C_2H_4 but reaches its maximum evolution of 0.13 nmol/s slightly later, after which it only slowly levels off again, making it the gas with the second largest ratio in total. As described for the previous experiment, it can be assumed that the formation of H_2 is caused by reactions of trace water. However, in small proportions, probably also by the formation of VC, as shown in equation (7.2). The higher amount of formed H_2 ($\approx$ 400 nmol in the present measurement vs. $\approx$ 230 nmol with FEC_{only}) could correspondingly be attributed to higher amounts of trace water or increased kinetics towards the formation of VC. The latter one is assumed to be more likely, since hydrogen generation in connection with water is considered to occur at a lower potential at the beginning of the lithiation process. Therefore, it could be concluded that the formation of VC from FEC is increased using the present electrolyte mixture compared to FEC_{only}. Nevertheless, in total 1.92 µmol of gaseous products are generated, which is only two-third compared to the FEC_{only}-experiment. The monitored gasses C_2H_4 and CO clearly indicate that, this electrolyte mixture already results in the formation of a SEI layer, which seems to protect the electrode surface from further reactions leading to less gas formation.

Lastly, the gas evolution of the commercial electrolyte was investigated, depicted in the right section of Figure 74. This electrolyte contains the former mentioned carbonates (see replicate), but also two unknown additives, known as WCA, added with a mass fraction of up to 6 wt.% (see table 6). The main evolving gas in this experiment is again CO_2 at rather low potentials with a maximum of 3.0 nmol/s. Parallel to this, CO is detected with up to 1.4 nmol/s. The formation of C_2H_4 occur delayed at around 17 min with a maximum of 0.3 nmol/s and an accompanied evolution of H_2 with max. 0.03 nmol/s. In sum, 3.6 µmol are generated until the end of the formation procedure.

This experiment reveals that significantly more gas is produced in comparison to the earlier performed experiments, which does not contain those additives. The increase is related to the elevated evolution of CO_2 and CO. While the intensity of the gassing rate of C_2H_4 does not show any change. The gassing rate of H_2 seems solely to be reduced. Since the development of H_2 is remarkably lower and is attributed to the presence of trace water, it can be concluded that less trace water was present in this electrolyte or the reduction of FEC towards VC (see Eq.(7.2)) is hindered by the use of those additives. Nevertheless, the described reduction reactions of FEC and EC also occur in this measurement and explain a portion of the herein detected CO_2 evolution and the formation of C_2H_4. The alteration in the composition of the electrolyte, especially due to the presence of the two unidentified additives, is the sole variable that differed between the previous and current measurement. An exemplarily chosen decomposition reaction of a typical used additive, within state of the art battery cells is shown in the following scheme.[281,282] As illustrated in Equation (7.3), the decomposition reaction

of the additive LiDFBOB causes the evolution of CO and CO_2, which could explain the findings within this experiment. However, the exact composition of this electrolyte is still unknown. However, those measurements highlight, that OEMS can be used as unbeatable technique, to gain a deep understanding into battery cells chemistry´s and identifying even the impact of a single additive compound *in-operando*.

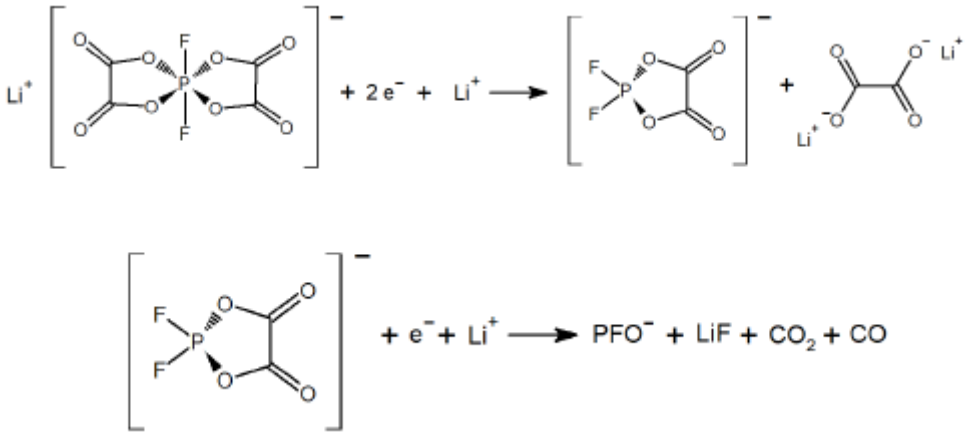

(7.3)

7.3 Study of Automotive Cylindrical Cells

The objective of this section is to highlight a novel analysis concept for cylindrical automotive cells. This concept can be seen as further-development of the former shown analysis of large-format prismatic cells. For the new emerging cell dimension a novel concept was needed, without a special designed adapter, as it was found to be inconvenient within cell production and cell investigation in industrial environment.

The developed cell housing should allow, to analyze any kind of cylindrical cell, either in-house produced or commercially available ones. For the in-house cells, especially the gas evolution during initial charge (formation) within cell production is from great interest which is a very time and cost intensive step during cell production. The analysis of commercial available cells should allow an in-depth study within the true behavior of those cells. OEMS should highlight the importance of advancing the understanding of gassing phenomena in battery cells, which is fundamental for the development of safer and more efficient energy storage systems. Therefore, the OEMS analysis should be used as complimentary method, before the cell underwent the usually applied cell opening procedure, for post-mortem analysis.

For full integration of the analysis of cylindrical cells into the OEMS system it had to make sure that the developed analysis chamber is working accurately, especially when operating with rather strong applied currents. Hence, the analysis chamber underwent several optimization procedures, including tightness and electrical isolation tests, see appendix. As next milestone the cell formation experiment were planned. The benefit in those experiments lies in the fact, that the cells do not have any electrical potential at the beginning and thus a short circuit within the cell setup, would not have such strong impacts. In a second and final investigation a conventional cell at any state of aging should be cycled (charge/discharge) with this setup as proof of concept.

I. Experimental

The used battery cell has a nominal capacity of 32.5 Ah and is based on NMC811 and a composition of SiOx and graphite as active materials of the electrodes (see Tab. 9). Cell production and electrolyte filling was done in BMW in-house prototype production. During the filling process, 43 g of the commercial electrolyte (see Tab. 6) were filled into the cylindrical cell. After filling the cell underwent a soaking and wetting procedure, accordingly to the process scheme, shown in Figure 13. Then the cell was inserted into the developed housing, shown and described in Figure 27. The setup was sealed within glovebox atmosphere and subsequently transferred towards the OEMS system. The overall procedure is very similar to the procedure carried out with large format prismatic cells, see chapter 6 for further information. After a resting period of 4 h, the formation procedure was carried out with a CCCV-protocol starting by applying a charging current of C/20 for 2 h, followed by a charging step of C/10 for 2 h. Due to the amount of gas produced, a gas burette was attached to the chamber in which the cell was placed for the measurement (see also chapter 6). This procedure allows to measure the released gases later via GC. Since for the correct calculation of the produced amount of each gas besides the change of the pressure inside the cell also the change of the volume has to be considered, the final evaluation of the data becomes challenging and was only done for the experiments on prismatic cells.

II. Time-and Potential-Resolved Gas Analysis During Formation

First, results of a single cell formation experiment are shown and explained in detail. Besides the general proof of concept of formation within the developed cell housing, also the comparison of those online results with offline measured gas analysis via GC was performed. Additionally to that, the influence of temperature onto the gas release was conducted and are shown.

Single Formation Procedure at a Glance

Figure 75 shows the time- and potential-resolved gas evolution during formation of a 4695 cylindrical cell. The electrochemical data are shown in the upper Part A. The electrochemical protocol consist of GCPL procedure with 2 h of C/20, followed by 2 h of C/10. A plateau is being formed, once the cell reaches 2.75 V vs. Li/Li^+. Before that a peak within the cell voltage can be seen, most probably due to sluggish kinetics within the cell and higher over potential due to the setup. Part B shows the gas evolution rate, monitored simultaneously on the connected gas buret. Part C shows the time-resolved evolution of the gasses H_2 and CO, while part D shows C_2H_4 and CO_2, respectively .

In general it can be seen, that the gassing consists of two successive processes. During the first, CO and CO_2 are exclusively formed and emitting the cell housing as sharp peak. The monitored evolution on the gas buret indicated a strong evolution rate of up to 11 mL/min. While the gas evolution rate on the gas buret dropped nearly to zero at 30 min. of charging, a slow level of CO_2 and CO was monitored by the OEMS. This behavior can be most probably attributed to mixing phenomena of the individual gasses within the setup. The subsequent formation of H_2 and C_2H_4 is compared to that an elongated process. Signal fluctuations occurring at e.g. 1.8 h are considered artifacts with no definite explanation. Possible factors that impact them include vibrations in the system, the unheated transfer line, and bubble-like release of the gases from the electrolyte.

Comparing the results with those of the experiment with the same electrolyte in the model cell, it can be seen that the ratio of CO_2 to CO has changed markedly towards lower CO_2-proportions. The peaks also exhibit a significantly greater elongation. The reason for the latter one is probably the fact that the gases in the case of the cylindrical battery cell first have to diffuse through the winded electrode stack before they can be detected as part of the volume of the headspace. This also increases the probability of CO_2 that has a high solubility in common electrolyte components to be dissolved and react further. Since CO_2, as previously described, reacts under the formation of SEI forming substances such as lithium oxalate and lithium formate (see eq. 6.2 and 6.9), which are presumably intensified by a higher concentration of CO_2 dissolved in the electrolyte, it can be assumed that the SEI is composed differently in cylindrical cells than in the previously investigated model cell. This is also corroborated by the lower detected ratio of CO_2 to CO compared to the model cell.

The increase in the proportion of H_2 in relation to all other gasses and compared to the model cell is probably due to the increased trace water content inside the cylindrical cell. These findings are in accordance with the results from large-format prismatic cells. It can be assumed that due to the production environment (dry-room) conditions, not the same conditions can be achieved as it is the case for the model cell experiments. It is also worth to mention again, that the anode slurry for the cylindrical cells, was water based. However, after a charging time of 4 h, the gas evolution has mostly stopped.

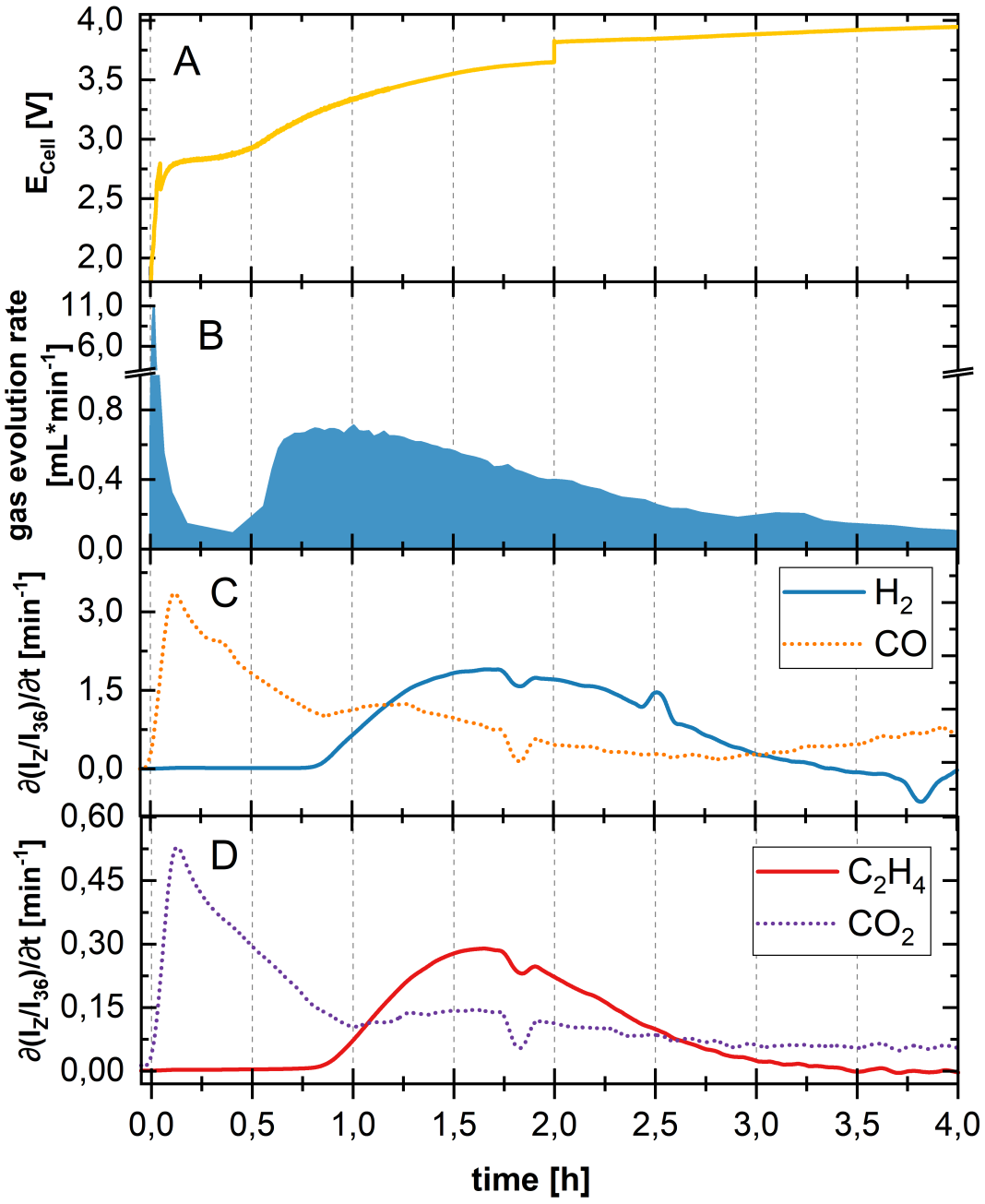

Figure 75: A: Electrochemical data for the applied GCPL with C/20-rate, followed by a C/10-rate, each for 2 h at 25 °C. B: gas evolution rate (mL/min.) monitored on the gas buret; C: first derivative of the normalized mass traces for H_2 and CO to obtain gas evolution rates; D: first derivative of the normalized mass traces for C_2H_4 and CO_2 to obtain gas evolution rates.

Comparison of Online Gas Analytics versus Offline

The comparison between online resolved gas evolution via OEMS and offline measured gas composition via GC was carried out and is depicted in Figure 76. This comparison was also done for the experiments on prismatic cells and the reader is therefore referred to Fig. 65 and its description.

The strongest deviation between both methods can be seen for H_2, with almost 10 % and CO with 6 %. However, several reasons for deviations were already explained in the former chapter and it is expected, that they also play a role within this series. The most important finding there was, that due to the OEMS calculation routine, gasses with a ratio are overestimated, while gasses with a lower partial ratio are generally underestimated. Both failures rely on the fact, that a normalization towards the strongest gas (^{36}Ar) is carried out. Besides this, it can be said that the deviation of H_2 can be most likely attributed due to difficulties of storing the gas inside the gas buret, as hydrogen is well known for leaking through all kind of materials.

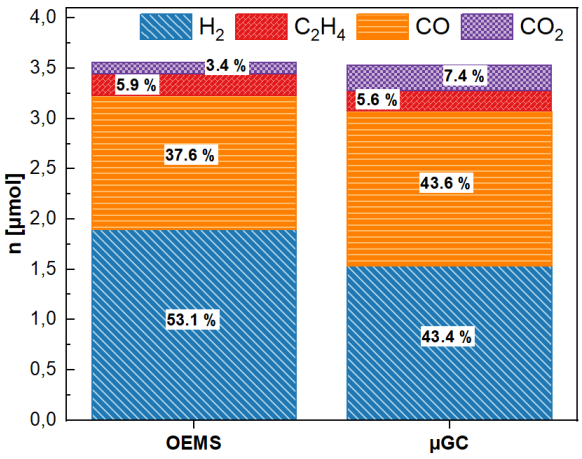

Figure 76: Comparison of the composition of released gases during formation of a 4695 type cylindrical cell. Left: Online measured and integrated results for the OEMS measurement. Right: Offline measured and column separated gas composition measured via GC. The discrepancies are explained within the text and the former investigation on large format prismatic cells, see chapter 6.

Influence of Temperature on the Gas Release

Several formation experiments were performed with cylindrical cells, using the same temperature variation as it was done for the large-format prismatic cells (see chapter 6). The results of the herein performed experiments are meanwhile depicted within Figure 77. The left side highlights the monitored gas evolution on the connected gas buret, the right side shows the partial gas composition, after formation.

In general a higher gas evolution at elevated temperature can be seen for all gasses and can be attributed to faster kinetics of the occurring reactions and the diffusion of the evolved gases within the cell. It seems like that the reduction of FEC is being mostly influenced by the temperature, as more CO_2 is being emitted, following Equation (7.1). The reaction of FEC towards VC, seems to have its maximum at an elevated temperature of 25 °C as more hydrogen percentage are emitted under these conditions through Equation (7.2).

On the other side more CO is being produced, while using the lowest formation temperature of 10 °C. Here, most probably the two electron reduction of EC is taking place, leading to CO as side product (see Eq.(6.3)). Some deviations might be attributed to the different behavior of the gasses in terms of solubility. Even when the gas evolution behavior itself strongly deviates from the prismatic cell evolution, the general behavior of gas amount and composition versus temperature variation is in an overall good comparison to the experiments on prismatic cells, shown in the former chapter.

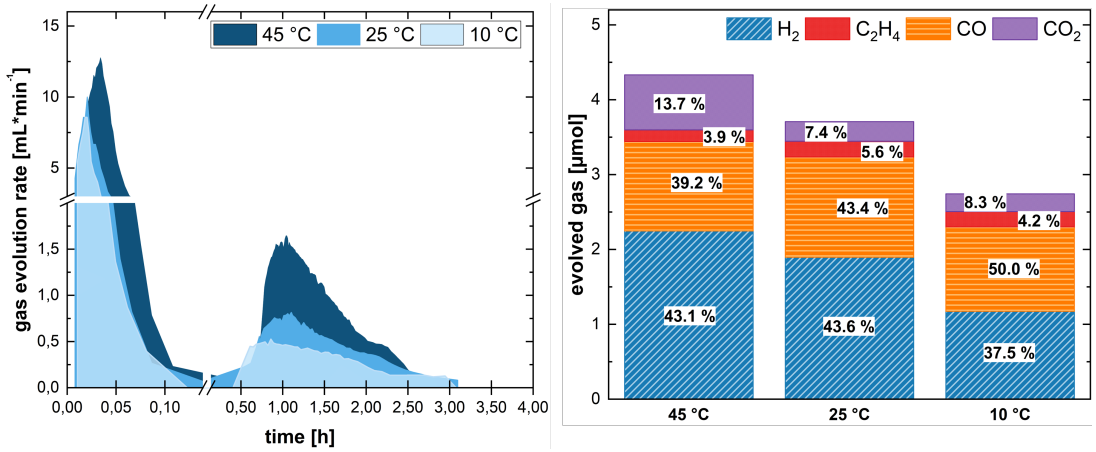

Figure 77: Summary of the conduced formation experiments with large-format cylindrical cells (4695 type). Left: Visual collected gas evolution data from the gas buret. Right: Calculated moles for the individual experiment, using the data from left and the online collected gas composition ratios. Experiments were carried out varying between 10 °C and 45 °C. GCPL with C/20 for 2 h, followed by 2 h with C/10 was applied to all experiments.

III. Time-and Potential-Resolved Gas Analysis of a Conventional 4695 Cell - A Proof of Concept Study -

Apart from analyzing the gassing behavior during the initial charge (formation), the main purpose of the developed cell chamber is the analysis of any available cell at any point of cycle life, e.g. end of life or commercially available ones. Therefore, the cell housing must deal with higher currents, higher cell potentials as well as cells in an inadequate status. It should be mentioned, that large format cells can be dangerous in case of a fatal short circuit. This is especially important, when the anode additionally contains silicon. Therefore, the experiment was carefully conducted and observed all the time, to react immediately. A fatal accident would led to an enormous pressure increase within the semi-closed analysis chamber. A following thermal run-away would lead to serious damage on the overall OEMS system.

Experimental

A battery cell which already went through formation and life cycle test within the BMW test faculty was chosen, as the dimensions as well as materials are well known for this type of cell. However, the total number of charging cycles prior to this experiment is unknown. The cell consist similar to the former used cells of a SiO_x-anode and NMC811 on the cathode side. Besides the linear carbonates DEC and DMC, also EC and FEC are contained as electrolyte. The nominal capacity of the cell is 33 Ah. Prior analysis the cell was discharge to 30 % SOC. Then the cell underwent a piercing procedure, with the tool described in Figure 34. To confirm an accurate piercing and minimizing the risk of short circuits, the cell underwent CT scan, which is exemplarily shown in Figure 35. The piercing occurred within glovebox conditions and the cell was then carefully sealed into a pouch bag for CT-scan under ambient air-conditions. After that, the cell was relocated within the glovebox and transferred into the cell housing (see Figure 27). Finally, the housing was connected to the OEMS system where the time-resolved charging procedure was carried out.

Results

The results of the potential-resolved gas analysis experiment can be seen within Figure 78. Similar to all other experiments within this work a resting period of 4.5 h was conducted, until the mass traces were stabilized. However, as it can be seen within the figure, this assumption is not fulfilled for CO_2. Most probably is the electrolyte vapor pressure still not in its equilibrium. On the other side, electrodes with silicon content are well known for the fact, that a continuous pressure increase due to ongoing side-reactions within the cell might occur. Assuming a pressure increase of 120 pmol/day of CO_2 and a free cell can volume of 10 mL, this would lead to an pressure increase of 0.9 µbar/month, which seems a reasonable low value, as background. However, for

all other mass traces the assumption was fulfilled even more clearly. After the resting period a constant current of 2.2 A was initially used to charge the cell to a potential of 4.25 V vs. Li/Li^+, which was then maintained while adjusting the current until the cell was in total charged by 14.92 Ah.

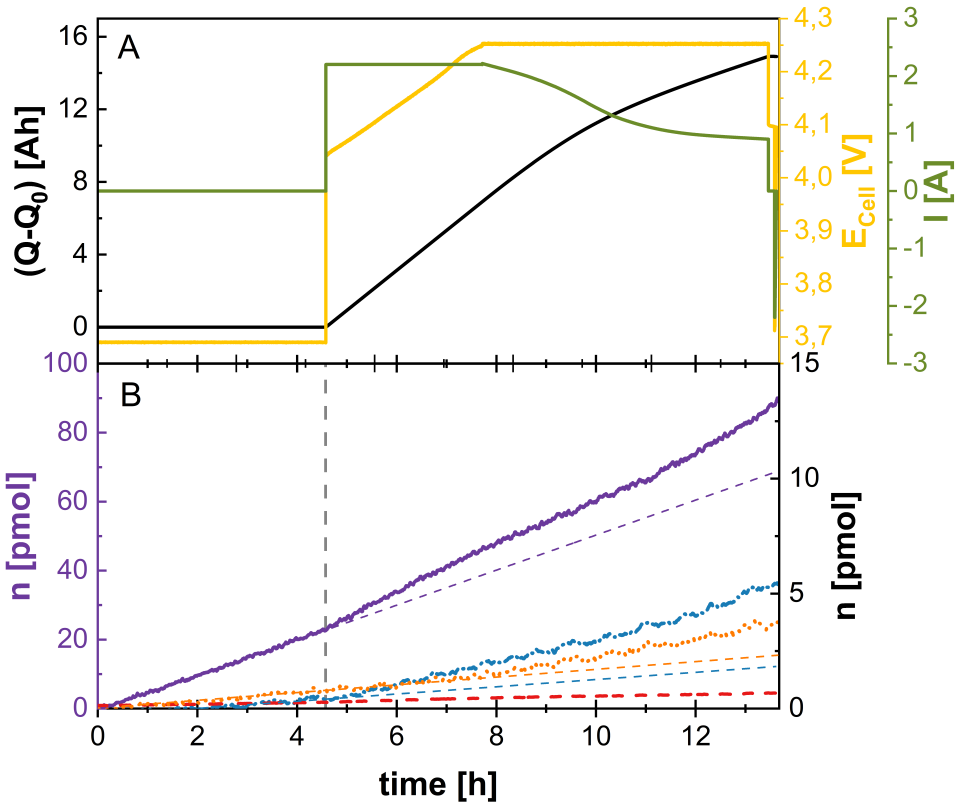

Figure 78: Time- and potential resolved gas analysis of a commercial cylindrical automotive battery cell (4695 format) in the herein developed OEMS chamber. Upper-Figure A: State of charge (black), cell voltage (yellow) and charging current (green) during the measurement. Lower-Figure B: Amounts of the evolving gasses; Left y-axis: CO_2 (purple) and right y-axis: H_2 (blue), C_2H_4 (red), and CO (orange); Gray dashed vertical line: Starting point of charging; thinner dashed lines: Linear fit of the associated gassing curve before the start of the charging process. Experiment was conducted at 30 °C.

The resulting gas evolution during this experiment is as expected significantly lower (range of pmol), as during the former formation experiments. During the charge period (start at the gray dashed line) a change in the evolving gas fractions can be clearly monitored. The gas that increases the most is CO_2 ($\approx$ 90 pmol) with the mentioned linear share of the increase that is observable even before charging begins. An increase in the concentration of H_2 and CO can also be observed during the charge, although to a much lesser degree (CO $\approx$ 4.3 pmol; H_2 $\approx$ 5.5 pmol). An evolution of C_2H_4 is not detectable and was also not expected, as it should be only released when a SEI is formed.

The results are thus similar to those of *Schiele et al.*, who observed the formation of CO_2 and H_2 during the first seven charging cycles of a battery cell with a silicon-based anode and an electrolyte containing FEC and EMC.[46,280] They identified the high volume changes of silicon during charging, due to which the SEI is damaged, as the reason for gas formation during normal charging. In the same measurements with an electrolyte consisting of EC and EMC, by contrast, they found H_2 and C_2H_4 as decomposition products. Since it is also assumed that FEC is almost exclusively reduced in such parasitic reactions, it is considered that its decomposition also causes the development of CO_2 and H_2 in this analysis. The formation of CO_2 can be explained by Equation (7.1) and that of H_2 using equation (7.2), whereby LiF is formed as a further product in both cases. Since it is known that VC, which is also produced during the reduction of FEC (see Eq. (7.2)), it can be also further reduced under CO formation (see Eq. (7.4)),[283,284] its detection is also comprehensible and may only be measurable by the increased formation caused by the comparatively large size of the cell.

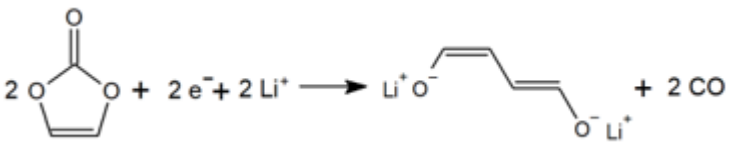

(7.4)

In sum this proof of concept measurement finally shows, that the developed cell housing for large format cylindrical cells, can be used to charge and discharge battery cells under in-operando conditions. Unfortunately, in this proof of concept study the setup had a rather high overpotential and consequently the cell was charged until 4.1 V vs. Li/Li^+. However its working principle was successfully shown. Hence it can be used as novel method, to study the time-and potential-depended gas formation within cylindrical cells in future studies, e.g. above 100 % SOC.

Summary and Discussion

In this Ph.D work[1], a truly unique custom-made online electrochemical mass spectrometry (OEMS)-system was put into operation. Besides the system itself, several smaller electrochemical cells (coin cells) for *in-operando* analysis, as well as the workflow steps within an industrial battery research environment, were newly established. Particular attention was paid towards the analysis of large automotive battery cells (prismatic & cylindrical), which was rarely seen in the past. The various possible settings, excellent adaptability and scalability towards large format cells as well as its full mobility and high technical standards, regarding cleanliness and robustness makes the herein described OEMS system comparable to nothing else.

In the further course of this work, the coin cell approach was used to understand the electrochemical triggered gas evolution reactions down to single electrode-material level. Large-format cells with the same cell chemistry where then used and studied towards their gassing behavior mainly during the critical battery formation procedure (first charging). The automotive cells were produced within BMW´s prototype cell production line and were handed over for *in-operando* studies after cell assembly. Hence, they provided a unique opportunity to study them from their early beginning of life. For both cell sizes two results chapters are available within this work, while the major findings are summarized on the following pages.

Besides manifold examples of OEMS systems and their applications, a clear analytical view on their response-characteristics was missing and therefore given for the first time within this work in chapter 4. Due to the various interactions of the evolving gasses within the cell environment and OEMS configurations, the response-characteristics are a valuable and unique characteristic for each system. Chronoamperometry as a simple electroanalytical method was used to generate a well-defined stimulus for a short time interval to follow the response characteristics of the respective experimental configuration. The two parameters, namely the applied potential and the pulse duration, were used to precisely trigger the electrochemical reactions, when charging a battery

[1] In-Operando Investigations on Lithium Ion Battery Cells to Improve the Performance for the Use in Electric Vehicles

cell (NMC811/graphite in LP40) for the first time. The simultaneously recorded mass spectra were used to evaluate the responding gassing behavior. The response time determination demonstrated that a custom-made highly porous electrode configuration had an overall better response behavior within seconds. Differences for the respective gasses of interest, where found compared to a standard foil-based current collector configurated cell.

Following the characterization of the OEMS system, the further developed model cell (coin cell basis) was then used in a second study. Here, the impact of electrode densification, onto the electrochemical properties as well as the accompanied gas evolution of the poly-crystalline transition metal oxide $Li[Ni_{0.9}Mn_{0.04}Co_{0.06}]O_2$ so-called NMC955, was investigated. Experiments were carried out on highly porous mesh or custom-made laser-perforated current collector foils using EC_{only} (1.5 M $LiPF_6$ + EC) electrolyte. Static compression of electrodes revealed the expected behavior in terms of decreasing porosity and electrode thickness, as identified via SEM. Analysis of the electrochemistry within a half-cell configuration, while delithiating the NMC up to 4.8 V vs. Li/Li^+ revealed a rather strong dependence of the cells capacity on the degree of compaction, while the volumetric energy density was increased.

The potential resolved gas evolution showed reduced amounts of gas (CO_2, CO, and O_2) for densified electrodes, as the porosity is being reduced, while compacting the electrode. A large portion of the released CO_2 was identified to originate from Li_2CO_3 impurities. Nevertheless, significant amounts of other gases, e.g. O_2 from the NMC-lattice reconstruction were detected for more porous electrodes. Hence, the degree of compaction seems to influence the reaction between highly reactive lattice oxygen and its attack on single electrolyte components. Due to the fact that future battery cell electrodes are more and more densified, the link between compaction and gas release needs to be studied in more depth. It is assumed that at an certain degree of compaction, the CAM-particle breakdown might be increase the surface area. Following that, more interactions and side-reactions, followed by an increase of gassing could be observed. This issue could lead to a large-pressure increase over lifetime of the battery cells. A pressure increase could end in collapse of the safety vent of the battery cell and its shut-down, finally leading to a decrease in km-range of the individual electric vehicle. Apart from providing novel insights into the compaction-dependent gas evolution within electrodes, this work demonstrated that OEMS can be used as a powerful *in-operando* technique to investigate the impact of even single process steps within the LIB production chain onto the final performance of the cell.

Building on the knowledge and experience gained from the model cell investigations, the third and fourth chapter are subsequently dealing with large format cells. These works unraveled for the first time the true internal behavior during the critical SEI formation

procedure. *In-operando* studies were carried out, by the time-and potential-resolved detection of gaseous side-products due to the electrochemical breakdown of electrolyte components on the negative electrode surface area. Hence, unique insights into the nature, extent, and duration of those reactions including thermodynamic unstable intermediate products and their dependence of external parameters, e.g. temperature, were gained.

For large format prismatic cells (chapter 6) a specially designed adapter was integrated within the battery cell´s lid during cell production. This adapter allowed to connect the cell directly to the OEMS system. The investigation was carried out with identical chemical compositions of the model cell and prismatic cell (NMC811//graphite; LP40), to proof the adaptability and scalability of the setup. Although the composition and amounts of gas were found to be highly comparable, even when validated against *ex-situ* analysis (GC), the gas release rate was found to be lower from the larger cell size and likely limited by gas bubble transport through the electrode stack of the cell. Higher temperatures were found to accelerate the formation process, but also alters the composition and extent of gas released. Although the gassing time is shortened, a higher temperature induces stronger evolution of C_2H_4 and H_2 gas and indicates that a more organic and porous SEI is formed.
For the newly emerged cylindrical cell format (chapter 7) a more sophisticated and universal usable cell housing was developed. In this housing the cell can be inserted and investigated *in-operando*, without any additional adapter unit. Therewith this approach can be integrated within battery cell production line´s to ultimately analyze the formation step *in-line*, regarding various cell chemistries and external parameters. The formation step of those cells was more advanced, compared to prismatic cells. Following that, the investigations were compared to model cell experiments, to understand the effect of the rather complex electrolyte mixture and new cell format. Here significant differences were found, due to the more complex cell system (NMC811//C/SiO_x), compared to prismatic cells. However, overall similar behavior towards various temperatures during formation were found.

The usually unknown first charging/discharging protocol is a hidden gem for each battery producer, as the SEI formation is a critical and lifetime determining production step. Due to the slow and cautious procedure it usually presents the bottleneck in cell production as it can last for hours up to days. Hence, the findings within this work, can help battery cell producer to improve the cost-intensive formation procedure. This can ultimately lead to lower battery pack prices and thus making electric vehicles even more affordable. Last but not least, the conclusion which where drawn from the gas release towards the composition of the SEI layer are valuable inputs to further optimize the performance and lifetime of LIB´s.

In the last part it was proven, that the developed cell housing for cylindrical cells can be also used to investigate any available cylindrical cell (type 4695) *in-operando* during normal cycling, where less gassing is being expected. The introduced setup can be used to understand which conditions (Temperature, Charging rate, Upper/Lower cut-off voltage) trigger the parasitic side-reactions in large format cells.

The ability of the herein developed OEMS system provide a fundamental level of detailed, time-resolved information on the complex interplay between single materials as well as manufacturing process steps and their influence onto the electrochemical performance. Special emphasis is paid towards parasitic side reactions in form of gas evolution reactions. Apart from novel insights into the formation processes of large-format automotive cells, the herein developed and described setup provides unique opportunities to further optimize and accelerate battery production, ultimately reducing the cost of each cell, while further improve their performance and longevity. OEMS-analysis can be used as a critical tool for advancing the state-of-the-art battery research and development.

Outlook

Further studies on this instrument should deal with the following topics. I.) System optimization, II.) Systematic in-depth studies on material level, and III.) Studies on the gas evolution behavior of large-format cylindrical cells in regards of typical used operating parameters and beyond.

Firstly, further efforts should be taken to improve the quality and quantity of the measurements. The precision and selectivity of the gas analysis would significantly benefit from lower background signals, especially when dealing with large-format cells. Hence, a heating unit of the interface region should be implemented. Alternatively a cold-trap could be used. Experiments on large-format cells also highlighted the need for a more powerful potentiostat. Additionally, a larger climate-chamber would be beneficial as it simplifies the connection between electrochemical cell and OEMS system.

Secondly, a state of the art model cell was employed and was used to study the electrochemical behavior on material level. In order to speed up those investigations, more model cells from the same type should be built. A personal recommendation would be at least three. One for the current measurement, one for preparation within glovebox and one which underwent cleaning/drying procedures or just as spare cell. If these are established, many research questions from industrial viewpoint can be processed within the near future. *In-operando* gas analysis could be used in a same way as typical research investigations on swagelok-cell level looks like. Numerous gas evolution processes were described and some of them were explored within this work. However, to further optimize future battery cells more of those parasitic side-reactions need to be studied. Hence, the OEMS could be used to explore and to establish a database of gas evolution reactions of various materials. On the negative electrode side various carbon materials including carbon additives, CNT´s, surface coatings and carbon blacks could be investigated as their surface morphology will influence the SEI film formation. The continuous development of new (high energy) CAM´s provide also great potential for further OEMS studies. Here especially the context of recycled CAM´s (in-process or end-of life recycling) could play a crucial role in the near future.

Due to the European battery regulation act, battery manufacturers will be forced to use recycled materials within their cells. However, the recycling method and hence the morphology might be different to the original material. Here, OEMS can provide detailed insights within a short spare of time. Furthermore, new electrolyte formulations with ever increasing amounts of solvents, salts and additives provide great potential for unknown side-reaction and hence great opportunities, where OEMS can be used to study those materials under in-operando conditions to track their role during SEI film formation. Lastly, all separate studies could be used to build a reference database for the selection of cell materials and components used for the development of large-format cells. Further efforts should be also taken into account to investigate the industrial relevant questions in terms of process parameters during cell production. As it was shown based on the calendering process step, many of the herein described production steps have an influence on the battery cell performance and hence also their degradation. Here, the OEMS could be used to find the relevant parameter which has to be tuned in order to built cells with good performance as well as decreased costs, without the need of typical used long-term cycling procedure. For example the formation step, calendering, laser cutting (thermal impact), dry-coating/multi-layer coating techniques, and electrolyte wetting time &-temperature onto the degradation behavior should be investigated in the near future.

Thirdly, even if the analysis of large-format cells is challenging and the complexity in materials and electrolyte is ever increasing, the method development should be continued. As the proof of concept study was done for the herein described cell housing, which allows to analyze 4695 and 46110 cylindrical cells, now several important questions still remain open and can be answered by a further use of this setup. Relevant questions would be to investigate the upper/lower cut-off voltage, the influence of temperature during charge/discharge cycles as well as influence of the current density in terms of fast charging topics. A special focus can be also set again onto the formation procedure, as here solely the cell temperature as a parameter was investigated. However, the question of "when is the right time to seal the cell" will always be popping up, while changing the cell chemistry or electrolyte system. Furthermore, several other parameters, like applied voltage or optimized charging protocols could be investigated, to reduce the costly time in dry-room environments as much as possible.

All in all many questions arises with further battery cell development, especially in the automotive sector, where a lot of competition is taking place for new and safe future battery cells as well as improved production processes, as manufacturing costs are a crucial part of cell development in this segment. This makes the herein developed OEMS system to a suitable tool as it can provide an in-depth understanding within battery cells in a short spare of time. However, the mechanisms of electrolyte degradation and

concomitant gas evolution could be much better understood when both, gas and other reaction by-products are determined by combining several techniques, e.g. OEMS with other surface-sensitive techniques such as XPS, x-ray diffraction (XRD), in-situ Raman, and fourier transform-infrared spectroscopy (FT-IR)-microscopy, as it was partially done within this work. Last but not least, in situ gas analysis is expected to be useful in other future energy storage system, e.g. Li-S batteries and ASSB.

Appendices

Manual Working Steps of the Adapter Integration into the Lid of a Prismatic EV32 Cell

The inhouse production of EV32, allowed the unique possibility to integrate an adapter for gas analysis directly into the cell housing. These working steps were carried out manually, prior cell assembly and are shown within Figure 79.

Figure 79: Manual working steps of the adapter integration into the lid of a prismatic cell, prior cell assembling. First the position of the adapter was defined with a metal scriber, to secure precise drilling process (II). Then the parts were technically cleaned, before the adapter was inserted and secured with a bolt nut, from the inside of the lid. The bolt nut was heated up, using a heat gun, to melt it into the plastic of the lid.

Connection Principle of the Gas Burette for Formation Studies on Large–Format Automotive Cells

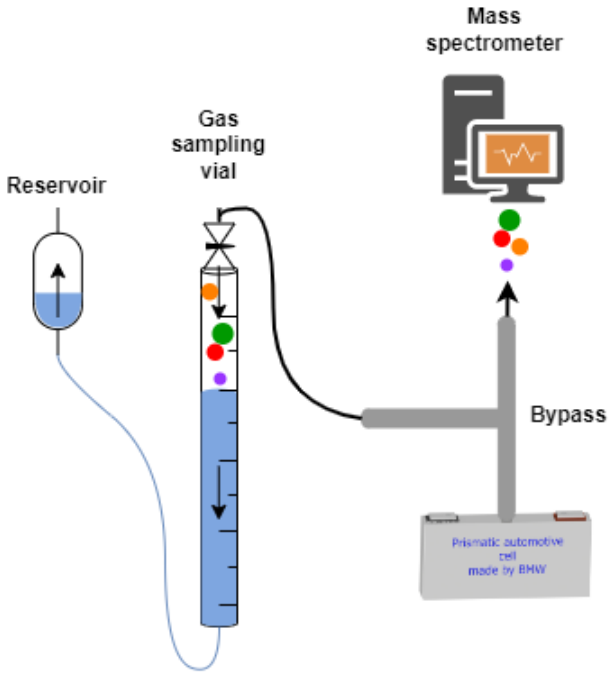

Figure 80: Experimental OEMS Setup for gas analysis on large format cells, with integrated swagelok-adapter. The gases were sampled within a bypass-arrangement and collected in a glas sampling tube (gas buret).

Exemplary Offline GC Measurement Routine

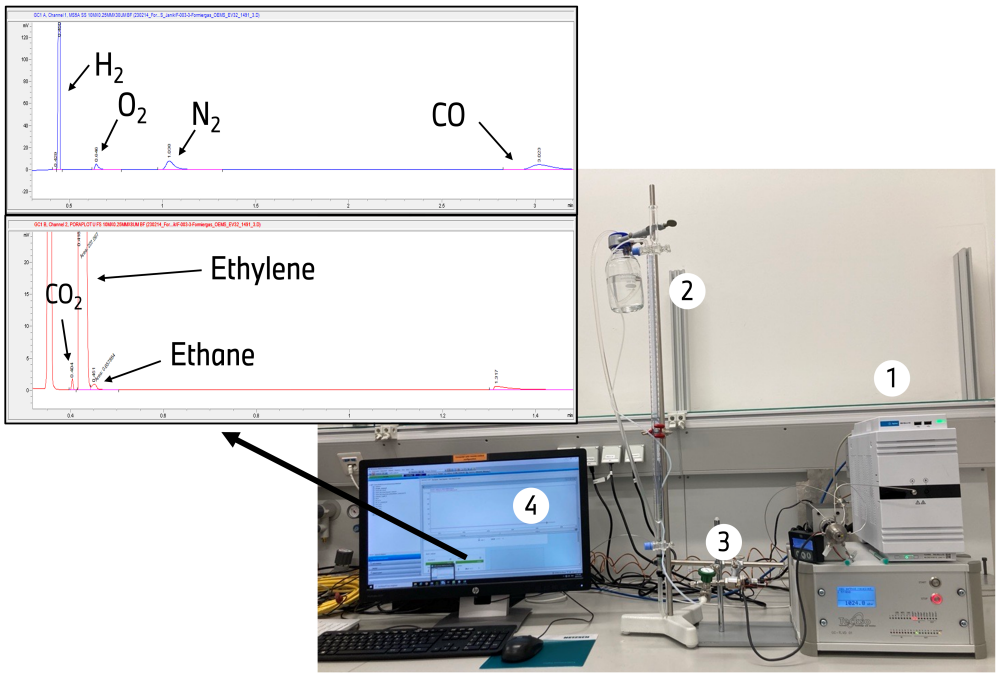

Figure 81: Example of an typical µGC measurement of the collected formation gasses from large-format cells. 1) µGC system; 2) gas buret with formation gas; 3) interface; 4) computer and software. The red and blue chromatograms are obtained due to the two different columns, used to separate the different gasses (separation of hydrocarbons, e. g. C_2H_4 from smaller gases, e.g. H_2, N_2).

Table 12: Data of several components identified via HPLC-Orbitrap-MS measurement of extracted electrolyte samples from automotive cells after cell formation within chapter 6.

Component	**Molecular Formula**	**$[M+H]^+$ [Da]**	**Retention time [min.]**	**Temperature [°C]**	**Peak area [10^6*counts]**
Diethyl-2,5-dioxahexan-dicarboxylat (DEDOHC)	$C_8H_{14}O_6$	206.08	6.50	10	0.5416
				25	0.5673
				40	0.6118
Diethyl-oxydi-2,1-ethanediyl-biscarbonate	$C_{10}H_{18}O_7$	250.1	6.66	10	33.457
				25	38.522
				40	35.723
Oligomeric tri-carbonate (di-ethyl terminated)	$C_{11}H_{18}O_9$	294.2	7.74	10	18.432
				25	20.675
				40	16.493
Oligomeric tetra-carbonate (di-ethyl terminated)	$C_{14}H_{22}O_{12}$	382.3	7.98	10	7.078
				25	10.356
				40	8.524

Table 13: Overview on OEMS experiments either with the model cell or large format cell. † visual collected data; ‡ Full Width at Half Maximum

Parameter	unit	species	model cell	Large format cell		
Temperature	°C		25.0	10.0	25.0	40.0
released gas volume†	mL		/	212	280	340
max. gas evolution rate $\dot{V}$†	mL*min^{-1}		/	10.5	13.0	18.5
Area ratio I_x/I_{36} within 4 h	%	H_2	5.76	10.4	13.8	12.1
		C_2H_4	78.0	62.0	71.0	71.6
		CO	15.4	27.0	14.9	15.9
		O_2	0.02	0.52	0.05	0.00
		CO_2	0.83	0.13	0.24	0.50
Area ratio of I_x/I_{36} at 3.3 V	%	H_2	6.35	9.08	12.0	9.99
		C_2H_4	70.7	64.3	70.4	79.6
		CO	12.5	26.5	17.2	9.76
		O_2	1.53	0.00	0.05	0.06
		CO_2	-8.9	0.10	0.26	0.48
Peak maximum & FWHM‡ **of I_x/I_{36}**	min.	H_2	15.2 & 25.4	53.0 & 28.9	45.1 & 43.1	37.5 & 37.4
		C_2H_4	15.8 & 17.2	46.1 & 34.0	39.8 & 39.9	29.3 & 30.8
		CO	13.7 & 13.8	42.9 & 39.2	32.8 & 37.3	27.5 & 30.8
		O_2	/	/	39.9 & 41.5	33.0 & 34.1
		CO_2	13.5 & /	41.9 & 40.2	39.7 & 43.1	29.2 & 31.8

Tightness and Leakage Rate Determination of the Automotive Cell Housing for Cylindrical Cells

To test the tightness of the housing, it was placed inside the climate chamber of the OEMS at 25 °C and an absolute pressure of 1.78 bar argon was applied. The pressure drop was then recorded over a time of 65 hours by the attached pressure sensor. As shown in Figure 15, the measured value decreases approximately linear (R2 = 0.96394). With a pressure drop of about 0.19 mbar/h and the known volume of the chamber (179.52 mL), the leakage rate can be calculated (Eq. 1)
to 9.5E-6 mbar*L/s.

$$Q_L = \frac{\Delta p \cdot V}{\Delta t} \tag{1}$$

As a result, the level of tightness of the chamber reaches the classification of oil-tight (leckrate). The next higher level would be gas-tight (leckrate).[105] Since further steps to improve tightness, such as increasing the number of screws that hold the cover to the rest of the chamber, would often be contrary to the interest of simply opening and closing the chamber repeatedly to place the battery cell in it, this level of tightness is considered adequate. However, other approaches, such as varying the gasket material, would be conceivable and could be investigated in the future to increase the tightness. It should also be noted that the applied test conditions were harsher than during normal OEMS measurements due to the significantly higher internal pressure at the beginning.

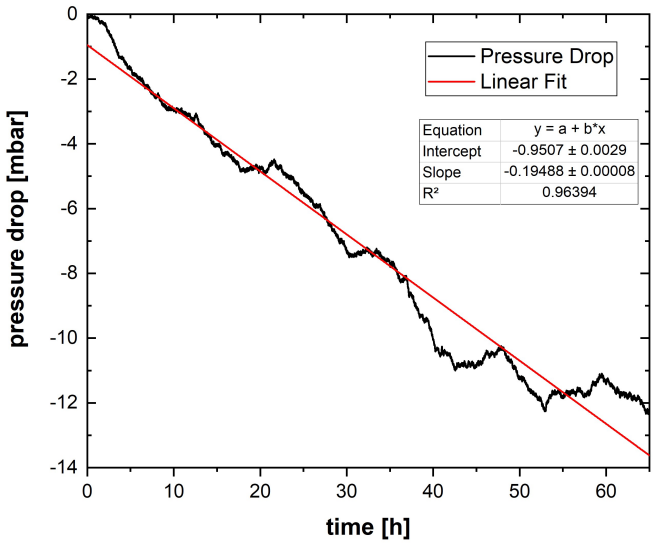

Figure 82: Pressure drop (black curve) versus time for the sealed and empty cylindrical cell housing to validate the tightness and determine the leakage rate. Linear regression (red) was performed in order to allow an accurate leakage rate determination.

Scientific Contributions

A.1 Published Manuscripts

1. **J. Scharf**, C. von Lüders, F.-M. Matysik, C. Misiewicz, J. Wandt, E. J. Berg, Gas Evolution in Large-Format Automotive Lithium-Ion Battery Cells during Formation: Effect of Cell Size and Temperature, Journal of Power Sources, 603, 234419, **(2024)**.

2. **J. Scharf**, F.-M.- Matysik, Study of the response characteristics of an online electrochemical mass spectrometry system for gas analysis of lithium-ion cells using chronoamperometry, Monatshefte für Chemie - Chemical Monthly, 154, 1025–1033, **(2023)**.

3. **J. Scharf**, M. Kübler, V. Gridin, W.D.Z. Wallace, L. Ni, S.D. Paul, U.I. Kramm, Relation between half-cell and fuel cell activity and stability of FeNC catalysts for the oxygen reduction reaction, SusMat., 2:630–645, **(2022)**.

A.2 Conference Oral Presentations

1. "Gas Analysis of Large-Format Automotive Lithium-Ion Battery Cells during Formation", 243rd Conference of the Electrochemical Society (ECS); Abstract# A02-0626, Boston, USA, 28. May to 2. June **2023**.

2. "Interfacing mass spectrometry with electrochemistry in the field of industrial battery research; Response time determination of an online-electrochemical mass spectrometry (OEMS) setup"; 19th International Student Conference of Modern Analytical Chemistry, Prague, Czech Republic, 14.-15. September **2022**.

A.3 Poster Presentations

1. J. Scharf, F.-M. Matysik, "Monitor the decomposition of Cathode Active Materials in high voltage regimes of Lithium-Ion Batteries by the use of Online Electrochemcial Mass Spectrometry", Analytica Conference, April 09-12, **2024**, Munich, Germany.

2. J. Scharf, C. Hupbauer, M. Laifi, M. Leitl, J. Wandt, E. J. Berg, F.-M. Matysik, "Monitor the gas evolution of automotive Lithium-Battery-Cells during operation by the use of online electrochemical mass spectrometry", 7^{th} Electrochemistry Conference, September 27-30., **2022**, Berlin, Germany.

3. J. Scharf, F.-M. Matysik, "In Quest of Battery Degradation - using online electrochemical mass spectrometry", BMW Dialogday for PhD Students, September 14., **2022**, Munich, Germany.

4. J. Scharf, C. Hupbauer, M. Laifi, M. Leitl, J. Wandt, E. J. Berg, F.-M. Matysik, "Online electrochemical mass spectrometry (OEMS) in the field of Industrial Battery Research", Analytica Conference, June 21-23, **2022**, Munich, Germany.

Curriculum Vitae

Janik Scharf

*23.11.1992
in Marburg/Lahn
Janik.Scharf@t-online.de

Education

May 21 – April 24 **Doctoral Thesis Chemistry (Dr. rer. nat.)**, *BMW Group*, Munich
- Cooperation of the BMW Group, University of Regensburg Germany (Analytical Chemistry), and University of Uppsala Sweden (Structural Chemistry)

Oct. 18 – May 20 **Master of Science (Chemistry)**, *Technical University of Darmstadt*
- Thesis: Effect of Pyrolysis Temperature and Duration on Fuel Cell Performance and Composition of the Fe-N-C Catalysts

Oct. 14 – Sept. 17 **Bachelor of Science (Chemistry)**, *Technical University of Darmstadt*
- Thesis: Nozzle optimization for preparation of metal clusters in a molecular beam

Sept. 11 – Apr. 14 **Apprenticeship as Lab technician**, *Merck Group*, Darmstadt
- Finishing prematurely after 3 years with an exam by the Chamber of Commerce and Industry

Vocational Experience

May 24 – current **Sustainability Specialist High Voltage Battery Pack (HVS)**, *BMW Group*, Munich
- Responsibility for HVS/electronic recycling topics in the context of research & pre-development
- HVS-requirement management for sustainability & recycling
- Evaluation of sustainability (CO_2/secondary material share) for future battery cells

Oct. 20 – April 21 **Sales Co-worker**, *IKEA Germany*, Eching
- Customer service and sales in the textiles department

Oct. 18 – Sept. 19 **Research assistant**, *Working group of Jun. Prof. Dr. U. Kramm*, TU Darmstadt
- Development and Optimization of nonprecious catalysts for the oxygen reduction reaction and their electrochemical characterization, e.g. cyclic voltammetry, fuel cell tests, rotating ring disc electrode setup (RRDE)

Apr. 18 – Sept. 18 **Lab technician**, *Merck Group*, Darmstadt
- R&D in the department of medicinal chemistry
- Synthesis of biologically active substances in the department of medicinal chemistry, both on a synthesis scale from a few grams and to release substances on a milligram scale, as well as their purification and characterization

Apr. 14 – Sept. 14 **Lab technician**, *Merck Group*, Darmstadt
- R&D of new OLED materials reaching from gramm to kilogramm scale
- Typical analytical measurements and evaluation, e.g. NMR, HPLC-MS, stability measurements

International Experience

Nov. 23 – Dec. 23 **Doctoral Educational Trip**, *People's Republic of China*

- Self-organized trip within the doctoral network at BMW
- BBA production facility in Shenyang and BMW technology office in Shanghai
- Archermind Technology Hub in Nanjing
- Exchange with the Northeastern University Shenyang and Tongji University in Shanghai

Aug. 17 – Dec. 17 **Self organized Internship**, *Syft Technologies™*, Christchurch, New Zealand

- Production of SIFT-mass spectrometers (**S**elected-**I**on-**F**low-**T**ube)
- Programming of a data search and extraction tool using Python
- Organization of events, trade fairs and the European roadshow

Jan. 14 – Apr. 14 **Leonardo da Vinci Exchange Program**, *Merck Ltd.*, England

- Acquisition of professional knowledge in an international frame
- Synthesis of new and existing CLC mixtures (Cholesteric Liquid Crystals)

Awards

2016 **August-Wilhelm-von-Hofmann Foundation**, *German Chemical Society (GdCh)*

2022 **Deans Award for the best presentation**, *18th International Student Conference*, Prague

Computer Skills

Basic	SAP, Python
Intermediate	Microsoft Offices, Reaxys, MestreNova
Advanced	Origin, Latex, AutoCAD

Bibliography

[1] IEA World Energy Outlook 2023. Access: 06/2024; https://www.iea.org/reports/world-energy-outlook-2023.

[2] UBS How much oil did you consume today? Access: 06/2024; https://www.ubs.com/us/en/wealth-management/insights/market-news/article.1600665.html#:~:text=One%20barrel%20of%20oil%20contains,consumption%20is%20around%202.01%20liters.

[3] The World Factbook - Petroleum. Access: 09/2024; https://www.cia.gov/the-world-factbook/field/petroleum/.

[4] Blomgren, G. E. *Journal of The Electrochemical Society* **2016**, *164*, A5019.

[5] Andre, D.; Kim, S.-J.; Lamp, P.; Lux, S. F.; Maglia, F.; Paschos, O.; Stiaszny, B. *Journal of Materials Chemistry A* **2015**, *3*, 6709–6732.

[6] Schmuch, R.; Wagner, R.; Hörpel, G.; Placke, T.; Winter, M. *Nature Energy* **2018**, *3*, 2058–7546.

[7] Li, W.; Erickson, E. M.; Manthiram, A. *Nature Energy* **2020**, *5*, 2058–7546.

[8] Lithium-Ion Battery Pack Prices Hit Record Low. Access: 09/2024; https://about.bnef.com/blog/lithium-ion-battery-pack-prices-hit-record-low-of-139-kwh/.

[9] Der neue vollelektrische Mini Cooper. Access: 09/2024; https://www.mini.de/de_DE/home/range/electric.html.

[10] Tesla Model 3. Access: 09/2024; https://www.tesla.com/de_de/model3.

[11] Xu, K. *Chemical Reviews* **2014**, *114*, 11503–11618, PMID: 25351820.

[12] Goodenough, J. B.; Kim, Y. *Chemistry of Materials* **2010**, *22*, 587–603.

[13] Goodenough, J. B.; Park, K.-S. *Journal of the American Chemical Society* **2013**, *135*, 1167–1176, PMID: 23294028.

[14] Nishi, Y. *Journal of Power Sources* **2001**, *100*, 101–106.

[15] Andre, D.; Hain, H.; Lamp, P.; Maglia, F.; Stiaszny, B. *Journal of Materials Chemistry A* **2017**, *5*, 17174–17198.

[16] Lu, J.; Chen, Z.; Pan, F.; Cui, Y.; Amine, K. *Electrochemical Energy Reviews* **2018**, *1*, 35.

[17] Goriparti, S.; Miele, E.; De Angelis, F.; Di Fabrizio, E.; Proietti Zaccaria, R.; Capiglia, C. *Journal of Power Sources* **2014**, *257*, 421–443.

[18] Kozen, A.; Lin, C.; Pearse, A.; Schroeder, M.; Han, X.; Hu, L.; Lee, S.; Rubloff, G.; Noked, M. *ACS Nano.* **2015**, *23*, 5884–92.

[19] Xu, W.; Wang, J.; Ding, F.; Chen, X.; Nasybulin, E.; Zhang, Y.; Zhang, J.-G. *Energy and Environmental Science* **2014**, *7*, 513–537.

[20] Winter, M.; Besenhard, J. O.; Spahr, M. E.; Novák, P. *Advanced Materials* **1998**, *10*, 725–763.

[21] Peled, E.; Menachem, C.; Bar-Tow, D.; Melman, A. *Journal of The Electrochemical Society* **1996**, *143*, L4.

[22] Nishi, Y. *The Electrochemical Society Interface* **2016**, *25*, 71.

[23] Besenhard, J. O.; Fritz, H. P. *Angewandte Chemie int. Edition in English* **1983**, *22*, 950–975.

[24] Dahn, J. R. *Physical Review B* **1991**, *44*, 9170–9177.

[25] Zampardi, G.; La Mantia, F. *Batteries & Supercaps* **2020**, *3*, 672–697.

[26] Buqa, H.; Golob, P.; Winter, M.; Besenhard, J. *Journal of Power Sources* **2001**, *97-98*, 122–125.

[27] Shu, Z. X.; McMillan, R. S.; Murray, J. J. *Journal of The Electrochemical Society* **1993**, *140*, 922.

[28] Metzger, M.; Strehle, B.; Solchenbach, S.; Gasteiger, H. A. *Journal of The Electrochemical Society* **2016**, *163*, A798.

[29] Peled, E. *Journal of The Electrochemical Society* **1979**, *126*, 2047.

[30] Fong, R.; von Sacken, U.; Dahn, J. R. *Journal of The Electrochemical Society* **1990**, *137*, 2009.

[31] Winter, M.; Novák, P.; Monnier, A. *Journal of The Electrochemical Society* **1998**, *145*, 428.

[32] Keil, P.; Jossen, A. *Journal of Energy Storage* **2016**, *6*, 125–141.

[33] Liu, Q.; Du, C.; Shen, B.; Zuo, P.; Cheng, X.; Ma, Y.; Yin, G.; Gao, Y. *RSC Advances* **2016**, *6*, 88683–88700.

[34] Zhao, B.; Ran, R.; Liu, M.; Shao, Z. *Materials Science and Engineering: R: Reports* **2015**, *98*, 1–71.

[35] Sun, X.; Radovanovic, P. V.; Cui, B. *New Journal of Chemistry* **2015**, *39*, 38–63.

[36] Zhao, B.; Ran, R.; Liu, M.; Shao, Z. *Nature Communications* **2011**, *2*, 516.

[37] Ronci, F.; Reale, P.; Scrosati, B.; Panero, S.; Rossi Albertini, V.; Perfetti, P.; di Michiel, M.; Merino, J. M. *The Journal of Physical Chemistry B* **2002**, *106*, 3082–3086.

[38] Zhu, N.; Liu, W.; Xue, M.; Xie, Z.; Zhao, D.; Zhang, M.; Chen, J.; Cao, T. *Electrochimica Acta* **2010**, *55*, 5813–5818.

[39] Bernhard, R.; Metzger, M.; Gasteiger, H. A. *Journal of The Electrochemical Society* **2015**, *162*, A1984.

[40] Nesper, R. *Progress in Solid State Chemistry* **1990**, *20*, 1–45.

[41] McDowell, M. T.; Lee, S. W.; Nix, W. D.; Cui, Y. *Advanced Materials* **2013**, *25*, 4966–4985.

[42] Obrovac, M. N.; Chevrier, V. L. *Chemical Reviews* **2014**, *114*, 11444–11502, PMID: 25399614.

[43] Wetjen, M.; Pritzl, D.; Jung, R.; Solchenbach, S.; Ghadimi, R.; Gasteiger, H. A. *Journal of The Electrochemical Society* **2017**, *164*, A2840.

[44] Ding, Y.; Cano, Z.; Yu, A.; Lu, J.; Chen, Z. *Electrochemical Energy Reviews* **2019**, *2*, 1.

[45] Key, B.; Bhattacharyya, R.; Morcrette, M.; Seznéc, V.; Tarascon, J.; Grey, C. *Journal of the American Chemical Society* **2009**, *131*, 9239–49.

[46] Schiele, A.; Breitung, B.; Mazilkin, A.; Schweidler, S.; Janek, J.; Gumbel, S.; Fleischmann, S.; Burakowska-Meise, E.; Sommer, H.; Brezesinski, T. *ACS Omega* **2018**, *3*, 16706–16713, PMID: 31458300.

[47] Qi, Y.; Harris, S. J. *Journal of The Electrochemical Society* **2010**, *157*, A741.

[48] Liang, B.; Liu, Y.; Xu, Y. *Journal of Power Sources* **2014**, *267*, 469–490.

[49] Mansour, A. N.; McBreen, J.; Melendres, C. A. *Journal of The Electrochemical Society* **1999**, *146*, 2799.

[50] Boukamp, B. A.; Lesh, G. C.; Huggins, R. A. *Journal of The Electrochemical Society* **1981**, *128*, 725.

[51] Daily metal spot prices. Access: 01/2024; `https://www.dailymetalprice.com/metalprices`.

[52] Manganese Price. Access: 01/2024; `https://www.metalary.com/manganese-price/`.

[53] Mizushima, K.; Jones, P. C.; Wiseman, P. J.; Goodenough, J. *Solid State Ionics* **1981**, 171–174.

[54] Manthiram, A. *Nature Communications* **2020**, *55*, 2041–1723.

[55] Zheng, J.; Myeong, S.; Cho, W.; Yan, P.; Xiao, J.; Wang, C.; Cho, J.; Zhang, J.-G. *Advanced Energy Materials* **2016**, *7*, 1601284.

[56] Liang, Y.; Zhao, C.-Z.; Yuan, H.; Chen, Y.; Zhang, W.; Huang, J.-Q.; Yu, D.; Liu, Y.; Titirici, M.-M.; Chueh, Y.-L.; Yu, H.; Zhang, Q. *InfoMat* **2019**, *1*, 6–32.

[57] Dahn, J.; von Sacken, U.; Michal, C. *Solid State Ionics* **1990**, *44*, 87–97.

[58] Deng, T.; Fan, X.; Cao, L.; Chen, J.; Hou, S.; Ji, X.; Chen, L.; Li, S.; Zhou, X.; Hu, E.; Su, D.; Yang, X.-Q.; Wang, C. *Joule* **2019**, *3*, 2550–2564.

[59] Kalyani, P.; Kalaiselvi, N. *Science and Technology of Advanced Materials* **2005**, *6*, 689–703.

[60] Bianchini, M.; Roca-Ayats, M.; Hartmann, P.; Brezesinski, T.; Janek, J. *Angewandte Chemie International Edition* **2019**, *58*, 10434–10458.

[61] Yoon, C. S.; Jun, D.-W.; Myung, S.-T.; Sun, Y.-K. *ACS Energy Letters* **2017**, *2*, 1150–1155.

[62] Thackeray, M.; David, W.; Bruce, P.; Goodenough, J. *Materials Research Bulletin* **1983**, *18*, 461–472.

[63] Thackeray, M. M. *Progress in Solid State Chemistry* **1997**, *25*, 1–71.

[64] Jang, D. H.; Shin, Y. J.; Oh, S. M. *Journal of The Electrochemical Society* **1996**, *143*, 2204.

[65] Amine, K.; Tukamoto, H.; Yasuda, H.; Fujita, Y. *Journal of The Electrochemical Society* **1996**, *143*, 1607.

[66] Zhong, Q.; Bonakdarpour, A.; Zhang, M.; Gao, Y.; Dahn, J. R. *Journal of The Electrochemical Society* **1997**, *144*, 205.

[67] Amine, K.; Tukamoto, H.; Yasuda, H.; Fujita, Y. *Journal of Power Sources* **1997**, *68*, 604–608.

[68] G. Bruce, P.; Robert Armstrong, A.; L. Gitzendanner, R. *Journal of Materials Chemistry* **1999**, *9*, 193–198.

[69] Padhi, A. K.; Nanjundaswamy, K. S.; Goodenough, J. B. *Journal of The Electrochemical Society* **1997**, *144*, 1188.

[70] Ling, J.; Karuppiah, C.; Krishnan, S. G.; Reddy, M. V.; Misnon, I. I.; Ab Rahim, M. H.; Yang, C.-C.; Jose, R. *Energy & Fuels* **2021**, *35*, 10428–10450.

[71] Julien, C. M.; Mauger, A.; Zaghib, K.; Groult, H. *Inorganics* **2014**, *2*, 132–154.

[72] Sides, C. R.; Croce, F.; Young, V. Y.; Martin, C. R.; Scrosati, B. *Electrochemical and Solid-State Letters* **2005**, *8*, A484.

[73] Chen, Z.; Zhu, H.; Ji, S.; Fakir, R.; Linkov, V. *Solid State Ionics* **2008**, *179*, 1810–1815.

[74] Elektroautos mit LFP-Batterie. Access: 01/2024; `https://praxis-elektroauto.de/e-autos/lfp-batterie.html`.

[75] CATL launches fast-charging LFP battery. Access: 01/2024; `https://europe.autonews.com/suppliers/catl-launches-fast-charging-lfp-battery`.

[76] Myung, S.-T.; Maglia, F.; Park, K.-J.; Yoon, C. S.; Lamp, P.; Kim, S.-J.; Sun, Y.-K. *ACS Energy Letters* **2017**, *2*, 196–223.

[77] Mao, C.; Wood, M.; David, L.; An, S. J.; Sheng, Y.; Du, Z.; Meyer, H. M.; Ruther, R. E.; Wood, D. L. *Journal of The Electrochemical Society* **2018**, *165*, A1837.

[78] Liu, Z.; Yu, A.; Lee, J. Y. *Journal of Power Sources* **1999**, *81-82*, 416–419.

[79] Noh, H.-J.; Youn, S.; Yoon, C. S.; Sun, Y.-K. *Journal of Power Sources* **2013**, *233*, 121–130.

[80] Whittingham, M. S. *Chemical Reviews* **2004**, *104*, 4271–4302, PMID: 15669156.

[81] Jung, R.; Metzger, M.; Maglia, F.; Stinner, C.; Gasteiger, H. A. *Journal of The Electrochemical Society* **2017**, *164*, A1361.

[82] LG to supply NCMA battery for Tesla next year. Access: 01/2024; `https://www.koreatimes.co.kr/www/tech/2024/01/129_301037.html`.

[83] Bak, S.-M.; Hu, E.; Zhou, Y.; Yu, X.; Senanayake, S. D.; Cho, S.-J.; Kim, K.-B.; Chung, K. Y.; Yang, X.-Q.; Nam, K.-W. *ACS Applied Materials & Interfaces* **2014**, *6*, 22594–22601, PMID: 25420188.

[84] de Biasi, L.; Kondrakov, A. O.; Geßwein, H.; Brezesinski, T.; Hartmann, P.; Janek, J. *The Journal of Physical Chemistry C* **2017**, *121*, 26163–26171.

[85] Schmitt, J.; Kraft, B.; Schmidt, J. P.; Meir, B.; Elian, K.; Ensling, D.; Keser, G.; Jossen, A. *Journal of Power Sources* **2020**, *478*, 228661.

[86] Jung, R.; Strobl, P.; Maglia, F.; Stinner, C.; Gasteiger, H. A. *Journal of The Electrochemical Society* **2018**, *165*, A2869.

[87] Watanabe, S.; Kinoshita, M.; Hosokawa, T.; Morigaki, K.; Nakura, K. *Journal of Power Sources* **2014**, *260*, 50–56.

[88] Freiberg, A. T. S.; Roos, M. K.; Wandt, J.; de Vivie-Riedle, R.; Gasteiger, H. A. *The Journal of Physical Chemistry A* **2018**, *122*, 8828–8839, PMID: 30354136.

[89] Wandt, J.; Freiberg, A. T.; Ogrodnik, A.; Gasteiger, H. A. *Materials Today* **2018**, *21*, 825–833.

[90] Nitta, N.; Wu, F.; Lee, J. T.; Yushin, G. *Materials Today* **2015**, *18*, 252–264.

[91] Shafique, M.; Akbar, A.; Rafiq, M.; Azam, A.; Luo, X. *Waste Management & Research* **2023**, *41*, 376–388, PMID: 36373335.

[92] Momma, K.; Izumi, F. *Journal of Applied Crystallography* **2011**, *44*, 1272–1276.

[93] Manthiram, A. *Nature Communications* **2020**, *11*, 1550.

[94] Malik, M.; Chan, K. H.; Azimi, G. *Materials Today Energy* **2022**, *28*, 101066.

[95] Zhu, J.; Yoo, K.; Denduluri, A.; Hou, W.; Guo, J.; Kisailus, D. *Journal of Materials Research* **2015**, *30*, 286–294.

[96] Xu, K. *Chemical Reviews* **2004**, *104*, 4303–4418, PMID: 15669157.

[97] Zhang, Q.-K.; Zhang, X.-Q.; Yuan, H.; Huang, J.-Q. *Small Science* **2021**, *1*, 2100058.

[98] Xia, L.; Tang, B.; Yao, L.; Wang, K.; Cheris, A.; Pan, Y.; Lee, S.; Xia, Y.; Chen, G. Z.; Liu, Z. *Chemistry Select* **2017**, *2*, 7353–7361.

[99] Väli, R.; Jänes, A.; Lust, E. *Journal of The Electrochemical Society* **2016**, *163*, A851.

[100] Pu, Z.; Xia, J.; Liu, X.; Wang, Q.; Liu, J.; He, X.; Zhong, J. *Journal of Materials Science: Materials in Electronics* **2021**, *32*, 967–976.

[101] Peled, E.; Menkin, S. *Journal of The Electrochemical Society* **2017**, *164*, A1703.

[102] Landesfeind, J.; Gasteiger, H. A. *Journal of The Electrochemical Society* **2019**, *166*, A3079.

[103] Täubert, C.; Fleischhammer, M.; Wohlfahrt-Mehrens, M.; Wietelmann, U.; Buhrmester, T. *Journal of The Electrochemical Society* **2010**, *157*, A721.

[104] Liu, J.; Chen, Z.; Busking, S.; Amine, K. *Electrochemistry Communications* **2007**, *9*, 475–479.

[105] Yang, T.; Zeng, H.; Wang, W.; Zhao, X.; Fan, W.; Wang, C.; Zuo, X.; Zeng, R.; Nan, J. *J. Mater. Chem. A* **2019**, *7*, 8292–8301.

[106] Armand, M.; Axmann, P.; Bresser, D.; Copley, M.; Edström, K.; Ekberg, C.; Guyomard, D.; Lestriez, B.; Novák, P.; Petranikova, M.; Porcher, W.; Trabesinger, S.; Wohlfahrt-Mehrens, M.; Zhang, H. *Journal of Power Sources* **2020**, *479*, 228708.

[107] Sharova, V.; Moretti, A.; Diemant, T.; Varzi, A.; Behm, R.; Passerini, S. *Journal of Power Sources* **2018**, *375*, 43–52.

[108] Aurbach, D.; Gamolsky, K.; Markovsky, B.; Gofer, Y.; Schmidt, M.; Heider, U. *Electrochimica Acta* **2002**, *47*, 1423–1439.

[109] Soto, F. A.; Ma, Y.; Martinez de la Hoz, J. M.; Seminario, J. M.; Balbuena, P. B. *Chemistry of Materials* **2015**, *27*, 7990–8000.

[110] Zhang, S. S. *Journal of Power Sources* **2006**, *162*, 1379–1394.

[111] Burns, J. C.; Kassam, A.; Sinha, N. N.; Downie, L. E.; Solnickova, L.; Way, B. M.; Dahn, J. R. *Journal of The Electrochemical Society* **2013**, *160*, A1451.

[112] Burns, J. C.; Petibon, R.; Nelson, K. J.; Sinha, N. N.; Kassam, A.; Way, B. M.; Dahn, J. R. *Journal of The Electrochemical Society* **2013**, *160*, A1668.

[113] Gauthier, R.; Hall, D. S.; Lin, K.; Baltazar, J.; Hynes, T.; Dahn, J. R. *Journal of The Electrochemical Society* **2020**, *167*, 080540.

[114] Teufl, T.; Pritzl, D.; Krieg, P.; Strehle, B.; Mendez, M. A.; Gasteiger, H. A. *Journal of The Electrochemical Society* **2020**, *167*, 110505.

[115] Jena, A.; Tong, Z.; Bazri, B.; Iputera, K.; Chang, H.; Hu, S.-F.; Liu, R.-S. *The Journal of Physical Chemistry C* **2021**, *125*, 16921–16937.

[116] de Biasi, L.; Schwarz, B.; Brezesinski, T.; Hartmann, P.; Janek, J.; Ehrenberg, H. *Advanced Materials* **2019**, *31*, 1900985.

[117] Adenusi, H.; Chass, G. A.; Passerini, S.; Tian, K. V.; Chen, G. *Advanced Energy Materials* **2023**, *13*, 2203307.

[118] An, S. J.; Li, J.; Daniel, C.; Mohanty, D.; Nagpure, S.; Wood, D. L. *Carbon* **2016**, *105*, 52–76.

[119] Dey, A. N.; Sullivan, B. P. *Journal of The Electrochemical Society* **1970**, *117*, 222.

[120] Nazri, G.; Muller, R. H. *Journal of The Electrochemical Society* **1985**, *132*, 2050.

[121] Aurbach, D.; Daroux, M. L.; Faguy, P. W.; Yeager, E. *Journal of The Electrochemical Society* **1987**, *134*, 1611.

[122] Peled, E.; Golodnitsky, D.; Ardel, G.; Eshkenazy, V. *Electrochimica Acta* **1995**, *40*, 2197–2204.

[123] Aurbach, D.; Markovsky, B.; Levi, M.; Levi, E.; Schechter, A.; Moshkovich, M.; Cohen, Y. *Journal of Power Sources* **1999**, *81-82*, 95–111.

[124] Peljo, P.; Girault, H. H. *Energy and Environmental Science* **2018**, *11*, 2306–2309.

[125] Gauthier, M.; Carney, T. J.; Grimaud, A.; Giordano, L.; Pour, N.; Chang, H.-H.; Fenning, D. P.; Lux, S. F.; Paschos, O.; Bauer, C.; Maglia, F.; Lupart, S.; Lamp, P.; Shao-Horn, Y. *The Journal of Physical Chemistry Letters* **2015**, *6*, 4653–4672, PMID: 26510477.

[126] Etacheri, V.; Marom, R.; Elazari, R.; Salitra, G.; Aurbach, D. *Energy and Environmental Science* **2011**, *4*, 3243–3262.

[127] Imhof, R.; Novák, P. *Journal of The Electrochemical Society* **1998**, *145*, 1081.

[128] Pereira, D. J.; McRay, H. A.; Bopte, S. S.; Jalilvand, G. *ACS Applied Materials & Interfaces* **2024**, *16*, 5745–5757, PMID: 38286992.

[129] Misiewicz, C.; Lundström, R.; Ahmed, I.; Lacey, M. J.; Brant, W. R.; Berg, E. J. *Journal of Power Sources* **2023**, *554*, 232318.

[130] Zhang, Y.; Du, N.; Yang, D. *Nanoscale* **2019**, *11*, 19086–19104.

[131] Spotte-Smith, E. W. C.; Kam, R. L.; Barter, D.; Xie, X.; Hou, T.; Dwaraknath, S.; Blau, S. M.; Persson, K. A. *ACS Energy Letters* **2022**, *7*, 1446–1453.

[132] BatteryBits; Battery Manufacturing from CATL´s Cell Production Line. Access: 01/2021; `https://medium.com/batterybits/battery-manufacturing-basics-from-catls-cell-production-line-part-1-d6bb6aa0b499`.

[133] Infographics Battery Making at a Glance - Battery LAB 2023. Access: 01/2024; https://inside.lgensol.com/en/2023/06/infographics-3-battery-making-at-a-glance/.

[134] RWTH-Aachen Lithium ion battery cell production process - RWTH Aachen - 3rd edition. Access: 01/2024; https://www.pem.rwth-aachen.de/global.

[135] Schmitt, M.; Baunach, M.; Wengeler, L.; Peters, K.; Junges, P.; Scharfer, P.; Schabel, W. *Chemical Engineering and Processing: Process Intensification* **2013**, *68*, 32–37.

[136] Primo, E. N.; Chouchane, M.; Touzin, M.; Vazquez, P.; Franco, A. A. *Journal of Power Sources* **2021**, *488*, 229361.

[137] Morasch, R.; Keilhofer, J.; Gasteiger, H. A.; Suthar, B. *Journal of The Electrochemical Society* **2021**, *168*, 080519.

[138] Abdollahifar, M.; Cavers, H.; Scheffler, S.; Diener, A.; Lippke, M.; Kwade, A. *Advanced Energy Materials* **2023**, *13*, 2300973.

[139] Logakannan, K. P.; Zhu, F.; Sypeck, D.; Deng, J.; Kim, S. *International Journal of Impact Engineering* **2022**, *170*, 104352.

[140] Battery, B. Winding vs. Stacking, which works best for lithium-ion batteries. Access: 01/2024; https://www.bonnenbatteries.com/winding-vs-stacking-which-technology-works-best-for-lithium-ion-batteries/.

[141] Meyer, C.; Bockholt, H.; Haselrieder, W.; Kwade, A. *Journal of Materials Processing Technology* **2017**, *249*, 172–178.

[142] Shim, J.; Striebel, K. A. *Journal of Power Sources* **2003**, *119-121*, 934–937.

[143] Kang, H.; Lim, C.; Li, T.; Fu, Y.; Yan, B.; Houston, N.; De Andrade, V.; De Carlo, F.; Zhu, L. *Electrochimica Acta* **2017**, *232*, 431–438.

[144] Wood, D. L.; Li, J.; An, S. J. *Joule* **2019**, *3*, 2884–2888.

[145] Wood, D. L.; Li, J.; Daniel, C. *Journal of Power Sources* **2015**, *275*, 234–242.

[146] Drees, R.; Lienesch, F.; Kurrat, M. *Journal of Energy Storage* **2021**, *36*, 102345.

[147] Oh, S. M.; Song, J.; Lee, S.; Jang, I.-C. *Electrochimica Acta* **2021**, *397*, 139269.

[148] Solchenbach, S.; Metzger, M.; Egawa, M.; Beyer, H.; Gasteiger, H. A. *Journal of The Electrochemical Society* **2018**, *165*, A3022.

[149] Wang, L.; Menakath, A.; Han, F.; Wang, Y.; Zavalij, P. Y.; Gaskell, K. J.; Borodin, O.; Iuga, D.; Brown, S. P.; Wang, C.; Xu, K.; Eichhorn, B. W. *Nature Chemistry* **2019**, *11*, 789–796.

[150] Winter, M. *Zeitschrift für Physikalische Chemie* **2009**, *223*, 1395–1406.

[151] Verma, P.; Maire, P.; Novák, P. *Electrochimica Acta* **2010**, *55*, 6332–6341.

[152] An, S. J.; Li, J.; Du, Z.; Daniel, C.; Wood, D. L. *Journal of Power Sources* **2017**, *342*, 846–852.

[153] Link, S.; Neef, C.; Wicke, T. *Batteries* **2023**, *9*.

[154] Tesla applies to expand Shanghai plant and add pouch battery cell output. Access: 01/2024; https://www.reuters.com/business/autos-transportation/tesla-applies-expand-shanghai-plant-add-pouch-battery-cell-output-2023-05-16/.

[155] Electric vehicles and their batteries. Access: 02/2024; https://www.evexpert.eu/eshop1/knowledge-center/electric-vehicles-and-their-batteries#:~:text=BMW%20and%20Volkswagen%20use%20prismatic,of%20charge%20and%20discharge%20cycles.

[156] BMW Press Club. Access: 08/2024; https://www.press.bmwgroup.com/deutschland/.

[157] Potentials of 46 mm cylindrical cells: On the way to the new standard format. Access: 01/2024; https://www.isi.fraunhofer.de/en/blog/themen/batterie-update/46-mm-rundzellen-potenziale-standardformat-batteriezellen.html.

[158] Innovative Product: Lithium ion rechargeable battery. Access: 02/2024; https://holdings.panasonic/global/corporate/about/history/chronicle/1994.html.

[159] Lundström, R.; Berg, E. J. *Journal of Power Sources* **2021**, *485*, 229347.

[160] Li, H.; Guo, S.; Zhou, H. *Journal of Energy Chemistry* **2021**, *59*, 191–211.

[161] Grant, A.; O'Dwyer, C. **2022**, Operando Methods and Probes for Battery Electrodes and Materials.

[162] Liu, D. et al. *Advanced Materials* **2019**, *31*, 1806620.

[163] Fawdon, J.; Ihli, J.; Mantia, F. L.; Pasta, M. *Nature Communications* **2021**, *12*, 4053.

[164] Bray, J. M.; Doswell, C. L.; Pavlovskaya, G. E.; Chen, L.; Kishore, B.; Au, H.; Alptekin, H.; Kendrick, E.; Titirici, M.-M.; Meersmann, T.; Britton, M. M. *Nature Communications* **2020**, *11*, 2083.

[165] Iffelsberger, C.; Wert, S.; Matysik, F.-M.; Pumera, M. *ACS Applied Materials & Interfaces* **2021**, *13*, 35777–35784, PMID: 34283572.

[166] Eidenschink, J.; Bagherimetkazini, S.; Matysik, F.-M. *Monatshefte für Chemie - Chemical Monthly* **2022**, *153*, 775–780.

[167] Cindric, M.; Matysik, F.-M. *TrAC Trends in Analytical Chemistry* **2015**, *70*, 122–127.

[168] Bruckenstein, S.; Gadde, R. R. *Journal of the American Chemical Society* **1971**, *93*, 793–794.

[169] Wolter, O.; Heitbaum, J. *Berichte der Bunsengesellschaft für physikalische Chemie* **1984**, *88*, 2–6.

[170] Novák, P.; Joho, F.; Imhof, R.; Panitz, J.-C.; Haas, O. *Journal of Power Sources* **1999**, *81-82*, 212–216.

[171] Kitz, P. G.; Lacey, M. J.; Novák, P.; Berg, E. J. *Journal of Power Sources* **2020**, *477*, 228567.

[172] He, M.; Castel, E.; Laumann, A.; Nuspl, G.; Novák, P.; Berg, E. J. *Journal of The Electrochemical Society* **2015**, *162*, A870.

[173] McCloskey, B. D.; Bethune, D. S.; Shelby, R. M.; Girishkumar, G.; Luntz, A. C. *The Journal of Physical Chemistry Letters* **2011**, *2*, 1161–1166, PMID: 26295320.

[174] Berkes, B. B.; Jozwiuk, A.; Vračar, M.; Sommer, H.; Brezesinski, T.; Janek, J. *Analytical Chemistry* **2015**, *87*, 5878–5883, PMID: 25965095.

[175] He, M.; Boulet-Roblin, L.; Borel, P.; Tessier, C.; Novák, P.; Villevieille, C.; Berg, E. J. *Journal of The Electrochemical Society* **2015**, *163*, A83.

[176] Tsiouvaras, N.; Meini, S.; Buchberger, I.; Gasteiger, H. A. *Journal of The Electrochemical Society* **2013**, *160*, A471.

[177] Oak Ridge, U., TN Vacuum Technology Incorporation. Access: 01/2023; `https://vacuumtechnology.com/`.

[178] Aiken, C. P.; Xia, J.; Wang, D. Y.; Stevens, D. A.; Trussler, S.; Dahn, J. R. *Journal of The Electrochemical Society* **2014**, *161*, A1548.

[179] Aiken, C. P.; Self, J.; Petibon, R.; Xia, X.; Paulsen, J. M.; Dahn, J. R. *Journal of The Electrochemical Society* **2015**, *162*, A760.

[180] Ellis, L. D.; Allen, J. P.; Thompson, L. M.; Harlow, J. E.; Stone, W. J.; Hill, I. G.; Dahn, J. R. *Journal of The Electrochemical Society* **2017**, *164*, A3518.

[181] Matasso, A.; Wetz, D.; Liu, F. *Journal of The Electrochemical Society* **2014**, *162*, A92.

[182] Schmiegel, J.-P.; Leißing, M.; Weddeling, F.; Horsthemke, F.; Reiter, J.; Fan, Q.; Nowak, S.; Winter, M.; Placke, T. *Journal of The Electrochemical Society* **2020**, *167*, 060516.

[183] Mattinen, U.; Klett, M.; Lindbergh, G.; Wreland Lindström, R. *Journal of Power Sources* **2020**, *477*, 228968.

[184] Oehme, M. *Praktische Einführung in die GC-MS-Analytik mit Quadrupolen - Grundlagen und Anwendungen*; Hüthig: Heidelberg, 1996.

[185] Wien, W. *Annalen der Physik* **1904**, *318*, 669–677.

[186] Squires, G. *J. Chem. Soc., Dalton Trans.* **1998**, 3893–3900.

[187] Dempster, A. J. *Phys. Rev.* **1918**, *11*, 316–325.

[188] Grayson, M. A. *Journal of the American Society for Mass Spectrometry* **1992**, *3*, 685–694.

[189] March, R. E. *Journal of Mass Spectrometry* **1997**, *32*, 351–369.

[190] Atkins, P. W.; Paula, J. d.; Bär, M. *Physikalische Chemie* -, 5th ed.; John Wiley & Sons: New York, 2013.

[191] Kromidas, S. *Das HPLC-MS-Buch für Anwender* -; John Wiley & Sons: New York, 2017.

[192] Gross, J. H. *Massenspektrometrie - Spektroskopiekurs kompakt*; Springer-Verlag: Berlin Heidelberg New York, 2019.

[193] Lundström, R.; Gogoi, N.; Hou, X.; Berg, E. J. *Journal of The Electrochemical Society* **2023**, *170*, 040516.

[194] Mott Corporation Porous Metal Products. Access: 01/2023; `https://mottcorp.com/de/`.

[195] Kissinger, P.; Heineman, W. R. *Laboratory Techniques in Electroanalytical Chemistry*, 2nd ed.; CRC Press: Boca Raton, USA, 2018.

[196] Bard, A. J.; Faulkner, L. R. *Electrochemical Methods: Fundamentals and Applications*, 2nd ed.; John Wiley & Sons: New York, 2000.

[197] Lazraq, O.; Abduh, A.; Goncharova, I.; Yazami, R. *International Journal of Engineering Science* **2019**, *8*, 57–64.

[198] Tran, H. Y.; Greco, G.; Täubert, C.; Wohlfahrt-Mehrens, M.; Haselrieder, W.; Kwade, A. *Journal of Power Sources* **2012**, *210*, 276–285.

[199] Littlewood, A. B. *Gas Chromatography: Principles, Techniques, and Applications*; Elsevier, 2013.

[200] Brunauer, S.; Emmett, P. H.; Teller, E. *Journal of the American Chemical Society* **1938**, *60*, 309–319.

[201] Langmuir, L. *Nobel Lecture* **1932**, *14*, 287–325.

[202] Sing, K. S. *Advances in Colloid and Interface Science* **1998**, *76-77*, 3 – 11.

[203] Cross-Section-Value. Access: 02/2023; `https://chem.libretexts.org/Bookshelves/Physical_and_Theoretical_Chemistry_Textbook_Maps/Supplemental_Modules_%28Physical_and_Theoretical_Chemistry%29/Kinetics/Modeling_Reaction_Kinetics/Collision_Theory/Collisional_Cross_Section`.

[204] Bhutada, G. Visualizing 25 Years of Lithium Production, by Country. Access: 02/2023; `https://www.visualcapitalist.com/visualizing-25-years-of-lithium-production-by-country/`.

[205] Sångeland, C.; Mindemark, J.; Younesi, R.; Brandell, D. *Solid State Ionics* **2019**, *343*, 115068.

[206] Teng, X.; Zhan, C.; Bai, Y.; Ma, L.; Liu, Q.; Wu, C.; Wu, F.; Yang, Y.; Lu, J.; Amine, K. *ACS Applied Materials & Interfaces* **2015**, *7*, 22751–22755, PMID: 26417916.

[207] Rowden, B.; Garcia-Araez, N. *Energy Reports* **2020**, *6*, 10–18.

[208] Herl, T.; Heigl, N.; Matysik, F.-M. *Monatshefte für Chemie - Chemical Monthly* **2018**, *149*, 1685–1691.

[209] Strehle, B.; Solchenbach, S.; Metzger, M.; Schwenke, K. U.; Gasteiger, H. A. *Journal of The Electrochemical Society* **2017**, *164*, A2513.

[210] Anouti, M.; Dougassa, Y. R.; Tessier, C.; El Ouatani, L.; Jacquemin, J. *The Journal of Chemical Thermodynamics* **2012**, *50*, 71–79.

[211] Raghibi, M.; Xiong, B.; Phadke, S.; Anouti, M. *Electrochimica Acta* **2020**, *362*, 137214.

[212] Solchenbach, S.; Hong, G.; Freiberg, A. T. S.; Jung, R.; Gasteiger, H. A. *Journal of The Electrochemical Society* **2018**, *165*, A3304.

[213] Guéguen, A.; Streich, D.; He, M.; Mendez, M.; Chesneau, F. F.; Novák, P.; Berg, E. J. *Journal of The Electrochemical Society* **2016**, *163*, A1095.

[214] Barani weather stations and meteorological sensors. Access: 02/2024; `https://www.baranidesign.com/`.

[215] Li, W.; Reimers, J.; Dahn, J. *Solid State Ionics* **1993**, *67*, 123–130.

[216] Lenze, G.; Röder, F.; Bockholt, H.; Haselrieder, W.; Kwade, A.; Krewer, U. *Journal of The Electrochemical Society* **2017**, *164*, A1223.

[217] Oswald, S.; Gasteiger, H. A. *Journal of The Electrochemical Society* **2023**, *170*, 030506.

[218] Smekens, J.; Gopalakrishnan, R.; Steen, N. V. d.; Omar, N.; Hegazy, O.; Hubin, A.; Van Mierlo, J. *Energies* **2016**, *9*.

[219] Schmidt, D.; Kamlah, M.; Knoblauch, V. *Journal of Energy Storage* **2018**, *17*, 213–223.

[220] DuBeshter, T.; Sinha, P. K.; Sakars, A.; Fly, G. W.; Jorne, J. *Journal of The Electrochemical Society* **2014**, *161*, A599.

[221] Tran, N.; Croguennec, L.; Ménétrier, M.; Weill, F.; Biensan, P.; Jordy, C.; Delmas, C. *Chemistry of Materials* **2008**, *20*, 4815–4825.

[222] Sharifi-Asl, S.; Lu, J.; Amine, K.; Shahbazian-Yassar, R. *Advanced Energy Materials* **2019**, *9*, 1900551.

[223] Kaufman, L. A.; McCloskey, B. D. *Chemistry of Materials* **2021**, *33*, 4170–4176.

[224] Hatsukade, T.; Schiele, A.; Hartmann, P.; Brezesinski, T.; Janek, J. *ACS Applied Materials & Interfaces* **2018**, *10*, 38892–38899, PMID: 30335934.

[225] Hu, J.; Li, L.; Bi, Y.; Tao, J.; Lochala, J.; Liu, D.; Wu, B.; Cao, X.; Chae, S.; Wang, C.; Xiao, J. *Energy Storage Materials* **2022**, *47*, 195–202.

[226] Xiong, D. J.; Ellis, L. D.; Li, J.; Li, H.; Hynes, T.; Allen, J. P.; Xia, J.; Hall, D. S.; Hill, I. G.; Dahn, J. R. *Journal of The Electrochemical Society* **2017**, *164*, A3025.

[227] de Biasi, L.; Schiele, A.; Roca-Ayats, M.; Garcia, G.; Brezesinski, T.; Hartmann, P.; Janek, J. *ChemSusChem* **2019**, *12*, 2240–2250.

[228] Lu, Z.; Dahn, J. R. *Journal of The Electrochemical Society* **2002**, *149*, A815.

[229] Mu, L.; Lin, R.; Xu, R.; Han, L.; Xia, S.; Sokaras, D.; Steiner, J. D.; Weng, T.-C.; Nordlund, D.; Doeff, M. M.; Liu, Y.; Zhao, K.; Xin, H. L.; Lin, F. *Nano Letters* **2018**, *18*, 3241–3249, PMID: 29667835.

[230] Scharf, J.; Matysik, F.-M. *Monatshefte für Chemie - Chemical Monthly* **2023**, *154*, 1025–1033.

[231] Scharf, J.; von Lüders, C.; Matysik, F.-M.; Misiewicz, C.; Wandt, J.; Berg, E. J. *Journal of Power Sources* **2024**, *603*, 234419.

[232] Marks, T.; Trussler, S.; Smith, A. J.; Xiong, D.; Dahn, J. R. *Journal of The Electrochemical Society* **2010**, *158*, A51.

[233] Haselrieder, W.; Ivanov, S.; Christen, D. K.; Bockholt, H.; Kwade, A. *ECS Transactions* **2013**, *50*, 59.

[234] Stock, S.; Hagemeister, J.; Grabmann, S.; Kriegler, J.; Keilhofer, J.; Ank, M.; Dickmanns, J. L.; Schreiber, M.; Konwitschny, F.; Wassiliadis, N.; Lienkamp, M.; Daub, R. *Electrochimica Acta* **2023**, *471*, 143341.

[235] Bockholt, H.; Indrikova, M.; Netz, A.; Golks, F.; Kwade, A. *Journal of Power Sources* **2016**, *325*, 140–151.

[236] Kuchler, K.; Prifling, B.; Schmidt, D.; Marköttter, H.; Manke, I.; Bernthaler, T.; Knoblauch, V.; Schmidt, V. *Journal of Microscopy* **2018**, *272*, 0022–2720.

[237] Hamed, H.; Henderick, L.; Choobar, B. G.; D'Haen, J.; Detavernier, C.; Hardy, A.; Safari, M. *iScience* **2021**, *24*, 103496.

[238] Gnanaraj, J.; Cohen, Y. S.; Levi, M.; Aurbach, D. *Journal of Electroanalytical Chemistry* **2001**, *516*, 89–102.

[239] Park, K.-J.; Jung, H.-G.; Kuo, L.-Y.; Kaghazchi, P.; Yoon, C. S.; Sun, Y.-K. *Advanced Energy Materials* **2018**, *8*, 1801202.

[240] Chung, H.; Li, Y.; Zhang, M.; Grenier, A.; Mejia, C.; Cheng, D.; Sayahpour, B.; Song, C.; Shen, M. H.; Huang, R.; Wu, E. A.; Chapman, K. W.; Kim, S. J.; Meng, Y. S. *Chemistry of Materials* **2022**, *34*, 7302–7312.

[241] Lebens-Higgins, Z. W. et al. *Mater. Horiz.* **2019**, *6*, 2112–2123.

[242] Wolfman, M.; May, B. M.; Goel, V.; Du, S.; Yu, Y.-S.; Faenza, N. V.; Pereira, N.; Grenier, A.; Wiaderek, K. M.; Xu, R.; Wang, J.; Chapman, K. W.; Amatucci, G. G.; Thornton, K.; Cabana, J. *Advanced Energy Materials* **2023**, *13*, 2300895.

[243] Li, Z.; Yin, L.; Mattei, G. S.; Cosby, M. R.; Lee, B.-S.; Wu, Z.; Bak, S.-M.; Chapman, K. W.; Yang, X.-Q.; Liu, P.; Khalifah, P. G. *Chemistry of Materials* **2020**, *32*, 6358–6364.

[244] Park, J.; Zhao, H.; Kang, S. D.; Lim, K.; Chen, C.-C.; Yu, Y.-S.; Braatz, R. D.; Shapiro, D. A.; Hong, J.; Toney, M. F.; Bazant, W. C., Martin Z.and Chueh *Nature Materials* **2021**, *20*, 991–999.

[245] Dose, W. M.; Morzy, J. K.; Mahadevegowda, A.; Ducati, C.; Grey, C. P.; De Volder, M. F. L. *J. Mater. Chem. A* **2021**, *9*, 23582–23596.

[246] Freiberg, A. T.; Sicklinger, J.; Solchenbach, S.; Gasteiger, H. A. *Electrochimica Acta* **2020**, *346*, 136271.

[247] Mahne, N.; Renfrew, S. E.; McCloskey, B. D.; Freunberger, S. A. *Angewandte Chemie International Edition* **2018**, *57*, 5529–5533.

[248] Lambrecht, M. Klimaschutz im Verkehr. Access: 07/2023; `https://www.umweltbundesamt.de/themen/verkehr/klimaschutz-im-verkehr`.

[249] Howell, D. **2020**, Electrochemical Energy Storage R&D Overview.

[250] Northvolt - the future of energy. Access: 07/2023; `https://northvolt.com/`.

[251] Metzger, M.; Gasteiger, H. A. *Energy & Environmental Materials* **2022**, *5*, 688–692.

[252] Ding, M. S.; Xu, K.; Zhang, S.; Jow, T. R. *Journal of The Electrochemical Society* **2001**, *148*, A299.

[253] Stock, S.; Diller, F.; Böhm, J.; Hille, L.; Hagemeister, J.; Sommer, A.; Daub, R. *Journal of The Electrochemical Society* **2023**, *170*, 060539.

[254] Matthew, L.; James, F.; Ulderico, U. *Nature Communications* **2023**, *14*, 420.

[255] Sloop, S. E.; Kerr, J. B.; Kinoshita, K. *Journal of Power Sources* **2003**, *119-121*, 330–337.

[256] Darensbourg, D. J.; Holtcamp, M. W. *Coordination Chemistry Reviews* **1996**, *153*, 155–174.

[257] Aurbach, D.; Gofer, Y.; Ben-Zion, M.; Aped, P. *Journal of Electroanalytical Chemistry* **1992**, *339*, 451–471.

[258] Mogi, R.; Inaba, M.; Iriyama, Y.; Abe, T.; Ogumi, Z. *Journal of Power Sources* **2003**, *119-121*, 597–603.

[259] Schwenke, K. U.; Solchenbach, S.; Demeaux, J.; Lucht, B. L.; Gasteiger, H. A. *Journal of The Electrochemical Society* **2019**, *166*, A2035.

[260] Melin, T.; Lundström, R.; Berg, E. J. *Advanced Materials Interfaces* **2022**, *9*, 2101258.

[261] Metzger, M.; Strehle, B.; Solchenbach, S.; Gasteiger, H. A. *Journal of The Electrochemical Society* **2016**, *163*, A1219.

[262] Cussler, E. L. *Diffusion: Mass Transfer in Fluid Systems*; Cambridge University Press, 1997.

[263] Ota, H.; Sakata, Y.; Otake, Y.; Shima, K.; Ue, M.; ichi Yamaki, J. *Journal of The Electrochemical Society* **2004**, *151*, A1778.

[264] Onuki, M.; Kinoshita, S.; Sakata, Y.; Yanagidate, M.; Otake, Y.; Ue, M.; Deguchi, M. *Journal of The Electrochemical Society* **2008**, *155*, A794.

[265] Leung, K. *ECS Meeting Abstracts* **2013**, *MA2013-01*, 342.

[266] Wang, Y.; Balbuena, P. B. *The Journal of Physical Chemistry B* **2002**, *106*, 4486–4495.

[267] Metzger, M.; Marino, C.; Sicklinger, J.; Haering, D.; Gasteiger, H. A. *Journal of The Electrochemical Society* **2015**, *162*, A1123.

[268] Sasaki, T.; Abe, T.; Iriyama, Y.; Inaba, M.; Ogumi, Z. *Journal of Power Sources* **2005**, *150*, 208–215.

[269] Laruelle, S.; Pilard, S.; Guenot, P.; Grugeon, S.; Tarascon, J.-M. *Journal of The Electrochemical Society* **2004**, *151*, A1202.

[270] Dougassa, Y. R.; Tessier, C.; El Ouatani, L.; Anouti, M.; Jacquemin, J. *The Journal of Chemical Thermodynamics* **2013**, *61*, 32–44.

[271] Leißing, M.; Peschel, C.; Horsthemke, F.; Wiemers-Meyer, S.; Winter, M.; Nowak, S. *Batteries & Supercaps* **2021**, *4*, 1731–1738.

[272] Henschel, J.; Peschel, C.; Klein, S.; Horsthemke, F.; Winter, M.; Nowak, S. *Angewandte Chemie International Edition* **2020**, *59*, 6128–6137.

[273] Peschel, C.; Horsthemke, F.; Leißing, M.; Wiemers-Meyer, S.; Henschel, J.; Winter, M.; Nowak, S. *Batteries & Supercaps* **2020**, *3*, 1183–1192.

[274] El Ouatani, L.; Dedryvère, R.; Ledeuil, J.-B.; Siret, C.; Biensan, P.; Desbrières, J.; Gonbeau, D. *Journal of Power Sources* **2009**, *189*, 72–80.

[275] Schmitz, R. W. et al. *Progress in Solid State Chemistry* **2014**, *42*, 65–84.

[276] Zhuang, G.; Wang, K.; Ross, P. *Surface Science* **1997**, *387*, 199–212.

[277] Wu, H.; Zheng, G.; Liu, N.; Carney, T. J.; Yang, Y.; Cui, Y. *Nano Letters* **2012**, *12*, 904–909, PMID: 22224827.

[278] Michan, A. L.; Parimalam, B. S.; Leskes, M.; Kerber, R. N.; Yoon, T.; Grey, C. P.; Lucht, B. L. *Chemistry of Materials* **2016**, *28*, 8149–8159.

[279] Ota, H.; Sakata, Y.; Inoue, A.; Yamaguchi, S. *Journal of The Electrochemical Society* **2004**, *151*, A1659.

[280] Schiele, A.; Breitung, B.; Hatsukade, T.; Berkes, B. B.; Hartmann, P.; Janek, J.; Brezesinski, T. *ACS Energy Letters* **2017**, *2*, 2228–2233.

[281] Wang, P.; Li, J.; Zhang, Y.; Cui, X.; Zhao, D.; Li, S. *Journal of Power Sources* **2023**, *565*, 232881.

[282] Li, S.; Li, J.; Wang, P.; Ding, H.; Zhou, J.; Li, C.; Cui, X. *Advanced Functional Materials* **2024**, *34*, 2307180.

[283] Jin, Y.; Kneusels, N.-J. H.; Marbella, L. E.; Castillo-Martínez, E.; Magusin, P. C. M. M.; Weatherup, R. S.; Jónsson, E.; Liu, T.; Paul, S.; Grey, C. P. *Journal of the American Chemical Society* **2018**, *140*, 9854–9867, PMID: 29979869.

[284] Jung, R.; Metzger, M.; Haering, D.; Solchenbach, S.; Marino, C.; Tsiouvaras, N.; Stinner, C.; Gasteiger, H. A. *Journal of The Electrochemical Society* **2016**, *163*, A1705.

List of Figures

List of Tables